Provided for non-commercial research and education use. Not for reproduction, distribution or commercial use.



This article appeared in a journal published by Elsevier. The attached copy is furnished to the author for internal non-commercial research and education use, including for instruction at the authors institution and sharing with colleagues.

Other uses, including reproduction and distribution, or selling or licensing copies, or posting to personal, institutional or third party websites are prohibited.

In most cases authors are permitted to post their version of the article (e.g. in Word or Tex form) to their personal website or institutional repository. Authors requiring further information regarding Elsevier's archiving and manuscript policies are encouraged to visit:

http://www.elsevier.com/copyright

### Author's personal copy

Materials Research Bulletin 44 (2009) 2206-2210



Contents lists available at ScienceDirect

#### Materials Research Bulletin

journal homepage: www.elsevier.com/locate/matresbu



# Flower-like microparticles and novel superparamagnetic properties of new binary $\text{Co}_{1/2}\text{Fe}_{1/2}(\text{H}_2\text{PO}_4)_2\cdot 2\text{H}_2\text{O}$ obtained by a rapid solid state route at ambient temperature

Banjong Boonchom a,b,\*, Montree Thongkam C, Samart Kongtaweelert C, Naratip Vittayakorn b,d

- <sup>a</sup> King Mongkut's Institute of Technology Ladkrabang, Chumphon Campus, 17/1M. 6 Pha Thiew District, Chumphon 86160, Thailand
- <sup>b</sup> Advanced Materials Science Research Unit, Department of Chemistry, Faculty of Science, King Mongkut's Institute of Technology Ladkrabang, Bangkok 10520, Thailand
- <sup>c</sup>Department of Chemistry, Faculty of Science, King Mongkut's Institute of Technology Ladkrabang, Ladkrabang, Bangkok 10520, Thailand
- <sup>d</sup> College of KMITL Nanotechnology, King Mongkut's Institute of Technology Ladkrabang, Bangkok 10520, Thailand

#### ARTICLE INFO

#### Article history: Received 7 July 2009 Received in revised form 19 July 2009 Accepted 4 August 2009 Available online 12 August 2009

Keywords:
A. Inorganic compounds
Ceramics
B. Chemical synthesis
C. Infrared spectroscopy
Thermogravimetric analysis (TGA)

#### ABSTRACT

A new binary  $Co_{1/2}Fe_{1/2}(H_2PO_4)_2 \cdot 2H_2O$  was synthesized by a simple, rapid and cost-effective method using  $CoCO_3 - Fe(c) - H_3PO_4$  system at ambient temperature. Thermal treatment of the obtained  $Co_{1/2}Fe_{1/2}(H_2PO_4)_2 \cdot 2H_2O$  at 600 °C yielded as a binary cobalt iron cyclotetraphosphate  $CoFeP_4O_{12}$ . The FTIR and XRD results of the synthesized  $Co_{1/2}Fe_{1/2}(H_2PO_4)_2 \cdot 2H_2O$  and its final decomposed product  $CoFeP_4O_{12}$  indicate the monoclinic phases with space group  $P2_1/n$  and C2/c, respectively. The particle morphologies of both binary metal compounds appear the flower-like microparticle shapes. Room temperature magnetization results show novel superparamagnetic behaviors of the  $Co_{1/2}Fe_{1/2}(H_2PO_4)_2 \cdot 2H_2O$  and its final decomposed product  $CoFeP_4O_{12}$ , having no hysteresis loops in the range of  $E_1O_1O0O$  Oe with the specific magnetization values of  $E_1O_1O0O$  Oe with the single compounds  $E_1O_1O0O$  Oe with the single compounds  $E_1O0O$  Oe with the single compounds of  $E_1O0O$  Oe with the single compounds of  $E_1O0O$  Oe of

© 2009 Elsevier Ltd. All rights reserved.

#### 1. Introduction

D. Magnetic properties

In recent years, a large number of inorganic natural or synthesized phosphates have the incremented use in order to supply the demands of industrial, commercial, scientific and heath sectors due to valuable physical–chemical properties and reactivity [1–4]. The metal phosphate compounds are divided by block unit as PO<sub>4</sub><sup>3-</sup>, HPO<sub>4</sub><sup>2-</sup>, H<sub>2</sub>PO<sub>4</sub><sup>-</sup>, P<sub>2</sub>O<sub>7</sub><sup>4-</sup> and P<sub>4</sub>O<sub>12</sub><sup>4-</sup> units, which have found widespread applications in catalysts and adsorbents, ion-exchange materials, solid electrolytes for batteries, in linear and non-linear optical components, chelating agents, tooth powder and doughs, artificial teeth and bones, corrosion-resistant coating, sewage purifying agents, glass-ceramics, refratories, fire extinguishers, cements, soap powders, biomaterials and implantates, forages for animals, superinonic conductors, piezo- and ferroelectrics, gas and moisture sensors, magnets, phosphors, detergents and high-quality fertilizers [5–11]. Synthesis of these materials by solid state reaction

at ambient temperature and the morphology and architecture at microscale and nanoscale levels is a significant challenge, which attracts increased attention because of their conveniences and their strong influence on material properties.

Metal dihydrogenphosphate (H<sub>2</sub>PO<sub>4</sub><sup>-</sup>) group, one of the important metal phosphates, has found widespread applications according to above mentioned. Additionally, this metal dihydrogenphosphate group is transformed to metal cyclotetraphosphate  $(P_4O_{12}^{4-})$  group by dehydration and polycondensation reactions at high temperature, which is advance material, such as ceramic pigment, catalyst and fertilizer [12-17]. Both metal dihydrogenphosphate and metal cyclotetraphosphate groups have received a great deal of attention due to simple, nontoxic and cheap synthetic routes and their friendly environment [5–11]. Consequently, in the last few years many works have been a successful attempt in the synthesis of metal (II) dihydrogenphosphate hydrates  $M_{1-x}A_x(H_2PO_4)_2\cdot nH_2O$  (M and A = Mg, Ca, Mn, Fe, Co, Ni, Zn, or Cu; x = 0-1; n = 1-4) [12–17] and metal (II) cyclotetraphosphates  $M_{2-\nu}A_{\nu}P_4O_{12}$  (y = 0-2) [15–17]. However, it is pertinent to synthesize binary metal dihydrogenphosphates, binary metal cyclotetraphosphates and their solid solutions. By varying the composition of the solid solution (within its homogeneity range), one can change its useful properties. So far, binary metal dihydrogen phosphates were synthesized from

<sup>\*</sup> Corresponding author at: King Mongkut's Institute of Technology Ladkrabang, Chumphon Campus, 17/1M. 6 Pha Thiew District, Chumphon 86160, Thailand. Tel.: +66 7750 6422x4565; fax: +66 7750 6410.

E-mail address: kbbanjon@kmitl.ac.th (B. Boonchom).

corresponding metal(II) carbonates (or metal oxides) and phosphoric acid at low temperature (40–80 °C) with long time periods (>48 h) [15–17]. While binary metal cyclotetraphosphate was synthesized by mix of corresponding metal cyclotetraphosphates, then melting them together on platinum dishes in an electric furnace at high temperature (>900 °C) with long time consumption (>5 h). However, binary metal cobalt iron dihydrogenphosphate and it decomposed product has not been reported in the literature.

The purpose of this work is to prepare new binary  $\text{Co}_{1/2}\text{Fe}_{1/2}(\text{H}_2\text{PO}_4)_2\text{·}2\text{H}_2\text{O}$  by solid state reaction at ambient temperature with short time consumption (<15 min). Thermal transformation product of the synthesized sample is binary cobalt iron cyclote-traphosphate  $\text{CoFeP}_4\text{O}_{12}$ . The synthesized powders of  $\text{Co}_{1/2}\text{Fe}_{1/2}(\text{H}_2\text{PO}_4)_2\text{·}2\text{H}_2\text{O}$  and its thermal transformation  $\text{CoFeP}_4\text{O}_{12}$  with flower-like microparticles and novel superparamagnetic properties were characterized by thermogravimetry–differential thermal gravimetry–differential thermal analysis (TG–DTG–DTA), X-ray diffraction (XRD), scanning electron microscopy (SEM), Fourier transform IR (FTIR), and vibrating sample magnetometer (VSM) techniques for the first time.

#### 2. Experimental

#### 2.1. Preparation

All chemicals (analytical grade or chemically pure grade) were purchased from Fluka and Merck. Following procedure, 4 mL of  $70\%\,H_3PO_4(86.4\%\,(w/w)\,H_3PO_4\,dissolved$  in DI water) was added to 1.1893 g of CoCO3 and 0.5593 g of Fe(c) (a mole ratio corresponding to the nominal composition of Fe:Co ratio of 1.0:1.0), the resulting suspension was continuously stirred at ambient temperature until CO2(g) was completely evolved and the precipitates were obtained. For this procedure, the increasing temperature of the precipitates from exothermic process was cooled to room temperature. The nearly dry sample was obtained and then 10 mL of acetone was added to allow highly crystalline product to be developed. The prepared solid was filtered by suction pump, washed with acetone and dried in air.

#### 2.2. Characterization

Thermal property of the studied compound was investigated on a TG-DTG-DTA Pyris Diamond Perkin Elmer Instruments. The experiment was performed in dynamic air at heating rate of 10 °C min<sup>-1</sup> over the temperature range from 30 to 600 °C and the flow rate of 100 mL  $\rm min^{-1}.$  Its final decomposition product seemed to occur at temperatures above 500 °C (Fig. 1). In order to gain its final thermal transformation product, the obtained Co<sub>1/2</sub>Fe<sub>1/2</sub> <sub>2</sub>(H<sub>2</sub>PO<sub>4</sub>)<sub>2</sub>·2H<sub>2</sub>O was heated in the furnace at 600 °C for 3 h and the thermal transformation products was further investigated. The cobalt and iron contents were determined by dissolving in 0.0126 M hydrochloric acid using atomic absorption spectrophotometry (AAS, Perkin Elmer, Analyst 100). The phosphorus content was determined by colorimetric analysis of the molybdophosphate complex. The water content was determined by TG data. The structure and crystallite size of the synthesized Co<sub>1/2</sub>Fe<sub>1/2</sub>(H<sub>2</sub>PO<sub>4</sub>)<sub>2</sub>·2H<sub>2</sub>O and the thermal transformation products were studied by X-ray powder diffraction using a X-ray diffractometer (Phillips PW3040, The Netherlands) with Cu K $\alpha$  radiation ( $\lambda$  = 0.15406 nm). The Scherrer method was used to evaluate the crystallite size [18]. The morphologies were examined with scanning electron microscope (SEM) using LEO SEM VP1450 after gold coating. The room temperature FTIR spectra were recorded in the range of 4000-370 cm<sup>-1</sup> with 8 scans on a Perkin-Elmer Spectrum GX FTIR/FT-Raman spectrometer with the resolution of 4 cm<sup>-1</sup> using KBr pellets (KBr, spectroscopy grade, Merck). The magnetic properties were

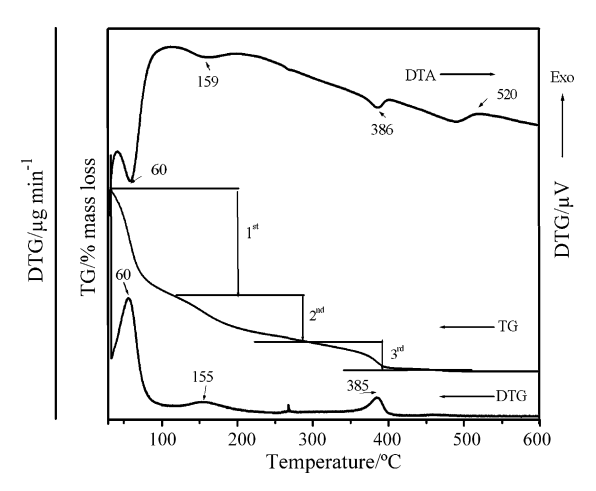


**Fig. 1.** TG-DTG-DTA curves of  $Co_{1/2}Fe_{1/2}(H_2PO_4)_2 \cdot 2H_2O$ .

examined at room temperature (20 °C) using a vibrating sample magnetometer (VSM 7403, Lake Shore, USA).

#### 3. Results and discussion

#### 3.1. Thermal analysis

The TG/DTG/DTA curves of Co<sub>1/2</sub>Fe<sub>1/2</sub>(H<sub>2</sub>PO<sub>4</sub>)<sub>2</sub>·2H<sub>2</sub>O are shown in Fig. 1. The TG curve shows the mass loss between 30 and 600 °C, which is related to the elimination of water molecules in crystallization water and an intermolecular phosphate condensation. The eliminations of water were observed in three areas: 45-130, 130–300 and 300–450  $^{\circ}$ C. The mass losses in three stages are 12.80, 7.42 and 5.61%, which correspond to 2.04, 1.18 and 0.89 mol of water for  $Co_{1/2}Fe_{1/2}(H_2PO_4)_2 \cdot 2H_2O$ , respectively. The DTA curve shows three endothermic effects over the temperature region at 60, 159 and 386 °C whereas the DTG curve shows three peaks at 60, 155, and 385 °C. Further, a small exothermic effect at 520 °C without appreciable mass loss is observed in the DTA curve, which can be ascribed to a transition phase from of CoFeP<sub>4</sub>O<sub>12</sub>. The thermal decomposition of Co<sub>1/2</sub>Fe<sub>1/2</sub>(H<sub>2</sub>PO<sub>4</sub>)<sub>2</sub>·2H<sub>2</sub>O in the range of 30-600 °C involves the dehydration of the coordination water molecules (2 mol H<sub>2</sub>O) and an intramolecular dehydration of the protonated dihydrogenphosphate groups (2 mol H<sub>2</sub>O) as shown in Eqs. (1)–(3):

$$\text{Co}_{1/2}\text{Fe}_{1/2}(\text{H}_2\text{PO}_4)_2 \cdot 2\text{H}_2\text{O} \rightarrow \text{Co}_{1/2}\text{Fe}_{1/2}(\text{H}_2\text{PO}_4)_2 + 2\text{H}_2\text{O} \tag{1}$$

$$Co_{1/2}Fe_{1/2}(H_2PO_4)_2 \rightarrow Co_{1/2}(H_2PO_4) \cdot [1/4Fe_2P_4O_{12}] \, + \, 1H_2O \quad \ (2)$$

$$Co_{1/2}(H_2PO_4)\cdot [1/4Fe_2P_4O_{12}] \to 1/2CoFeP_4O_{12} + 1H_2O \tag{3}$$

The intermediate compounds, such as acid polyphosphate  $Co_{1/2}Fe_{1/2}(H_2PO_4)_2$  and  $Co_{1/2}(H_2PO_4)\cdot[1/4Fe_2P_4O_{12}]$  and mixture of both intermediates have been registered.  $Co_{1/2}(H_2PO_4)\cdot[1/4Fe_2P_4O_{12}]$  is observed in Eq. (2) due to  $Fe_2P_4O_{12}$  is formed at lower temperature than  $Co_2P_4O_{12}$ , which related to thermal transformation of single dihydrogenphosphate dihydrate in our previous works [19,20]. The intermediates were similarly observed with single metal dihydrogen phosphate [9,10,12–15]. The binary cobalt iron cyclotetraphosphate,  $CoFeP_4O_{12}$  is found to be the final product of the thermal decomposition at T > 500 °C. The total mass loss is 25.83% (4.12 mol  $H_2O$ ), which is in agreement with those reported for other binary dihydrogenphosphate dihydrate in the literature (1 < mole of water < 4) [9,10,12–15]. The thermal stability, mechanism and phase transition temperature of the studied compound in this work are significantly different from

B. Boonchom et al./Materials Research Bulletin 44 (2009) 2206-2210

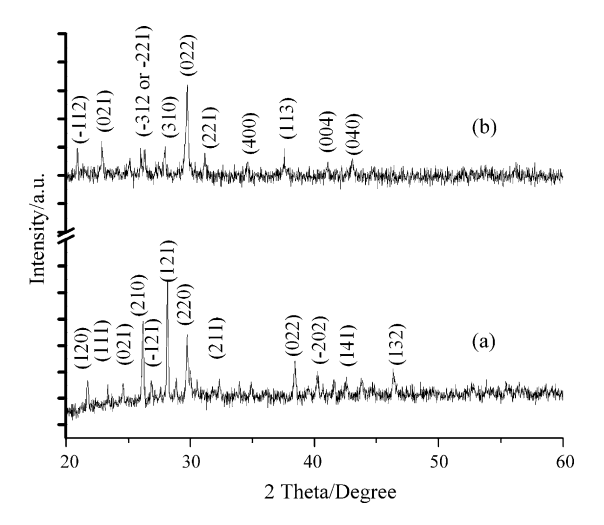


Fig. 2. XRD patterns of  $Co_{1/2}Fe_{1/2}(H_2PO_4)_2\cdot 2H_2O$  (a) and its decomposed product  $CoFeP_4O_{12}$  (b).

those of the decomposition reactions of individual metal compounds (Fe(H<sub>2</sub>PO<sub>4</sub>)<sub>2</sub>·2H<sub>2</sub>O [19] and Co(H<sub>2</sub>PO<sub>4</sub>)<sub>2</sub>·2H<sub>2</sub>O [20]). These results indicate that the incorporation of Fe and Co metals in the skeleton has the effects of thermal behaviors, which support the formations of new binary dihydrogen phosphate  $Co_{1/2}Fe_{1/2}$  (H<sub>2</sub>PO<sub>4</sub>)<sub>2</sub>·2H<sub>2</sub>O and binary metal cyclotetraphosphate CoFeP<sub>4</sub>O<sub>12</sub>.

#### 3.2. X-ray powder diffraction

The XRD patterns of Co<sub>1/2</sub>Fe<sub>1/2</sub>(H<sub>2</sub>PO<sub>4</sub>)<sub>2</sub>·2H<sub>2</sub>O and its decomposed product CoFeP<sub>4</sub>O<sub>12</sub> are similar to those obtained from the individual  $M(H_2PO_4)_2 \cdot 2H_2O$  and  $M_2P_4O_{12}$  (when M = Co and Fe) but the intensities are slightly different (Fig. 2). The spectrum peaks for the systems of binary cobalt iron solid solution and single metal dihydrogen phosphate (or metal cyclotetraphosphate) are quite similar due to the electronic charges and the radii of cations are equivalent and close to each other, respectively [13-17]. According to the XRD analysis, we can draw a conclusion that the synthesized Co<sub>1/2</sub>Fe<sub>1/2</sub>(H<sub>2</sub>PO<sub>4</sub>)<sub>2</sub>·2H<sub>2</sub>O and its decomposed product CoFeP<sub>4</sub>O<sub>12</sub> are solid solutions and not a mixture of the individual ones. In addition, the result confirmed that new binary metal (Co<sub>1/</sub> <sub>2</sub>Fe<sub>1/2</sub>(H<sub>2</sub>PO<sub>4</sub>)<sub>2</sub>·2H<sub>2</sub>O and CoFeP<sub>4</sub>O<sub>12</sub>) are isostructural to type series of the single metal (M(H<sub>2</sub>PO<sub>4</sub>)<sub>2</sub>·H<sub>2</sub>O and M<sub>2</sub>P<sub>4</sub>O<sub>12</sub>; where M or A = Mg, Mn, Co, Ni, Fe, Zn). All the reflections can be distinctly indexed as a pure monoclinic phase with space group  $P2_1/n$  (Z = 2) for  $Co_{1/2}Fe_{1/2}(H_2PO_4)_2 \cdot 2H_2O$  and C2/c (Z = 4) for the decomposed products CoFeP<sub>4</sub>O<sub>12</sub>, which noted to be similar to those of standard data of M(H<sub>2</sub>PO<sub>4</sub>)<sub>2</sub>·H<sub>2</sub>O (PDF no 390698 for Co and PDF no 751444 for Fe) and  $M_2P_4O_{12}$  (PDF no 842208 for Co and PDF no 782285 for Fe), respectively. The average crystallite sizes and lattice parameters of  $Co_{1/2}Fe_{1/2}(H_2PO_4)_2\cdot 2H_2O$  and the decomposed product  $CoFeP_4O_{12}$  were calculated from XRD patterns and also tabulated in Table 1. The lattice parameters of  $Co_{1/2}Fe_{1/2}(H_2PO_4)_2\cdot 2H_2O$  and the decomposed products  $CoFeP_4O_{12}$  are comparable to those of the standard data of individual ones. The average crystallite sizes of  $Co_{1/2}Fe_{1/2}(H_2PO_4)_2\cdot 2H_2O$  and the decomposed product  $CoFeP_4O_{12}$  were found to be  $77\pm27$  and  $73\pm18$  nm, respectively. However, the crystallite sizes for the obtained compounds in this work are larger than those from the single metal compounds (Table 1) in our previous works [13,14,18,19].

#### 3.3. FTIR spectroscopy

The FTIR spectra of  $Co_{1/2}Fe_{1/2}(H_2PO_4)_2\cdot 2H_2O$  and the decomposed products  $CoFeP_4O_{12}$  are shown in Fig. 3 and they are very similar to those of  $M(H_2PO_4)_2\cdot 2H_2O$  and  $M_2P_4O_{12}$  (M = Co or Fe), which confirmed their isostructural. Vibrational bands are identified in relation to the crystal structure in terms of the fundamental vibrating units namely  $H_2PO_4^-$  and  $H_2O$  for  $Co_{1/2}Fe_{1/2}(H_2PO_4)_2\cdot 2H_2O$  and  $[P_4O_{12}]^{4-}$  ion for  $CoFeP_4O_{12}$ , which are assigned according to the literature [9,10,12-15,21,22].

The FTIR spectrum of Co<sub>1/2</sub>Fe<sub>1/2</sub>(H<sub>2</sub>PO<sub>4</sub>)<sub>2</sub>·2H<sub>2</sub>O (Fig. 3a) is very similar to those observed by Koleva et al. [10] and Boonchom et al. [19,20]. The highest site symmetry of  $H_2PO_4^-$  ion is  $C_{2v}$ , in the crystallographic unit cell ( $P2_1/n$ , Z=2) [10], but the four  $H_2PO_4^$ ions are located on the set of non-equivalent site symmetry of  $C_1$ . A pair of H<sub>2</sub>PO<sub>4</sub><sup>-</sup> ions is related to each other by a center of symmetry. The four fundamental modes of the free phosphate ion undergo factor group splitting [22]. It is known that the existence of short OH···O hydrogen bonds in a variety of strongly hydrogenbonded solids is manifested by the appearance of the characteristic ABC structure of the  $\nu(OH)$  vibrational bands [9,10]. The problem of the origin of the ABC trio is discussed in many studies on acidic salts, but an explanation of this behaviour of strongly hydrogenbonded systems is still to be found [9,10]. One of the most popular interpretations of the ABC trio suggests a strong Fermi resonance between the  $\nu(OH)$  stretching fundamentals and the overtones [2 $\delta$ (OH) and 2 $\gamma$ (OH)] or combinations involving the  $\delta$ (OH) and  $\gamma$ (OH) vibrations. Usually, the ABC bands are very broad and consist of many ill-resolved components. Two bands centered at 3138 and 2427 cm<sup>-1</sup> in the FTIR spectra are referred to as bands A and B, respectively. The third component (band C) is observed around  $1749-1639 \,\mathrm{cm}^{-1}$ . The intense band at about  $1260 \,\mathrm{cm}^{-1}$  is due to the in plane P–O–H bending  $(A_2)$ , while the out of plane bending  $(A_1)$  vibration is observed at about 816 cm<sup>-1</sup>. Vibrational spectra of present hydrate are assigned by factor group analysis and derived from the same mode as in free H<sub>2</sub>PO<sub>4</sub><sup>-</sup> ion. A strong band at about

Table 1 Average crystallite sizes and lattice parameters of  $Co_{1/2}Fe_{1/2}(H_2PO_4)_2$ .  $2H_2O$  and its decomposed product  $CoFeP_4O_{1/2}$  calculated from XRD data.

Compound	Method	a (Å)	b (Å)	c (Å)	β (°)	Average particle sizes (nm)
Co(H <sub>2</sub> PO <sub>4</sub> ) <sub>2</sub> ·2H <sub>2</sub> O	PDF no 390698 Ref. [20]	7.27 7.21(3)	9.88 9.91(1)	5.33 5.29(5)	94.86 94.88(6)	26±2
$Co_{1/2}Fe_{1/2}(H_2PO_4)_2 \cdot 2H_2O$	This work	7.30(0)	9.92(0)	5.35(1)	95.01(2)	$77\pm27$
$Fe(H_2PO_4)_2 \cdot 2H_2O$	PDF no 751444 Ref. [19]	7.30 7.25(1)	9.92 10.10(0)	5.34 5.32(0)	95.14 95.71(0)	$\begin{matrix} - \\ 28 \pm 4 \end{matrix}$
$Co_2P_4O_{12}$	PDF no 842208 Ref. [20]	11.8 11.83(8)	8.297 8.22(6)	9.923 9.94(0)	118.72 118.51(1)	$40\pm10$
CoFeP <sub>4</sub> O <sub>12</sub> (calcined 600 °C)	This work	11.77(3)	8.56(0)	9.63(1)	119.09(0)	$73\pm18$
$Fe_2P_4O_{12}$	PDF no 782285 Ref. [19]	11.94 12.80(0)	8.37 8.80(4)	9.93 10.56(0)	118.74 118.67(4)	$\begin{matrix} - \\ 29 \pm 6 \end{matrix}$

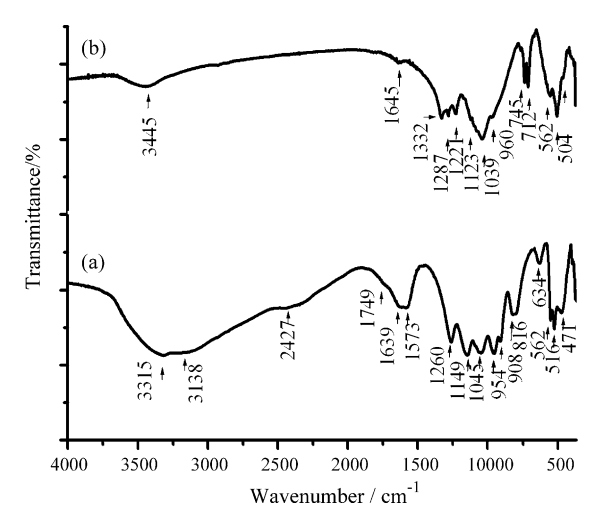
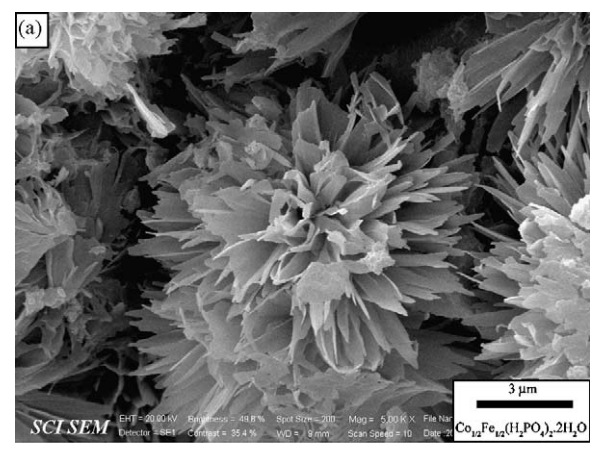


Fig. 3. FTIR spectra of  $Co_{1/2}Fe_{1/2}(H_2PO_4)_2 \cdot 2H_2O$  (a) and its decomposed product  $CoFeP_4O_{12}$  (b).

1149 cm<sup>-1</sup> in FTIR spectra is assigned to PO<sub>2</sub> asymmetric stretching  $(B_1)$ , while the other one at about  $1045 \, \mathrm{cm}^{-1}$ corresponds to  $PO_2$  symmetric stretching modes  $(A_1)$ . The FTIR frequency of the  $P(OH)_2$  asymmetric stretching  $(B_2)$  shows the strong band at about 954 cm<sup>-1</sup>. The weak band at about 908 cm<sup>-1</sup> is assigned to  $P(OH)_2$  symmetric stretching modes  $(A_1)$ . The medium band at about 562 cm<sup>-1</sup> is corresponding to PO<sub>2</sub> bending modes  $(B_1)$ . Two strong bands appeared at about 516 and 471 cm<sup>-1</sup> are attributed to  $PO_2$  rocking modes as  $B_1$  and  $A_2$  vibrations, respectively. The bands of water vibrations are illustrated in Fig. 3a as a doublet bands (1639 and 1573 cm<sup>-1</sup>) contribute both to the band C and to the water bending band. A weak band occurs in the FTIR spectra at approximately 634 cm<sup>-1</sup> is assigned to rocking mode involving water librations. The  $\nu_{OH}$  stretching modes of HOH in  $Co_{1/2}Fe_{1/2}(H_2PO_4)_2 \cdot 2H_2O$  appear at 3138 cm<sup>-1</sup> ( $\nu_1$  or A band) and 3315 cm  $^{-1}$  ( $\nu_3$ ). The bands associated with the  $\nu_{OH}$  stretching frequencies in H<sub>2</sub>PO<sub>4</sub><sup>-</sup> ions are observed at about 2850 and  $2427 \text{ cm}^{-1}$ .

The FTIR spectrum of the decomposed product CoFeP<sub>4</sub>O<sub>12</sub> (Fig. 3b) is very similar to those obtained from the individual  $M_2P_4O_{12}$  (M = Co and Fe) [13,14,18,19]. The band assignment is identified in terms of the fundamental vibrating modes of P<sub>4</sub>O<sub>12</sub><sup>4</sup>ion in the frequency range of 370-1400 cm<sup>-1</sup>, which are assigned according to the literature [13,14,18,19]. The anion contains the PO<sub>2</sub><sup>2-</sup> radical and the P-O-P bride, where are interpreted the FTIR spectra from viewpoint of the vibrations of these two groups. As the P-O bond strength in the P-O-P bride is weaker than in the PO2<sup>2-</sup> radical, the stretching frequencies of the P-O-P bride are expected to be lower than those in the PO22- radical. The asymmetric and symmetric stretching frequencies of the PO<sub>2</sub><sup>2-</sup> radical are generally observed in the areas 1325-1227 and 1151-1100 cm<sup>-1</sup>, respectively. The P-O-P bride has its asymmetric and symmetric stretching frequencies around 1000-900 and 900-700 cm<sup>-1</sup>, respectively. The bending modes are expected in the area: 600-400 cm<sup>-1</sup> (PO<sub>2</sub><sup>2-</sup> radical) and 400-370 cm<sup>-1</sup> (P-O-P bride). The metal-O stretching usually appears in the bending mode region as the bending modes of the P-O-P bride and absorption bands associated with these vibrations are usually very weak. The observation of a strong  $v_s$ POP band is known to be the most striking feature of cyclotetraphosphate spectra, along with the presence of the  $v_{as}OPO^-$  band. From X-ray diffraction data [10], it was shown that the crystal structure is monoclinic (space group (C2/c) with a cyclic structure of the  $[P_4O_{12}]^{4-}$  anion. This has been confirmed by the FTIR measurements.



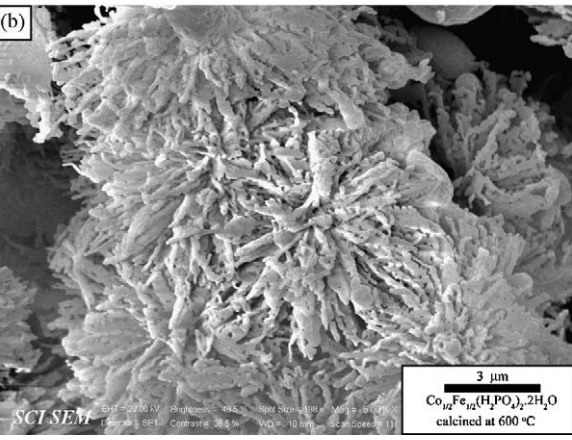


Fig. 4. SEM micrographs of  $Co_{1/2}Fe_{1/2}(H_2PO_4)_2\cdot 2H_2O$  (a) and its decomposed product  $CoFeP_4O_{12}$  (b).

#### 3.4. Scanning electron microscopy

The SEM micrographs of Co<sub>1/2</sub>Fe<sub>1/2</sub>(H<sub>2</sub>PO<sub>4</sub>)<sub>2</sub>·2H<sub>2</sub>O and the decomposed product CoFeP<sub>4</sub>O<sub>12</sub> are shown in Fig. 4. The particle shape and size are changed throughout the whole decomposition product. The SEM micrographs of  $Co_{1/2}Fe_{1/2}(H_2PO_4)_2 \cdot 2H_2O$  and the decomposed product CoFeP<sub>4</sub>O<sub>12</sub> show flower-like architectures, having sizes of 15-20 \(\mu\mathrm{m}\). The morphology of Co<sub>1/2</sub>Fe<sub>1/2</sub> <sub>2</sub>(H<sub>2</sub>PO<sub>4</sub>)<sub>2</sub>·2H<sub>2</sub>O (Fig. 4a) shows petal-bud-like microparticles, which exhibit the different features from Co(H<sub>2</sub>PO<sub>4</sub>)<sub>2</sub>·2H<sub>2</sub>O and  $Fe(H_2PO_4)_2 \cdot 2H_2O$  in the our previous reports [13,14,18,19]. The morphology of the decomposed product CoFeP<sub>4</sub>O<sub>12</sub> (Fig. 4b) shows filament-like structures and porosity on the filament surface, which are significant different grain from single metal cyclotetraphosphate  $(M_2P_4O_{12}; M = Mn \text{ or } Fe)$  in our previous reports [13,14,18,19]. The different morphologies between the single metal compounds  $(M(H_2PO_4)_2 \cdot 2H_2O)$  and  $M_2P_4O_{12}$ , M = Co or Fe) and the binary metal compounds confirm the formation of Co<sub>1/</sub> <sub>2</sub>Fe<sub>1/2</sub>(H<sub>2</sub>PO<sub>4</sub>)<sub>2</sub>·2H<sub>2</sub>O and CoFeP<sub>4</sub>O<sub>12</sub>, which support the presence of Co ions in substitution position of Fe ions.

#### 3.5. VSM magnetometer

The specific magnetization curves of  $\text{Co}_{1/2}\text{Fe}_{1/2}(\text{H}_2\text{PO}_4)_2 \cdot 2\text{H}_2\text{O}$  and the decomposed product  $\text{CoFeP}_4\text{O}_{12}$  obtained from room temperature VSM measurements are shown in Fig. 5. All samples demonstrate typical superparamagnetic behavior with negligible coercivity and remanence, in accordance with the theory that superparamagnetic behavior is often observed at room temperature. The specific magnetization curves are typical superparamagnetic

B. Boonchom et al./Materials Research Bulletin 44 (2009) 2206-2210

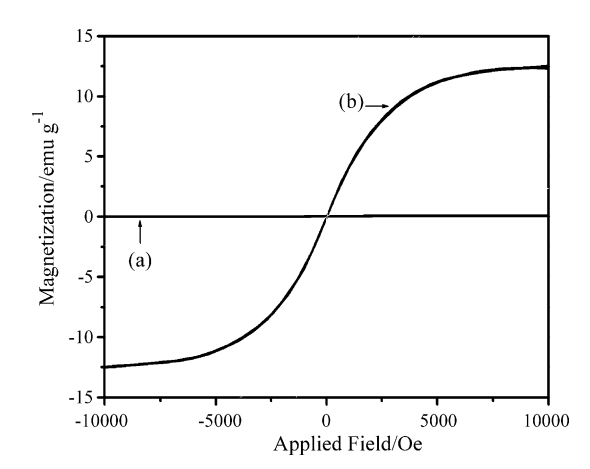


**Fig. 5.** The specific magnetizations of  $Co_{1/2}Fe_{1/2}(H_2PO_4)_2$ :  $2H_2O$  (a) and its decomposed product  $CoFeP_4O_{12}$  (b) as a function of field, measured at 293 K.

behavior without any hysteresis in the field range of  $\pm 10,000$  Oe. Specific saturated magnetization  $(M_s)$  values of  $Co_{1/2}Fe_{1/2}(H_2PO_4)_2 \cdot 2H_2O$  and the decomposed product  $CoFeP_4O_{12}$  are found to be 0.045 and 12.502 emu/g, respectively. It is worth nothing that these saturated magnetizations were compared with other magnetic materials  $(M_s$  of  $Fe_3O_4$  is 10-50 emu/g) [23-25]. It is seen that magnetizations of the  $Co_{1/2}Fe_{1/2}(H_2PO_4)_2 \cdot 2H_2O$  and  $CoFeP_4O_{12}$  are lower than those of  $Fe(H_2PO_4)_2 \cdot 2H_2O$  (96.28 emu/g) and  $Fe_2P_4O_{12}$  (85.01 emu/g) [20] but markedly distinct from the diamagnetic properties of  $Co(H_2PO_4)_2 \cdot 2H_2O$  and  $Co_2P_4O_{12}$  [19]. To our knowledge, it is worth nothing that superparamagnetic properties of the  $Co_{1/2}Fe_{1/2}(H_2PO_4)_2 \cdot 2H_2O$  and  $CoFeP_4O_{12}$  samples are reported for the first time in this study.

#### 4. Conclusion

Flower-like microparticle  $Co_{1/2}Fe_{1/2}(H_2PO_4)_2\cdot 2H_2O$  was successfully synthesized by solid state method from  $CoCO_3$ –Fe– $H_3PO_4$  system at ambient temperature with short time consumption (15 min).  $Co_{1/2}Fe_{1/2}(H_2PO_4)_2\cdot 2H_2O$  decomposes in three steps which correspond to the loss of water of crystallization in the first step, subsequently to a continuous intermolecular polycondensation and elimination of water of constituent in anion (the second and the third steps). The thermal behaviors, flower-like morphologies, particle sizes and superparamagnetic properties of  $Co_{1/2}Fe_{1/2}(H_2PO_4)_2\cdot 2H_2O$  and the thermal transformation products  $CoFeP_4O_{12}$  in this work are different from single metal compounds

in our previous reports. This work presents the simple, cost-effective and short time consuming method for the preparation of new binary metal  $\text{Co}_{1/2}\text{Fe}_{1/2}(\text{H}_2\text{PO}_4)_2\cdot 2\text{H}_2\text{O}$  and  $\text{CoFeP}_4\text{O}_{12}$  compounds, which may be used in many important applications such as catalytic, superinonic conductors, piezo- and ferroelectrics, magnets, electrochemical, bioceramic and environmental processes.

#### Acknowledgements

The authors would like to thank the Chemistry Department, Khon Kaen University for facilities. This work is financially supported by the Thailand Research Fund (TRF) and the Commission on Higher Education (CHE): Research Grant for New Scholar and King Mongkut's Institute of Technology Ladkrabang Research (KMITL Research), Ministry of Education, Thailand.

#### References

- [1] A. Durif, Solid State Sci. 7 (2005) 760.
- 2] H. Onoda, K.-I. Okumoto, I. Tanaka, Mater. Chem. Phys. 107 (2008) 339.
- [3] S.-L. Yang, H. Zhang, Z. Xie, D. Zhao, W.-L Zhang, W.-D. Cheng, J. Solid State Chem. 182 (2009) 855.
- [4] T. Dammak, N. Fourati, Y. Abid, A. Mlayah, C. Minot, J. Mol. Struct. 852 (2008) 83.
- [5] T. Kitsugi, T. Yamamuro, T. Nakamura, M. Oka, Biomaterials 16 (1995) 1101.
- [6] B. Jian-Jiang, K. Dong-Wan, H. Kug Sun, J. Eur. Ceram. Soc. 23 (2003) 2589. [7] I.-C. Marcu, I. Sandulescu, Y. Yves Schuurman, J.-M.M. Millet, Appl. Catal. A. 334
- [7] I.-C. Marcu, I. Sandulescu, Y. Yves Schuurman, J.-M.M. Millet, Appl. Catal. A. 334 (2008) 207.
- [8] M. Kaplanová, M. Trojan, D. Brandová, J. Navrátil, J. Lumin. 29 (1984) 199.
- [9] B. Boonchom, S. Maesiri, S. Youngme, C. Danvirutai, Solid State Sci. 11 (2009) 485.
- [10] V. Koleva, H. Effenberger, J. Solid State Chem. 180 (2007) 956.
- [11] Y. Tang, H.F. Chappell, M.T. Dove, R.J. Reeder, Y.J. Lee, Biomaterials 30 (2009) 2864.
- [12] M. Trojan, P. Šulcová, Dyes Pigments 47 (2000) 291.
- [13] B. Boonchom, S. Maensiri, C. Danvirutai, Mater. Chem. Phys. 109 (2008) 404.
- [14] B. Boonchom, C. Danvirutai, Ind. Eng. Chem. Res. 47 (2008) 2941 (and references therein).
- [15] N.M. Antraptseva, L.N. Shchegrov, I.G. Ponomareva, Russ. J. Inorg. Chem. 51 (2006) 1493.
- [16] M. Trojan, P. Šulcová, P. MoŠner, Dyes Pigments 44 (2000) 161.
- [17] D. Brandová, M. Trojan, F. Paulik, J. Paulik, M. Arnold, J. Therm. Anal. Calorimet. 36 (1990) 881.
- [18] B.D. Cullity, Elements of X-ray Diffraction, 2nd ed., Addison-Wesley Publishing, 1977.
- [19] B. Boonchom, C. Danvirutai, J. Chem. Eng. Data 54 (2009) 1225.
- [20] B. Boonchom, C. Danvirutai, S. Youngme, S. Maensiri, Ind. Eng. Chem. Res. 47 (2008) 7642.
- [21] N.B. Colthup, L.H. Daly, S.E. Wiberley, Introduction to Infrared and Raman Spectroscopy. Academic Press. New York, 1964.
- Spectroscopy, Academic Press, New York, 1964.
  [22] G. Herzberg Molekülspektren und Molekülstruktur. I. Zweiatomige Moleküle., Steinkopff, Dresden, 1939.
- [23] E.H. Soumhi, I. Saadoune, A. Driss, J. Solid State Chem. 56 (2001) 364.
- [24] J. Tang, M. Myers, K.A. Bosnick, L.E. Brus, J. Phys. Chem. B 107 (2003) 7501.
- [25] A.K. Gupta, M. Gupta, Biomaterials 26 (2005) 3995.

SS CONTRACTOR OF THE SEVIER

Contents lists available at ScienceDirect

#### **Materials Letters**

journal homepage: www.elsevier.com/locate/matlet



# Synthesis and ferromagnetic property of new binary copper iron pyrophosphate CuFeP<sub>2</sub>O<sub>7</sub>

Banjong Boonchom a,b,\*, Naratip Vittayakorn b,c

- <sup>a</sup> King Mongkut's Institute of Technology Ladkrabang, Chumphon Campus, 17/1 M. 6 Pha Thiew District, Chumphon, 86160, Thailand
- b Advanced Materials Science Research Unit, Department of Chemistry, Faculty of Science, King Mongkut's Institute of Technology Ladkrabang, Bangkok 10520, Thailand
- <sup>c</sup> College of KMITL Nanotechnology, King Mongkut's Institute of Technology Ladkrabang, Bangkok 10520, Thailand

#### ARTICLE INFO

Article history: Received 28 September 2009 Accepted 26 October 2009 Available online 30 October 2009

Keywords: CuFeP<sub>2</sub>O<sub>7</sub> New binary pyrophosphate Synthesis Ferromagnetic

#### ABSTRACT

The pyrophosphate of  $CuFeP_2O_7$  was synthesized through one step-thermal synthesis at 500 °C using the mixing of copper carbonate, iron metals and phosphoric acid. FTIR and XRD results indicate the dominant feature of pyrophosphate  $(P_2O_7^{4-})$  anion and a pure monoclinic phase with space group  $C_{2h}^6$  (Z=4), respectively. The crystallite size of  $25\pm 9$  nm for the  $CuFeP_2O_7$  was estimated by X-ray line broadening. Room temperature magnetization result shows ferromagnetic behavior of the  $CuFeP_2O_7$  powder, having hysteresis loop in the range of  $\pm 10,000$  Oe with the specific magnetization value of 1.57 emu g $^{-1}$ . This property is important for specific application and is presented for the first time.

© 2009 Elsevier B.V. All rights reserved.

#### 1. Introduction

Binary metal (II) pyrophosphates consisting of a homogeneous solid solution are characterized by high corrosion resistance, high tensile strengths, improved ductility and good malleability as compared with the corresponding single metals [1,2]. These materials are widely employed in various fields as catalysts, wastewater purification systems, ferroelectrics, lithium batteries, the steel and glass industries [2–4]. In the recent years, they have been proposed as the cathode in lithium batteries and lithium metal phosphates can be used as cathode or anode electrodes in lithium batteries because they are the next generation of positive-electrode materials for lithium batteries and offer additional advantages in practical applications due to their lower cost, safety, benign environmental properties, stability and low toxicity [5,6]. The binary metal  $M_{2-x}A_{x}P_{2}O_{7}$  (M or A = Mg, Mn, Co, Cu, Ni, Fe, Zn; 0 < x < 2) group, one of the important metal phosphates, has found widespread applications and is graining interesting according to above mentioned [7]. Because it appears economically advantageous to substitute a portion of the divalent metal with a less costly divalent element, which influences many properties, for example, the color of pigments, the relatively stable compounds-both thermally and chemically, anticorrosion ability and luminescence [1–4]. In addition, some metals, such as copper or iron, and  $(P_2O_7)^{4-}$  species are lower cost, safety, benign environmental properties and low toxicity [5,7].

E-mail address: kbbanjon@kmitl.ac.th (B. Boonchom).

Therefore, our laboratory has focused on the studies of the synthesis of new binary metal pyrophosphates [8,9], which are important for the development of new inorganic functional materials.

The present paper describes the synthesis and characterization of a new binary copper iron pyrophosphate, CuFeP $_2$ O $_7$  using powder X-ray diffraction (XRD), Fourier transform infrared (FTIR) and vibrating magnetometric (VSM) techniques. The information on the synthesis and characterization of a new binary copper iron pyrophosphate, CuFeP $_2$ O $_7$  are reported for the first time.

#### 2. Experimental

All the reagents used in this study were of A.R. grade. In typical procedure,  $\text{CuCO}_3$  and Fe (complexometric) were mixed together with mole ratio of 1.0:1.0 and then was ground for 10 min. Subsequently, 5 mL of 70 %  $\text{H}_3\text{PO}_4$  (86.4 %w/w  $\text{H}_3\text{PO}_4$  dissolved in DI water) was added slowly to the mixed solid with mechanically stirring at ambient temperature (10 min). Then, the mixed suspension was evaporated by heating in the furnace at 500 °C for 2 h. The obtained gray pink precursor was crushed into powder, which was washed repeatedly by DI water until no  $\text{PO}_4^{3-}$  was detected. Finally, the powder was washed again for several times with methanol and dried at room temperature. The reaction equation can be expressed as:

$$CuCO_3(s) + Fe(s) + 2H_3PO_4(aq) \rightarrow CuFeP_2O_7(s) + 3H_2O(g) + CO(g)$$
 (1)

The copper and iron contents of CuFeP<sub>2</sub>O<sub>7</sub> were determined by dissolving in 0.0126 M hydrochloric acid using atomic absorption

<sup>\*</sup> Corresponding author. King Mongkut's Institute of Technology Ladkrabang, Chumphon Campus, 17/1 M. 6 Pha Thiew District, Chumphon, 86160, Thailand. Tel.: +66 7750 6422x4565; fax: +66 7750 6410.

spectrophotometry (AAS, Perkin Elmer, Analyst100). The phosphorus content was determined by colorimetric analysis of the molybdophosphate complex. X-ray powder diffraction (XRD) was carried out by a Phillips PW3040 X-ray diffractometer (The Netherland) utilizing Cu  $\rm K\alpha$  radiation ( $\lambda\!=\!0.15406$  nm) at 40 kV/200 mA. The Scherrer method was used to evaluate the crystallite size [10]. The room temperature FTIR spectrum in the range of 4000–370 cm $^{-1}$  was recorded by a Perkin-Elmer Spectrum GX FT-IR/FT-Raman spectrometer with 8 scans and the resolution of 4 cm $^{-1}$  using KBr pellets. The magnetic property was examined at room temperature (20 °C) using a vibrating sample magnetometer (VSM 7403, Lake Shore, USA).

#### 3. Results and discussion

The XRD pattern of CuFeP<sub>2</sub>O<sub>7</sub> is similar to those obtained from the individual  $M_2P_2O_7$  (when M = Cu, Co, Mn and Fe) [1-4,11], but the intensities are slightly different (Fig. 1). The lower and higher intensities of XRD peaks indicate the differences of crystallization or amorphous phase as well as crystallite sizes of these materials. From literature, it indicates that the binary solid solutions  $(M_{2-x}A_xP_2O_7)$ and the single metal compounds for  $M_2P_2O_7$  (M or A = Mg, Mn, Co, Cu, Ni, Fe, Zn; 0 < x < 2) types are isostructural [1–4,11]. In the hypothesis of isostructural, the spectrum peaks for the systems of binary copper iron pyrophosphate (solid solution) and single metal pyrophosphate  $(M_2P_2O_7, M = Cu \text{ and } Fe)$  are quite similar because of the equivalent electronic charges and the close radii of cations. In addition, no characteristic peaks of other impurities (CuCO<sub>3</sub> or Fe) were observed. In this respect, we can draw a conclusion that the synthesized product CuFeP<sub>2</sub>O<sub>7</sub> is solid solution and not a mixture of the individual ones. Consequently, all reflections can be distinctly indexed based on a pure monoclinic phase with space group C2/c (Z=4) for  $CuFeP_2O_7$ , which noted to be similar to those of the standard XRD patterns of M<sub>2</sub>P<sub>2</sub>O<sub>7</sub> (PDF no. 79-2075 for Cu and PDF no.76-1762 for Fe), respectively. The average crystallite size of product is estimated from the strongest three diffraction peaks below 40° for  $2\theta$  and found to be  $25 \pm 9$  nm. The lattice parameters calculated from the XRD spectra are a = 6.73(0), b = 8.21(1), c = 9.39(0) Å and b = 110.65(4) °, which are close to those of the standard data file (a = 6.89 (5), b = 8.11(3), c = 9.16(4) Åand b = 109.62(0) o from PDF no. 79-2075 for  $Cu_2P_2O_7$  and a = 6.65(0), b = 8.48(4), c = 4.49(0) Å and b = 103.89(0) ° from PDF no.76-1762 for  $Fe_2P_2O_7$ ) and the literature [11,12].

FTIR spectrum of CuFeP<sub>2</sub>O<sub>7</sub> shown in Fig. 2 is very similar to those obtained from the single metal pyrophosphates  $M_2P_2O_7$  (M=Mn, Ni, Co and Fe) [7–9,12,14]. The vibrational modes of  $P_2O_7^{4-}$  ion observed in the frequency range of 370–1400 cm<sup>-1</sup> are assigned according to the literature [7–9,13,14]. The anion containing the PO<sub>3</sub> and the P–O–P bride are interpreted the FTIR spectrum from viewpoint of the vibrations of these two groups. The asymmetric and symmetric

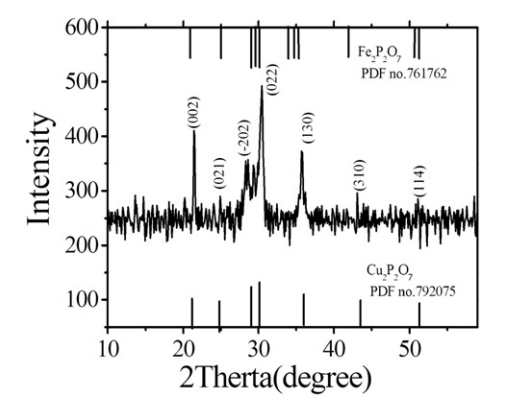


**Fig. 1.** XRD pattern of CuFeP<sub>2</sub>O<sub>7</sub>.

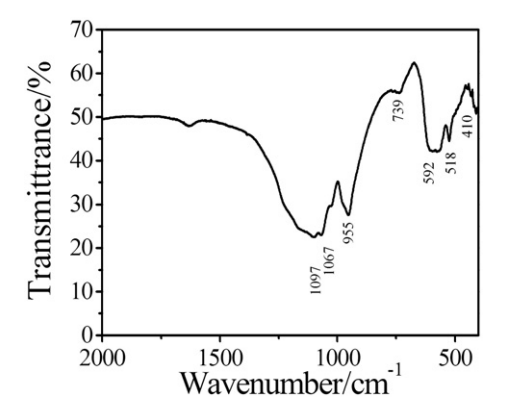
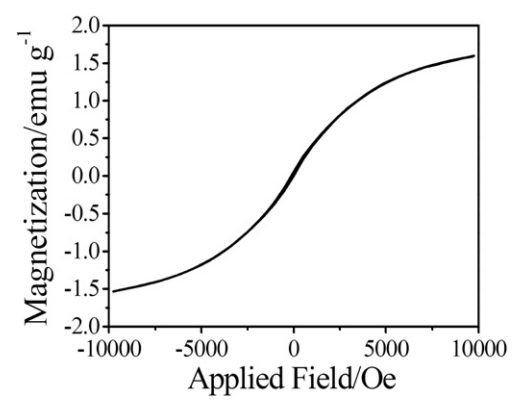


Fig. 2. FTIR spectrum of CuFeP<sub>2</sub>O<sub>7</sub>.

stretching frequencies of the PO<sub>3</sub> are generally observed at 1097 and 1067 cm<sup>-1</sup>, respectively. The bending modes of PO<sub>3</sub> are expected in the range of 592–518 cm<sup>-1</sup>. The metal-O stretching usually appears in the bending mode region as the bending modes of the PO<sub>3</sub> and absorption bands associated with these vibrations are usually very weak. The bands found at 955 and 739 cm<sup>-1</sup> are typical of the pyrophosphate group and correspond to the stretching and bending vibrations of the P-O-P bridge, respectively. The observation of a strong  $\nu_{\rm as}$ POP band is known to be the most striking feature of pyrophosphate spectra, along with the presence of the  $\nu_{\rm as}$ OPO<sup>-</sup> band. The PO<sub>3</sub> deformation and rocking modes, the POP deformations as well as the torsional and external modes are found in the 592–410 cm<sup>-1</sup> region. FTIR result is consistent with X-ray data [15], indicating that the crystal structure is monoclinic (space group C2/c) with pyrophosphate groups of the [P<sub>2</sub>O<sub>7</sub>]<sup>4-</sup> anion.

The specific magnetization curve of the CuFeP<sub>2</sub>O<sub>7</sub> sample obtained from room temperature VSM measurement is shown in Fig. 3. This curve is typical for a soft magnetic material and indicates hysteresis ferromagnetism in the field range of  $\sim \pm 10,000$  Oe while outside this range the specific magnetization increases with increasing field and saturates in the field range investigated ( $\pm 10 \text{ kOe}$ ). The specific saturation magnetization ( $M_s$ ) value of 1.57 emu g<sup>-1</sup> was observed for the CuFeP<sub>2</sub>O<sub>7</sub> sample. The coercive force (Hc) obtained on the increasing and decreasing filed sides (blanket) were 67.70 (-67.70)Oe for the CuFeP<sub>2</sub>O<sub>7</sub> sample. The ferromagnetic solid solution formed in CuFeP2O7 system is different from paramagnetic for Fe2P2O7 and diamagnetic for Cu<sub>2</sub>P<sub>2</sub>O<sub>7</sub>. The CuFeP<sub>2</sub>O<sub>7</sub> called pyrophosphate constitutes the largest family of condensed phosphates and contains different cations ( $Cu^{2+}$  and  $Fe^{2+}$ ) [15–18]. The ferromagnetic of the studied compound originates from magnetic moment of anti-parallel spins of between Cu<sup>2+</sup> (non-magnetic element) at octahedral sites and Fe<sup>2+</sup> (magnetic element) at distorted octahedral coordination



**Fig. 3.** The specific magnetization of  $CuFeP_2O_7$  as a function of field, measured at 20 °C.

[17,18]. This should be necessary for the appearance of ferromagnetism [18]. Additionally, it found that the tendency of Ms to increase is consistent with the enhancement of crystallinity or particle sizes, and the saturation value of Ms for  $CuFeP_2O_7$  is observed due to the obtained microstructure. This result has been essentially verified in a quantitative sense within the last two decades. Ferromagnetic property of the  $CuFeP_2O_7$  sample reported for the first time is important for specific applications such as magnetic resonance imaging contrast agents, data lifetime in high density information storage, ferrofluid technology, lithium batteries and magnetocaloric refrigeration [15,16].

#### 4. Conclusions

This research has successfully achieved a simple one-step thermal synthesis of a monoclinic phase of a new binary copper iron pyrophosphate CuFeP<sub>2</sub>O<sub>7</sub>. FTIR, XRD and VSM results suggested the formation of a binary metal CuFeP<sub>2</sub>O<sub>7</sub>. The FTIR and XRD data confirmed the dominant feature of pyrophosphate (P<sub>2</sub>O<sub>7</sub><sup>4</sup>) anion indicated the formation of a binary CuFeP<sub>2</sub>O<sub>7</sub>. The crystallize size of CuFeP<sub>2</sub>O<sub>7</sub> shows polycrystalline having crystallite size of  $25\pm 9$  nm, as estimated by XRD. The synthesized CuFeP<sub>2</sub>O<sub>7</sub> shows ferromagnetic property, which has hysteresis loop in the range of  $-10,000~{\rm Oe}\,{<}\,{\rm H}\,{<}\,10,000~{\rm Oe}\,{}$  with the specific magnetization of 1.57 emu  $^{-1}$  at 10 kOe. This research displays that the simple, cost effective and rapid time consumption is necessary for elaboration of technology and academic scientist to produce the pyrophosphate of transition metals, which may be useful for potentially applications as inorganic ceramic pigment, catalyst, fuel cell material and corrosion-proof compositions.

#### Acknowledgement

This work is financially supported by the Thailand Research Fund (TRF) and the Commission on Higher Education (CHE):Research Grant for New Scholar, Ministry of Education, Thailand.

#### Appendix A. Supplementary data

Supplementary data associated with this article can be found, in the online version, at doi:10.1016/j.matlet.2009.10.058.

#### References

- [1] Benkhouja K, Zahir M, Sadel A, Handizi A, Boukhari A, Holt EM, et al. Mater Res Bull
- [2] Ishikawa M, Enomoto H, Maisuuka M, Iwakura§ C. Electrochim Acta 1995;40:1663.
- [3] Masson NC, de Souza EF, Galembeck F. Colloids Surf A 1997;121:247.
- [4] Masala O, Mcinnes EJL, O'Brien P. Inorg Chem Acta 2002;339:366.
- [5] Masala O, O'Brien Pl, Rafeletos G. Cryst Growth Des 2003;3:431.
- [6] Shepelev YF, Petrova MA, Novikova AS, Lapshin AE. Glass Phys Chem 2002;28:317.
- [7] Onoda H, Yokouchi K, Kojima K, Nariai H. Mater Sci Eng B 2005;116:189.
- [8] Boonchom B, Phuwongpha N. Mater Lett 2009;63:1709. [9] Boonchom B, Danvirutai C. Ind Eng Chem Res 2008;47:5976.
- [10] Cullity BD. Elements of X-ray Diffraction. 2nd ed. Addison-Wesley Publishing; 1977.
- 11] Boukhari A, Mogine A, Flandrois S. J Solid State Chem 1990;87:251.
- [12] Xiao ZW, Hu GR, Peng ZD, Du K, Gao XG. Chinese Chem Lett 2007;18:1525.
- [13] Du Y, Xiong Y, Li J, Yang X. J Mol Catal A 2009;298:12.
- [14] Steger E, Käbner B. Spectrochim Acta 1968;24A:447.
- [15] Touaiher M, Rissouli K, Benkhouja K, Taibi M, Aride J, Boukhari A, et al. Mater Chem Phys 2004;85:41.
- [16] Handizi A, Boukhari A, Holt EM, Aride J, Flandrois S. Mater Res Bull 1993;28:1241.
- [17] Mahesh MJ, Gopalakrishna GS, Ashamanjari KG. Mater Sci Semicon Proc 2007:10:117.
- [18] Ino H, Hayashi K, Otsuka T, Isobe D, Tokumitsu K, Oda K. Mater Sci Eng 2001;A304– 306:972.



Contents lists available at ScienceDirect

### Powder Technology

journal homepage: www.elsevier.com/locate/powtec



# Floral-like microarchitectures of cobalt iron cyclotetraphosphate obtained by solid state synthesis

Banjong Boonchom a,b,\*, Naratip Vittayakorn b,c

- <sup>a</sup> King Mongkut's Institute of Technology Ladkrabang, Chumphon Campus, 17/1 M. 6 Pha Thiew District, Chumphon, 86160, Thailand
- b Advanced Materials Science Research Unit, Department of Chemistry, Faculty of Science, King Mongkut's Institute of Technology Ladkrabang, Bangkok 10520, Thailand
- <sup>c</sup> College of KMITL Nanotechnology, King Mongkut's Institute of Technology Ladkrabang, Bangkok 10520, Thailand

#### ARTICLE INFO

#### Article history: Received 5 August 2009 Received in revised form 7 October 2009 Accepted 13 October 2009 Available online 20 October 2009

Keywords: Floral-like microparticle CoFeP<sub>4</sub>O<sub>12</sub> Superparamagnetic behavior Solid state synthesis Inorganic ceramic pigment

#### ABSTRACT

Floral-like microparticle of a binary cobalt iron cyclotetraphosphate  $CoFeP_4O_{12}$  was synthesized through solid phase reaction using cobalt carbonate, iron metal and phosphoric acid with further calcinations at the temperature of  $500\,^{\circ}C$ . The XRD and FTIR results indicate that the prepared  $CoFeP_4O_{12}$  has a pure monoclinic phase without the presence of any phase impurities. The floral-like microparticle and superparamagnetic behavior of the synthesized  $CoFeP_4O_{12}$  are important properties for specific applications, which were revealed by SEM and VSM techniques, respectively. The dominant features of the synthesized  $CoFeP_4O_{12}$  in this work are compared with  $M_2P_4O_{12}$  (M=Co and Fe) and  $CoFeP_4O_{12}$  reported in our previous works.

© 2009 Elsevier B.V. All rights reserved.

#### 1. Introduction

In recent years, synthesis of the morphology and architecture of inorganic phosphates at micro-/nanoscale levels is a significant challenge, which attracts increased attention because of their strong influence on the chemical and physical properties of materials [1-3]. Morphology influences not only the intrinsic chemical, optical, and catalytic properties of micro-/nanoscale metal phosphates, but also their relevant applications in electronic, biocompartible and biodegradable in tissue [2,4]. As one of the members of phosphate material family, transition metal cyclotetraphosphate micro-/nanoparticles can be used in potential pigments, selective catalysts, phosphors, materials for corrosion-resistant coatings and biocompartible and biodegradable in tissue [5–8]. Several divalent including 3d metals, namely, Mn, Co, Fe, Zn, Cu, and Ni, are known to form the single metal cyclotetraphosphate M<sub>2</sub>P<sub>4</sub>O<sub>12</sub>, where M(II) stands for a divalent metal. The binary metal cyclotetraphosphates  $M_{2-x}A_{x}P_{4}O_{12}$  (M and A = Mg, Ca, Mn, Co, Ni, Zn, or Cu; x = 0-2), isostructural with the single metal cyclotetraphosphates M<sub>2</sub>P<sub>4</sub>O<sub>12</sub>, were prepared by Trojan et al. [5–8] and Boonchom et al. [9-11]. All these compounds have similar X-ray diffraction patterns and close unit cell parameters, which crystallize in monoclinic space group C2/c (Z=4) [12]. Various methods have been employed to synthesize binary metal cyclotetraphosphates, including two-step thermal method [5–8], hydrothermal synthesis [5] and the decompo-

E-mail addresses: kbbanjon@gmail.com, kbbanjon@kmitl.ac.th (B. Boonchom).

sition of binary metal (II) dihydrogenphosphates  $(M_{1-\nu}A_{\nu}(H_{2}PO_{4})_{2})$  $nH_2O$ ; where M and A = Ca, Mg, Mn, Fe, Co, Ni, Cu or Zn; y = 0-1; n = 1-4) [9-11]. This work is of interest because it appears economically advantageous to replace partially the divalent metal cations by some cheaper divalent element which could also improve special properties as above mentioned [1–4]. However, it is relevant to synthesize binary cyclotetraphosphate and its solid solution because changing the metal ratio influences its useful properties. Consequently, it is a major challenge to synthesize binary metal cyclotetraphosphate micro-/ nanoparticles with its intrinsic shape-dependent properties and resulting application. Recently, cobalt iron pyrophosphate CoFeP2O7 and cobalt iron cyclotetraphosphate CoFeP4O12 were prepared by mixing of CoCO<sub>3</sub>, Fe and H<sub>3</sub>PO<sub>4</sub> in water-methanol and in wateracetone, respectively [13,14]. The difference of media (solvents) in the precipitation process leads to the obtaining different phosphates, as revealed by XRD and FTIR data. Due to its solubility in water and its ability to associate with metal ions in media, solvent has been used as a binder cum gel for shaping materials (bulk, porous, micro- or nanoparticles) and a matrix for entrapment of ions to generate a gelled precursor which resulted in obtaining different material or same material with different size and morphology after heat treatment. The results obtained are also in agreement with other phosphate group reported in literature [15,16]. In this work, we report for the first time one step thermal synthesis of floral-like microarchitectures of binary cobalt iron cyclotetraphosphate CoFeP<sub>4</sub>O<sub>12</sub> by solid state reaction from cobalt carbonate, iron metal and phosphoric acid without organic media agent (or solvent). The different preparation routes of the CoFeP<sub>2</sub>O<sub>7</sub> between this work and our previous report [14] affect the differences of some physical and chemical properties such as morphology, particle size

<sup>\*</sup> Corresponding author. King Mongkut's Institute of Technology Ladkrabang, Chumphon Campus, 17/1 M. 6 Pha Thiew District, Chumphon, 86160, Thailand. Tel.: +66 7750 6422x4565: fax: +66 7750 6410.

and magnetic behavior. The synthesized sample was characterized by X-ray powder diffraction (XRD), Fourier transform infrared (FTIR), scanning electron microscope (SEM) and vibrating sample magnetometer (VSM) techniques.

#### 2. Experimental

All the reagents used in this study were of A.R. grade. A binary cobalt iron cyclotetraphosphate CoFeP $_4$ O $_{12}$  was prepared at laboratory temperature. In typical procedure, CoCO $_3$  and Fe (complexometric) were mixed together with mole ratio of 1.0:1.0 and then was ground for 10 min. Subsequently, 5 mL of 70 %  $H_3$ PO $_4$  (86.4 % w/w  $H_3$ PO $_4$  dissolved in DI water) was added slowly to the mixed solid with mechanically stirring at ambient temperature (10 min). Then, the mixed solution was evaporated by heating in the furnace at 500 °C for 2 h. The obtained gray pink precursor was crushed into powder and was washed repeatedly by DI water until no PO $_4^3$  was detected. Finally, the powder was washed again for several times with methanol and dried at room temperature. The reaction equation can be expressed as:

$$\begin{array}{c} 500\,^{\circ}\text{C} \\ \text{CoCO}_{3}(s) \ + \ \text{Fe}(s) \ + \ 4\text{H}_{3}\text{PO}_{4}(\text{aq}) \rightarrow \text{CoFeP}_{4}\text{O}_{12}(s) \ + \ 6\text{H}_{2}\text{O}(g) \ + \ \text{CO}(g) \end{array} \tag{1}$$

The cobalt and iron contents of CoFeP<sub>4</sub>O<sub>12</sub> were determined by dissolving in 0.0126 M hydrochloric acid using atomic absorption spectrophotometry (AAS, Perkin Elmer, Analyst100). The phosphorus content was determined by colorimetric analysis of the molybdophosphate complex. X-ray powder diffraction (XRD) was carried out by a Phillips PW3040 X-ray diffractometer (The Netherland) utilizing Cu K $\alpha$  radiation ( $\lambda$ =0.15406 nm) at 40 kV/200 mA. The Scherrer method was used to evaluate the crystallite size [17]. The room-temperature FTIR spectrum in the range of 4000–370 cm<sup>-1</sup> was recorded by a Perkin Elmer Spectrum GX FTIR/FT-Raman spectrometer with 8 scans and the resolution of 4 cm<sup>-1</sup> using KBr pellets. The morphology was examined with SEM picture by LEO SEM VP1450 scanning electron microscope. The magnetic property was examined at room temperature (20 °C) using a vibrating sample magnetometer (VSM 7403, Lake Shore, USA).

#### 3. Results and discussion

#### 3.1. Chemical analysis

The chemical analysis data showed that the cobalt, iron and phosphorus mass percentage were 13.58%, 12.92% and 28.75%, respectively. In other words, the molar ratio of  $Co_{total}$ :  $Fe_{total}$ :  $Fe_{total}$  in the synthetic product is equal to 1.00:1.00:4.03, which indicates that the general formula would be  $Fe_{total}$ 0.

#### 3.2. X-ray powder diffraction

XRD was used to characterize the phase the crystallographic structure of the product (Fig. 1). The XRD pattern of as prepared floral-like  $CoFeP_4O_{12}$  is similar to that of non-uniform particle  $CoFeP_4O_{12}$  reported by our previous work [14] but the intensities are slightly different. The lower and higher intensities of XRD peaks indicate the differences of crystallization or amorphous phase as well as particle sizes of these materials. In the hypothesis of isostructural, the spectrum peaks for the systems of binary cobalt iron cyclotetraphosphate (solid solution) and single metal cyclotetraphosphate ( $M_2P_4O_{12}$ , M=Co and Fe) are quite similar because of the equivalent electronic charges and the close radii of cations. Consequently, all the diffraction peaks in the figure are found to be in agreement with monoclinic  $M_2P_4O_{12}$  (PDF no. 842208 for  $Co_2P_4O_{12}$  and PDF no.782285 for  $Fe_2P_4O_{12}$ ), space group C2/c (Z=4). No characteristic peaks of other impurities ( $CoCO_3$  or Fe) were observed,

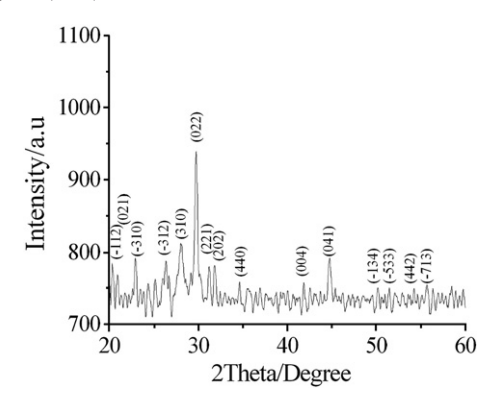


Fig. 1. XRD pattern of CoFeP<sub>4</sub>O<sub>12</sub>

and all the reflections could be indexed to the pure monoclinic phase of binary cobalt iron cyclotetraphosphate CoFeP<sub>4</sub>O<sub>12</sub>. From XRD analysis (Fig. 1), it can conclude that the as prepared floral-like CoFeP<sub>4</sub>O<sub>12</sub> is solid solution, not a mixture of the individual phases and isostructural with the single metal  $M_2P_4O_{12}$  (M = Co and Fe). According to the Scherrer formula:  $D = K\lambda/(\beta \cos \theta)$ , where *D* is particle diameter, K = 0.89 (the Scherrer constant),  $\lambda = 0.15406$  (wavelength of the X-ray used),  $\beta$  is the width of line at the half-maximum intensity and  $\theta$  is the corresponding angle. The average crystallite size of product is estimated from the strongest three diffraction peaks below 40° for  $2\theta$  and found to be  $49 \pm$ 20 nm. This crystallite size of the prepared CoFeP<sub>4</sub>O<sub>12</sub> in this work is smaller than that obtained from our previous work ( $65 \pm 24$  nm) [14] but it is larger than those for the single metal compounds ( $40 \pm 10 \text{ nm}$ for  $Co_2P_4O_{12}$  and  $29\pm6$  159 nm for  $Fe_2P_4O_{12}$ ) in our previous studies [9-11]. The lattice parameters calculated from the XRD spectra are a = 11.89(0), b = 8.33(0), c = 10.15(0) Å and  $b = 119.09(0)^{\circ}$ , which are close to those of the standard data file (from PDF no. 842208 for  $Co_2P_4O_{12}$  and PDF no.782285 for  $Fe_2P_4O_{12}$ ) and the literature [9–11,14].

#### 3.3. FTIR spectroscopy

The CoFeP<sub>4</sub>O<sub>12</sub> structure is characterized by a three- dimensional framework with MO<sub>6</sub> (M = Co or Fe) polyhedral linked with P<sub>4</sub>O<sub>12</sub> rings by M–O–P. The basic structure unit is the centrosymmetric cyclote-traphosphate ring P<sub>4</sub>O<sub>12</sub> and therefore vibrational modes can consider it as made up of the P<sub>4</sub>O<sup>4</sup><sub>12</sub> anion. The vibrational modes of P<sub>4</sub>O<sup>4</sup><sub>12</sub> ion observed in the frequency range of 370–1400 cm<sup>-1</sup> are assigned according to the literature (Fig. 2) [18–20]. The many peaks split in these regions indicate the different strength of the bond between cations (M = Co<sup>2+</sup> and Fe<sup>2+</sup>) and anion (P<sub>4</sub>O<sup>4</sup><sub>12</sub>), which confirm the inserting different cations in the skeletal as well as the formation of binary cobalt iron cyclotetraphosphate. The anion contains the PO<sup>2</sup><sub>2</sub> radical and the P–O–P bridge which differ in their bond strength. As the P–O bond strength in the PO<sup>2</sup><sub>2</sub> radical is stronger than in the P–O–P bridge, the

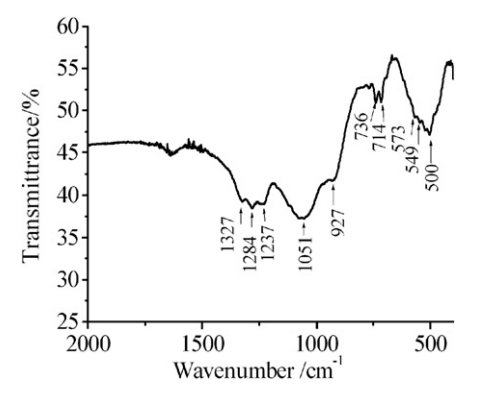


Fig. 2. FTIR spectrum of CoFeP<sub>4</sub>O<sub>12</sub>.

stretching frequencies of the PO<sub>2</sub><sup>2-</sup> radical are expected to be higher than those in the P-O-P bridge. The P-O bonds in the PO<sub>2</sub><sup>2-</sup> radical show its asymmetric and symmetric stretching frequencies around 1327–1237 and  $1150-1000\,\mathrm{cm}^{-1}$ , respectively. The asymmetric and symmetric stretching frequencies of the P-O-P bridge are observed in the regions of 1000–900 and 800–700 cm<sup>-1</sup>, respectively. The symmetric P–O–P bridge stretching modes occur at 736 and 714 cm<sup>-1</sup>. These observed bands are known to be the most striking feature of cyclotetraphosphate spectra, along with the presence of the  $\nu_{as} \text{OPO}^-$  band. From X-ray diffraction data [12], it was shown that the crystal structure is monoclinic (space group C2/c) with a cyclic structure of the [P<sub>4</sub>O<sub>12</sub>]<sup>4-</sup> anion. This has been confirmed by the FTIR measurements. The bending modes are expected in the area  $600-400 \text{ cm}^{-1}$  (PO<sub>2</sub><sup>2</sup> radical) and  $400-400 \text{ cm}^{-1}$  $370 \text{ cm}^{-1}$  (P–O–P bride). The metal–O stretching usually appears in the bending mode region as the bending modes of the P-O-P bridge and absorption bands associated with these vibrations are usually very weak. The weak FTIR band at 400 cm<sup>-1</sup> is probably due to metal-O stretching mode.

#### 3.4. Scanning electron microscopy

SEM micrograph of CoFeP<sub>4</sub>O<sub>12</sub> sample is shown in Fig. 3. It can be seen that the sample is composed of floral-like structures. There is soft agglomeration phenomenon among the particles of CoFeP<sub>4</sub>O<sub>12</sub>, which is attributed that the strong absorption of each other exists among particles with the layered structure compound. The floral-like morphology consists of similar petal-like flakes growing radically from the centre as can be observed under a higher magnification (inset). The different morphologies between the single metal compounds (M<sub>2</sub>P<sub>4</sub>O<sub>12</sub>, M = Co or Fe) and the binary  $CoFeP_4O_{12}$  indicate the presence of Co ionsin substitution position of Fe ions, which confirms the formation of binary cobalt iron cyclotetraphosphate CoFeP4O12. The result of SEM experiment indicates that the grain sizes of CoFeP<sub>4</sub>O<sub>12</sub> are not consistent with the crystallite sizes in the XRD analysis indicating the influence of media agents on particle nucleation and growth mechanisms. In addition, the floral-like morphology of the prepared CoFeP<sub>4</sub>O<sub>12</sub> in this work is different from the non-uniform particles of CoFeP<sub>4</sub>O<sub>12</sub> reported in our previous work [14]. These results indicate that the medium reagents for precipitation have the strong effect on the morphology of binary metal cyclotetraphosphate and are also in agreement with other reported other phosphate groups [12–15].

#### 3.5. VSM magnetometer

The room-temperature magnetization curves of the floral-like microparticle  $CoFeP_4O_{12}$  displays typical superparamagnetic behavior (Fig. 4). This curve is typical superparamagnetic behavior without any

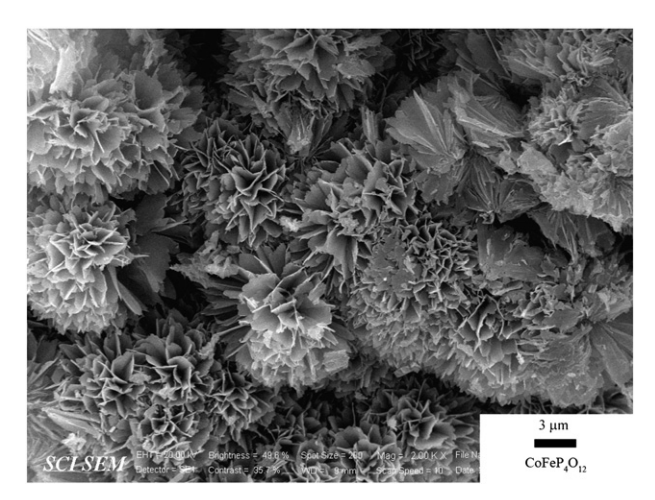


**Fig. 3.** SEM micrograph of CoFeP<sub>4</sub>O<sub>12</sub>.

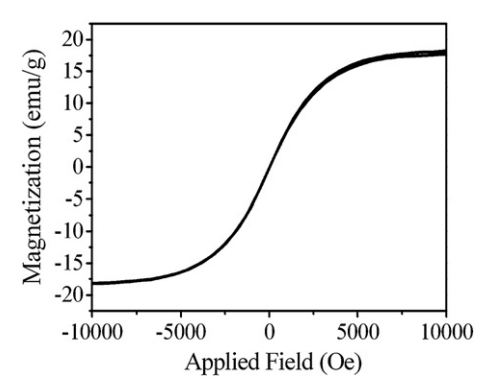


**Fig. 4.** The specific magnetization of CoFeP $_4$ O $_{12}$  as a function of field, measured at 20  $^{\circ}$ C.

hysteresis in the field range of  $\pm$  10,000 Oe. Specific saturated magnetization  $(M_s)$  value of the floral-like microparticle CoFeP<sub>4</sub>O<sub>12</sub> (18.202 emu/ g) in this work is higher than that of non-uniform microparticle CoFeP<sub>4</sub>O<sub>12</sub> (14.243 emu/g) reported in our previous work [14] because of their small size. The result is lower than the saturated magnetization for Fe<sub>3</sub>O<sub>4</sub> nanoparticles (in a range of 30–50 emu/g) [21,22]. It is seen that magnetization of the prepared CoFeP<sub>4</sub>O<sub>12</sub> is lower than that of Fe<sub>2</sub>P<sub>4</sub>O<sub>12</sub> (85.01 emu/g) but markedly distinct from the diamagnetic properties of Co<sub>2</sub>P<sub>4</sub>O<sub>12</sub> [9,10]. This result indicates that the presence of Co ions in substitution position of Fe ions has the strong effect on the magnetic behavior of CoFeP<sub>4</sub>O<sub>12</sub>. This study demonstrates that the floral-like microparticle CoFeP<sub>4</sub>O<sub>12</sub> is truly superparamagnetic, which is a unique feature of magnetic materials. This material may be used in modern technologies including magnetic resonance imaging contrast agents, data lifetime in high density information storage, ferrofluid technology, and magnetocaloric refrigeration [21-25].

#### 4. Conclusions

Floral-like microparticle CoFeP<sub>4</sub>O<sub>12</sub> was successfully synthesized by solid state route from cobalt carbonate, iron metal and phosphoric acid at 500 °C. The floral-like morphology and higher magnetization value of CoFeP<sub>4</sub>O<sub>12</sub> in this work are different from those obtained from other works indicating that this may be caused by the media agents. The morphology of CoFeP<sub>4</sub>O<sub>12</sub> shows floral-like crystals, as revealed by SEM data. The synthesized powder is polycrystalline, having crystallite size of  $49\pm20$  nm for CoFeP<sub>4</sub>O<sub>12</sub>, as estimated by XRD. The synthesized CoFeP<sub>4</sub>O<sub>12</sub> is superparamagnetic, having no hysteresis loop in the range of -10,000 Oe <H < 10,000 Oe with the specific magnetization of 18.202 emu/g at 10 kOe. The results obtained are necessary for elaboration of technology to produce the cyclotetraphosphate of transition metals, which may be useful for potentially applications as catalytic, ceramic and the biomedical materials etc.

#### Acknowledgements

This work is financially supported by the Thailand Research Fund (TRF), the Commission on Higher Education (CHE): Research Grant for New Scholar and the National Nanotechnology Center (NANOTEC) NSTDA, Ministry of Science and Technology, Thailand.

#### References

- H.N. Lim, A. Kassim, N.M. Huang, P.S. Khiewc, W.S. Chiu, Three-dimensional flower-like brushite crystals prepared from high internal phase emulsion for drug delivery application, Colloids Surf., A 345 (2009) 211–218.
- [2] F.-H. Lin, C.-J. Liao, K.-S. Chen, J.-S. Sun, C.-P. Lin, Petal-like apatite formed on the surface of tricalcium phosphate ceramic after soaking in distilled water, Biomaterials 22 (2001) 2981–2992.
- [3] L. Hong, Q. Li, H. Lin, Y. Li, Synthesis of flower-like silver nanoarchitectures at room temperature, Mater. Res. Bull. 44 (2009) 1201–1204.

- [4] M.T. Averbuch-Pouchot, A. Durif, Topics in Phosphate Chemistry, World Scientific Publishing Co. Pte. Ltd., Singapore, 1996.
- [5] M. Trojan, P. Šulcová, Binary Cu(II) Mn(II) cyclo-tetraphosphates, Dyes Pigm. 47 (2000) 291–294.
- [6] M. Trojan, P. Šulcová, P. MoŠner, The synthesis of binary zinc(II) nickel(II) cyclotetraphosphates as new special pigments, Dyes Pigm. 44 (2000) 161–164.
- [7] M. Trojan, Binary cyclotetraphosphates Zn<sub>2-x</sub>Ca<sub>x</sub>P<sub>4</sub>O<sub>12</sub> as new special pigments, Dyes Pigm. 13 (2000) 1–10.
- [8] M. Trojan, D. Brandová, A study of the thermal preparation of c-Cd<sub>4/3</sub>Ca<sub>2/3</sub>P<sub>4</sub>O<sub>12</sub>, Thermochim. Acta 160 (1990) 349–359.
- [9] B. Boonchom, S. Maensiri, S. Youngme, C. Danvirutai, A simple synthesis and room temperature magnetic properties of new binary Mn<sub>0.5</sub>Fe<sub>0.5</sub>(H<sub>2</sub>PO<sub>4</sub>)<sub>2</sub> xH<sub>2</sub>O obtained from a rapid co-precipitation at ambient temperature, Solid State Sci. 11 (2009) 485–490.
- [10] B. Boonchom, C. Danvirutai, Synthesis of MnNiP<sub>2</sub>O<sub>7</sub> and nonisothermal decomposition kinetics of a new binary Mn<sub>0.5</sub>Ni<sub>0.5</sub>HPO<sub>4</sub> H<sub>2</sub>O precursor obtained from a rapid coprecipitation at ambient temperature, Ind. Eng. Chem. Res. 47 (2008) 5976–5981.
- [11] B. Boonchom, C. Danvirutai, S. Youngme, A rapid co-precipitation and non-isothermal decomposition kinetics of new binary Mn<sub>0.5</sub>Co<sub>0.5</sub>(H<sub>2</sub>PO<sub>4</sub>)<sub>2</sub> 2H<sub>2</sub>O, Solid State Sci. 10 (2008) 129–136.
- [12] M. Bagieu-Beucher, M. Gondrand, M. Perroux, High-pressure study of tetrameta-phosphates of the M<sub>2</sub>P<sub>4</sub>O<sub>12</sub> type (M = Ni, Mg, Cu, Co, Fe, Mn, Cd). Crystallographic data on all M<sub>2</sub>P<sub>4</sub>O<sub>12</sub> compounds, J. Solid State Chem. 19 (1976) 353–357.
- [13] B. Boonchom, N. Phuvongpha, Synthesis of new binary cobalt iron pyrophosphate  $CoFeP_2O_7$ , Mater. Lett. 63 (2009) 1709–1711.
- [14] B. Boonchom, M. Thongkam, S. Kongtaweelert, N. Vittayakorn, A simple route to synthesize new binary cobalt iron cycloletraphosphate CoFeP<sub>4</sub>O<sub>12</sub> using aqueous and acetone media, J. Alloys Compd. 486 (2009) 689–692.
- [15] S. Scaccia, M. Carewska, A. Di Bartolomeo, P.P. Prosini, Thermoanalytical investigation of nanocrystalline iron (II) phosphate obtained by spontaneous precipitation from aqueous solutions, Thermochim. Acta 397 (2003) 135–141.

- [16] S. Scaccia, M. Carewska, P.P. Prosini, Thermoanalytical study of iron(III) phosphate obtained by homogeneous precipitation from different media, Thermochim. Acta 413 (2004) 81–86.
- [17] B.D. Cullity, Elements of X-ray Diffraction, 2nd edAddison-Wesley Publishing, 1977.
- [18] V. Ramakrishnan, G. Aruldhas, Vibrational spectra of Cu(II) and Co(II) tetrametaphosphates, Infrared Phys. 25 (1985) 665–670.
- [19] E.J. Baran, R.C. Mercader, A. Massaferro, E. Kremer, Vibrational and <sup>57</sup>Fe-Mössbauer spectra of some mixed cation diphosphates of the type M<sup>II</sup>Fe<sup>III</sup><sub>2</sub>(P<sub>2</sub>O<sub>7</sub>)<sub>2</sub>, Spectrochim Acta. 60 (2004) 1001–1005.
- [20] E.H. Soumhi, I. Saadoune, A. Driss, A new organic-cation cyclotetraphosphate C10H28N4P4012 4H2O: crystal structure, thermal analysis, and vibrational spectra, J. Solid State Chem. 156 (2001) 364–369.
- [21] A.K. Gupta, M. Gupta, Synthesis and surface engineering of iron oxide nanoparticles for biomedical applications, Biomaterials 26 (2005) 3995–4021.
- [22] C. Yang, J. Xing, Y. Guan, J. Liu, H. Liu, Synthesis and characterization of superparamagnetic iron nanocomposites by hydrazine reduction, J. Alloys Compd. 385 (2004) 283–287.
- [23] S. Gyergyek, M. Huskić, D. Makovec, M. Drofenik, Superparamagnetic nanocomposites of iron oxide in a polymethyl methacrylate matrix synthesized by in situ polymerization, Colloids Surf. A 317 (2008) 49–55.
- [24] H. Cao, J. He, L. Deng, X. Gao, Fabrication of cyclodextrin-functionalized superparamagnetic Fe<sub>3</sub>O<sub>4</sub>/amino-silane core–shell nanoparticles via layer-by-layer method, Appl. Surf. Sci. 255 (2009) 7974–7980.
- [25] X. Li, G. Wang, Low-temperature synthesis and growth of superparamagnetic Zn<sub>0.5</sub>Ni<sub>0.5</sub>Fe<sub>2</sub>O<sub>4</sub> nanosized particles, J. Magn. Magn. Mater. 321 (2009) 1276–1279.

## Dielectric properties and phase transition behaviors in (1-x)PbZrO<sub>3</sub>-xPb $(Mg_{1/2}W_{1/2})$ O<sub>3</sub> ceramics

Naratip Vittayakorn, <sup>1,2,3,a)</sup> Piyanut Charoonsuk, <sup>2</sup> Panisara Kasiansin, <sup>2</sup> Supamas Wirunchit, <sup>1,3</sup> and Banjong Boonchom <sup>4</sup>

<sup>1</sup>College of KMITL Nanotechnology, King Mongkut's Institute of Technology Ladkrabang, Bangkok 10520, Thailand

<sup>2</sup>Department of Chemistry, Advanced Materials Science Research Unit, Faculty of Science, King Mongkut's Institute of Technology Ladkrabang, Bangkok 10520, Thailand

<sup>3</sup>Thailand Center of Excellence in Physics (ThEP), CHE, 328 Si Ayutthaya Rd., Bangkok 10400, Thailand <sup>4</sup>King Mongkut's Institute of Technology Ladkrabang, Chumphon Campus, 17/1 M.6 Pha Thiew District, Chumphon 86160, Thailand

(Received 24 June 2009; accepted 1 August 2009; published online 16 September 2009)

The solid solution of lead zirconate [PbZrO<sub>3</sub> (PZ)] and lead magnesium tungstate [Pb(Mg<sub>1/2</sub>W<sub>1/2</sub>)O<sub>3</sub> (PMW)] has been synthesized by the wolframite precursor method. The crystal structure, phase transformations, dielectric and thermal properties of (1-x)PZ-xPMW, where x=0.00–0.10, were investigated. The crystal structure of sintered ceramics was analyzed by x-ray diffraction. Phase-pure perovskite was obtained for all compositions. Furthermore, a change from orthorhombic to rhombohedral symmetry was observed as the mole fraction of increased PMW. As a result, it was found that PbZrO<sub>3</sub>-Pb(Mg<sub>1/2</sub>W<sub>1/2</sub>)O<sub>3</sub> undergoes successive transitions from the antiferroelectric phase to the ferroelectric phase to the paraelectric state. The coexistence of orthorhombic and rhombohedral phases in this binary system is located near the composition x=0.1. © 2009 American Institute of Physics. [doi:10.1063/1.3212991]

#### I. INTRODUCTION

Antiferroelectric (AFE) materials are widely used for various devices: high charge storage capacitors, large strain actuators, and microelectromechanical systems. 1,2 The basic physics for these applications is due to the behaviors of electric-field-induced AFE to ferroelectric (FE) phase transformation. Lead zirconate [PbZrO3 (PZ)] has been considered as the prototype AFE since its discovery by Sawaguchi et al. in 1951.<sup>3</sup> At room temperature, PZ has an orthorhombic structure with the lattice parameters a=5.884 Å, b=11.768 Å, and c=8.22 Å. The orthorhombic unit cell consists of eight formula units and eight primitive cells with a tetragonal structure.<sup>3</sup> AFE PZ has spontaneous polarization, with adjacent rows of dipoles oriented antiparallel to each other, and no net spontaneous polarization at the equilibrium. AFE PZ has a phase transition to the paraelectric (PE) state, which occurs at approximately 236 °C. However, transition from the orthorhombic AFE to a rhombohedral FE structure, at a few degrees below the PE transition temperature, has been reported by several authors.<sup>5,6</sup> It is well known that the AFE to FE phase transformation in PZ ceramic requires a very strong electric field; otherwise, dielectric breakdown occurs.<sup>3</sup> Consequently, most commercial AFE ceramics are chemically modified by adding Ti<sup>4+</sup>, Nb<sup>5+</sup>, Sn<sup>4+</sup>, or La<sup>3+</sup> to reduce the critical field and optimize the physical and electrical properties.<sup>7,8</sup>

Lead magnesium tungstate [Pb(Mg<sub>1/2</sub>W<sub>1/2</sub>)O<sub>3</sub> (PMW)] is a complex perovskite compound with Mg<sup>2+</sup> and W<sup>6+</sup> ordered on the *B*-site of the  $ABO_3$  perovskite structure. <sup>9</sup> PMW-

based ceramics have been known as dielectric materials possessing low dielectric loss and low sintering temperature. Therefore, these materials can be used to fabricate multilayer capacitors with inner electrodes that melt in low temperature. At room temperature, PMW has an AFE phase, which has an orthorhombic structure. It undergoes a first order phase transition from an orthorhombic AFE phase to the cubic phase (*Fm3m*) at 38 °C. The room temperature x-ray diffraction (XRD) pattern of PMW shows the presence of superlattice reflections due to the *B*-site ordering.

Most studies of FE solid solutions have focused on relaxor-PT systems, such as  $Pb(Mg_{1/3}Nb_{2/3})O_3-PbTiO_3$ ,  $^{11}$   $Pb(Zn_{1/3}Nb_{2/3})O_3-PbTiO_3$ ,  $^{11,12}$  and  $Pb(Ni_{1/3}Nb_{2/3})O_3-PbTiO_3$ ,  $^{13}$  and AFE-PT systems, for example,  $PbZrO_3-PbTiO_3$ .  $^{14,15}$  A small number of studies have focused on AFE-AFE systems. Furthermore, the structure-property relationship between solid solution and an AFE-AFE system is still unclear.

Since PZ is an AFE with a sharp dielectric peak near  $T_c \sim 236~^{\circ}$ C, and PMW is a *B*-site ordered AFE with a sharp maximum permittivity at  $T_c \sim 38~^{\circ}$ C, the Curie temperature in the PZ-PMW system can be engineered over a wide range of temperatures by controlling the amount of PMW in the system. This study deals with the binary compound of PZ-PMW because, to the author's knowledge, there has been no detailed report on the structure and electrical properties of this entire system. In order to obtain more information about the combination of AFE and ordered AFE materials and recognize the properties of PZMW ceramics, this paper attempted to carry out synthesis of the quasibinary solid solu-

a) Author to whom correspondence should be addressed. Electronic mail: naratipcmu@yahoo.com. FAX: 66-2-326-4415.

tion,  $Pb[Zr_{(1-x)}(Mg_{1/2}W_{1/2})_x]O_3$  with x=0.0-0.1, using the wolframite precursor method. This paper also reported some properties of the ceramics obtained.

#### II. EXPERIMENTAL PROCEDURE

Samples of Pb[ $Zr_{(1-x)}(Mg_{1/2}W_{1/2})_x$ ]O<sub>3</sub>, x=0.00, 0.02, 0.04, 0.06, 0.08, and 0.10, were synthesized from high-purity (>99%) oxides via a modified wolframite-type route. The wolframite (MgWO<sub>4</sub>) was initially prepared by mixing starting magnesium oxide (MgO) and tungsten (VI) oxide (WO<sub>3</sub>). Single phase formation of MgWO<sub>4</sub> was confirmed by XRD. The wolframite precursor was then mixed and ball milled with predetermined amounts of PbO (with 2 at. % excess) and ZrO2 powders. The mixture was calcined in an alumina crucible at 900 °C for 2 h to form phase-pure perovskite powders. The calcined powders were milled for 6 h to reduce the particle size. After grinding and sieving, the calcined powder was mixed with a 5 wt % polyvinyl alcohol binder and uniaxially pressed into a pellet. The binder burnout occurred by slowly heating the pellets to 500 °C and holding them at that temperature for 2 h. Sintering occurred between 1100 and 1250 °C with a dwell time of 4 h depending on the composition. To mitigate the effects of lead loss during sintering, the pellets were sintered in a closed alumina crucible containing PbZrO3 powder. The density of the sintered PZ-PMW pellets was measured by the Archimedes water immersion method. The relative density of all the sintered pellets was approximately 96%-97% of the theoretical density. The crystal structure of the sintered ceramics was analyzed by XRD (Bruker D8 Advance diffractometer). To determine the dielectric and FE properties, the maximum density of each composition sample was lapped on their major faces, and silver electrodes were made from a lowtemperature silver paste by firing at 550 °C for 30 min to enable recording of electrical measurements. The relative permittivity  $(\varepsilon_r)$  (calculated from the capacitance using the sample dimensions and sample thickness) and dissipation factor (tan  $\delta$ ) of stress-free samples were measured using a precision LCR meter (HP-4284A, Hewlett-Packard, Palo Alto, CA). The capacitance and dissipation factors of the samples were measured at 100 Hz-1 MHz, the temperature varied between 25 and 300 °C, and a heating rate of 2 °C/min was used while measurements were being taken. The phase transitions were also measured by a differential scanning calorimeter (DSC 2920, TA Instrument) between ambient temperature and 350 °C at a rate of 10 °C/min. The FE polarization versus electric field (P-E) measurements were made using an RT66A standard FE test system with a frequency of about 4 Hz. The peak field was maintained at 30 kV/cm during measurement.

#### **III. RESULTS AND DISCUSSION**

#### A. Crystal structure

XRD patterns for the (1-x)PZ-xPMW, x=0.0–0.1, are presented in Fig. 1. The complete crystalline solutions of a perovskite structure were formed throughout the whole composition range. Evidence of the pyrochlore or other second

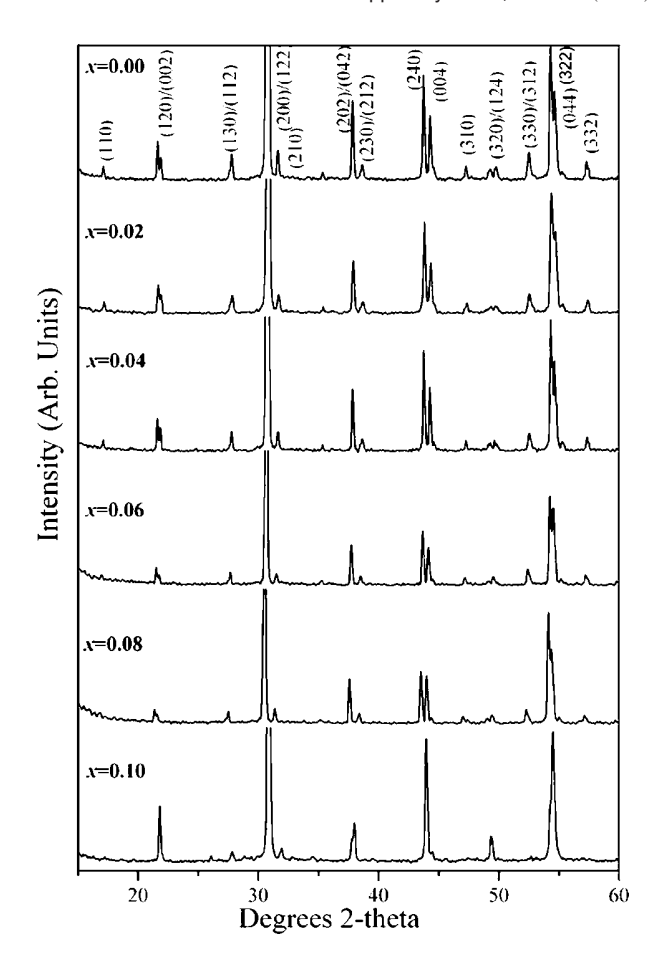


FIG. 1. XRD profiles for (1-x)PZ-xPMW obtained at optimum sintering temperature.

phases was not detected in the patterns. It is believed that Mg<sup>2+</sup> and W<sup>6+</sup> ions diffuse into PZ lattices to form a solid solution. In general, XRD patterns of pure PZ ceramic exhibit  $\frac{1}{4}$  (h k l) superlattice reflections arising from the antiparallel displacements of Pb2+ ions. Meanwhile, XRD patterns of perovskite PMW display  $\frac{1}{2}$  (h k l) superlattice reflections, resulting from the ordering of B-site ions in an  $ABO_3$  structure. Figure 1 shows that the  $\frac{1}{4}$  (h k l) superlattice reflections were clearly presented in all compositions. Unfortunately, the  $\frac{1}{2}$  (h k l) superlattice reflections were not detected, indicating that the long range Mg/W/Zr cation order was not developed. Furthermore, the intensity of  $\frac{1}{4}$ (h k l) superlattice reflections decreased with increased  $Mg^{2+}/W^{6+}$  content. This result indicates that the replacement of the Zr4+ ions by Mg2+/W6+ ions decreases the driving force for an antiparallel shift of Pb2+ ions.

Figure 2 shows enlarged profiles of the  $(1\ 1\ 1)$ ,  $(2\ 4\ 0)$ , and  $\frac{1}{4}$   $(h\ k\ l)$  superlattice reflections for determining the crystal structure of the as-sintered ceramics. Based on the careful XRD spectra study of the  $\frac{1}{4}$   $(h\ k\ l)$  superlattice reflection,  $(1\ 1\ 1)$  and  $(2\ 4\ 0)$  reflections in Fig. 2, a phase transformation from the orthorhombic to the rhombohedral structure was found to occur with increasing PMW content. The XRD data show that the  $\frac{1}{4}$   $(h\ k\ l)$  superlattice reflection peak (\*) and splitting of  $(2\ 4\ 0)$  peaks are clearly observed in the composition x=0.0-0.08, indicating that the major

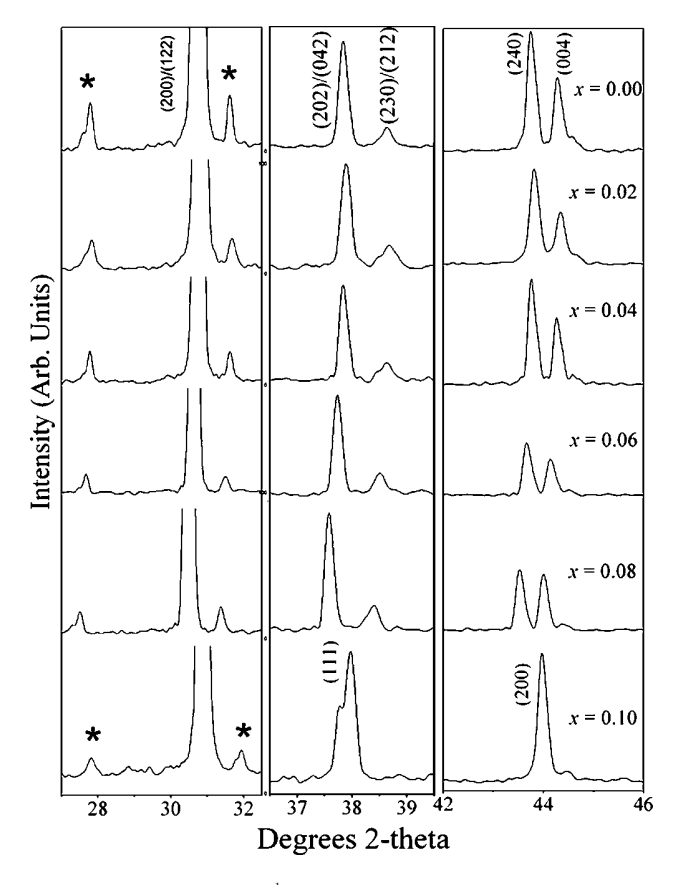


FIG. 2. XRD profiles for the  $\frac{1}{4}$  ( $h \ k \ l$ ) superlattice reflection (\*) and (200) peaks of (1-x)PZ-xPMW, x=0.00–0.10, ceramics.

phase in those compositions had an orthorhombic symmetry. At x=0.1 composition, the split (2 4 0) peaks from an orthorhombic symmetry were rapidly combined into a single peak, and the (1 1 1) diffraction peaks began to split, indicating that the crystal transformed into a rhombohedral symmetry. However, the  $\frac{1}{4}$  (h k l) superlattice reflections still remained. This indicates that both orthorhombic and rhombohedral phases coexist in this composition. Nevertheless, hysteresis loop results indicated that the x=0.1 composition shows an AFE phase at room temperature. We believe that this composition is within the orthorhombic-rich side of the coexistent phase. It is interesting to note that the phase evolution sequence in the present PZ-PMW system is very similar to that in the Pb<sub>(1-x)</sub>Ba<sub>x</sub>ZrO<sub>3</sub>,  $^{16}$  PbZrO<sub>3</sub>-Pb(Co<sub>1/3</sub>Nb<sub>2/3</sub>)O<sub>3</sub>,  $^{17}$  PbZrO<sub>3</sub>-Pb(Ni<sub>1/3</sub>Nb<sub>2/3</sub>)O<sub>3</sub>,  $^{18}$ -20 and PbZrO<sub>3</sub>-Pb(Zn<sub>1/3</sub>Nb<sub>2/3</sub>)O<sub>3</sub>,  $^{21,22}$  systems.

#### **B.** Dielectric properties

The temperature dependencies of the relative permittivity and dielectric losses during as-sintered ceramic heating are shown in Fig. 3. A pure PZ ceramic shows the first order phase transition. The temperature dependence of relative permittivity shows discontinuities at the transitions, and the maximum relative permittivity is 3600. Above the Curie temperature, the relative permittivity follows the Curie–Weiss law,  $\varepsilon_r = C/(T-T_0)$ , with the Curie constant  $C \sim 1.59 \times 10^{-5}$  K and Curie–Weiss temperature  $T_0 \sim 191$  °C. The fact that the Curie–Weiss temperature  $T_0$  is lower than the transition temperature ( $T_c = 231$  °C) confirms the first order type of the phase transition in PbZrO<sub>3</sub>. The measured Curie

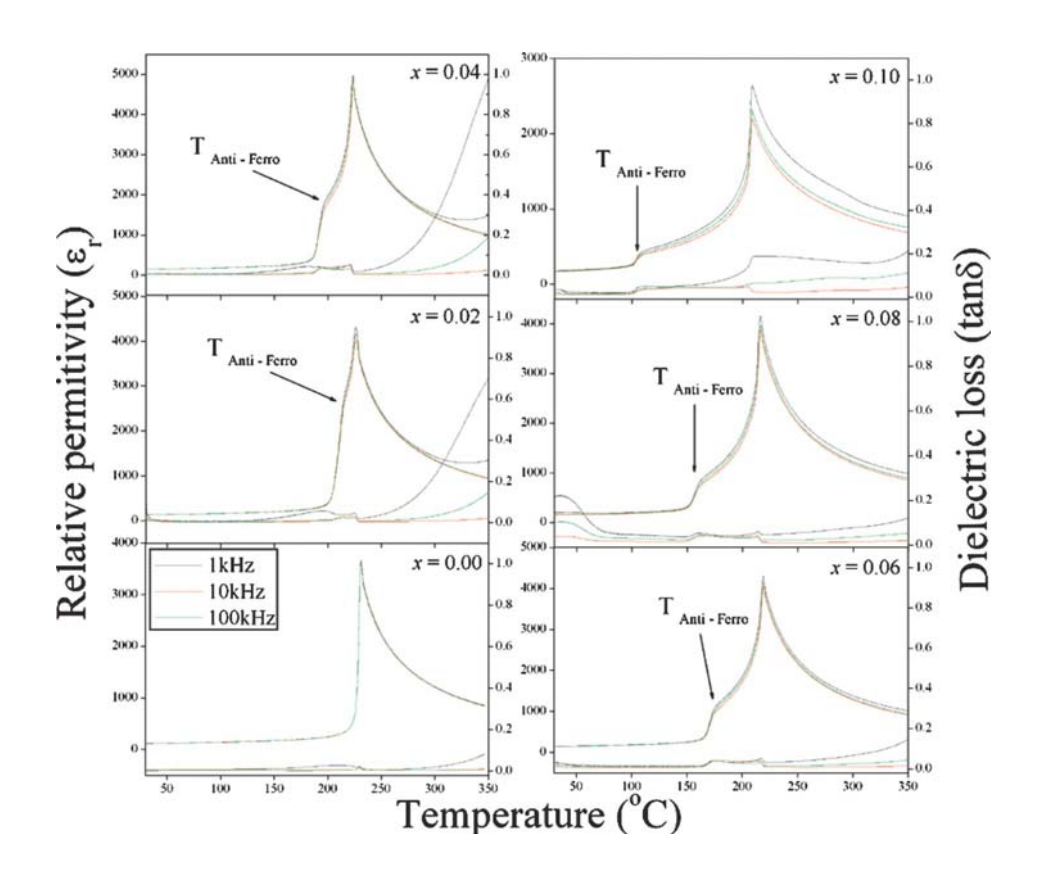


FIG. 3. (Color online) Relative permittivity  $(\varepsilon_r)$  and dielectric loss (tan  $\delta$ ) as a temperature function of (1-x)PZ-xPMW, x=0.00-0.10, ceramics.

TABLE I. Dielectric properties of (1-x)PZ-xPMW, x=0.00-0.10, ceramics.

Compositions	Crystal structure	$arepsilon_{r, ext{room}}$	$arepsilon_{r, ext{max}}$	$T_{ ext{AFE-FE}}$ (°C)	T <sub>FE-PE</sub> (°C)
x = 0.00	O	116	3670		231
x = 0.02	O	140	4318	214	226
x = 0.04	O	150	4836	195	222
x = 0.06	O	155	4057	174	219
x = 0.08	0	200	4160	160	216
x = 0.10	O+R	180	2643	105	206

O is the orthorhombic phase and R is the rhombohedral phase.

constant and Curie-Weiss temperature are in close agreement with that reported by Sawaguchi. 18,19 For the composition x=0.02, there were two distinct changes in both dielectric peak and loss. The first one occurred at around 214 °C, where both relative permittivity and dielectric loss increased by one order of magnitude. This anomaly is due to the transformation from the AFE to the FE intermediate phase. Later FE data descriptions supported this assumption.

The dielectric anomaly corresponding to the AFE-FE transition was also observed at 195, 174, and 160 °C, and at 105 °C for compositions x=0.04, 0.06, 0.08, and 0.1. The value of relative permittivity at the AFE-FE phase transition temperature decreases with increasing PMW content from 2700 for x=0.02 to 400 for x=0.1. Crystal structure, dielectric data, and transition temperature are summarized in Table I. The temperature range width of the FE phase increases progressively with PMW content. It is interesting to note that all compositions show the AFE-FE phase transition temperature higher than room temperature, and an AFE state is expected to be observed in all compositions at room temperature.

The second abrupt change occurred at the dielectric maximum ( $\varepsilon_{r,\text{max}}$ ). This anomaly is linked to the transition of the FE into the cubic PE phase. Dielectric results have shown a significant difference in  $\varepsilon_{r,\text{max}}$  across the composition range. This may be due to the ionic size difference between Zr<sup>4+</sup> and Mg<sup>2+</sup>/W<sup>6+</sup>. However, the transition temperature is well dispersed over the compositions. The FE-PE transition temperature  $(T_{\text{FE-PE}})$  decreases nearly linearly at the rate of 2.28  $^{\circ}\text{C/mol}$  % of PMW when compared with its value for pure PZ. It is noticeable that this rate is much less than PZ-PNN (2.81 °C/mol %). 18,19

#### C. FE properties

To clarify the dielectric behavior of the FE intermediate phases further in the PZ-PMW system, electrical polarization hysteresis loop measurements were performed under a peak field of 30 kV. At 30 °C, no FE hysteresis loop was observed in the composition  $0.0 \le x \le 0.1$ . The linear polarization was observed, as a function of electric fields, in a range of up to 30 kV/cm. This could indicate that ceramics with the composition  $x \le 0.1$  have an AFE behavior at room temperature. For AFE ceramics, the net remanent polarization  $(P_r)$  is zero due to the existence of the antiparallel dipole moments. To induce an AFE-FE phase transition, an intense electric field needs to be applied to the ceramics. However, it is well known that the electric field required for inducing the AFE-FE transition at room temperature in PZ ceramics is usually higher than the breakdown strength of the ceramics. FE data support the assumption of an existing AFE stage at room temperature in dielectric results.

Figures 4(a)-4(d) show the changes in the hysteresis loop with rising temperature for the 0.9PZ-0.1PMW ceramic. The FE hysteresis loop was recorded after the temperature was stabilized for at least 5 min. As shown in Fig. 4(a), very small polarizations can be induced by the electric field applied in the ceramic at room temperature. This is typical of an AFE ceramic subjected to electric fields that are not sufficient enough to induce the AFE to FE phase transition. Such linear behavior with minimum polarization remains at temperatures of up to 100 °C [Fig. 4(b)].

When the temperature was raised to 150 °C, a regular hysteresis loop exhibiting ferroelectricity was clearly demonstrated, corresponding to the intermediate phase between 105 °C and  $T_{\text{FE-PE}}$  [Fig. 4(c)]. At 150 °C, the  $P_r$ =19.2  $\mu$ C/cm<sup>2</sup> and  $E_c$ =7.9 kV/cm were observed. Above  $T_{\text{FE-PE}}$ , a linear curve was also seen as an indication of the cubic PE phase [Fig. 4(d)].

#### D. Thermal properties

The DSC technique was used as the secondary tool to investigate and confirm the phase transition of PZ-PMW ceramics with increasing PMW concentration. The phase transition temperature in PZ-PMW ceramics, clearly confirmed by DSC measurement, is presented in Fig. 5, which shows that two distinct endothermic peaks were observed for PZ-PMW samples with  $0.0 \le x \le 0.10$ . The lower temperature corresponds to the transition temperature of the AFE→FE phase transition, while the higher temperature corresponds to the FE→PE phase transition. AFE→FE phase transition, FE $\rightarrow$ PE phase transition,  $\Delta H$ ,  $\Delta S$ , and  $\Delta S/T_t$  are summarized in Table II. The AFE→FE phase transition was found in the composition  $0.0 \le x \le 0.10$ . The peaks shifted to lower temperatures with higher compositions of x. In Table II, the temperature range width of progressive FE phase continuously increases with PMW content. The temperature range widths of the FE phase are around 7.5, 25, 40, 52.6, 67.5, and 80 °C for compositions x=0.00, 0.02, 0.04, 0.06, 0.08,and 0.10, respectively. The peak value of heat capacity became weaker, and the heat capacity anomaly gradually broader, with increasing PMW concentration. These results

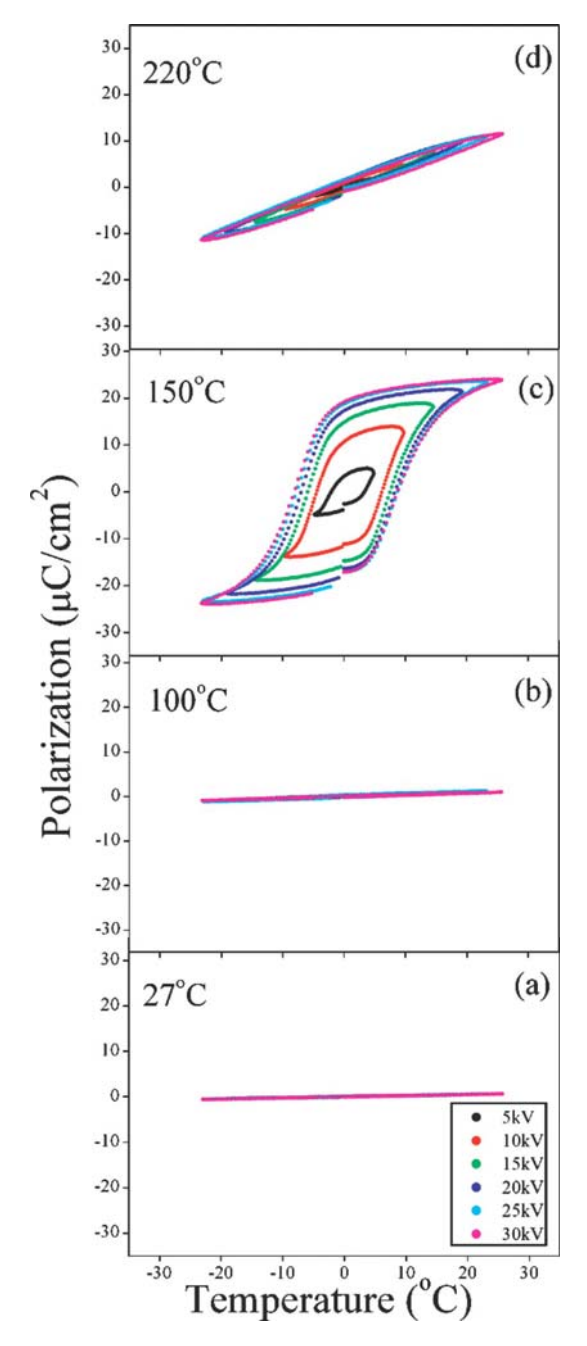


FIG. 4. (Color online) Polarization hysteresis loops recorded from 0.9PZ-0.1PMW at 4 Hz during heating at (a) 25 °C, (b) 100 °C, (c) 150 °C, and (d) 200 °C.

indicated that the phase transition deviates gradually from the first order type. Stenger and Burggraaf<sup>23</sup> observed that the change in entropy ( $\Delta S$ ) and  $\Delta S/T_t$  correlates with the fluctuation probability in conjunction with a small spontaneous lattice deformation and polarization. They explained that large values of the ratio,  $\Delta S/T_t$ , give sharp transition and lower values, which lead to diffuse behavior. Table II shows small  $\Delta S$  and  $\Delta S/T_t$  values for the PMW doped sample when compared to the pure PZ sample, indicating existence of diffuseness in the phase transition behavior that increases with increased PMW content, which coincides well with the dielectric results in the composition range investigated.

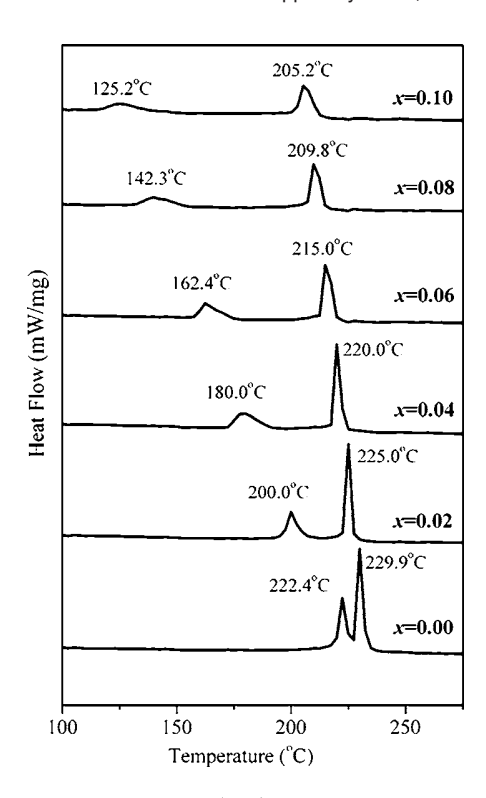


FIG. 5. Typical DSC curves for (1-x)PZ-xPMW, x=0.0-0.1, ceramics.

#### E. FE phase diagram

After accumulating all these data, a FE phase diagram for the (1-x)PZ-xPMW, x=0.0–0.1, was finally determined and is shown in Fig. 6. The phase diagram consists of three distinct crystallographic phases in this system: high-temperature PE cubic, FE rhombohedral, and AFE orthorhombic. At room temperature, the composition  $0.0 \le x \le 0.08$  has an AFE orthorhombic phase. With increasing temperature, an AFE orthorhombic to a FE rhombohedral phase was observed in the samples with  $0.02 \le x \le 0.10$ . The temperature range width of the FE rhombohedral phase increases progressively with PMW content. At room temperature, the phase boundary between the AFE orthorhombic and FE rhombohedral phases was observed near x=0.10.

#### **IV. CONCLUSIONS**

In this work, the phase transition and dielectric properties of the solid solution between AFE PZ and AFE PMW have been investigated. AFE PMW has been found to strongly influence the phase development and physical property responses of PZ ceramics. The crystal structure data obtained from XRD indicate that the solid solution, (1-x)PZ-xPMW, where x=0.0-0.1, successively transforms from orthorhombic to rhombohedral phase with an increase in PMW concentration. The coexistence of orthorhombic and rhombohedral phases in this binary system is located near the composition x=0.1.

#### **ACKNOWLEDGMENTS**

This work was supported by the Thailand Research Fund (TRF), National Research Council of Thailand (NRCT), and

TABLE II. Thermal properties of (1-x)PZ-xPMW, x=0.00-0.10, ceramics.

Compositions	$T_{ ext{AFE-FE}}$ (°C)	T <sub>FE-PE</sub> (°C)	Δ <i>H</i> (J g <sup>-1</sup> )	$\Delta S \times 10^3$ (J g <sup>-1</sup> K <sup>-1</sup> )	$(\Delta S/T_t) \times 10^6$ (J g <sup>-1</sup> K <sup>-2</sup> )
x = 0.00	222	230	2.227	9.682	42.096
x = 0.02	200	224	2.148	9.568	42.169
x = 0.04	180	220	2.354	10.676	48.416
x = 0.06	163	216	2.325	10.764	49.830
x = 0.08	140	211	1.956	9.270	43.934
x = 0.10	123	205	1.855	9.049	44.141

the National Nanotechnology Center (NANOTEC) NSTDA, Ministry of Science and Technology, Thailand through its program of Center of Excellence Network.

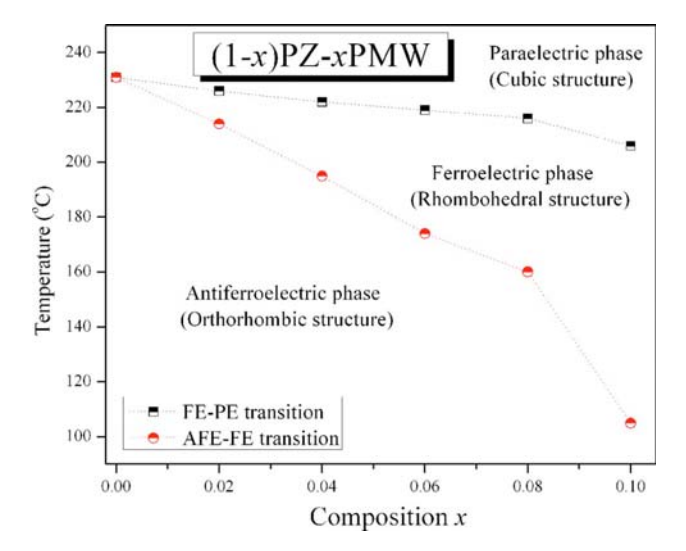


FIG. 6. (Color online) FE phase diagram of (1-x)PZ-xPMW, x=0.0–0.1, system.

- <sup>1</sup>K. Uchino, Ferroelectric Devices (Dekker, New York, 2000).
- <sup>2</sup>B. Jaffe and W. R. Cook, *Piezoelectric Ceramic* (Academic, New York, 1971).
- Sawaguchi, G. Shirane, and S. Hoshino, Phys. Rev. 83, 1078 (1951).
   Jona, G. Shirane, F. Mazzi, and R. Pepinsky, Phys. Rev. 105, 849 (1957).
- <sup>5</sup>L. E. Balyunis, V. Y. Topolov, I. S. Bah, and A. V. Turik, J. Phys.: Condens. Matter 5, 1419 (1993).
- <sup>6</sup>B. P. Pokharel and D. Pandey, Phys. Rev. B **65**, 214108 (2002).
- <sup>7</sup>H. He and X. Tan, Phys. Rev. B **72**, 024102 (2005).
- <sup>8</sup>L. J. Zhou, Z. Zhao, A. Zimmermann, F. Aldinger, and M. Nygren, J. Am. Ceram. Soc. 87, 606 (2004).
- <sup>9</sup>G. Baldinozzi, P. Sciau, M. Pinot, and D. Grebille, Acta Crystallogr., Sect. B: Struct. Sci. 51, 668 (1995).
- <sup>10</sup>L. Ruan, L. Li, and Z. Gui, J. Mater. Res. 13, 253 (1998).
- <sup>11</sup>S.-E. Park and T. R. Shrout, IEEE Trans. Ultrason. Ferroelectr. Freq. Control 44, 1140 (1997).
- <sup>12</sup>T. Takenaka, K. Muramata, and T. Fujii, Ferroelectrics **134**, 133 (1992).
- <sup>13</sup>I. A. Cornejo, B. Jadidian, E. K. Akdogan, and A. Safari, in *Proceedings of the 11th IEEE International Symposium on Applications of Ferroelectrics (ISAF 98)*, Montrex, Switzerland (Institute of Electrical and Electronic Engineers, Piscataway, NJ, 1998), pp. 337–340.
- <sup>14</sup>E. Sawaguchi, J. Phys. Soc. Jpn. **8**, 615 (1953).
- <sup>15</sup>G. A. Samara and E. L. Venturini, Phase Transitions 79, 21 (2006).
- <sup>16</sup>N. Vittayakorn, T. Bongkarn, and G. Rujijanagul, Physica B 387, 415 (2007).
- <sup>17</sup>W. Banlue and N. Vittayakorn, Appl. Phys. A: Mater. Sci. Process. **93**, 565 (2008)
- <sup>18</sup>S. Wirunchit, P. Laoratanakul, and N. Vittayakorn, J. Phys. D: Appl. Phys. 41, 125406 (2008).
- <sup>19</sup>S. Wirunchit and N. Vittayakorn, J. Appl. Phys. **104**, 024103 (2008).
- <sup>20</sup>N. Vittayakorn and S. Wirunchit, Smart Mater. Struct. **16**, 851 (2007).
- <sup>21</sup>W. Banlue and N. Vittayakorn, Ferroelectrics **382**, 122 (2009).
- <sup>22</sup>N. Vittayakorn and W. Banlue, Ferroelectrics **382**, 110 (2009).
- <sup>23</sup>C. Stenger and A. J. Burggraaf, Phys. Status Solidi A 61, 275 (1980).

### Antiferroelectric-ferroelectric phase transition in lead zinc niobate modified lead zirconate ceramics: crystal studies, microstructure, thermal and electrical properties

Usa Sukkha · Rangson Muanghlua · Surasak Niemcharoen · Banjong Boonchoma · Naratip Vittayakorn

Received: 11 February 2010 / Accepted: 8 June 2010 / Published online: 20 June 2010 © Springer-Verlag 2010

**Abstract** The combination of antiferroelectric PbZrO<sub>3</sub> (PZ) and relaxor ferroelectric Pb(Zn<sub>1/3</sub>Nb<sub>2/3</sub>)O<sub>3</sub> was prepared via the columbite precursor method. The basic characterizations were performed using X-ray diffraction (XRD), scanning electron microscopy (SEM), linear thermal expansion, differential scanning calorimetry (DSC) techniques, dielectric spectroscopy, and hysteresis measurement. The XRD result indicated that the solid solubility limit of the (1-x)PZ-xPZN system was about x=0.40. The crystal structure of (1-x)PZ-xPZN transformed from orthorhombic to rhombohedral symmetry when the concentration of PZN was increased. A ferroelectric intermediate phase began to appear between the paraelectric and antiferroelectric phases of pure PZ, with increasing PZN content. In addition,

U. Sukkha · N. Vittayakorn (☒)
Electroceramic Research Laboratory, College of KMITL
Nanotechnology, King Mongkut's Institite of Technology
Ladkrabang, Bangkok 10520, Thailand
e-mail: naratipcmu@yahoo.com

Fax: +66-2-3264415

R. Muanghlua · S. Niemcharoen
Department of Electronics, Faculty of Engineering,
King Mongkut's Institute of Technology Ladkrabang,
Bangkok 10520, Thailand

#### B. Boonchoma

King Mongkut's Institute of Technology Ladkrabang, Chumphon Campus, 17/1M. 6 Pha Thiew District, Chumphon 86160, Thailand

#### N. Vittayakorn

Department of Chemistry, Faculty of Science, King Mongkut's Institute of Technology Ladkrabang, Bangkok 10520, Thailand

U. Sukkha · N. Vittayakorn ThEp Center, CHE, 328 Si Ayutthaya Road, Bankok 10400, Thailand the temperature range of the ferroelectric phase increased with increasing PZN concentration. The morphotropic phase boundary (MPB) in this system was located close to the composition, x = 0.20.

#### 1 Introduction

Ferroelectric materials are extensively used for many different electronic devices, such as actuators, transducers, and multilayer capacitors [1–3]. Study over several decades has focused mainly on the development of physical and electrical properties of ferroelectric materials [2, 3]. Many ferroelectric ceramics have been developed from binary systems containing a combination of antiferroelectric and normal ferroelectric ceramics such as (1 - x)PbZrO<sub>3</sub>xPbTiO<sub>3</sub> (PZ-PT, PZT) [3, 4], and (1-x)SrTiO<sub>3</sub>-xPbZrO<sub>3</sub> [4, 5]. Among them, PZT is a very famous ferroelectric ceramic, due to its exhibition of high piezoelectric coefficient and electromechanical coupling factor around the morphotropic phase boundary (MPB) [3, 4]. The combination of normal ferroelectric and relaxor ferroelectric ceramics also shows excellent piezoelectric and dielectric properties such as  $Pb(Mg_{1/3}Nb_{2/3})O_3-PbTiO_3(PMN-PT)$ [5], Pb(Zn<sub>1/3</sub>Nb<sub>2/3</sub>)O<sub>3</sub>-PbTiO<sub>3</sub>(PZN-PT) [6, 7], Pb(Zn<sub>1/3</sub>- $Nb_{2/3})O_3-Pb(Zr_{1/2}Ti_{1/2})O_3(PZN-PZT)$  [8], and  $Pb(Ni_{1/3}-PZT)$  $Nb_{2/3})O_3-Pb(Zr_{1/2}Ti_{1/2})O_3(PNN-PZT)$  [9]. Furthermore, PZN-PZT, PNN-PZT, and  $Pb(Zr_{1/2}Ti_{1/2})O_3-Pb(Co_{1/3}-D_1)O_2$ Nb<sub>2/3</sub>)O<sub>3</sub>(PZT-PCN) [8-10] ceramics show high, relative permittivity.

Metal oxide Lead zirconate (PbZrO<sub>3</sub>, PZ) is a prototype of antiferroelectric ceramics. The PZ phase changes from the orthorhombic antiferroelectric phase (AFE) to cubic paraelectric phase (PE) at 236°C, and a ferroelectric phase (FE) exists over a very narrow temperature range



552 U. Sukkha et al.

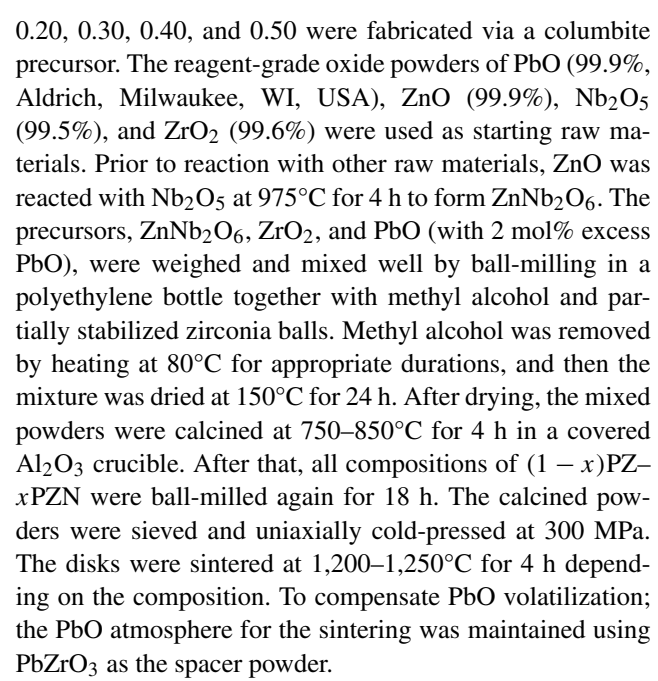
(230–233°C) [11]. Stability of the ferroelectric phase can be altered by substitutions such as  $Ba^{2+}$  ions or  $La^{3+}$  ions at the A-site of the perovskite structure (ABO<sub>3</sub>) [12–14]. Besides, PZ-based thin films are also particularly interesting because of the characteristic hysteresis loop resulting from the electric field-induced antiferroelectric-to-ferroelectric phase switching [14, 15]. Our recent work reported that the combination of antiferroelectric PZ and relaxor ferroelectric (RFE), Pb(Co<sub>1/3</sub>Nb<sub>2/3</sub>)O<sub>3</sub> (PCoN), or Pb(Ni<sub>1/3</sub>Nb<sub>2/3</sub>)O<sub>3</sub> (PNN) can also induce the ferroelectric phase of PZ [16, 17]. Nevertheless, due to PCoN and PNN having a low transition temperature ( $T_m \sim -90^{\circ}$ C and  $\sim -120^{\circ}$ C for PCoN and PNN, respectively), the transition temperature of PZ–PCoN and PZ–PNN systems was dramatically decreased [17, 18].

Complex metal oxide lead zinc niobate (Pb(Zn<sub>1/3</sub>Nb<sub>2/3</sub>) O<sub>3</sub>, PZN) is an RFE material with a rhombohedral perovskite structure at room temperature. A diffuse phase transition from paraelectric to ferroelectric polar state occurs at the high temperature of 140°C [6, 7]. There has been extensive research carried out on single PZN crystals because of their high relative permittivity ( $\varepsilon_{r,10\,\text{kHz}}$  reaching 50,000), pyroelectric constant ( $P_{20^{\circ}\text{C}} = 7 \times 10^{-12} \text{ C/m}^2 \text{ K}$ ) [6], high piezoelectric coefficient ( $d_{33} \approx 1100 \text{ pC/N}$ ), and high electromechanical coupling factors ( $k_{33} \approx 92\%$ ) [7]. Single crystals of PZN can be prepared by the flux-growth method, but pure perovskite PZN ceramics are difficult to synthesize via the conventional mixed-oxide method under atmospheric pressure [19, 20]. It is well known that forming solid solutions with other perovskites such as Ba(Zn<sub>1/3</sub>Nb<sub>2/3</sub>)O<sub>3</sub>, BaTiO<sub>3</sub>, and SrTiO<sub>3</sub> [20, 21] is considered an effective way to stabilize the perovskite PZN ceramic.

As both PZ and PZN have a perovskite structure, it has been suggested that PZN can be alloyed with PZ in order to stabilize the perovskite structure and find a suitable composition across the MPB. To the best of the author's knowledge, there has been no detailed report on the structure, solubility limit, dielectric properties, thermal properties, or phase transition in this system. Additionally, as PZN is a relaxor ferroelectric with broad dielectric peak near  $T_m \sim 140$  °C, and PZ is an antiferroelectric with sharp maximum permittivity at  $T_c \sim 230$ °C, the Curie temperature in the PZ-PZN system can be engineered over a wide range of temperatures via control of the PZN amount in the system. With a complementary characteristic, it is expected that excellent properties can be obtained from PZ-PZN ceramics. The relationship between the phase evolution and the properties was emphasized.

#### 2 Experiment

The composition series of (1-x)PbZrO<sub>3</sub>-xPb(Zn<sub>1/3</sub>Nb<sub>2/3</sub>) O<sub>3</sub> ceramics, where x = 0.00, 0.02, 0.04, 0.06, 0.08, 0.10,



The crystal structure and phase transition of the sintered pellets were characterized using an X-ray diffractometer (XRD; Bruker-AXS D8,  $CuK\alpha$  radiation). The density of PZ-PZN ceramics was measured via Archimedes water immersion method. Scanning electron microscopy (SEM; Hitachi, s4007) was employed to investigate the microstructure of sintered pellets. The phase transition of samples was investigated using a differential scanning calorimeter (DSC 2920, TA Instrument) between room temperature and 300°C at a heating rate of 10°C/min. To confirm the phase transition of samples, the sintered pellets were measured by a dilatometer (DIL 402 PC, Netzsch) between 25-300°C at a rate of 1°C/min. For the measurement of electrical properties, both sides of the maximum density of each composition sample were polished and electroded with silver paste (C1000, Heraeus). An LCR meter (HP4284A, Hewlett-Packard, Palo Alto, CA) was used to measure the dielectric properties, and the temperature varied between 25–350°C with a heating rate of 2°C/min. The polarizationelectric field (P-E) hysteresis loops were obtained at room temperature using a standardized ferroelectric tester system (RT-66A, Radiant Technologies, Albuquerque, NM) at a frequency of 4 Hz.

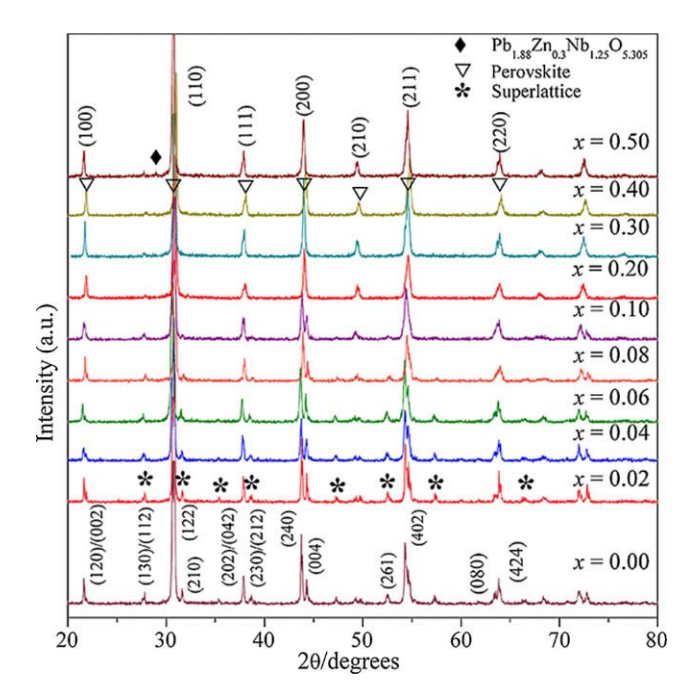
#### 3 Results and discussion

#### 3.1 Crystal structure

The XRD patterns of the sintered (1 - x)PZ-xPZN ceramics for  $0.00 \le x \le 0.50$  are shown in Fig. 1. At the composition,  $0.00 \le x \le 0.40$ , ceramic samples had a pure perovskite structure. Evidence for the secondary phases was



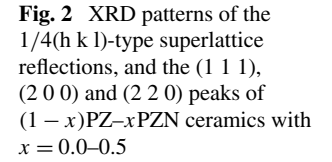
not observed in the patterns, indicating homogeneous solid solution of PZ–PZN. However, increasing the amount of PZN further to 50 mol%, gave rise to formation of the pyrochlore phase,  $Pb_{1.88}Zn_{0.3}Nb_{1.25}O_{5.305}$ , which could be matched with JCPDS No. 25-0446. This result could explain the larger ionic size of  $Zn^{2+}$  (0.88 Å) [22], as compared to

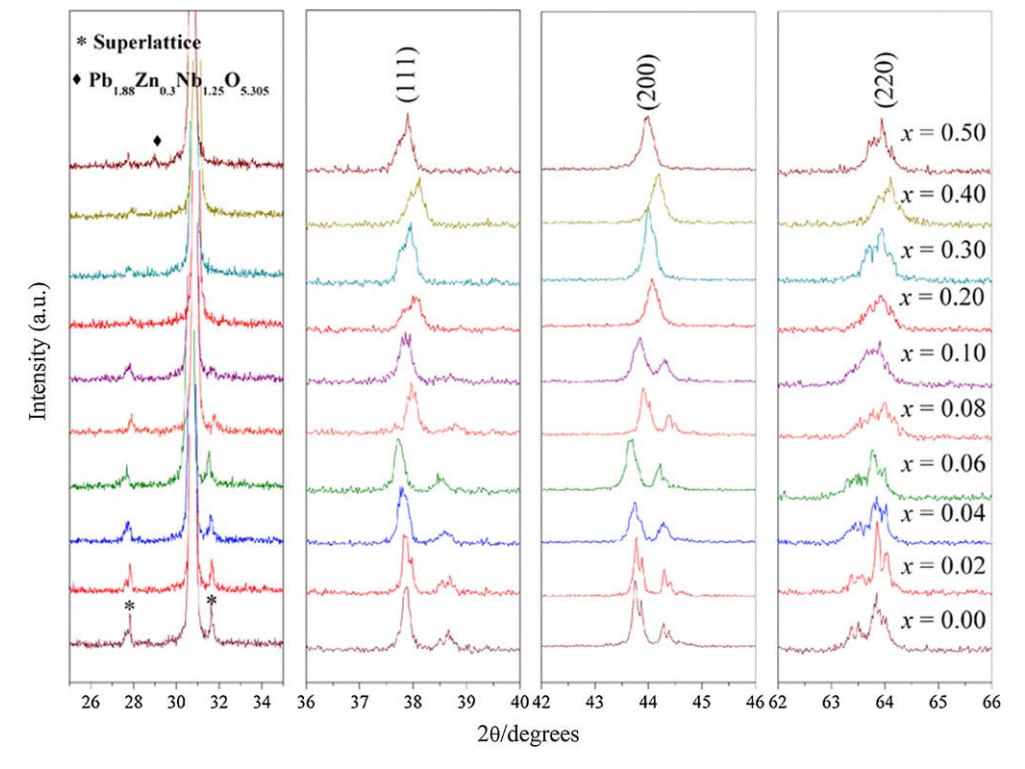


**Fig. 1** XRD patterns of sintered ceramics for various compositions of (1-x)PbZrO<sub>3</sub>-xPb(Zn<sub>1/3</sub>Nb<sub>2/3</sub>)O<sub>3</sub>, where x = 0.0-0.5

the sixfold lattice sites formed by the oxygen octrahedra. Then,  $Zn^{2+}$  cannot enter the B-site of the perovskite structure as a replacement for  $Zr^{4+}$  (0.86 Å) ions [22]. This result indicated that the solubility limit of the (1-x)PZ-xPZN system was found at x=0.40. Furthermore, the 1/4 (h k l)-type superlattice reflection peaks, identified with "\*", arise from antiparallel displacement of  $Pb^{2+}$  cations, and this was clearly seen in all compositions. The relative intensity of 1/4 (h k l)-type superlattice reflection peaks decreased with increasing PZN, which indicated that the substitution of  $Zr^{4+}$  ions by  $Zn^{2+}/Nb^{5+}$  ions decreased the driving force for an antiparallel shift of  $Pb^{2+}$  ions.

Figure 2 shows enlarged profiles of the 1/4 (h k l)-type superlattice reflections (\*): (1 1 1), (2 0 0), and (2 2 0) reflections. At the composition,  $0.00 \le x \le 0.10$ , the XRD data exhibit the superlattice reflections and splitting of (2 4 0) peak at roughly 43°, indicating that the crystal structure of samples at the composition, 0.00 < x < 0.10, are orthorhombic perovskite. Furthermore, the compositions,  $0.20 \le x \le 0.50$ , showed a split (1 1 1) and (2 2 0) reflection, and single (2 0 0) reflection, indicating that the crystal structure transformed into a rhombohedral structure. Moreover, the XRD patterns of  $0.20 \le x \le 0.50$  compositions also showed 1/4 (h k l)-type superlattice reflections. Therefore, it could be assumed that the orthorhombic and rhombohedral phase coexist in these compositions. Consequently, the composition, x = 0.20, is expected to be close to the MPB, whereas the  $0.30 \le x \le 0.50$  compositions are in the rhombohedral-rich region of the coexistent phase. Elu-

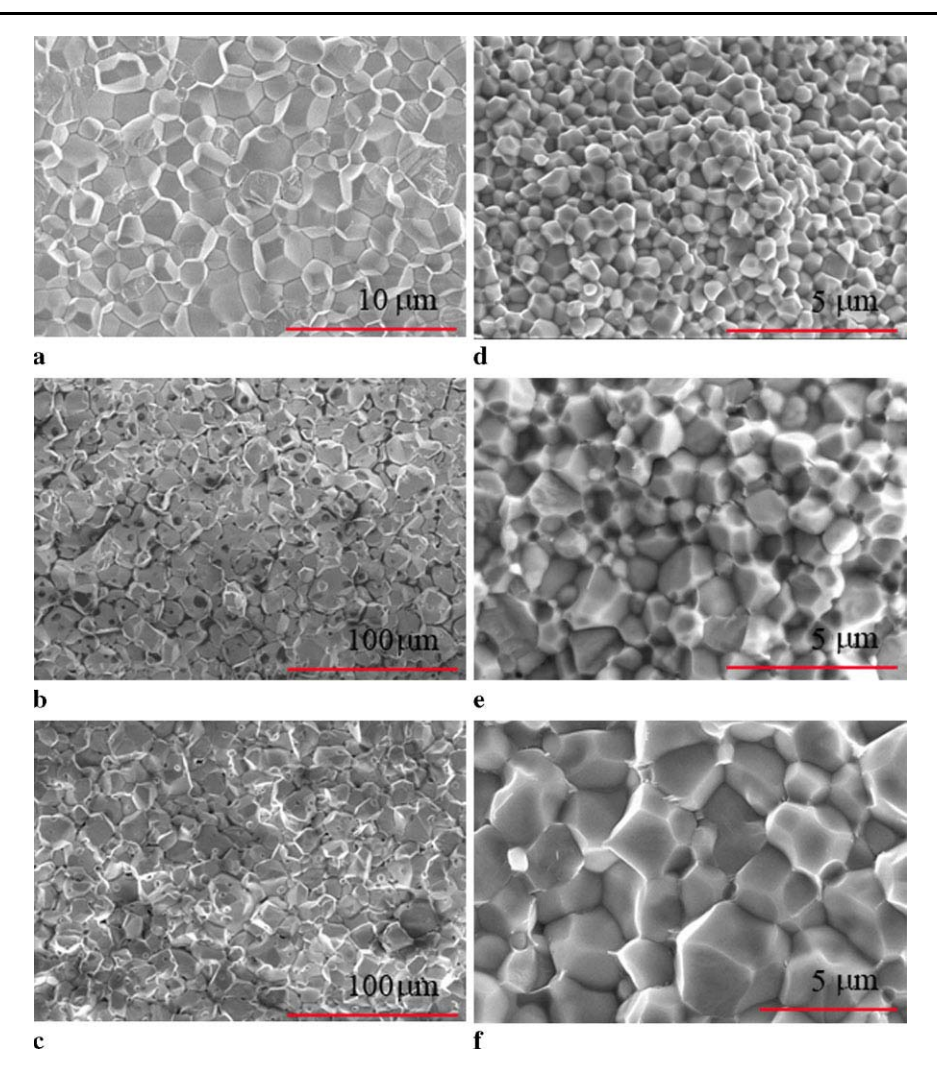






554 U. Sukkha et al.

Fig. 3 SEM micrographs of the fractured surfaces of (1-x)PbZrO<sub>3</sub>-xPb(Zn<sub>1/3</sub>-Nb<sub>2/3</sub>)O<sub>3</sub> with various compositions (a) x=0.00, (b) x=0.02, (c) x=0.04, (d) x=0.10, (e) x=0.30, and (f) x=0.50



cidated electrical property data later confirmed this assumption. It is interesting to note that the influence of additional  $Pb(Zn_{1/3}Nb_{2/3})O_3$  on phase transition of the  $PbZrO_3$  system was similar to that of PZ-PMW and PZ-PCoN systems [17, 23].

#### 3.2 Microstructure

The effects of PZN amount on the microstructure of (1-x) PZ-xPZN, where  $x=0.00,\,0.02,\,0.04,\,0.10,\,0.30,\,$  and 0.50 ceramics, are shown in Fig. 3. From these micrographs, specimens show the absence of pyrochlore formation. It is interesting to note that at the composition, x=0.50, the pyrochlore phase was detected by XRD but not observed from the SEM micrograph in Fig. 3(f). As the pyrochlore phase was probably located at the surface, and the scale was too small, it did not appear in the SEM micrograph of the fractured surface. This result was similar to that in the PMN system [24]. The ceramics displayed a dense microstructure, and most of the grains were fractured in an intergranular manner. The grain boundaries could be clearly observed,

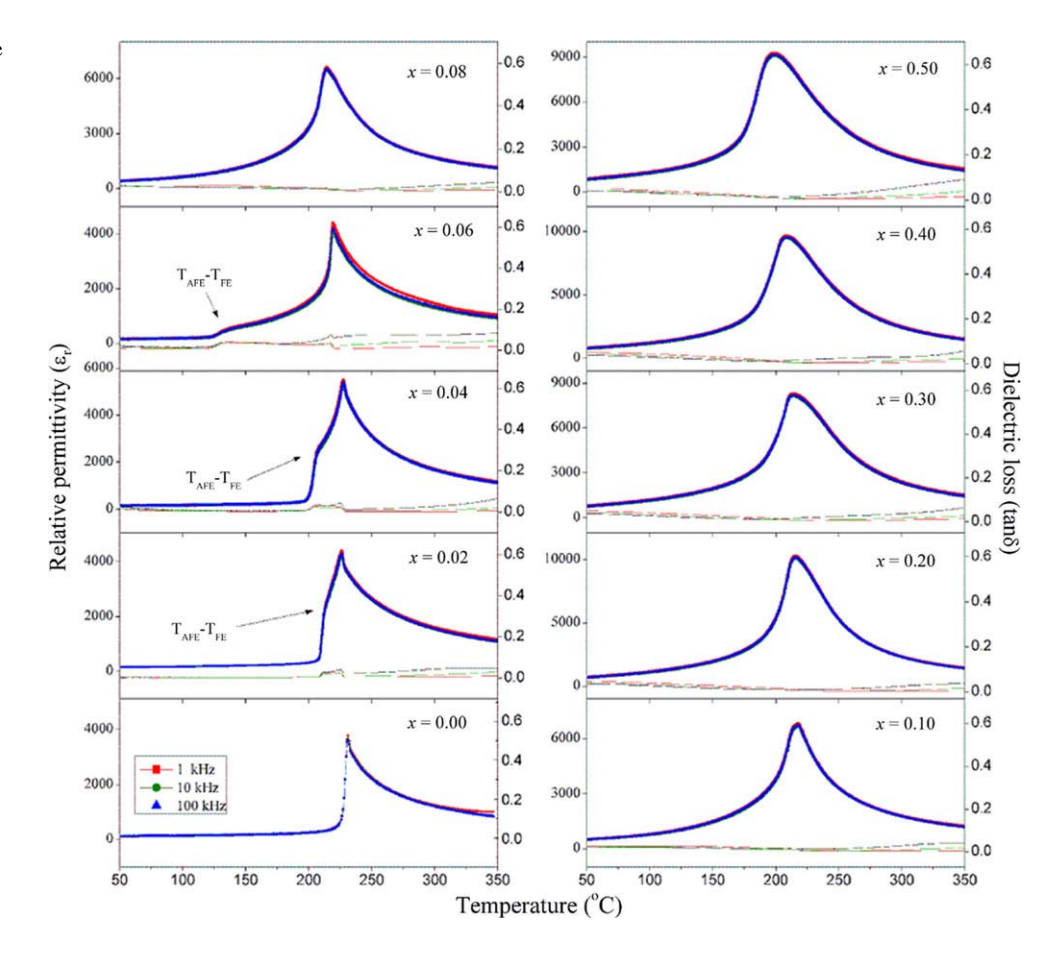
and then the average grain size was calculated directly by the linear interception method [25]. Physical properties of the sintered (1 - x)PZ-xPZN ceramics are listed in Table 1. The SEM images in Fig. 3 reveal that the addition of PZN resulted in significant changes in the microstructure of the ceramics. All ceramics exhibited high density with an average grain size range of about  $0.54 \pm 0.09$  to  $17.02 \pm 0.19$  µm. The relative densities were obtained in the range of 90-97% of theoretical density. Additionally, shrinkage of about 11-17% of (1-x)PZ-xPZN ceramics could be achieved in this study. This value is consistent with other lead-based systems [26]. The average grain size dramatically increased from  $\sim$ 1.80  $\mu$ m in the composition, x = 0.0, to approximately 17.02 µm in the composition, x = 0.06. Conversely, in concentrations of PZN increasing to x = 0.08, the grain size significantly decreased with increasing PZN. From these results, it can be assumed that a small amount of PZN substitution improves the sinterability of the ceramic. While excessive PZN substitution was segregated at the grain boundary, which acts as impuri-



Table 1 Physical properties of (1-x)PbZrO<sub>3</sub>-xPb(Zn<sub>1/3</sub>Nb<sub>2/3</sub>)O<sub>3</sub> ceramics (R, Rhombohedral; O, Orthorhombic; Pyr, Pyrochlore)

Composition	Crystal structure	Average grain size	Shrinkage	Relative density
(x)		(µm)	(%)	(%)
0.00	O	$1.80 \pm 0.31$	15.0±0.02	97.2±0.11
0.02	O	$11.96 \pm 0.21$	$11.0 \pm 0.01$	$89.8 \pm 0.21$
0.04	O	$12.22 \pm 0.17$	$12.7 \pm 0.03$	$93.3 \pm 0.33$
0.06	O	$17.02 \pm 0.19$	$13.5 \pm 0.03$	$92.5 \pm 0.30$
0.08	O	$1.20 \pm 0.15$	$12.9 \pm 0.02$	91.1±0.13
0.10	O	$0.54 \pm 0.09$	$13.9 \pm 0.01$	$94.3 \pm 0.09$
0.20	O + R	$0.77 \pm 0.26$	$13.9 \pm 0.02$	$93.0 \pm 0.16$
0.30	R-rich	$0.95 \pm 0.16$	$15.6 \pm 0.01$	$93.8 \pm 0.14$
0.40	R-rich	$1.59 \pm 0.31$	$17.1 \pm 0.01$	95.1±0.18
0.50	R-rich + Pyr	$1.96 \pm 0.48$	$17.3 \pm 0.01$	$94.4 \pm 0.39$

**Fig. 4** Temperature dependence of dielectric properties of (1-x)PbZrO<sub>3</sub>-xPb(Zn<sub>1/3</sub>-Nb<sub>2/3</sub>)O<sub>3</sub> ceramics



ties, the grain growth was inhibited. This phenomenon was similar to those in other solid solution systems [27].

#### 3.3 Dielectric properties

The relative permittivity of (1 - x)PZ–xPZN ceramics, as a function of temperature at differently applied frequencies between 1 and 100 kHz, are given in Fig. 4. At the compo-

sition,  $0.00 < x \le 0.06$ , two distinct dielectric peaks were observed. The phase transitions at lower temperatures were due to transformation from the orthorhombic antiferroelectric phase to rhombohedral ferroelectric phase [16], while the maximum dielectric was linked with the transformation of the rhombohedral ferroelectric phase into the cubic paraelectric phase [17, 23]. Later descriptions in ferroelectric data supported this finding.



556 U. Sukkha et al.

<b>Table 2</b> Phase transition temperatures and enthalpy of $(1-x)$ PbZrO <sub>3</sub> - $x$ Pb(Zn <sub>1/3</sub> Nb <sub>2/3</sub> )O <sub>3</sub> cerami-	ics
--	-----

Composition	Phase transition temperature (°C)						$\Delta H$	$\Delta S \times 10^3$	$\Delta S/T_t \times 10^6$
( <i>x</i> )	Dielectric c	onstant	Thermal ex	pansion	DSC		$(Jg^{-1})$	$(J g^{-1} K^{-1})$	$(J g^{-1} K^{-2})$
	$T_{AFE-FE}$	$T_{\rm FE-PE}$	$T_{\text{AFE-FE}}$	$T_{\mathrm{FE-PE}}$	$T_{\text{AFE-FE}}$	$T_{\rm FE-PE}$			
x = 0.00	_	233	212	220	208.4	225.6	2.6	11.6	51.7
x = 0.02	212	226	192	213	193.1	224.9	3.3	14.6	64.8
x = 0.04	207	227	181	215	184.7	223.2	3.3	14.7	65.8
x = 0.06	130	219	110	205	137.4	222.1	3.6	16.2	72.8
x = 0.08	_	214	-	200	94.7	219.5	3.3	15.1	68.9
x = 0.10	_	217	_	_	59.0	217.3	2.6	11.8	54.2
x = 0.20	_	216	_	_	_	211.2	1.5	7.1	33.8
x = 0.30	_	213	_	_	_	209.4	0.8	4.0	19.4
x = 0.40	_	210	_	_	_	188.5	0.6	3.4	18.0
x = 0.50	-	200	-	_	-	_	_	_	_

Phase transition temperature of (1 - x)PZ - xPZN ceramics is summarized in Table 2. The transition temperatures of the AFE to FE phase became lower, and the temperature range width of the FE phase also increased continuously with increasing PZN. For the composition,  $x \ge 0.08$ , transition of the orthorhombic antiferroelectric phase to rhombohedral ferroelectric phase was not observed. As PZN concentration increased, the diffuse phase transition (DPT) behavior, with broad maximum and frequency dispersion, became more self-evident. The FE to PE transition decreased nearly linearly at the rate of 0.48°C/mol% of PZN, when compared with its value for pure PZ. Noticeably, this rate was much lower than that of PZ–PCoN (2.20°C/mol%) [17] and PZ-PNN (2.81°C/mol%) [18]. The maximum relative permittivity for all compositions is listed in Table 3. The composition, x = 0.20, showed the highest value of relative permittivity, and existence of the MPB near this composition was expected. This result is consistent with the X-ray diffraction finding that both orthorhombic and rhombohedral phases coexist in this composition. It was found that the addition of PZN also shifts the transition temperature  $(T_m)$ value of PZ-PZN ceramics down from 243°C (T<sub>c</sub> for PZ) in the composition, x = 0.0, to 199°C in the composition, x = 0.5. A similar trend has also been found in the PZ-PNN [18] and PZ-PCoN system [17].

It is well known that the relative permittivity of a normal ferroelectric, which is above the maximum relative permittivity temperatures, can be described by the Curie–Weiss law [4]:

$$\frac{1}{\varepsilon_r} = \frac{T - T_0}{C},\tag{1}$$

where  $T_0$  is the Curie-Weiss temperature, and C the Curie constant. Above the Curie temperature, the relative permittivity of pure PZ obeys the Curie-Weiss law, with the Curie

constant  $C \sim 1.70 \times 10^{5}$  °C and Curie–Weiss temperature  $T_0 \sim 179$  °C. However, a broad relative permittivity of relaxor ferroelectric can be described by a simple quadratic law. The relative permittivity of relaxor ferroelectric above the maximum relative permittivity temperatures can be derived via the following expression [28]:

$$\frac{\varepsilon_m'}{\varepsilon'(f,T)} = 1 + \frac{(T - T_m(f))^{\gamma}}{2\delta_{\gamma}^2} \quad (1 \le \gamma \le 2), \tag{2}$$

where  $\varepsilon'_m$  is the maximum value of the permittivity at T= $T_m(f)$ . The value of  $\gamma$  expresses the degree of dielectric relaxation in the relaxor ferroelectric material, when  $\gamma = 1$  (2) expresses Curie-Weiss behavior, while  $\gamma = 2$  in this equation is identical to the quadratic relationship. Many relaxor ferroelectric materials can fit (2) with  $\gamma = 2$  at temperatures above  $T_{\rm max}$ . The parameter  $\delta_{\nu}$  can be used to measure the degree of diffuseness of the phase transition in mixed relaxor antiferroelectric materials. The values  $\gamma$  and  $\delta_{\gamma}$  are both material constants depending on the structure and composition of the material. The  $\delta_{\gamma}$  value can be determined from the slope of  $\varepsilon'_m/\varepsilon'$  versus  $(T-T_m)^2$ , which should be linear. By plotting  $ln(1/\varepsilon - 1/\varepsilon_{max})$  versus  $ln(T - T_m)$ ,  $\gamma$  can be determined directly from the gradient. According to (2), the values of  $\ln(1/\varepsilon - 1/\varepsilon_{\text{max}})$  for the sintered ceramics measured at 100 kHz are plotted against  $ln(T - T_m)$ in Fig. 5. As shown in the figure, the plotted lines for all samples demonstrate significantly good linearity within the measured temperature range. The intercept and gradient of lines in Fig. 5 are used to calculate and demonstrate  $\gamma$  and  $\delta_{\gamma}$  for each sample in Table 3. The value of  $\gamma$  presented in Table 3 varies between 1.02 and 1.81. The  $\delta_{\gamma}$  values are increased also from 11.5 to 15.6 with increasing PZN content, thus confirming that a diffuse phase transition occurs in the PZ-PZN system. Nevertheless, a minor swing of  $\gamma$  values



Table 3	Dielectric and ferroelectric	properties of $(1 - x)$	$PbZrO_3-xPb(Zn_{1/3}N)$	Nb <sub>2/3</sub> )O <sub>3</sub> ceramics
---------	------------------------------	-------------------------	--------------------------	--

Composition (x)	$T_m$ (°C)	$\varepsilon_{r \max}$	$\delta_{\gamma}$	γ	$P_r$ ( $\mu$ C/cm <sup>2</sup> )	$P_s$ ( $\mu$ C/cm <sup>2</sup> )	E <sub>c</sub> (kV/cm)
0.00	233	2850	11.5	1.02	_	_	_
0.02	226	4400	11.6	1.02	_	_	_
0.04	227	5500	11.8	1.04	_	_	_
0.06	219	4400	11.8	1.08	_	_	_
0.08	214	6600	13.5	1.33	20.20	22.86	17.88
0.10	217	6800	12.6	1.09	22.69	25.69	19.59
0.20	216	10300	14.8	1.55	26.90	31.45	15.52
0.30	213	8300	16.0	1.81	18.59	25.66	13.34
0.4	209	9700	15.3	1.59	20.73	27.48	13.04
0.5	199	9300	15.6	1.65	19.65	26.18	14.80

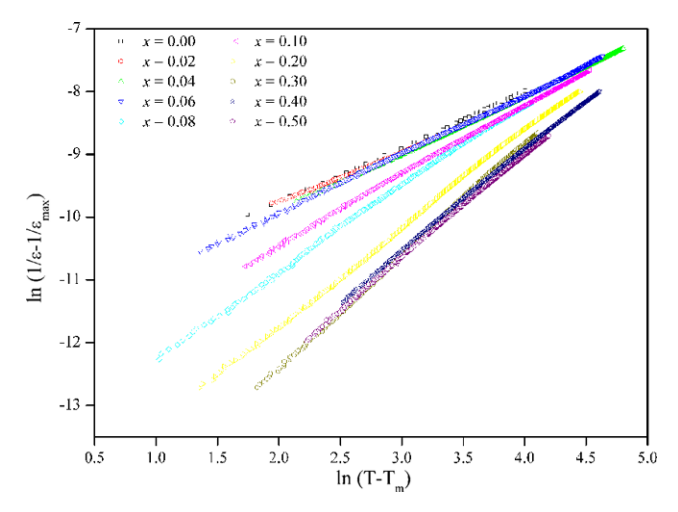


**Fig. 5** The  $\ln(1/\varepsilon-1/\varepsilon_{\rm max})$  vs.  $\ln(T-T_m)$  plots for (1-x)PZ-xPZN ceramics with x=0.00-0.50

as a function of composition was found in some compositions. For ferroelectric ceramics, it has been established that the degree of dielectric relaxation could also be caused by the decrease of grain size [29], and the observed difference of  $\gamma$  value could be a result of grain size variation. A similar propensity also has been detected in several prior investigations [29, 30].

#### 3.4 Thermal properties

The DSC technique was used as a primary tool to confirm the phase transition of the PZ–PZN system. DSC analysis results of the PZ–PZN ceramics are presented in Fig. 6, in which two distinct endothermic peaks for the composition,  $0.0 \le x \le 0.10$ , are observed. The lower temperature corresponds to the transition temperature of the AFE $\rightarrow$ FE phase transition, while the higher temperature corresponds to the FE $\rightarrow$ PE phase transition. The AFE $\rightarrow$ FE peaks shift to lower temperatures, with a higher composition of x. This

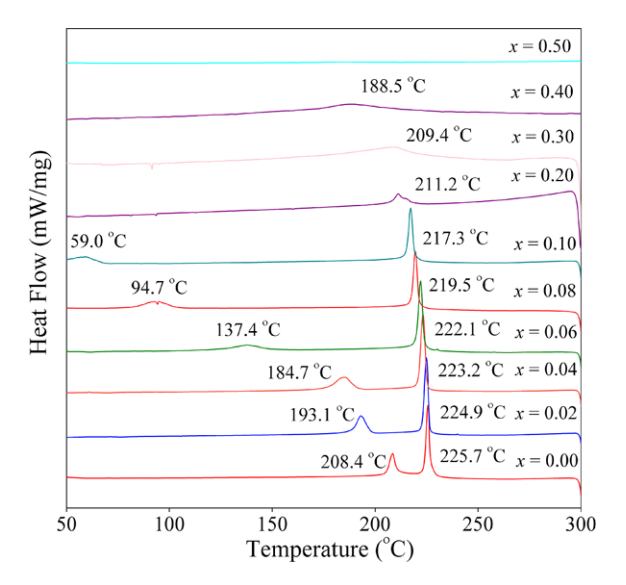


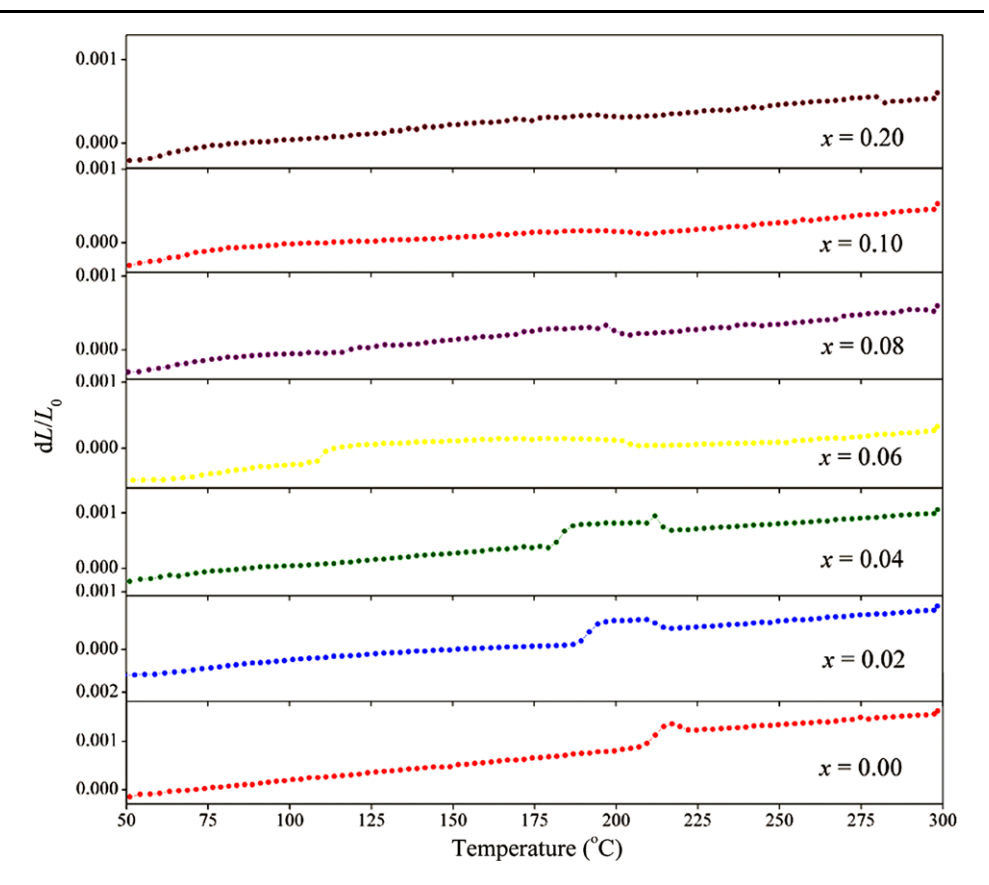
**Fig. 6** Typical differential scanning calorimetry (DSC) curves for (1-x)PZ-xPZN ceramics with x=0.00–0.50

result corresponds to a decreasing AFE phase, and the temperature range width of the FE phase increases, with increasing amounts of PZN content. Moreover, the endothermic peaks become progressively broader, while the areas under these peaks  $(\Delta H)$  decrease with increasing PZN content. These results indicate that phase transition diverges from the first-order type. Burggraaf et al. [31] reported that the change in entropy ( $\Delta S$ ) and  $\Delta S/T_t$  related to fluctuation in conjunction with a small spontaneous lattice deformation and polarization. They also reported that large values of the  $\Delta S/T_t$  ratio give sharp phase transition, whereas the lower values lead to diffusing phase transition. Transition temperatures and the values of  $\Delta H$ ,  $\Delta S$ , and  $\Delta S/T_t$  for all compositions are calculated and summarized in Table 2. Notably, the values of  $\Delta S/T_t$  gradually reduce, which indicates that the diffuse phase transition behavior of PZ-PZN increases with increased PZN.



558 U. Sukkha et al.

Fig. 7 Thermal expansion curves of (1-x)PbZrO<sub>3</sub>-xPb(Zn<sub>1/3</sub>-Nb<sub>2/3</sub>)O<sub>3</sub> ceramics in heating



It is well known that in phase transition from AFE to FE or FE to PE the volume of material yields abrupt changes. Therefore, the thermal expansion measurement was employed as a secondary tool to confirm the phase transition sequence. Figure 7 shows thermal expansion curves for the PZ-PZN system. In the expansion curves of 0.00 < x < 0.000.06, with rising temperature, the volume expansion that resulted from the transformation of AFE to FE, and the small volume contraction of FE to PE transition, were observed. The thermal expansion curves exhibited FE to PE phase transition only when the amount of PZN increased to x = 0.08; however, the transition temperature tended to decrease continuously with increasing PZN. There was no clear anomaly in the thermal expansion at transition temperature for the composition,  $x \ge 0.10$ , because these compositions showed the second-order phase transition, which is the behavior of relaxor-like FE [16]. This occurrence was similar to those in other researches on different solid solution systems [32]. In demonstrating phase transition of PZ-PZN ceramics by relative permittivity, DSC, and thermal expansion measurements, it is noteworthy that all compositions showed the difference of transition temperature in each technique, as listed in Table 2. This result attributed to the different heating rates used during the measurements.

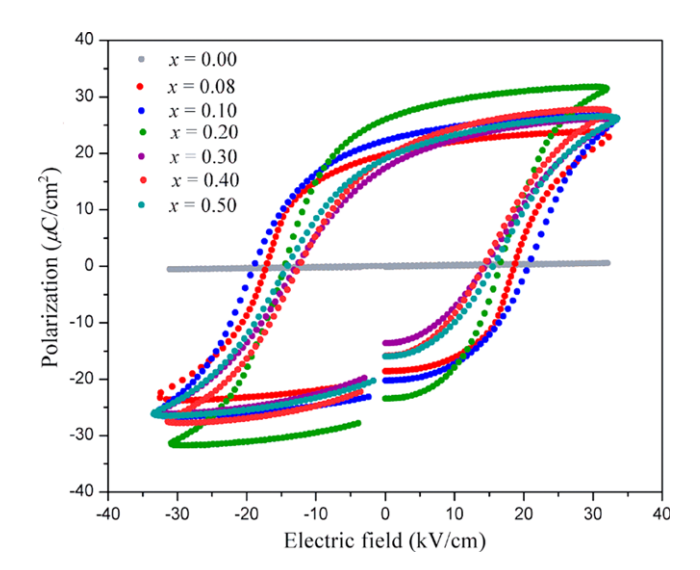


**Fig. 8** Polarization–electric field hysteresis loops of (1 - x)Pb-ZrO<sub>3</sub>–xPb(Zn<sub>1/3</sub>Nb<sub>2/3</sub>)O<sub>3</sub> ceramics

#### 3.5 Ferroelectric properties

The ferroelectric measurement was used to clarify further dielectric behavior of the FE phase in the PZ–PZN system. The P–E hysteresis loops for all composition ceramics at room temperature are shown in Fig. 8. At the composition,  $0.00 \le x \le 0.06$ , a near-linear relationship of P–E



loop is observed, due to electric fields being insufficient to switch any ferroelectric domains. It is well known that in PZ ceramics, the electric field required for inducing the AFE to FE phase transition at room temperature is higher than the breakdown strength of the ceramics [11, 33]. This result indicated that the AFE phase of pure PZ persisted in the PZ-PZN system for x < 0.08 at room temperature, which corresponded to the dielectric and thermal expansion results. For  $0.08 \le x \le 0.50$ , at the 35 kV/cm electric field strength, fully and symmetrical hysteresis loops were detected. The driving force for an antiparallel shift of Pb<sup>2+</sup> ions was decreased, due to the replacement of the Zr<sup>4+</sup> ion by Zn<sup>2+</sup>/Nb<sup>5+</sup> ions, which interrupted the translational symmetry. Then, the ferroelectric phase appeared when the amount of PZN was more than 6 mol%. Moreover, the hysteresis loop of ceramics at 0.08 < x < 0.50 showed normal-like ferroelectric behavior with the square loop. The remanent polarization  $(P_r)$  and coercive field  $(E_c)$  value of ceramics at  $0.08 \le x \le 0.50$  did not change significantly. However, the highest  $P_r$  value of this system was found in the composition, x = 0.20, where  $P_r = 26.90 \,\mu\text{C/cm}^2$  and  $E_c = 15.52 \text{ kV/cm}$ . The ferroelectric properties, together with the basis of XRD and dielectric measurements, led to the conclusion that the MPB of the (1-x)PZ-xPZN system exists at x = 0.20. Interestingly, the MPB of the (1 - x)PZxPZN system shows higher remanent polarization and coercive field when compared to that of the PZT system [34, 35]. It is well known that the MPB and grain size effect are important parameters that strongly influence electrical properties of lead-based piezoelectric ceramics. However, this study showed that the MPB in the PZ-PZN system is more influential to electrical properties than the grain size effect. For the composition, x = 0.50, the value of  $P_r$  decreased to 19.65 µC/cm<sup>2</sup>, due to the coexistence of a pyrochlore phase, as observed by the XRD technique.

#### 4 Conclusion

The solid solubility limit of the  $(1-x)\text{PbZrO}_3-x\text{Pb}(\text{Zn}_{1/3}\text{Nb}_{2/3})\text{O}_3$  system, which was prepared via the columbite method, was about x=0.40. Relaxor ferroelectric PZN was found to strongly influence crystal structure, and electrical and thermal properties of PZ ceramics. The XRD results indicate that the crystal structure of solid solution (1-x)PZ-xPZN, where x=0.00-0.50, successively transforms from orthorhombic to rhombohedral symmetry, with increased PZN concentration. The AFE $\rightarrow$ FE phase transition shifts to lower temperatures with higher compositions of x. The temperature range width of the FE phase increases with the amount of PZN increase. The dielectric properties of PZ-PZN exhibited significant improvement with PZN loading. The MPB of the (1-x)PZ-xPZN system exists close to the composition, x=0.20.

**Acknowledgements** This research was supported by a grant from the program for Strategic Scholarships for Frontier Research Network for the Join Ph.D. Program Thai Doctoral degree of the Commission on Higher Education (CHE), the Thailand Research Fund (TRF), and the National Nanotechnology Center (NANOTEC) NSTDA, Ministry of Science and Technology, Thailand, through its "Center of Excellence Network" program.

#### References

- 1. A.S. Bhalla, R. Guo, R. Roy, Mater. Res. Innov. 4, 3 (2000)
- 2. G.H. Haertling, J. Am. Ceram. Soc. 82, 797 (1999)
- Y. Xu, Ferroelectric Materials and Their Application (Elsevier, Amsterdam, 1991)
- 4. B. Jaffe, W.R. Cook, *Piezoelectric Ceramic* (R.A.N. Publishers, 1971)
- P. Seung-Eek, T.R. Shrout, IEEE Trans. Ultrason. Ferroelectr. Freq. Control 44, 1140 (1997)
- T. Takenaka, K. Muramata, T. Fujii, Ferroelectrics 134, 133 (1992)
- 7. J. Kuwata, K. Uchino, S. Nomura, Ferroelectrics 37, 579 (1981)
- N. Vittayakorn, C. Puchmark, G. Rujijanagul, X. Tan, D.P. Cann, Curr. Appl. Phys. 6, 303 (2006)
- N. Vittayakorn, G. Rujijanagul, X. Tan, M.A. Marquardt, D.P. Cann, J. Appl. Phys. 96, 5103 (2004)
- 10. N. Vittayakorn, T. Tunkasiri, Phys. Scr. T 129, 199 (2007)
- 11. E. Sawaguchi, G. Shirane, S. Hoshino, Phys. Rev. 83, 1078 (1951)
- 12. G. Shirane, Phys. Rev. 86, 219 (1952)
- N. Vittayakorn, T. Bongkarn, G. Rujijanagul, Physica B, Condens. Matter 387, 415 (2007)
- 14. B. Xu, N.G. Pai, L.E. Cross, Mater. Lett. 34, 157 (1998)
- X. Hao, J. Zhai, J. Zhou, J. Yang, X. Song, S. An, J. Cryst. Growth 312, 667 (2010)
- 16. S. Wirunchit, N. Vittayakorn, J. Appl. Phys. 104, 024103 (2008)
- 17. W. Banlue, N. Vittayakorn, Appl. Phys. A 93, 565 (2008)
- S. Wirunchit, P. Laoratanakul, N. Vittayakorn, J. Phys. D, Appl. Phys. 41, 125406 (2008)
- A. Halliyal, U. Kumar, R.E. Newham, L.E. Cross, Am. Ceram. Soc. Bull. 66, 671 (1987)
- 20. T.R. Shrout, A. Halliyal, Am. Ceram. Soc. Bull. 66, 704 (1987)
- J.R. Belsick, A. Halliyal, U. Kumar, R.E. Newham, Am. Ceram. Soc. Bull. 66, 664 (1987)
- 22. R.D. Shannon, Acta Crystallogr. A32, 751 (1976)
- N. Vittayakorn, P. Charoonsuk, P. Kasiansin, S. Wirunchit, B. Boonchom, J. Appl. Phys. 106, 064104 (2009)
- A.L. Costa, C. Galassi, G. Fabbri, E. Roncari, C. Capiani, J. Eur. Ceram. Soc. 21, 1165 (2001)
- J.C. William, Materials Science and Engineering: An Introduction (Wiley, New York, 2007)
- 26. S. Wirunchit, N. Vittayakorn, Ferroelectrics 382, 135 (2009)
- J. Yoo, K. Kim, C. Lee, L. Hwang, D. Paik, H. Yoon, H. Choi, Sens. Actuators A, Phys. 137, 81 (2007)
- 28. K. Uchino, S. Nomura, Ferroelectr. Lett. 44, 55 (1982)
- V. Koval, C. Alemany, J. Briancin, H. Brunckova, J. Electroceram. 10, 19 (2003)
- 30. X.J. Lu, X.M. Chen, J. Electroceram. 7, 127 (2001)
- 31. C. Stenger, A.J. Burggraaf, Phys. Status Solidi 61, 275 (1980)
- 32. N. Vittayakorn, D.P. Cann, Appl. Phys. A 86, 403 (2007)
- 33. S. Roberts, J. Am. Ceram. Soc. 33, 63 (1953)
- R. Yimnirun, S. Ananta, P. Laoratanakul, J. Eur. Ceram. Soc. 25, 3235 (2005)
- S. Wongsaenmai, Y. Laosiritaworn, S. Ananta, R. Yimnirun, Mater. Sci. Eng. B 128, 83 (2005)





Contents lists available at ScienceDirect

### Powder Technology

journal homepage: www.elsevier.com/locate/powtec



# Grass blade-like microparticle $MnPO_4 \cdot H_2O$ prepared by a simple precipitation at room temperature

Banjong Boonchom a,\*, Rattanai Baitahe b,c,d, Zongporn Joungmunkong e, Naratip Vittayakorn b,c,d

- <sup>a</sup> King Mongkut's Institute of Technology Ladkrabang, Chumphon Campus, 17/1 M. 6 Pha Thiew District, Chumphon 86160, Thailand
- b Electroceramic Research Laboratory, College of KMITL Nanotechnology, King Mongkut's Institute of Technology Ladkrabang, Bangkok 10520, Thailand
- Advanced Materials Science Research Unit, Department of Chemistry, Faculty of Science, King Mongkut's Institute of Technology Ladkrabang, Bangkok 10520, Thailand
- <sup>d</sup> ThEP Center, CHE, 328 Si Ayutthaya Rd., Bangkok 10400, Thailand
- <sup>e</sup> Faculty of Pharmaceutical Sciences, Ubon Ratchathani University, Ubonratchathani 34190, Thailand

#### ARTICLE INFO

#### Article history: Received 4 February 2010 Received in revised form 12 May 2010 Accepted 14 May 2010 Available online 8 June 2010

Keywords: Grass blade-like particle MnPO₄·H₂O FTIR Thermogravimetric analysis Powder synthesis

#### ABSTRACT

Grass blade-like microparticle  $MnPO_4 \cdot H_2O$  was synthesized by a simple precipitation at room temperature using a mixture of manganese sulphate monohydrate, phosphoric acid and water at pH=7. The thermogravimetric study indicates that the synthesized compound is stable below 500 °C and its final decomposed product is  $Mn_2P_2O_7$ . The pure monoclinic phases of the synthesized  $MnPO_4 \cdot H_2O$  and its final decomposed product  $Mn_2P_2O_7$  are verified by XRD data. FTIR spectra indicate the presences of the  $PO_4^{3-}$  ion and water molecules in the  $MnPO_4 \cdot H_2O$  structure and the  $P_2O_7^{4-}$  ion in the  $Mn_2P_2O_7$  structure. The thermal stability, crystallite size, and grass blade-like microparticle of  $MnPO_4 \cdot H_2O$  in this work are different from previous reports, which may be caused by the starting reagents and reaction condition for the precipitation. © 2010 Elsevier B.V. All rights reserved.

#### 1. Introduction

In the recent years, a large number of inorganic natural and synthesized metal phosphates have the incremented use in order to supply the demands of industrial, commercial, agricultural, scientific and heath sectors because of their valuable physical-chemical properties and reactivity [1,2]. The metal phosphate compounds are divided by phosphate block unit as  $PO_4^{3-}$ ,  $HPO_4^{2-}$ ,  $H_2PO_4^{-}$ ,  $P_2O_7^{4-}$ and  $P_4O_{12}^{4-}$  units [3], which have found widespread applications in laser host [4], ceramic [5], dielectric [6], electric [7], magnetic [8], fertilizer [9], and catalytic [10] processes. Synthesis of these phosphate materials by precipitation reaction at room temperature with short time consumption and the morphology and architecture at micro-/nanoscale levels have attracted the interest of many researchers due to their conveniences and their strong influence on material properties [4-10]. Compared with hydrothermal method, solid state method, and sol-gel method, the remarkable advantages of precipitation reaction are its flexibility of operation, simple and rapid route, and environmental benign and cost-effective technique [7,11-13].

Manganese phosphate monohydrate (MnPO<sub>4</sub>·XH<sub>2</sub>O, x = 1.0– 1.7 mol), non-toxic foundational compound, has been applied widely in catalysis, fertilizer, and electrical fields, was synthesized by various methods (hydrothermal method, sol-gel method, solid state route or high-temperature method) and was also found in nature [14,15]. Christensen [16] reported for the first time the synthesis of MnPO<sub>4</sub>·-XH<sub>2</sub>O by manganese(II) nitrate-phosphoric acid system in the presence of nitric acid, which was used for the oxidation of manganese(II) nitrate. The another preparation method involved the oxidation of manganese(II) carbonate by nitric acid in the presence of phosphoric acid [17-19]. Recently, our group reported the synthesis of MnPO<sub>4</sub>·H<sub>2</sub>O by soft solution route using manganese (II) nitrate-phosphoric acid-methanol system at 40 °C [20]. To improve its functional properties and enlarge its application, many attempts have been conducted during the last two decades, one of which is to control shaping powder material (bulk, porous, micro- or nanoparticles) [11-13,21]. So far, there have been structural and spectroscopic reports on MnPO<sub>4</sub>·XH<sub>2</sub>O (x = 1.0-1.7 mol), to our knowledge, little are the morphology and architecture data available.

In this present,  $MnPO_4 \cdot H_2O$  powder was prepared by simple precipitation at room temperature using manganese sulphate monohydrate, phosphoric acid and water at pH = 7. This method is simple, rapid, cost-effective and has non-toxic routes to synthesize grass blade-like microparticle  $MnPO_4 \cdot H_2O$ . The precipitates were characterized by TG/DTG, DSC, XRD, SEM and FTIR techniques. The data obtained will be important for further studies of the compound.

<sup>\*</sup> Corresponding author. Tel.: +66 7750 6422x4565; fax: +66 7750 6411. E-mail address: kbbanjon@kmitl.ac.th (B. Boonchom).

#### 2. Experimental

 $MnPO_4\cdot H_2O$  crystalline powder was prepared by a solution precipitation method using  $MnSO_4\cdot H_2O$  (>99% purity, Fluka) and phosphoric acid (86.4% w/w  $H_3PO_4$ , Merck) as starting materials. Following procedure, 1.70 g of  $MnSO_4\cdot H_2O$  was dissolved in 18 mL of 1 M  $H_3PO_4$ . The pH of the manganese- and phosphate-containing solution was adjusted to 7 by the addition of NaOH, and  $MnPO_4\cdot H_2O$  was precipitated at room temperature. The powder was obtained, then isolated by filtration, washed with deionized water and dried in air. This process can be explained by the following reaction:

$$Mn_{(s)}^{2+} \rightarrow Mn^{3+} + e^{-}$$
 (anodic)  
 $H^{+} + e^{-} \rightarrow 1/2H_{2}\uparrow$  (cathodic)  $\rightarrow H_{3}PO_{4} \rightarrow 3H^{+} + PO_{4}^{3-}$   
 $Mn^{3+} + PO_{4}^{3-} \rightarrow Mn(PO_{4})\downarrow$ 

Therefore, the overall reaction can be rewritten by:

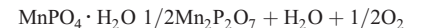
NaOH pH = 7 at room temperature

$$\begin{aligned} &M{n^{2+}}S{O_4} \cdot {H_2}O + 3{H^ + } + P{O_4^{3 - }} {\to } M{n^{3 + }}P{O_4} \cdot {H_2}O {\downarrow } + 1/2{H_2} {\uparrow } \\ &+ 2{H^ + }(2{H_2}O) + S{O_4^{2 - }}(N{a_2}S{O_4}) \end{aligned}$$

Thermal property of the studied compound was investigated on a TG-DTG (Thermogravimetry, TG; Derivative Thermogravimetry, DTG) Pyris One Perkin-Elmer instrument and a DSC (Differential Scanning Calorimetry) 204 F1 Phoenix Perkin-Elmer apparatus with α-Al<sub>2</sub>O<sub>3</sub> powder as the reference material. On the basis of TG data, its final decomposed product seemed to occur at a temperature above 500 °C and the water content was determined. In order to gain the thermal decomposition phase, the synthesized MnPO<sub>4</sub>·H<sub>2</sub>O was heated in a box furnace at 500 °C for 2 h. The manganese contents of the synthesized MnPO<sub>4</sub>·H<sub>2</sub>O and its decomposed product Mn<sub>2</sub>P<sub>2</sub>O<sub>7</sub> were determined by dissolving in 0.0126 M hydrochloric acid using atomic absorption spectrophotometry (AAS, Perkin-Elmer, Analyst100). The phosphorus contents were analyzed by colorimetric method of the molybdophosphate complex [22]. The structure and crystallite sizes of the prepared powder and its decomposed product were studied by X-ray powder diffraction using a D8 Advanced powder diffractometer (Bruker AXS, Karlsruhe, Germany) with Cu K $\alpha$  radiation ( $\lambda = 0.1546$  nm). The Scherrer method was used to evaluate the crystalline size [23]. The room temperature FTIR spectra were recorded in the range of 4000-400 cm<sup>-1</sup> with 8 scans on a Perkin-Elmer Spectrum GX spectrometer with the resolution of 4 cm<sup>-1</sup>. The morphology was examined by SEM using Hitachi S4700 after gold coating.

#### 3. Results and discussion

The TG/DTG curves of MnPO $_4\cdot$  H $_2$ O are shown in Fig. 1. The TG curve shows the weight loss between 50 and 600 °C, which is related to the elimination of crystallization water and oxygen. The first weight loss in the range of 50–320 °C was 10.80%, which corresponds to the elimination of one molecule of crystallization water. The second weight loss in the range of 320–500 °C was 5.20%, which corresponds to the consequent release of oxygen due to the reduction of manganese (III) to manganese (II) [17,18]. Total weight loss of 16.00% is close to the reported values by previous works [17–20]. The mass retained of about 84% is comparable with the value expected for the formation of Mn $_2$ P $_2$ O $_7$ , which is verified by XRD and FTIR measurements. In the DTG curve, the corresponding peaks at 120, 190, 260 and 330 °C are observed. The overall reaction formally could be presented as:



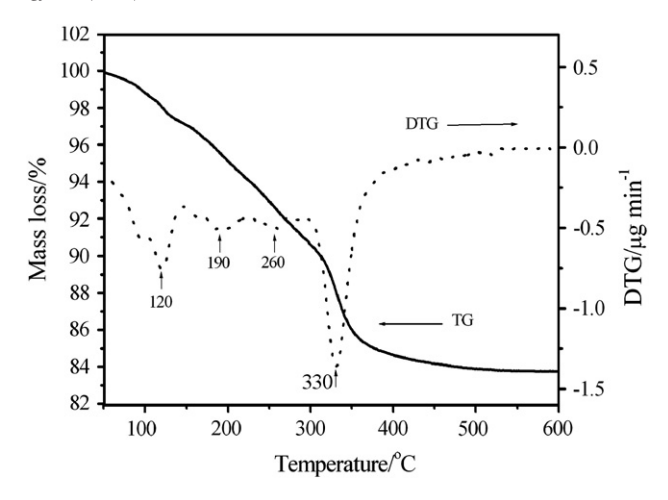


**Fig. 1.** TG/DTG curves of the synthesized MnPO<sub>4</sub>· $H_2O$  at the heating range of 10 °C min<sup>-1</sup>.

The temperature at which theoretical mass loss is achieved can be also determined from TG trace and considered to be the minimum temperature needed for the calcinations process. Thus, the MnPO $_4$ ·H $_2$ O powder was calcined at 500 °C for 2 h in a box furnace, which is lower temperature comparable with this phosphate reported by previous works [17–20]. The thermal behavior of the prepared MnPO $_4$ ·H $_2$ O powder in this work is significantly different from that of the decomposition reactions of MnPO $_4$ ·H $_2$ O reported in the literature [17–20]. The result indicates that starting reagent and reaction condition for the precipitation have the effects on the thermal transformation of MnPO $_4$ ·H $_2$ O.

The DSC curve of MnPO<sub>4</sub>· H<sub>2</sub>O in N<sub>2</sub> is shown in Fig. 2. The DSC trace shows three endothermic peaks and one exothermic peak at 130, 268, 324, and 475 °C (onset peak at 117, 250, 300, and 450 °C) which are due to two dehydration, reduction and phase transformation reactions of this compound, respectively. According to the DSC curve, the heat of two dehydration, reduction and phase transformation reactions can be calculated and were found to be 20.70, 19.65, 140.88 and - 17.18 J g $^{-1}$ , respectively. The reduction step exhibits higher heat energy in comparison with other ones. This result indicates that it occurs harder than the dehydration and phase transformation reactions.

The XRD patterns of MnPO<sub>4</sub>·H<sub>2</sub>O and its decomposed product Mn<sub>2</sub>P<sub>2</sub>O<sub>7</sub> are shown in Fig. 3. The five strong peaks ( $2\theta$  data) were observed at 27.898(021), 30.988(-202), 34.003(-221), 41.1204 (-311), and 55.961(042) for the MnPO<sub>4</sub>·H<sub>2</sub>O and 28.837(111),

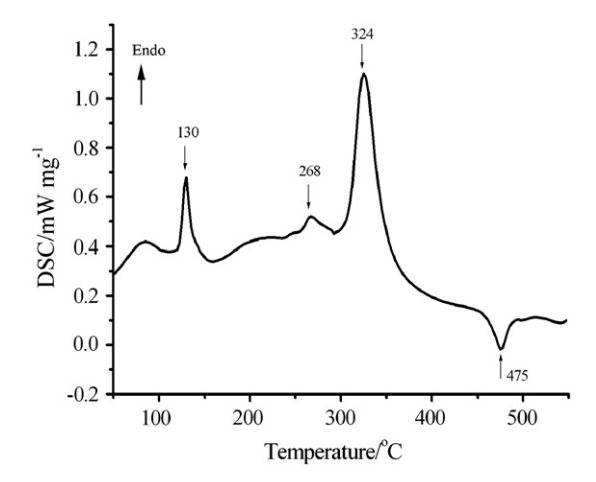


Fig. 2. DSC curve of the synthesized MnPO $_4\cdot H_2O$  at the heating range of 10  $^{\circ}C$  min $^{-1}$ .

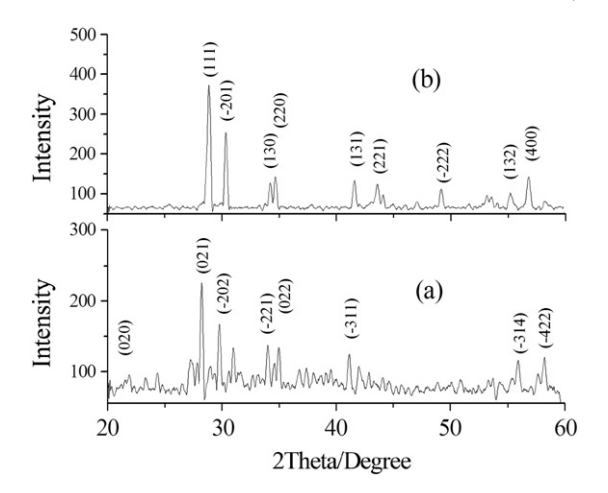
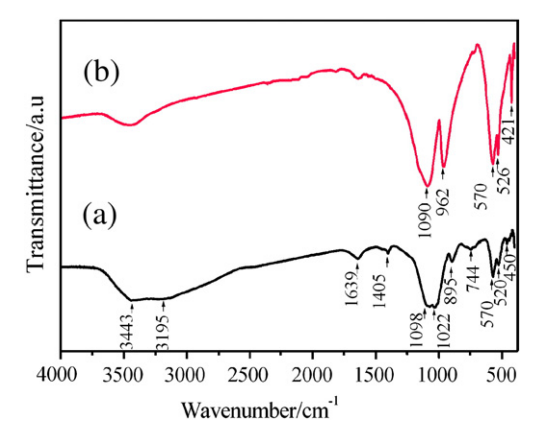


Fig. 3. XRD patterns of the synthesized MnPO<sub>4</sub>·H<sub>2</sub>O (a) and its decomposed product Mn<sub>2</sub>P<sub>2</sub>O<sub>7</sub> (b).

30.317(-201), 34.206(130), 34.661(220), and 41.657(131) for Mn<sub>2</sub>P<sub>2</sub>O<sub>7</sub>, respectively (indices are given in parentheses). The patterns match the standard XRD data for the MnPO<sub>4</sub>·H<sub>2</sub>O of PDF no. 511548 and for Mn<sub>2</sub>P<sub>2</sub>O<sub>7</sub> of PDF no. 771243. These results indicated that both crystal structures are monoclinic systems with space group C2/c (Z=4) for MnPO<sub>4</sub>·H<sub>2</sub>O and C2/m (Z=2) for Mn<sub>2</sub>P<sub>2</sub>O<sub>7</sub>. The average crystallite sizes and lattice parameters of the MnPO<sub>4</sub>·H<sub>2</sub>O and the decomposed product Mn<sub>2</sub>P<sub>2</sub>O<sub>7</sub> were calculated from XRD patterns and also tabulated in Table 1. The lattice parameters of MnPO<sub>4</sub>·H<sub>2</sub>O and Mn<sub>2</sub>P<sub>2</sub>O<sub>7</sub> are close to those of the standard data PDF no. 511548 and PDF no. 771243, respectively. However, the problem here is that the XRD patterns are very weak, so the lattice parameters obtained from these data are different from the value presented by other researchers. The result is caused by the different synthetic methods, which are in agreement with the results reported in the literature [11,12,19,20]. The average crystallite size of  $41 \pm 13$  nm for  $MnPO_4 \cdot H_2O$  sample and  $38 \pm 11$  nm for  $Mn_2P_2O_7$  in this work are smaller than those prepared from Mn(NO<sub>3</sub>)<sub>2</sub>·4H<sub>2</sub>O-H<sub>3</sub>PO<sub>4</sub>-CH<sub>3</sub>OH system reported by Boonchom et al. ( $66 \pm 28$  nm for MnPO<sub>4</sub>·H<sub>2</sub>O and  $54 \pm 18$  nm for  $Mn_2P_2O_7)[20]$ . The crystallite size of  $Mn_2P_2O_7$  in this work is close to that from  $Mn_2P_2O_7$  prepared at 800 °C (31 ± 13 nm) in our previous study [24], although the Mn<sub>2</sub>P<sub>2</sub>O<sub>7</sub> in this work was obtained from the lower temperature (500 °C). These results confirmed that the different crystallite sizes of the synthesized MnPO<sub>4</sub>·H<sub>2</sub>O and Mn<sub>2</sub>P<sub>2</sub>O<sub>7</sub> depend on the starting reagent and reaction condition for the precipitations, which is consistent with the literature [25–27].

The FTIR spectrum of the synthesized MnPO $_4$ ·H $_2$ O powder (Fig. 4a) reflects characteristic vibrations of PO $_4^3$ <sup>-</sup> ion and H $_2$ O molecules. Water bonding at 1639 cm $^{-1}$  and O–H stretching broad



**Fig. 4.** FTIR spectra of the synthesized MnPO<sub>4</sub>·H<sub>2</sub>O (a) and its decomposed product Mn<sub>2</sub>P<sub>2</sub>O<sub>7</sub> (b).

band center at  $3443 \text{ cm}^{-1}$  can be observed, implying the presence of crystalline hydrate. Spectra involving phosphate vibrations center on four regions because of the idealized  $T_d$  symmetry of the phosphate ion. Vibrational bands of PO<sub>4</sub><sup>3-</sup> ion are observed in the regions of 990-950, 1100–1020, 480–400 and 650–500 cm<sup>-1</sup>, which are assigned to the symmetric stretching region  $(v_1)$ , the antisymmetric stretching region  $(\nu_3)$ , the symmetric bending region  $(\nu_2)$ , and the antisymmetric bending region  $(\nu_4)$ , respectively [28,29]. The several strong and sharp bands in the ranges of 1100-890 and 600-500 cm<sup>-1</sup>, which split into several peaks, report complexes of stretching and bending of PO<sub>4</sub><sup>3-</sup> group, respectively. Antisymmetric stretching and bending vibrations are found at higher wavenumbers than symmetric stretching and bending vibrations, are more intense in infrared spectroscopy and weaker in Raman spectroscopy. Hence most absorptions in the 1000-1100 cm<sup>-1</sup> region are attributable to antisymmetric  $(v_3)$  vibrations. For the synthesized MnPO<sub>4</sub>·H<sub>2</sub>O powder strong band was observed at 1098 and 1022 cm<sup>-1</sup>. Another strong band observed at 895 cm<sup>-1</sup> was attributed to the symmetric stretching mode of  $PO_4^{3-}$ . Antisymmetric bending  $(\nu_2)$  vibrations are observed at 570 and 520 cm<sup>-1</sup>. These phosphate band positions are in excellent agreement with published data [28,29]. The weak bands at 1639 and 1405 cm<sup>-1</sup> are the H-O-H bending broad. The last band is assigned to the very low bending of water molecule, which is in excellent agreement with the literature [28,29]. The middle intense bands at 3443 and 3195  $cm^{-1}$  are assigned to the antisymmetric and symmetric stretchings of water molecule, respectively. In addition, a weak band observed at  $744 \, \text{cm}^{-1}$  is assigned to water libration (rocking mode) [28,29]. There results show that only the tribasic form of PO<sub>4</sub><sup>3-</sup> was present and some crystalline water existed in the title compound.

**Table 1**Average crystallite sizes and lattice parameters of MnPO<sub>4</sub>·H<sub>2</sub>O and Mn<sub>2</sub>P<sub>2</sub>O<sub>7</sub> calculated from XRD data.

Lattice parameters	$MnPO_4 \cdot H_2O$			$Mn_2P_2O_7$	$Mn_2P_2O_7$		
	This work	PDF #511548	DIF (This work-PDF)	This work	PDF #771243	DIF (This work-PDF)	
a (Å)	7.009(0)	6.913	+0.096	6.845(0)	6.633	+0.212	
b (Å)	7.666(0)	7.474	+0.192	8.651(4)	8.584	+0.067	
c (Å)	7.234(0)	7.363	-0.129	4.657(0)	4.646	+0.011	
β (°)	113.27(0)	112.30	+0.97	102.17(0)	102.67	-0.50	
Average crystallite size (nm)	$41\pm13$	-	-	$38 \pm 11$	-	-	

FTIR spectrum of the calcined MnPO<sub>4</sub>·H<sub>2</sub>O powder at 500 °C (Fig. 4b) exhibits the same characteristic as that of Mn<sub>2</sub>P<sub>2</sub>O<sub>7</sub>. FTIR bands are assigned according to the literature [24,30] based on the fundamental vibrating unit  $P_2O_7^{4-}$  anion. One of the most noteworthy features of the spectrum is the presence of the strong bands at 1090, 962, 570, 526, and 421 cm<sup>-1</sup>. These bands can be assigned to  $\nu_{as}(PO_3)$ ,  $\nu_{as}(POP)$ ,  $\delta$  (PO<sub>3</sub>),  $\delta$  (PO<sub>3</sub>), and  $\rho$  (PO<sub>3</sub>), respectively. The symmetric and asymmetric vibrations of the POP bridge ( $v_{as}$  POP and  $v_{s}$  POP) observed in the range 700–970 cm<sup>-1</sup> [24,30], which indicate the presence of the  $P_2O_7^{4-}$  anions with a bent POP angles in this salt.

The morphologies of MnPO<sub>4</sub>·H<sub>2</sub>O and its decomposed product  $Mn_2P_2O_7$  powders are shown in Fig. 5a and b. The  $MnPO_4 \cdot H_2O$  shapes in this work show well-defined grass blade-like microparticles, which are not similar to those of MnPO<sub>4</sub>·H<sub>2</sub>O reported in previous works [18-20]. The grass blade-like morphology consists of similar leaf-like flakes growing radically from the inside. Its decomposed product Mn<sub>2</sub>P<sub>2</sub>O<sub>7</sub> shows high agglomerate of non-uniform polyhedral particles, which is possibly caused by the dehydration and reduction processes. The morphology of Mn<sub>2</sub>P<sub>2</sub>O<sub>7</sub> indicates further nucleation/ growth of the nanocrystals inside the powder. This phenomenon is still not clear. The morphologies of the synthesized  $\text{MnPO}_4\!\cdot\! \text{H}_2\text{O}$  and its decomposed product Mn<sub>2</sub>P<sub>2</sub>O<sub>7</sub> in this work are significantly different from those of our previous reports [20,24,25]. The results indicate that the starting reagent and reaction condition of the

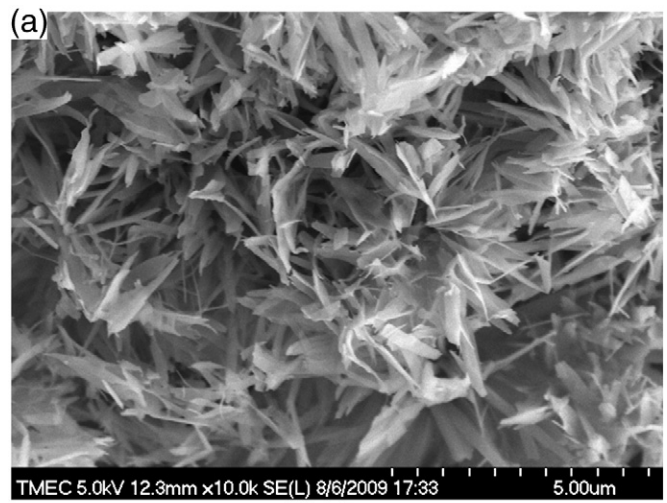




Fig. 5. SEM micrographs of the synthesized MnPO<sub>4</sub>·H<sub>2</sub>O (a) and its decomposed product Mn<sub>2</sub>P<sub>2</sub>O<sub>7</sub> (b).

precipitation have the strong effect in the morphologies of the studied compounds.

#### 4. Conclusion

Grass blade-like microparticle MnPO<sub>4</sub>·H<sub>2</sub>O was successfully synthesized by simple precipitation at room temperature using the mixture of manganese sulphate monohydrate, phosphoric acid and water at pH = 7. The MnPO<sub>4</sub>·H<sub>2</sub>O decomposes in more complex steps which correspond to the loss of crystallization water in the first step, subsequently to the reduction of manganese(III) to manganese(II) and the consequent release of oxygen (last step). The XRD and FTIR results confirmed the formation of MnPO<sub>4</sub>·H<sub>2</sub>O and its decomposed product Mn<sub>2</sub>P<sub>2</sub>O<sub>7</sub>. The thermal behaviors, grass blade-like shapes, particle size and crystallite sizes of the synthesized MnPO<sub>4</sub>·H<sub>2</sub>O and Mn<sub>2</sub>P<sub>2</sub>O<sub>7</sub> are different from previous reports. This is possibly due to the effects of the starting reagents and reaction condition for the precipitation. The results obtained are necessary for theoretical study, application development, and industrial production to produce the MnPO<sub>4</sub>·H<sub>2</sub>O and Mn<sub>2</sub>P<sub>2</sub>O<sub>7</sub>, which play potential applications as catalytic, ceramic and the biomedical materials etc.

#### Acknowledgments

This work was financially supported by the Thailand Research Fund (TRF), the Commission on Higher Education (CHE): Research Grant for New Scholar and the National Nanotechnology Center (NANOTEC) NSTDA, Ministry of Science and Technology, Thailand.

#### References

- [1] G. Chen, T.J. Richardson, Thermal instability of Olivine-type LiMnPO<sub>4</sub> cathodes, J. Power Sources 195 (2010) 1221-1224.
- W. Massa, O.V. Yakubovich, O.V. Dimitrova, A novel modification of manganese orthophosphate  $Mn_3(PO_4)_2$ , Solid State Sci. 7 (2005) 950–956. M.T. Averbuch-Pouchot, A. Durif, Topics in Phosphate Chemistry, World Scientific
- Publishing Co. Pte. Ltd., Singapore, 1996.
- A. Jouini, J.C. Gâcon, M. Ferid, M. Trabelsi-Ayadi, Luminescence and scintillation properties of praseodymium poly and diphosphates, Opt. Mater. 24 (2003) 175-180.
- [5] H.I. Hsiang, L.T. Mei, Y.H. Lin, Formation and growth of manganese phosphate passivation layers for NTC ceramics, J. Alloys Compd. 48 (2009) 723-728.
- L. Adam, A. Guesdon, B. Raveau, Unique charge ordering of manganese in a new mixed valent phosphate K<sub>3</sub>Mn<sup>II</sup><sub>3</sub>Mn<sup>III</sup>(PO<sub>4</sub>)(H<sub>0.5</sub>PO<sub>4</sub>)<sub>2</sub>(HPO<sub>4</sub>)<sub>2</sub>, J. Solid State Chem. 182 (2009) 2338-2343.
- N.N. Bramnik, H. Ehrenberg, Precursor-based synthesis and electrochemical performance of LiMnPO<sub>4</sub>, J. Alloys Compd. 464 (2008) 259–264.
- D. Feng, C. Wang, W. Cheng, G. Li, S. Tian, F. Liao, M. Xiong, J. Lin, Synthesis, crystal structure, and magnetic properties of K<sub>4</sub>Mn<sub>3</sub>(HPO<sub>4</sub>)<sub>4</sub>(H<sub>2</sub>PO<sub>4</sub>)<sub>2</sub>, Solid State Sci. 11 (2009) 845-851.
- A. Yuan, Wu, L. Bai, S. Ma, Z. Huang, Z. Tong, Standard molar enthalpies of formation for ammonium/3d-transition metal phosphates  $NH_4MPO_4\cdot H_2O$  ( $M\,Mn^{2+},\,Co^{2+},\,Ni^{2+},\,Cu^{2+}$ ), J. Chem. Eng. Data. 53 (2008) 1066–1070.
- [10] B.Y. Jibril, S.M. Al-Zahrani, A.E. Abasaeed, Propane oxidative dehydrogenation over metal pyrophosphates catalysts, Catal. Lett. 74 (2001) 145-148.
- W. Xuehang, W. Wenwei, L. Sen, F. Yanjin, L. Shushu, Preparation via solid-state reaction at room temperature and characterization of layered nanocrystalline KMnPO<sub>4</sub>·H<sub>2</sub>O, J Alloys Compd. 479 (2009) 541-544.
- J.K. Kim, G.S. Chauhan, J.H. Ahn, H.J. Ahn, Effect of synthetic conditions on the electrochemical properties of LiMn $_{0.4}$ Fe $_{0.6}$ PO $_4$ /C synthesized by sol-gel technique, J. Power Sources 189 (2009) 391-396.
- [13] C. Delacourt, P. Poizot, M. Morcrette, J.-M. Tarascon, C. Masquelier, One-step lowtemperature route for the preparation of electrochemically active LiMnPO<sub>4</sub> powders, Chem. Mater. 16 (2004) 93-99.
- M.A.G. Aranda, S. Bruque, Characterization of manganese(III) orthophosphate hydrate, Inorg. Chem. 29 (1990) 1334-1337.
- F.W. Boyle Jr., W.L. Lindsay, Diffraction patterns and solubility product of several divalent manganese phosphate compounds, Soil Sci. Soc. Am. J. 50 (1986) 761-766.
- O.T. Christensen, Beiträge zur Kenntniss der Oxyde des Mangans, J Prakt. Chem. 28 (1883) 1-37.
- Y. Cudennec, A. Riou, Y. Gerault, Manganese(II) hydrogenphosphate trihydrate, Acta Cryst. C45 (1989) 1411-1412.
- [18] P. Lightfoot, A.K. Cheetham, A.W. Sleight, Structure of manganese(3+) phosphate monohydrate by synchrotron x-ray powder diffraction, Inorg. Chem. 26 (1987) 3544-3547.

- [19] T. Witzke, R. Wegner, T. Doering, H. PÖllmann, W. Schuckmann, Serrabrancaite, MnPO<sub>4</sub>·H<sub>2</sub>O, a new mineral from the Alto Serra Branca pegmatite, Pedra Lavrada, Paraiba, Brazil, Am. Min. 85 (2000) 847–849.
- [20] B. Boonchom, S. Youngme, S. Maensiri, C. Danvirutai, Nanocrystalline serrabrancaite (MnPO<sub>4</sub>·H<sub>2</sub>O) prepared by a simple precipitation route at low temperature, J. Alloys Compd. 454 (2008) 78–82.
- [21] B. Boonchom, N. Vittayakorn, Floral-like microarchitectures of cobalt iron cyclotetraphosphate obtained by solid state synthesis, Powder Tech. 198 (2010)
- [22] A.I. Vogel, A Textbook of Quantitative Inorganic Analysis, 3rd edn, Green and Co. Ltd, Longmans, 1969.
- [23] B.D. Cullity, Elements of X-ray Diffraction, second ed, Addison-Wesley Publishing, 1977.
- [24] B. Boonchom, R. Baitahe, Synthesis and characterization of nanocrystalline manganese pyrophosphate  $\rm Mn_2P_2O_7$ , Mater. Lett. 63 (2009) 2218–2220.
- [25] B. Boonchom, C. Danvirutai, S. Maensiri, Soft solution synthesis, non-isothermal decomposition kinetics and characterization of manganese dihydrogen phosphate dihydrate  $Mn(H_2PO_4)_2\cdot 2H_2O$  and its thermal transformation products, Mater. Chem. Phys. 109 (2008) 404–410.
- [26] C. Danvirutai, B. Boonchom, S. Youngme, Nanocrystalline manganese dihydrogen phosphate dihydrate Mn(H2PO4)2  $\cdot$  2H2O and its decomposition product (Mn2P4O12) obtained by simple precipitation route, J. Alloys Compd. 457 (2008) 75-80.
- [27] A. Cuneyt Tas, Monetite ( $Ca(HPO_4)$  synthesis in ethanol at room temperature, J. Am. Cerm. Soc. 93 (2009) 2907–2912.
- [28] G. Herzberg, Molekülspektren und Molekülstruktur. I., Zweiatomige Moleküle, Steinkopff, Dresden, 1939.
- [29] N.B. Colthup, L.H. Daly, S.E. Wiberley, Introduction to Infrared and Raman Spectroscopy, Academic Press, New York, 1964.
  [30] E. Steger, B. Käßner, Die infrarotspektren von wasserfreien schwermetall-diphosphaten, Spectrochim Acta 24A (1968) 447–456.

$$3ZnO(s) + 2H_3PO_4 + H_2O \xrightarrow[\text{ambient temperature}]{C_3H_6O, \, \text{acetone}} Zn_3(PO_4)_2 \cdot 4H_2O(s) \quad (1)$$

<sup>\*</sup> To whom correspondence should be addressed. Tel: +66-7750-6422, ext. 4546. Fax: +66-7750-6410. E-mail: kbbanjon@kmitl.ac.th. 

† King Mongkut's Institute of Technology Ladkrabang, Chumphon

 <sup>&</sup>lt;sup>†</sup> King Mongkut's Institute of Technology Ladkrabang, Chumphon Campus.
 <sup>‡</sup> Advanced Materials Science Research Unit, Department of Chem-

<sup>\*</sup> Advanced Materials Science Research Unit, Department of Chemistry, Faculty of Science, King Mongkut's Institute of Technology Ladkrabang.

Ladkrabang.

§ Department of Chemistry, Faculty of Science, King Mongkut's Institute of Technology Ladkrabang.

Institute of Technology Ladkrabang.

"College of KMITL Nanotechnology, King Mongkut's Institute of Technology Ladkrabang.

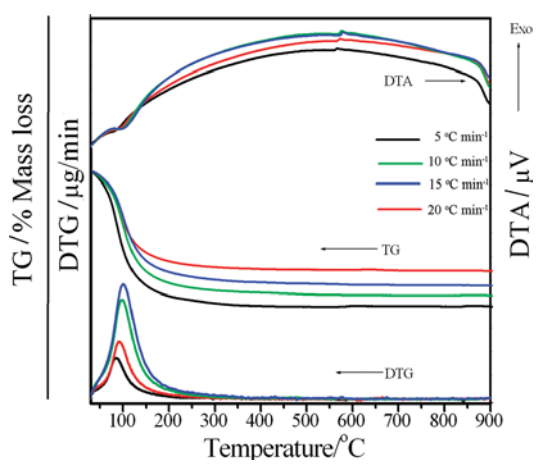


Figure 1. TG-DTG-DTA curves of Al<sub>0.5</sub>Fe<sub>0.5</sub>PO<sub>4</sub>·2.5H<sub>2</sub>O in dry air at heating rates of (5, 10, 15, and 20) °C·min<sup>-1</sup>.

reaches pH 3.80. The precipitates were filtered by suction, washed by hot deionized water, and dried in air. The resultant solid was kept in a desiccator for further investigation.

2.2. Sample Characterization. Thermal analysis measurements of about (8.0  $\pm$  0.3) mg sample mass were carried out by a Pyris1 Perkin-Elmer apparatus with an alumina crucible at heating rates of (5, 10, 15, and 20) °C·min<sup>-1</sup> in dynamic air in the range of (30 to 900) °C. DSC was carried out for samples ((5 to 10) mg) in aluminum crucibles, over the temperature range of (50 to 500) °C using DSC, a Perkin-Elmer DSC 204 F1 Phoenix apparatus. The heating rate employed was 10 °C ⋅ min<sup>-1</sup>. The structures of the prepared sample and its decomposed product were studied by X-ray powder diffraction using a D8 Advanced powder diffractometer (Bruker AXS, Karlsruhe, Germany) with Cu K $\alpha$  radiation ( $\lambda = 0.1546$  nm). The room temperature Fourier transform infrared (FTIR) spectra were recorded in the range of (4000 to 400) cm<sup>-1</sup> with eight scans on a Perkin-Elmer Spectrum GX spectrometer with a resolution of 4 cm<sup>-1</sup>. The morphology was examined by scanning electron microscopy (SEM) using Hitachi S4700 after gold coating.

#### 3. Results and Discussion

3.1. Thermal Analysis. Figure 1 shows the TG-DTG-DTA curves of the thermal decomposition of Al<sub>0.5</sub>Fe<sub>0.5</sub>PO<sub>4</sub>•2.5H<sub>2</sub>O at four heating rates. TG curves of Al<sub>0.5</sub>Fe<sub>0.5</sub>PO<sub>4</sub>•2.5H<sub>2</sub>O show a single well-defined dehydration in the range of (30 to 300) °C. The water eliminated below 100 °C is related to the physical adsorbed water, whereas water eliminated at 100 °C and above (200 °C) can be considered as crystal water and coordinated water. The dehydration temperature obtained in this work suggest that the water in hydrated binary aluminum iron phosphate can be considered as physical adsorbed water and crystal water. 8,9,17,18 The peaks in the DTG and DTA curves closely correspond to the mass loss observed on the TG traces. All TG-DTG-DTA curves are approximately the same shape. However, the dehydration stage was shifted toward higher temperatures when the heating rates increase, which indicate that the mass loss is dependent on the heating rate. The average observed mass losses of four TG curves are 26.22 % by mass, which correspond to 2.51 mol of water, which is close to the theoretical value for  $Al_{0.5}Fe_{0.5}PO_4 \cdot 2.5H_2O$  (26.11 %, 2.50  $H_2O$ ). An endothermic effect in the DTA curves is observed at about 100 °C that agrees with the respective DTG peak. Further, an exothermic effect at 572 °C without appreciable weight loss is observed in the DTA curve, which can be ascribed to a transition phase from an amorphous to crystalline form of Al<sub>0.5</sub>Fe<sub>0.5</sub>PO<sub>4</sub>. 11

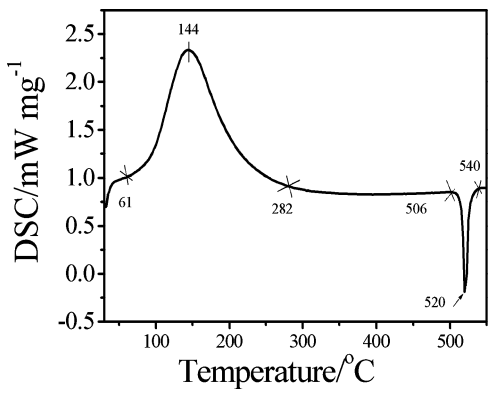


Figure 2. DSC curve of Al<sub>0.5</sub>Fe<sub>0.5</sub>PO<sub>4</sub>·2.5H<sub>2</sub>O at the heating rate of 10 K•min<sup>-1</sup> in a N<sub>2</sub> atmosphere.

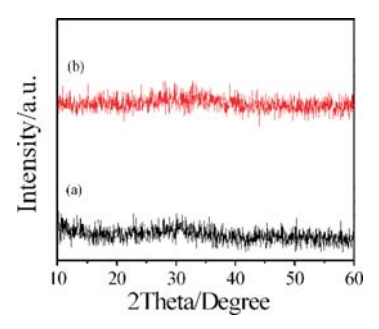


Figure 3. XRD patterns of Al<sub>0.5</sub>Fe<sub>0.5</sub>PO<sub>4</sub>·2.5H<sub>2</sub>O (a) and its decomposed product  $Al_{0.5}Fe_{0.5}PO_4$  (b).

The retained mass of about 73.78 % is compatible with the value expected for the formation of Al<sub>0.5</sub>Fe<sub>0.5</sub>PO<sub>4</sub>. The overall reaction is:

$$Al_{0.5}Fe_{0.5}PO_4 \cdot 2.5H_2O \rightarrow Al_{0.5}Fe_{0.5}PO_4 + 2.5H_2O$$
 (1)

The binary iron aluminum phosphate, Al<sub>0.5</sub>Fe<sub>0.5</sub>PO<sub>4</sub>, is found to be the final product of the thermal decomposition at T > 300°C. The thermal stability, mechanism, and phase transition temperature of the synthesized Al<sub>0.5</sub>Fe<sub>0.5</sub>PO<sub>4</sub>•2.5H<sub>2</sub>O are lower than those of the dehydration reactions of individual metal phosphates (AlPO<sub>4</sub>•2H<sub>2</sub>O<sup>17</sup> and FePO<sub>4</sub>•2H<sub>2</sub>O<sup>18</sup>). On the basis of these results, we can conclude that the different thermal properties are caused by the incorporation of Fe and Al metals in the skeleton.

The DSC curve of Al<sub>0.5</sub>Fe<sub>0.5</sub>PO<sub>4</sub>•2.5H<sub>2</sub>O (Figure 2) shows an endothermic peak at 144 °C (onset peak at 61 °C) and an exothermic peak at 520 °C (onset peak at 506 °C) due to the dehydration and the transition phase from an amorphous to crystalline form of this compound, respectively. The temperatures of the DSC peaks are well in accordance with that of the DTG and DTA peaks (Figure 1), so results of the TG/DTG/ DTA and DSC methods are credible.

3.2. XRD Analysis. The XRD studies of Al<sub>0.5</sub>Fe<sub>0.5</sub>PO<sub>4</sub>. 2.5H<sub>2</sub>O and its dehydrated product Al<sub>0.5</sub>Fe<sub>0.5</sub>PO<sub>4</sub> revealed that the structures remained in the amorphous or poor crystallization phases as well as nanoparticles of these compounds (Figure 3). The problem here is that the XRD data show poorly crystalline patterns, which are no indication of Al<sub>0.5</sub>Fe<sub>0.5</sub>PO<sub>4</sub>•2.5H<sub>2</sub>O and Al<sub>0.5</sub>Fe<sub>0.5</sub>PO<sub>4</sub> as separated phases. The studied compounds synthesized by the precipitation route in this work were poor crystalline phases, which differ from crystallization phases of those synthesized by a hydrothermal method.  $^{5-10}$  These results are in agreement with the results reported in the literature. $^{5-10}$ 

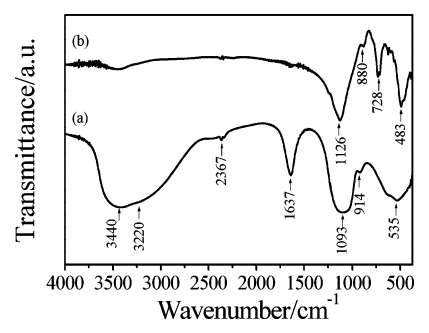


Figure 4. FTIR spectra of Al<sub>0.5</sub>Fe<sub>0.5</sub>PO<sub>4</sub>·2.5H<sub>2</sub>O (a) and its decomposed product Al<sub>0.5</sub>Fe<sub>0.5</sub>PO<sub>4</sub> (b).

3.3. FTIR Analysis. Figure 4 shows FTIR spectra of Al<sub>0.5</sub>Fe<sub>0.5</sub>PO<sub>4</sub>•2.5H<sub>2</sub>O and its dehydrated product Al<sub>0.5</sub>Fe<sub>0.5</sub>PO<sub>4</sub>. The vibrational motions of Al<sub>0.5</sub>Fe<sub>0.5</sub>PO<sub>4</sub>•2.5H<sub>2</sub>O are divided into two block units of the water molecule H<sub>2</sub>O and phosphate anion  $PO_4{}^{3-}$ , whereas  $Al_{0.5}Fe_{0.5}PO_4$  is divided into a block unit of the only phosphate anion PO<sub>4</sub><sup>3-</sup>. It is worth mentioning that the antisymmetric stretching ( $\nu_{OH}$ ), the symmetric stretching  $(\nu_{\mathrm{OH}})$ , and the bending  $(\delta_{\mathrm{OH}})$  vibrations of water molecules are solely observed at (3440, 3220, and 1637) cm<sup>-1</sup>, respectively. These bands disappear in the FTIR spectrum of Al<sub>0.5</sub>Fe<sub>0.5</sub>PO<sub>4</sub> (Figure 4b), implying the presence of anhydrous crystal. For the intramolecular vibrations of the PO<sub>4</sub><sup>3-</sup> anion, we identify the symmetric stretching mode at  $v_1 = 990 \text{ cm}^{-1}$ , the doublet at  $v_2 = (447 \text{ to } 485) \text{ cm}^{-1}$ , the triplets  $v_3$  at (1000 to 1085) cm<sup>-1</sup>, and the triplet  $\nu_4$  in the region (570 to 640) cm<sup>-1</sup>. For condensed phosphates, the intensity of the P-O stretching IR bands near 1000 cm<sup>-1</sup> are always greater than those near 880 cm<sup>-1</sup>, assigned to the stretching vibration  $\nu_{P-O-P}$  of P-O-P bridges. These phosphate band positions of Al<sub>0.5</sub>Fe<sub>0.5</sub>PO<sub>4</sub>•  $2.5H_2O$  and  $Al_{0.5}Fe_{0.5}PO_4$  are in excellent agreement with published data. 19,20

3.4. SEM Analysis. The scanning electron micrographs of Al<sub>0.5</sub>Fe<sub>0.5</sub>PO<sub>4</sub>•2.5H<sub>2</sub>O (Figure 5a) and Al<sub>0.5</sub>Fe<sub>0.5</sub>PO<sub>4</sub> (Figure 5b) powders showed different uniform morphological features due to the loss of crystallization waters. It can be seen that the Al<sub>0.5</sub>Fe<sub>0.5</sub>PO<sub>4</sub> powders were clearly coarser than the Al<sub>0.5</sub>Fe<sub>0.5</sub>PO<sub>4</sub>·2.5H<sub>2</sub>O powders. The Al<sub>0.5</sub>Fe<sub>0.5</sub>PO<sub>4</sub> powders consisted of round particles near 100 nm in size along with a narrow size distribution Additionally, the SEM photographs show that both crystals have grown through a combination of surface deposition and agglomeration.

3.5. Kinetics Analysis. In the rate equation for the isothermal decomposition of a solid-state process, <sup>21</sup> A (solid) → B (solid) + C (gas) is often written from:

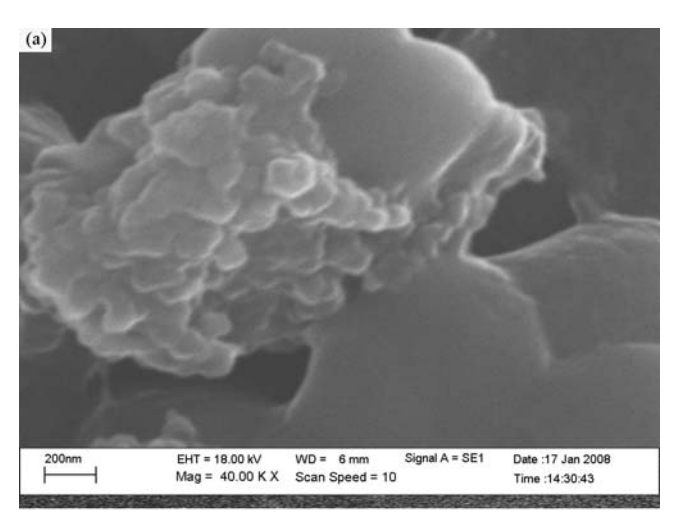
$$d\alpha/dt = A \exp(-E_{\alpha}/RT) f(\alpha)$$
 (2)

In most thermal analysis experiments, the heating rate  $\beta$  = dT/dt is a constant value, so eq 2 may also lead to the corresponding equations of Ozawa<sup>22</sup> and Kissinger—Akahira—Sunose (KAS)<sup>23</sup> methods after integration.

Ozawa equation: 
$$\ln \beta = \ln \left( \frac{AE_{\alpha}}{R g(\alpha)} \right) - 5.3305 - 1.0516 \left( \frac{E_{\alpha}}{RT} \right)$$
 (3

KAS equation: 
$$\ln\left(\frac{\beta}{T^2}\right) = \ln\left(\frac{AE_{\alpha}}{R g(\alpha)}\right) - \left(\frac{E_{\alpha}}{RT}\right)$$
 (4)

where A (the pre-exponential factor) and  $E_a$  (the activation energy) are the Arrhenius parameters and *R* is the gas constant.



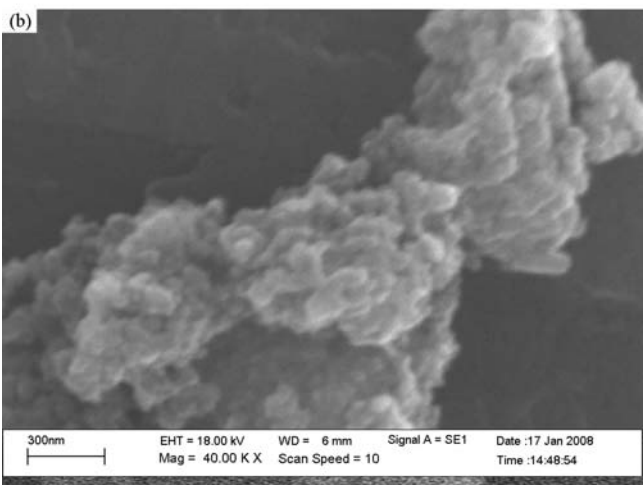


Figure 5. SEM photographs of Al<sub>0.5</sub>Fe<sub>0.5</sub>PO<sub>4</sub>•2.5H<sub>2</sub>O (a) and its decomposed product Al<sub>0.5</sub>Fe<sub>0.5</sub>PO<sub>4</sub> (b).

The  $g(\alpha) = \int_0^{\alpha} (d\alpha / f(\alpha))$  is the integral form of  $f(\alpha)$ , which is the reaction model that depends on the reaction mechanism. The reaction can be expressed through the temperatures corresponding to fixed values of the extent of conversion ( $\alpha = (m_i)$  $-m_a$ )/ $(m_i - m_f)$ , where  $m_i$ ,  $m_a$ , and  $m_f$  are the initial, actual, and final sample mass at time t) from experiments at different heating rates  $(\beta)$ .

Hence, the dependences of  $\ln \beta$  and  $\ln \beta/T^2$  on 1000/T, calculated for the same  $\alpha$  values (0.10 to 0.90) at different heating rates  $\beta$  ((5, 10, 15, and 20) °C·min<sup>-1</sup>) can be used to calculate the activation energy, so we can obtain the activation energies through the experimental data for the dehydration of Al<sub>0.5</sub>Fe<sub>0.5</sub>PO<sub>4</sub>•2.5H<sub>2</sub>O as shown in Table 1. The activation energies  $E_{\alpha}$  can be calculated from the slopes of the straight lines with a good coefficient of determination ( $R^2 > 0.99$ ). The activation energies worked out through the Ozawa and the KAS methods vary slightly, so the results are credible. If  $E_{\alpha}$  values are independent of  $\alpha$ , the decomposition may be a simple reaction, while the dependence of  $E_{\alpha}$  on  $\alpha$  should be interpreted in terms of multistep reaction mechanisms. 24,25 From Table 1 it can be seen that the activation energies decrease first and increase at  $\alpha$  higher than 0.6. A decreasing dependence of  $E_{\alpha}$ on  $\alpha$  is found for consecutive reactions, while an increasing dependence of  $E_{\alpha}$  on  $\alpha$  is found for competitive reactions. According to the decreasing  $E_{\alpha}$  at  $\alpha$  < 0.6, the kinetics scheme of which corresponds to a reversible reaction followed by an irreversible one. In addition, the increasing  $E_{\alpha}$  at  $\alpha > 0.6$ corresponds to a two-pathway competitive reaction model.<sup>24,25</sup>

Table 1. Activation Energies  $(E_\alpha)$  Versus the Coefficient of Determination  $(R^2)$  Calculated by Ozawa and KAS Methods for the Dehydration of  $Al_{0.5}Fe_{0.5}PO_4\cdot 2.5H_2O$ 

	Ozawa me	ethod	KAS method		
α	$E_{\alpha}/\mathrm{kJ}\cdot\mathrm{mol}^{-1}$	$R^2$	$E_{\alpha}/\mathrm{kJ}\cdot\mathrm{mol}^{-1}$	$R^2$	
0.1	231.14	0.9985	237.50	0.9985	
0.2	158.58	0.9937	160.99	0.9933	
0.3	136.83	0.9968	137.98	0.9965	
0.4	129.85	0.9984	130.54	0.9983	
0.5	126.05	0.9972	126.44	0.9970	
0.6	125.90	0.9970	126.16	0.9966	
0.7	136.37	0.9976	137.02	0.9974	
0.8	167.18	0.9989	169.21	0.9988	
0.9	275.09	0.9959	323.93	0.9957	

So it is concluded that there is a fourth reaction for the dehydration reaction. Additionally, the obtained activation energy values of the dehydration reaction of the studied compound are higher than those of individual metal phosphates  $(69.68 \pm 7 \text{ kJ} \cdot \text{mol}^{-1} \text{ (Kissinger method) for AlPO}_4 \cdot 2\text{H}_2\text{O}^{17}$  and  $68.48 \pm 1 \text{ kJ} \cdot \text{mol}^{-1} \text{ (Flynn-Wall-Ozawa method)}$  and  $65.55 \pm 1 \text{ kJ} \cdot \text{mol}^{-1} \text{ (KAS method)}$  for FePO $_4 \cdot 2\text{H}_2\text{O}^{18}$  reported in our previous works. As can be clearly seen, there is a direct relationship between the cation radius of Al(III) and Fe(III) and its thermal stability and activation energy of the dehydration reaction. A common conclusion is that the reason for this is the different interaction of iron and aluminum with water molecules in the structure, which supports the incorporation of Fe and Al metals in the skeleton and forms the Al $_{0.5}$ Fe $_{0.5}$ PO $_4 \cdot 2.5\text{H}_2$ O solid solution.

The Arvami exponent, n, can be evaluated by the Ozawa equation. First, the volume fraction of phase transition x, at the same temperature, T, from four crystallization steps under different heating rates is calculated by the ratio of partial area at T to the total area of crystallization. After plotting  $\ln[-\ln(1-x)]_T$  versus  $\ln(\beta)$  and if the data can be fitted to the linear function, then the slope of the function is -n,  $^{26}$  which is really the combined process of nucleation and growth. The most common approach used to describe the overall nonisothermal crystallization is given below:

$$-n = \frac{\mathrm{d}\ln[-\ln(1-x)]}{\mathrm{d}\ln(\beta)} \tag{5}$$

The volumetric function of the growth mechanism directly affects the transformation rate, and the dimensionality of the transformation is reflected in the value of the Avrami exponent. Therefore, determination of the Avrami exponent allows one to determine which geometric model of the phase transformation is the best fit: one-, two-, or three-dimensional growth. For the dehydration step of  $Al_{0.5}Fe_{0.5}PO_4 \cdot 2.5H_2O$ , the Avrami exponent, n, has a value of  $1.11 (R^2 = 0.991)$ , indicating a one-dimensional growth mechanism. The Avrami exponent, in addition to giving information regarding the dimensionality of the growth, can also yield insight into the rate-determining step (phase boundary control or diffusion control). An analysis of the Avrami exponent suggests a phase boundary mechanism.

3.6. Thermodynamic Analysis. Thermodynamic parameters, that is, enthalpy change  $(\Delta H^*/J \cdot \text{mol}^{-1})$ , heat capacity  $(C_p/J \cdot \text{mol}^{-1} \cdot \text{K}^{-1})$ , entropy change  $(\Delta S^*/J \cdot \text{mol}^{-1} \cdot \text{K}^{-1})$ , and Gibbs energy change  $(\Delta G^*/J \cdot \text{mol}^{-1})$  were calculated from the DSC experiment. The enthalpy change was calculated directly from the amount of heat change involved in each step per unit mass of the test sample.  $\Delta H^*$ ,  $\Delta S^*$ , and  $\Delta G^*$  were calculated using the following equations: <sup>15,16</sup>

$$C_p = \frac{\Delta H}{\Delta T} \tag{6}$$

$$\Delta S^* = 2.303 C_p \log \frac{T_2}{T_1} \tag{7}$$

$$\Delta G^* = \Delta H^* - T_p \Delta S^* \tag{8}$$

where  $\Delta T = T_2 - T_1$ ,  $T_1$  is the temperature at which the DSC peak begins to depart the baseline, and  $T_2$  is the temperature at which the peak lands.  $T_p$  is the DSC peak temperature at the corresponding stage.

The values of  $\Delta H^*$ ,  $\Delta S^*$ ,  $C_p$ , and  $\Delta G^*$  were calculated and found to be 104.64 kJ·mol<sup>-1</sup>, 72.40 J·K<sup>-1</sup>·mol<sup>-1</sup>, 290.75  $J \cdot K^{-1} \cdot \text{mol}^{-1}$ , and 744.57 kJ·mol<sup>-1</sup> for the dehydration reaction and  $-852.61 \text{ kJ} \cdot \text{mol}^{-1}$ ,  $-10.74 \text{ J} \cdot \text{K}^{-1} \cdot \text{mol}^{-1}$ , -968.21J⋅K<sup>-1</sup>⋅mol<sup>-1</sup>, and 5.77 J⋅mol<sup>-1</sup> for a transition form, respectively. The transition phase can be considered as the transformation of an amorphous to a crystalline form of this compound.<sup>7,8</sup> It is well-known that  $\Delta S^*$  can be less than, equal to, or higher than zero. In the case when  $\Delta S^* < 0$ , the reactions are classified as "slow" and when  $\Delta S^* > 0$  as "fast". <sup>28-30</sup> The positive value of  $\Delta S^*$  indicates a malleable activated complex that leads to a large number of degrees of freedom of rotation and vibration, whereas the negative value of  $\Delta S^*$  indicates a highly ordered activated complex, and the degrees of freedom of rotation as well as of vibration are less than they are in the nonactivated complex. Therefore, the dehydration reaction and a transition form of Al<sub>0.5</sub>Fe<sub>0.5</sub>PO<sub>4</sub> • 2.5H<sub>2</sub>O may be interpreted as "fast" and "slow" stages, respectively. 28-30 The positive and negative values of the enthalpy  $\Delta H^*$  for the dehydration reaction and a transition form are in good agreement with an endothermic and an exothermic effect in DTA and DSC data, respectively. The positive and negative values of  $\Delta G^*$  indicate that nonspontaneous and spontaneous processes for dehydration and a transition form stages, respectively. The thermodynamic parameters obtained indicate that the dehydration reaction is softer than the transition phase reaction. The results obtained in this work are different from those of the individual metal phosphates (AlPO<sub>4</sub>•2H<sub>2</sub>O<sup>17</sup> and FePO<sub>4</sub>•2H<sub>2</sub>O)<sup>18</sup> reported in our previous

#### 4. Conclusions

The results obtained in this study show that the dehydration behavior of an Al<sub>0.5</sub>Fe<sub>0.5</sub>PO<sub>4</sub>•2.5H<sub>2</sub>O solid solution varies with the function of their cations (Al(III) and Fe(III)). The feature of great interest here is that Al<sub>0.5</sub>Fe<sub>0.5</sub>PO<sub>4</sub>•2.5H<sub>2</sub>O decomposes at a relatively low temperature (< 300 °C). A fluctuating value of E for different  $\alpha$  can be assigned to a complex multistep reaction process, which corresponds to the different interactions of iron and aluminum with water molecules in the skeleton. The thermal behavior and kinetic and thermodynamic parameters of the dehydration reaction of Al<sub>0.5</sub>Fe<sub>0.5</sub>PO<sub>4</sub>•2.5H<sub>2</sub>O are different from those of individual metal phosphates (AlPO<sub>4</sub>·2H<sub>2</sub>O and FePO<sub>4</sub>•2H<sub>2</sub>O), which result from the perturbation of the molecular orbitals of the anion and cations occurring during the formation of the studied compound. The kinetic and thermodynamic data obtained from such studies can be directly applied in material science for the synthesis of various composite compounds.

#### Literature Cited

- Perri, E.; Tsamouras, D.; Dalas, E. Ferric Phosphate Precipitation in Aqueous Media. *J. Cryst. Growth* 2000, 213, 93.
   Lindsay, W. L.; Vlek, P. L. G.; Chien, S. H. Phosphate minerals. In
- (2) Lindsay, W. L.; Vlek, P. L. G.; Chien, S. H. Phosphate minerals. In Minerals in soil environment, 2nd ed.; Dixon, J. B., Weed, S. B., Eds.; Soil Science Society of America: Madison, WI, 1989; pp 1089–1130.

- (3) Kniep, R.; Mootz, D.; Vega, A. Variscite. Acta Crystallogr., Sect. B 1977, 33, 263–265.
- (4) Kniep, R.; Mootz, D. Metavariscite: A redetermination of its crystal structure. Acta Crystallogr., Sect. B 1973, 29, 2292–2294.
- (5) Scaccia, S.; Carewska, M.; Prosini, P. P. Thermoanalytical Study of Iron(III) Phosphate obtained by Homogeneous Precipitation from Different Media. *Thermochim. Acta* 2004, 41, 381.
- (6) Zaghib, K.; Julien, C. M. Structure and Electrochemistry of FePO<sub>4</sub>•2H<sub>2</sub>O Hydrate. *J. Power Sources* **2005**, *14*2, 279.
- (7) Song, Y.; Zavalij, P. Y.; Suzuki, M.; Whittingham, M. S. New Iron(III) Phosphate Phases: Crystal Structure and Electrochemical and Magnetic Properties. *Inorg. Chem.* 2002, 41, 5778.
- (8) Scaccia, S.; Carewska, M.; Bartolomeo, A. D.; Prosini, P. P. Thermoanalytical Investigation of Iron Phosphate obtained by Spontaneous Precipitation from Aqueous Solutions. *Thermochim. Acta* 2002, 383, 145.
- (9) Scaccia, S.; Carewska, M.; Bartolomeo, A. D.; Prosini, P. P. Thermoanalytical Investigation of Nanocrystalline iron(II) Phosphate obtained by Spontaneous Precipitation from Aqueous Solutions. *Thermochim. Acta* 2003, 397, 135.
- (10) Hsu, P. H. Crystallization of variscite at room temperature. *Soil Sci.* 1982, 133, 305–313.
- (11) Youssif, M. I.; Mohamedb, F. S.; Aziz, M. S. Chemical and physical properties of Al<sub>1-x</sub>Fe<sub>x</sub>PO<sub>4</sub> alloys Part I. Thermal stability, magnetic properties and related electrical conductivity. *Mater. Chem. Phys.* 2004, 83, 250–254.
- (12) Siva Kumar, V.; Padmasri, A. H.; Satyanarayana, C. V. V.; Ajit Kumar Reddy, I.; David Raju, B.; Rama Rao, K. S. Nature and mode of addition of phosphate precursor in the synthesis of aluminum phosphate and its influence on methanol dehydration to dimethyl ether. *Catal. Commun.* 2006, 7, 745–51.
- (13) Arjona, A. M.; Alario Franco, M. A. Kinetics of the thermal dehydration of variscite and specific surface area of the solid decomposition products. *J. Therm. Anal.* 1973, 5, 319–328.
- (14) Stojakovic, D.; Rajic, N.; Sajic, S.; Logar, N. Z.; Kaucic, V. A kinetic study of the thermal degradation of 3-methylaminopropylamine inside AIPO<sub>4</sub>-21. J. Therm. Anal. Calorim. 2007, 87, 337–343.
- (15) Ŝesták, J. Thermodynamical properties of solids; Academia Publishers: Prague, 1984.
- (16) Young, D. Decomposition of Solids; Pergamon Press: Oxford, 1966.
- (17) Boonchom, B.; Danvirutai, C. Kinetics and thermodynamics of thermal decomposition of synthetic AlPO<sub>4</sub>·2H<sub>2</sub>O. J. Therm. Anal. Calorim. 2009, 98, 771–777.

- (18) Boonchom, B. Thermodynamics and kinetics of the dehydration reaction of FePO<sub>4</sub> • 2H<sub>2</sub>O. *Physica B (Amsterdam, Neth.)* 2010, 405, 2350-2355.
- (19) Frost, R. L.; Weier, M. L. Vibrational Spectroscopy of Natural Augelite. J. Mol. Struct. 2004, 697, 207.
- (20) Breitinger, D. K.; Mohr, J.; Colognesi, D.; Parker, S. F.; Schukow, H.; Schwab, R. G. Vibrational Spectra of Augelites Al<sub>2</sub>(OH)<sub>3</sub>(XO<sub>4</sub>) (X = P, As, V). J. Mol. Struct. 2001, 563-564, 377.
- (21) Vyazovkin, S. Computational Aspects of Kinetic Analysis: Part C. The ICTAC Kinetics Project—the light at The End of The Tunnel? Thermochim. Acta 2000, 355, 155.
- (22) Ozawa, T. A New Method of Analyzing Thermogravimetric Data. Bull. Chem. Soc. Jpn. 1965, 38, 1881.
- (23) Kissinger, H. E. Reaction Kinetics in Differential Thermal Analysis. J. Anal. Chem. 1957, 29, 1702.
- (24) Li, Z.; Shen, X.; Feng, X.; Wang, P.; Wu, Z. Non-isothermal kinetics studies on the thermal decomposition of zinc hydroxide carbonate. *Thermochim. Acta* 2005, 438, 102–106.
- Thermochim. Acta 2005, 438, 102–106.
  (25) Ioiţescu, A.; Vlase, G.; Vlase, T.; Doca, N. Kinetics of decomposition of different acid calcium phosphates. J. Therm. Anal. Calorim. 2007, 88, 121–125.
- (26) Afify, N. A new method to study the crystallization or chemical reaction kinetics using thermal analysis technique. J. Phys. Chem. Solids 2008, 69, 1691–1697.
- (27) Zhang, Y.; Lv, M.; Chen, D. D.; Wu, J. Q. Leucite Crystallization Kinetics with Kalsilite as a Transition Phase. *Mater. Lett.* 2007, 61, 2978–2981.
- (28) Vlaev, L. T.; Nikolova, M. M.; Gospodinov, G. G. Non-Isothermal Kinetics of Dehydration of Some Selenite Hexahydrates. *J. Solid State Chem.* 2004, 177, 2663.
- (29) Vlaev, L.; Nedelchev, N.; Gyurova, K.; Zagorcheva, M. A comparative study of non-isothermal kinetics of decomposition of calcium oxalate monohydrate. J. Anal. Appl. Pyrolysis 2008, 81, 253–262.
- (30) Singh, B. K.; Sharma, R. K.; Garg, B. S. Kinetics and molecular modeling of biologically active glutathione complexes with lead(II) ions. J. Therm. Anal. Calorim. 2006, 84, 593–600.

Received for review January 29, 2010. Accepted May 16, 2010. This work is financially supported by the Thailand Research Fund (TRF), the Commission on Higher Education (CHE): Research Grant for New Scholar, and the National Nanotechnology Center (NANOTEC) NSTDA, Ministry of Science and Technology, Thailand, through its "Center of Excellence Network" program.

JE100096E



Contents lists available at ScienceDirect

### Journal of Alloys and Compounds

journal homepage: www.elsevier.com/locate/jallcom



## The phase evolution with temperature in $0.94 PbZrO_3 - 0.06 Pb(Mg_{1/2}W_{1/2})O_3$ antiferroelectric ceramic

Piyanut Charoonsuk<sup>a,b</sup>, Supamas Wirunchit<sup>a,b</sup>, Rangson Muanghlua<sup>c</sup>, Surasak Niemcharoen<sup>c</sup>, Banjong Boonchom<sup>d</sup>, Naratip Vittayakorn<sup>a,b,e,\*</sup>

- <sup>a</sup> Electroceramic Research Laboratory, College of KMITL Nanotechnology, King Mongkut's Institute of Technology Ladkrabang, Bangkok 10520, Thailand
- <sup>b</sup> ThEP Center, CHE, 328 Si Ayutthaya Rd., Bangkok 10400, Thailand
- c Department of Electronics, Faculty of Engineering, King Mongkut's Institute of Technology Ladkrabang, Bangkok 10520, Thailand
- d King Mongkut's Institute of Technology Ladkrabang, Chumphon Campus, 17/1M. 6 Pha Thiew District, Chumphon 86160, Thailand
- e Advanced Materials Science Research Unit, Department of Chemistry, Faculty of Science, King Mongkut's Institute of Technology Ladkrabang, Bangkok 10520, Thailand

#### ARTICLE INFO

# Article history: Received 14 May 2010 Received in revised form 28 June 2010 Accepted 30 June 2010 Available online 7 July 2010

Keywords: Antiferroelectric Wolframite precursor method Lead Zirconate Lead Magnesium Tungstate

#### ABSTRACT

The perovskite structure of the lead zirconate–lead magnesium tungstate ceramic,  $0.94\text{PbZrO}_3-0.06\text{Pb}(\text{Mg}_{1/2}\text{W}_{1/2})\text{O}_3$  (0.94Pz-0.06PmW), was prepared by the wolframite precursor method. The phase evolution with temperature in the 0.94Pz-0.06PmW ceramic was investigated, with dielectric permittivity, differential scanning calorimetry and polarization measurements. The ceramic was in the antiferroelectric phase when below  $177\,^{\circ}\text{C}$ , based on dielectric measurement, and an intermediate phase was detected between  $177\,^{\circ}\text{c}$  and  $219\,^{\circ}\text{C}$ . Evidence from ferroelectric data was found to suggest that this intermediate phase is ferroelectric.

© 2010 Elsevier B.V. All rights reserved.

#### 1. Introduction

Active studies of antiferroelectric (AFE) materials have been recently enhanced for next-generation electronic systems, for example, microelectromechanical systems consisting of sensors and actuators and high performance energy storage devices [1,2]. The phase transition from AFE to the field-forced ferroelectric (FE) state, induced by an electric field [3,4], is characterized by typical double P-E hysteresis loops. These materials are suitable for nonlinear charge storage capacitors because a field-forced ferroelectric state releases all polarized charges and can therefore supply very high instantaneous currents at the ferroelectric to antiferroelectric reverse phase transition. Recently, AFE materials, including Pb(Zr,Ti)O<sub>3</sub>, (Pb,Ba)ZrO<sub>3</sub>, (Pb,Sr)TiO<sub>3</sub>, (Pb,La)(Zr,Ti)O<sub>3</sub>, NaNbO<sub>3</sub> and (Bi<sub>0.5</sub>Na<sub>0.5</sub>)TiO<sub>3</sub> systems, have attracted increasing scientific attention [3–9]. Among them, lead zirconate (PbZrO<sub>3</sub>; PZ) and PbZrO<sub>3</sub>-based are the most attractive AFE materials, due to their high longitudinal strain response, and the latter is a proto-type of AFE ceramics that belongs to an ABO3-type perovskite family of oxides [10,11]. At temperatures below the Curie temperature (230 °C), PZ displays an orthorhombic perovskite structure with

lattice parameters of a = 5.87 Å, b = 11.74 Å and c = 8.20 Å [12]. This structure possesses an antiparallel shift of Pb ions along the [110], resulting in antiferroelectricity [13]. At temperatures above 230 °C, PbZrO<sub>3</sub> is in the paraelectric phase, with cubic m3m symmetry [13,14]. An intermediate phase, characterized by  $1/2\{1\ 1\ 0\}_c$ -type superlattice diffractions, is in between the AFE and paraelectric phase, within a narrow temperature range of 225–230 °C [13,14]. It is well known that the AFE to FE phase transformation in PZ ceramic requires a very strong electric field; otherwise, dielectric breakdown occurs. Consequently, most commercial AFE ceramics are chemically modified by adding Ba<sup>2+</sup>, Sr<sup>2+</sup>, Ti<sup>4+</sup> or Sn<sup>4+</sup> to reduce the critical field and optimize the physical and electrical properties [3–9]. Sawaguchi [15] studied the effect of Ti<sup>4+</sup> substitution in PZ on temperature variation of the P-E hysteresis loop and established the ferroelectric intermediate phase between the AFE and PE phase. Shirane [16] investigated the phase transition behavior of Ba<sup>2+</sup> doping in PZ and reported that the ferroelectric intermediate phase between the AFE and PE phase for Ba<sup>2+</sup> concentrations was lower than x = 0.175. Pokharel and Pandey [17,18] reported that relaxor ferroelectric behavior for Ba<sup>2+</sup> concentrations was higher than x = 0.25. Recently, it was reported that antiferroelectric (Pb<sub>1-x</sub>Ba<sub>x</sub>)ZrO<sub>3</sub> (PBZ) films, with a higher barium content of more than 45 mol%, were in paraelectric state at room temperature and possessed excellent dielectric properties comparable to (Ba,Sr)TiO<sub>3</sub> [6]. On the contrary, a ferroelectric intermediate phase was not observed in lanthanum doping in PZ. Otherwise, lanthanum

<sup>\*</sup> Corresponding author at: Department of Chemistry, Faculty of Science, King Mongkut's Institute of Technology Ladkrabang, Bangkok 10520, Thailand. E-mail address: naratipcmu@yahoo.com (N. Vittayakorn).

doping in PZ would be found to increase the stability range of the antiferroelectric phase [19,20]. Furthermore, Tan et al. [20] studied the doping effect of various metal oxide elements on field-induced polarization in PZ ceramics and found that addition of Bi<sup>3+</sup> and K<sup>+</sup> substantially increased stability of the antiferroelectric phase. Chen et al. [21] observed antiferroelectric-like or double hysteresis loops  $behavior\ in\ (Pb,Sr)TiO_3.\ However, the\ antiferroelectric\ nature\ is\ different properties of the control of the control$ ferent from PZ ceramics. Rubia et al. [22] investigated the effect of Hf<sup>4+</sup> substitution in PZ on phase transition, when the intermediate phase was found to increase with increasing Hf<sup>4+</sup> concentrations. Up to now, scientific information about the effect of metal oxide substitution in PZ and nature of the intermediate phase is still unclear. Recently, our research work reported that the intermediate phase can also be introduced by partial replacement of Zr<sup>4+</sup> ions with complex B-site ions such as Ni<sup>2+</sup>/Nb<sup>5+</sup> [23,24], Zn<sup>2+</sup>/Nb<sup>5+</sup> [25], or Co<sup>2+</sup>/Nb<sup>5+</sup> [26]. Furthermore, our previous study found that by adding minor amounts (2-10 mol%) of antiferroelectric  $Pb(Mg_{1/2}W_{1/2})O_3$  (PMW) into antiferroelectric PZ, the temperature range expanded to an intermediate phase, which was characterized by evident frequency dispersion in dielectric permittivity [27]. As a consequence, a series of outstanding phase transitions were revealed by the dielectric measurement [27]. Nevertheless, the nature of the intermediate phase is still open for debate. The  $0.94PbZrO_3-0.06Pb(Mg_{1/2}W_{1/2})O_3$  ceramic was selected in this study for further investigation of phase transformation sequence, while heating to 250 °C with ferroelectric measurement.

#### 2. Experimental procedures

The perovskite structure of the lead zirconate-lead magnesium tungstate ceramic,  $0.94PbZrO_3 - 0.06Pb(Mg_{1/2}W_{1/2})O_3$  (0.94PZ - 0.06PMW), was prepared by the wolframite precursor method via the ball-milling technique. The wolframite structure (MgWO<sub>4</sub>) was synthesized first before stoichiometric amounts of the precursor (MgO and WO $_3$ ) were mixed and milled in ethyl alcohol for 18 h. The mixture was then dried and calcined at 1100 °C for 4h, and MgWO<sub>4</sub> and ZrO<sub>2</sub> were subsequently mixed with PbO. After re-milling and drying, the mixtures were calcined at 900°C for 4h in a closed alumina crucible. Pellets measuring 15 mm in diameter were pressed using 5% PVA, the binder was burned out slowly by heating to 500 °C over 2 h, and the samples were sintered at 1150 °C for 4 h. Phase formation of 0.94PZ-0.06PMW was investigated by X-ray diffraction (XRD). Scanning electron microscopy (SEM; Hitachi, s4007) was employed to investigate the microstructure of the sintered pellets. The major faces of the samples were lapped to determine their dielectric and ferroelectric properties, and silver electrodes were made from a low-temperature silver paste by firing at  $550\,^{\circ}\text{C}$  for  $30\,\text{min}$  to enable electrical measurements to be taken. The relative permittivity  $(\epsilon_r)$  and dissipation factor  $(\tan\delta)$ were measured using an HP-4284A LCR meter. The capacitance and dissipation factors of the sample were measured at 1-100 kHz, and the temperature varied between 25 and 350 °C. A heating rate of 2 °C/min was used during measurement, and the phase transitions also were measured by differential scanning calorimeter (DSC 2920, TA Instrument) between ambient temperature and  $350\,^{\circ}\text{C}$  at a rate of 10 °C/min. The electrical polarization versus field hysteresis loops was recorded at a series of temperatures by a standardized ferroelectric test system (RT-66A, Radiant Technologies). The peak field was maintained at 30 kV/cm during measurement, and the ferroelectric hysteresis loop was recorded after the temperature was stabilized

#### 3. Results and discussion

The XRD pattern of 0.94PZ–0.06PMW ceramic is presented in Fig. 1. The 0.94PZ–0.06PMW ceramic was identified from the patterns as a single-phase material with a perovskite structure having orthorhombic symmetry. Evidence of the pyrochlore or other second phases was not detected in the pattern, but the 1/4(hkl) superstructure lines were present in the 0.94PZ–0.06PMW ceramic, indicating that the Pb<sup>2+</sup> ions suffer antiparallel displacements with respect to their original position in the cubic perovskite lattice. The indexed pattern with the least number of refinement squares gave a cell with dimensions of a = 5.85(1) Å, b = 11.67(3) Å and c = 8.16(8) Å. The cell parameters of 0.94PZ–0.06PMW were close to those of the standard data: PDF#751607 [a = 5.88(4), b = 11.76(0) and c = 8.22(0)]. A 97.8% relative density of the ceramic was measured

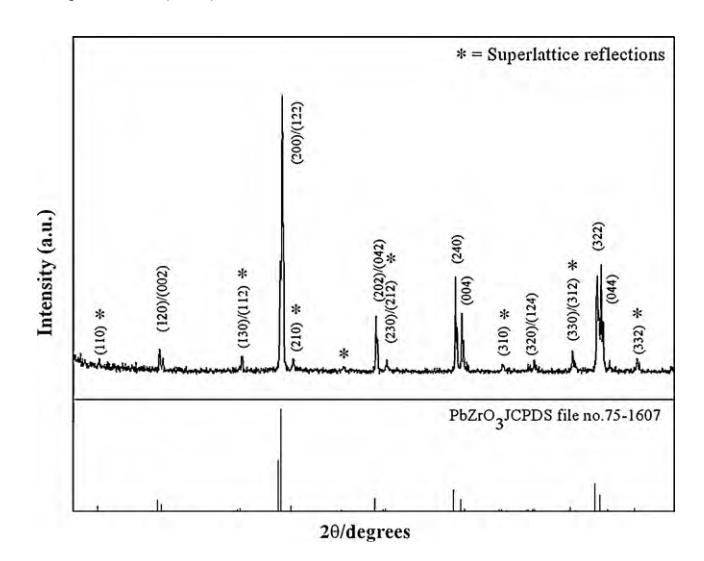
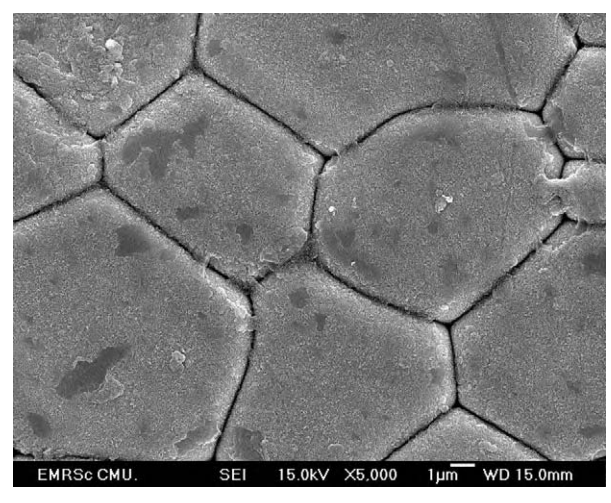


Fig. 1. XRD pattern of 0.94PZ-0.06PMW ceramic.

using the Archimedes method, and the grain size was examined by scanning electron microscopy (SEM). The fresh surface of the 0.94PZ–0.06PMW ceramic was almost free of pores, with a grain size in the range of  $10-14\,\mu m$ , as shown in Fig. 2.

The temperature dependence of relative permittivity and dielectric loss was measured at frequencies of 1, 10 and 100 kHz, while heating from 25 to 350 °C, and the results are displayed in Fig. 3. There were clearly two abrupt changes in both relative permittivity and dielectric loss in the 0.94PZ-0.06PMW ceramic. The first one occurred at around 177 °C, where both relative permittivity and dielectric loss increased by one order of magnitude. The other one took place at the Curie temperature of 219°C, where significant suppression of dielectric loss was seen. Therefore, the dielectric response in the 0.94PZ-0.06PMW ceramic can be divided into three stages. At temperatures below 177 °C, both the relative permittivity and the dielectric loss have low values and show negligible increases with increasing temperatures. At temperatures above 219 °C, the relative permittivity begins to decrease following the Curie-Weiss law [3,4]. In the intermediate temperature range (177-219°C), the relative permittivity increases dramatically, while the dielectric loss remains high at around 0.08.

To elucidate further on the dielectric behavior of different phases in the 0.94PZ-0.06PMW ceramic, electrically polarized hysteresis loop measurements were performed at a series of tem-



**Fig. 2.** SEM image of 0.94PZ-0.06PMW ceramic surfaces.

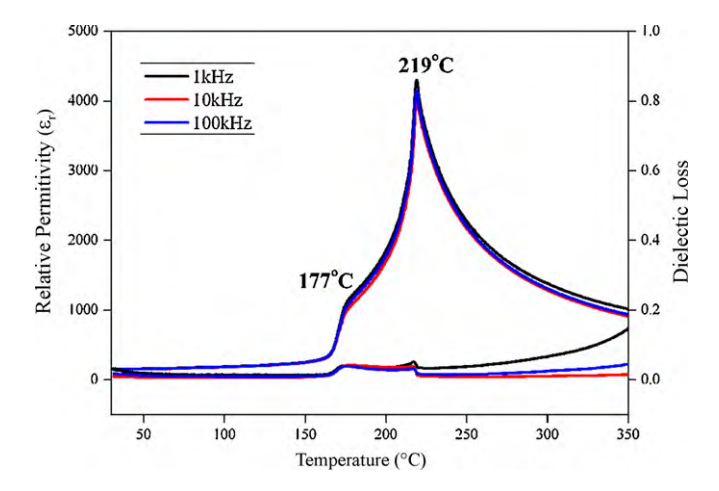


**Fig. 3.** Dielectric properties during heating at 1, 10 and 100 kHz in a bulk 0.94PZ-0.06PMW ceramic.

peratures under a peak field of 30 kV/cm. A circular disk specimen, with a diameter of about 10 mm and thickness of around 800  $\mu$ m, was used. The loop was recorded after the temperature had been stabilized for at least 5 min. Linear polarization was displayed as a function of electric field between room temperature and 155 °C, as shown in Fig. 4(a)–(d). This could indicate that the 0.94PZ–0.06PMW ceramic has AFE behavior between room temperature and less than 150 °C [Fig. 4(a)]. Regarding bulk AFE ceramic specimens, the net remnant polarization ( $P_{\rm r}$ ) was zero, due to the existence of antiparallel dipole moments. To induce an AFE–FE phase transition, an intense electric field needs to be applied to the ceramics.

Hysteretic behavior starts to develop when the temperature increases to 155 °C, and a regular hysteresis loop has a coercive  $E_C$  field of 8.29 kV/cm, as shown in Fig. 4(b). However, the hystere-

sis loop observed does not indicate the presence of a ferroelectric phase. As seen in Fig. 4(b), close examination of the hysteresis loop at 155 °C reveals that slight distortions, which are marked by two circles, occurred at  $\sim$ 10 kV/cm. Similar distortions were found on the hysteresis loop in  $0.98PbZrO_3-0.02Pb(Ni_{1/3}Nb_{2/3})O_3$  and  $Pb_{0.99}Nb_{0.02}[Zr_{0.57}Sn_{0.43}]_{1-x}Ti_x]_{0.98}O_3$  ceramics, and these have been attributed to the onset of electric field-induced AFE to FE transition [28,29]. Therefore, the 0.94PZ-0.06PMW ceramic is still in the AFE phase at this temperature and it should be noted that the distortions marked at 155  $^{\circ}\text{C}$  in Fig. 4(b) indicate the AFE-FE phase transition. A regular hysteresis loop, exhibiting ferroelectricity, clearly demonstrated the intermediate phase between the AFE and PE phase when the temperature was raised to 190°C [Fig. 4(c)]. Moreover, hysteretic behavior transition from the FE to PE phase occurred when the temperature increased to over 220 °C [Fig. 4(d)]. It is well known that the occurrence of antiferroelectricity in pure PZ is due to an antiparallel shift of Pb ions along the [1 1 0] direction and it also results in a superstructure line in the XRD pattern. It is apparent that replacement of the Zr<sup>4+</sup> ion by Mg<sup>2+</sup>/W<sup>6+</sup> ions decreases the driving force for the antiparallel shift of Pb2+ ions, because they interrupt the translational symmetry. This interruption causes the appearance of an intermediate ferroelectric phase and similar behavior has been found in PZ-PNN ceramics [28]. The DSC technique was used as the third tool to confirm the phase transition of PZ-PMW ceramics. Fig. 5 shows the temperature dependence of the heat flow (DSC curves) obtained when heating the 0.94PZ-0.06PMW sample at a rate of 10°C/min. Two phase transitions in the 0.94PZ-0.06PMW ceramic were obtained with dielectric measurement and clearly confirmed by DSC measurement. The lower temperature of 163 °C corresponded to the transition temperature of the AFE → FE phase transition, while the higher one (215 °C) corresponded to the FE → PE phase transition. It is interesting to note that the difference in values of AFE-FE and FE-PE transition temperature in dielectric, ferroelectric and DSC measurement techniques is due to that in heating

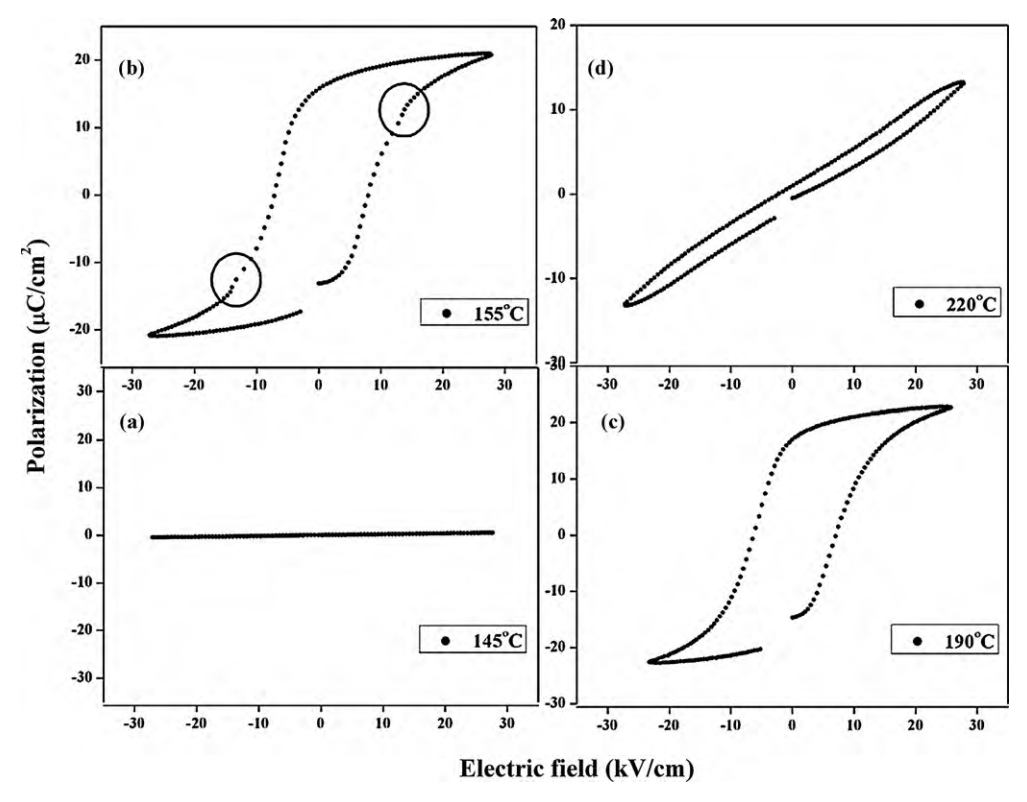


Fig. 4. Hysteresis loops of 0.94PZ-0.06PMW ceramic from temperatures of 145-220 °C.

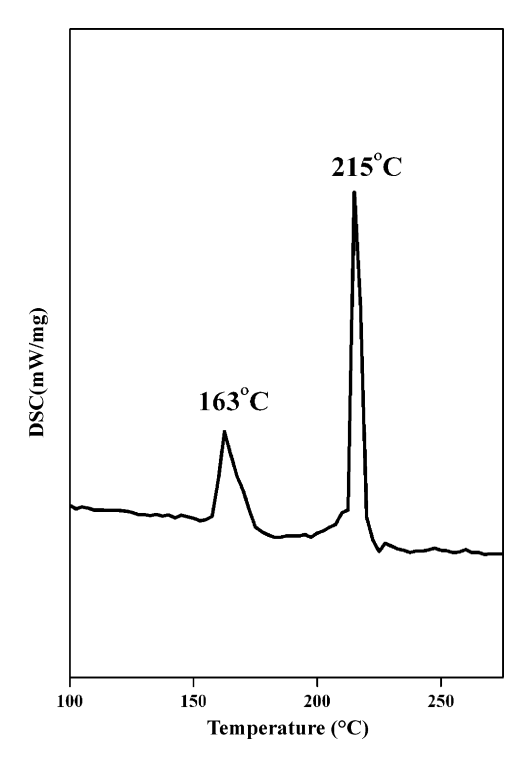


Fig. 5. DSC curves of 0.94PZ-0.06PMW ceramic.

rate and dwell time measurement. Thermodynamic parameter, enthalpy  $(\Delta H^*/J \, \mathrm{g}^{-1})$ , heat capacity  $(C_p/J \, \mathrm{g}^{-1} \, \mathrm{K}^{-1})$ , entropy change  $(\Delta S^*/J \, \mathrm{g}^{-1} \, \mathrm{K}^{-1})$ , and Gibbs energy change  $(\Delta G^*/J \, \mathrm{g}^{-1})$  were calculated from the DSC results. The enthalpy change was calculated directly from the amount of heat change involved in each step per unit mass of the sample. The  $\Delta H^*$  was thus determined and implemented to calculate the specific heat capacity  $(C_p)$  using the following equation [30,31]:

$$C_p = 2.303C_p \log(T_2/T_1) \tag{1}$$

where  $\Delta T = T_2 - T_1$ ,  $T_1$  is the temperature at which the DSC peak begins to depart from the baseline, and  $T_2$  is the temperature at which the peak lands. Consequently, the changes of entropy ( $\Delta S^*$ ) and Gibbs energy ( $\Delta G^*$ ) were calculated using the following equations [30,31]:

$$\Delta S* = 2.303C_p \log(T_2/T_1) \tag{2}$$

$$\Delta H * = \Delta G * -T_p \Delta S * \tag{3}$$

On the basis of DSC data, the value of  $\Delta H^*$ ,  $\Delta S^*$ ,  $C_p$  and  $\Delta G^*$  for the phase transition can be calculated according to Eqs. (1)–(3), which are presented in Table 1. In terms of the activated complex theory (transition theory), the higher value of  $\Delta S^*$  for the AFE to FE phase transition indicates a lower ordered activated complex. Also, the degree of rotation freedom as well as vibration is higher than that in non-activated complex antiferroelectric and paraelectric phases, which corresponds well with the formation of a non-stability phase. This means that the rate of AFE to FE phase transition is higher than that of the FE to PE phase transition

**Table 1**Values of thermodynamic parameters for phase transition of 0.94PZ-0.06PMW ceramics calculated from DSC data.

Temperature ranges/K	T <sub>p</sub> /K	$\Delta H^*/\mathrm{J}\mathrm{g}^{-1}$	$C_p/J\mathrm{g}^{-1}\mathrm{K}^{-1}$	$\Delta S^*/J g^{-1} K^{-1}$	$\Delta G^*/\mathrm{J}\mathrm{g}^{-1}$
431-441 487-491	436 488	1.207 2.325	$\begin{array}{c} 2.768 \times 10^{-3} \\ 4.764 \times 10^{-3} \end{array}$	$\begin{array}{c} 6.350 \times 10^{-5} \\ 3.858 \times 10^{-5} \end{array}$	1.179 2.308

of thermal transformation. Therefore, the FE to PE transformation step occurs harder than the AFE to FE transformation step. On the other hand, the thermodynamic parameter,  $\Delta H^*$  and  $\Delta G^*$ , was calculated according to Eqs. (1)–(3) and gave the positive values for both steps, thus indicating that the AFE to FE to PE phase transitions are connected to the introduction of heat, and phase transitions are non-spontaneous processes.

#### 4. Conclusions

The investigation of 0.94PZ–0.06PMW ceramics using XRD, dielectric behavior, differential scanning calorimetry and ferroelectric measurements has clearly shown a series of phase transitions that occur above room temperature. When the ceramic is in an antiferroelectric nature below 177 °C, both the dielectric property and the loss tangent are low and stable against temperature change. One order of magnitude increase in dielectric property occurs at around 177 °C, and loss tangent results within a narrow temperature range. The ceramic is in an intermediate phase at a temperature range of 177–219 °C, when it is believed to be ferroelectric. When the ceramic is above 219 °C, it is in the cubic paraelectric phase, with relative permittivity following the Curie–Weiss law. A thermodynamic parameter indicated that the AFE to FE to PE phase transitions are connected to the introduction of heat, and phase transitions are non-spontaneous processes.

#### Acknowledgements

This research was supported by a grant from the Thailand Research Fund (TRF), the Royal Golden Jubilee Ph.D. Program, and the National Nanotechnology Center (NANOTEC) NSTDA, Ministry of Science and Technology, Thailand, through its "Center of Excellence Network" program.

#### References

- [1] G.R. Love, J. Am. Ceram. Soc. 73 (2005) 323–328.
- [2] G.H. Haertling, J. Am. Ceram. Soc. 82 (1999) 797–818.
- [3] Y. Xu, Ferroelectric Materials and Their Application, Elsevier Science Publishers B.V., Amsterdam, 1991.
- [4] B. Jaffe, W.R. Cook, H. Jaffe, Piezoelectric Ceramics, Academic Press, London, 1971.
- [5] L.B. Kong, J. Ma, W. Zhu, O.K. Tan, J. Alloys Compd. 322 (2001) 290–297.
- 6] X. Hao, Z. Zhang, J. Zhou, S. An, J. Zhai, J. Alloys Compd. 501 (2010) 358–361.
- [7] S.H. Leala, M.T. Escote, F.M. Pontes, E.R. Leite, M.R. Joya, P.S. Pizani, E. Longo, J.A. Varela, J. Alloys Compd. 475 (2009) 940–945.
- [8] K. Bhattacharyya, A.K. Tyagi, J. Alloys Compd. 470 (2009) 580–583.
- [9] L. Liu, H. Fan, S. Ke, X. Chen, J. Alloys Compd. 458 (2008) 504–508. [10] A.S. Bhalla, R. Guo, R. Roy, Mater. Res. Innov. 4 (2000) 3–26.
- [10] A.S. Bhalla, R. Guo, R. Roy, Mater. Res. Innov. 4 (2000) 3–26.
   [11] E. Sawaguchi, H. Maniwa, S. Hoshino, Phys. Rev. 83 (1951) 1078.
- [12] S. Roberts, J. Am. Ceram. Soc. 33 (1953) 63–66.
- [13] F. Jona, G. Shirane, F. Mazzi, R. Pepinsky, Phys. Rev. 105 (1957) 849–856.
- [14] X. Dai, J.F. Li, D. Viehland, Phys. Rev. B 51 (1995) 2651–2655.
- [15] E. Sawaguchi, J. Phys. Soc. Jpn. 8 (1951) 615–629.
- [16] G. Shirane, Phys. Rev. 86 (1952) 219–227.
- [17] B.P. Pokharel, D. Pandey, Phys. Rev. B 65 (2002) 214108.
- [18] B.P. Pokharel, D. Pandey, J. Appl. Phys. 86 (1999) 3327–3332.
- [19] B. Xu, N.G. Pai, L.E. Cross, Mater. Lett. 34 (1998) 157-160.
- [20] Q. Tan, Z. Xu, D. Viehland, J. Mater. Res. 14 (1999) 4251-4258.
- [21] H. Chen, C. Yang, J. Zhang, Y. Pei, Z. Zhao, J. Alloys Compd. 486 (2009) 615–620.
  [22] D.L. Rubia, M.A. Alonso, R.E. Lopez-Garcia, A.R.D. Frutos, IEEE Trans. Ultrason.
- [22] D.L. Rubia, M.A. Alonso, R.E. Lopez-Garcia, A.R.D. Frutos, IEEE Trans. Ultrason Ferroelectr. Freq. Control 56 (2009) 1799–1805.
- [23] S. Wirunchit, P. Laoratanakul, N. Vittayakorn, J. Phys. D: Appl. Phys. 41 (2008) 125406.
- [24] S. Wirunchit, N. Vittayakorn, J. Appl. Phys. 104 (2008) 024103.
- [25] W. Banlue, N. Vittayakorn, Ferroelectrics 382 (2009) 122–126.
- [26] W. Banlue, N. Vittayakorn, Appl. Phys. A 93 (2008) 565-569.
- 27] N. Vittayakorn, P. Charoonsuk, P. Kasiansin, S. Wirunchit, B. Boonchom, J. Appl. Phys. 106 (2009) 064104.
- [28] W. Qu, X. Tan, N. Vittayakorn, S. Wirunchit, M.F. Besser, J. Appl. Phys. 105 (2009) 014106.
- [29] H. He, X. Tan, Phys. Rev. B 72 (2005) 024102.
- [30] S.A. Halawy, N.E. Fouad, M.A. Mohamed, M.I. Zaki, J. Therm. Anal. Calorim. 82
- [31] R.H. Abu-Eittah, N.G. Zaki, M.M.A. Mohamed, L. Kamel, J. Anal. Appl. Pyrol. 77 (2006) 1–11.





# Soft Synthesis Route and Characterization of Superparamagnetic $Mn_{1/2}$ - $Fe_{1/2}(H_2PO_4)_2 \cdot 2H_2O$ and Its Decomposed Product

Banjong Boonchom $^{*,\dagger,\ddagger}$  and Naratip Vittayakorn $^{\ddagger,\$,\parallel}$ 

<sup>†</sup>King Mongkut's Institute of Technology Ladkrabang, Chumphon Campus, 17/1 M. 6 Pha Thiew District, Chumphon, 86160, Thailand Electroceramic Research Laboratory, <sup>‡</sup>College of KMITL Nanotechnology, and Advanced Materials Science Research Unit, <sup>§</sup>Department of Chemistry, Faculty of Science, King Mongkut's Institute of Technology Ladkrabang, Bangkok 10520, Thailand <sup>II</sup>ThEP Center, CHE, 328 Si Ayutthaya Road, Bangkok 10400, Thailand

**ABSTRACT:** The superparamagnetic  $Mn_{1/2}Fe_{1/2}(H_2PO_4)_2 \cdot 2H_2O$  was synthesized by a soft synthesis method using a  $Mn_{1/2}Fe_{1/2}(H_2PO_4)_2 \cdot 2H_2O$  decomposed through the dehydration and the phosphate condensation reactions at high temperature and yielded binary manganese iron cyclotetraphosphate  $MnFeP_4O_{12}$ . The XRD and FTIR results of the synthesized  $Mn_{1/2}Fe_{1/2}(H_2PO_4)_2 \cdot 2H_2O$  and the decomposed  $MnFeP_4O_{12}$  indicate the pure monoclinic phase with space group  $P2_1/n$  and C2/c, respectively. The thermal behaviors and superparamagnetic properties of  $Mn_{1/2}Fe_{1/2}(H_2PO_4)_2 \cdot 2H_2O$  and  $MnFeP_4O_{12}$  in this work differed from the single compounds  $(M(H_2PO_4)_2 \cdot 2H_2O)$  and  $M_2P_4O_{12}$ , where M=Mn, Fe) and the binary compounds  $(Mn_{0.5}Fe_{0.5}(H_2PO_4)_2 \cdot xH_2O)$  reported in previous works. The kinetic and thermodynamic functions for thermal decomposition of  $Mn_{1/2}Fe_{1/2}(H_2PO_4)_2 \cdot 2H_2O$  were studied and confirmed as reaction mechanisms. Vibrational frequencies of breaking bonds in two thermal transformation stages were estimated and assigned by comparison with the observed FTIR spectra.

#### 1. INTRODUCTION

Binary metal(II) dihydrogenphosphate hydrates  $M_{1-x}A_{x-}(H_2PO_4)_2 \cdot nH_2O$  (M and A = Mg, Ca, Mn, Fe, Co, Ni, Zn, or Cu; x=0-1; n=1-4) have been investigated for over 30 years and have been widely applied as potential pigments, selective catalysts, phosphors, and materials for corrosion-resistant coatings, and they are biocompatible and biodegradable in tissue. This phosphate hydrate group is transformed to binary metal(II) cyclotetraphosphate group  $M_{2-y}A_yP_4O_{12}$  (y=0-2) via the reactions of dehydration and deprotonation of dihydrogenphosphate groups as well as polycondensation at high temperatures. Both phosphate groups are good sources for macro- and micronutrients (P, Mg, Ca, Mn, Fe, Co, Ni, Zn, Cu) required by plants. Consequently, these phosphate materials have been become a hot research topic in materials science in recent years.

Some binary metal  $M_{1-x}A_x(H_2PO_4)_2 \cdot nH_2O$  were prepared for the first time by Trojan et al. using corresponding metal carbonates and phosphoric acid at low temperature (313–353 K) with long time periods (2-60 h),  $^{1-16}$  and releasing toxic gas  $(CO_2)$ . Recently,  $M_{1-x}Ni_x(H_2PO_4)_2 \cdot xH_2O$  (M = Mg, Mn, Fe, Co, Zn, and Cd) were prepared by corresponding metal carbonates and phosphoric acid at 293 K for 2–90 days. More recently,  $Mn_{1-x}A_x(H_2PO_4)_2 \cdot xH_2O$  (A = Ca, Fe, Co, Ni, and Cu) were prepared by metal sources (Mn (c; complexometric) or MnCO<sub>3</sub> and A(II) = CaCO<sub>3</sub>, Fe, CoCO<sub>3</sub>, NiCO<sub>3</sub>, or CuCO<sub>3</sub>) and phosphoric acid  $H_3PO_4$  at ambient temperature for 20 s. These procedures were strong exothermic reactions and evolved gases (CO<sub>2</sub> and  $H_2$ ).  $^{17-21}$  However, a limited dose of  $M_{1-x}A_x(H_2PO_4)_2 \cdot nH_2O$  could be synthesized without toxic gases.

Synthesis of transition phosphates by a soft solid state reaction in media agents (ethanol, acetone, and water, etc.) at ambient temperature has received a great deal of attention due to their conveniences, cost-effectiveness, and that they are environmentally benign.  $^{22-24}$  Because of its solubility in water and its ability to associate with metal ions in media, solvent has been used as a binder cum gel for shaping materials (bulk, porous, micro- or nanoparticles) and as a matrix for entrapment of ions to generate a gelled precursor, which resulted in obtaining different material or the same material with different size and morphology. The presence of media agent (solvent) reduces strong exothermic reaction and protects the evolved gases, which will be necessary for elaboration of technology to produce transition metal phosphates. The use of solvent simplifies the process and would provide another alternative process for the environmental and economical synthesis of transition phosphate with different particle size and morphology.

Herein, this work reports the fabrication of  $Mn_{1/2}Fe_{1/2}$ - $(H_2PO_4)_2 \cdot 2H_2O$  through a soft solid state reaction from metals of manganese and iron with phosphoric acid in water—acetone medium at ambient temperature with short time consumption (<30 min). The synthesized  $Mn_{1/2}Fe_{1/2}(H_2PO_4) \cdot 2H_2O$  decomposed to binary manganese iron cyclotetraphosphate MnFe- $P_4O_{12}$  at 773 K. Consequently, kinetic ( $E_a$ , A) and thermodynamic ( $\Delta H^*$ ,  $\Delta S^*$ ,  $\Delta G^*$ ) functions of thermal transformation of  $Mn_{1/2}Fe_{1/2}(H_2PO_4)_2 \cdot 2H_2O$  playing an important role in

Received: July 4, 2010
Accepted: December 26, 2010
Revised: December 1, 2010
Published: January 19, 2011



theoretical study, application development, and industrial production have also been reported for the first time. The synthesized sample and its decomposed product were characterized by X-ray powder diffraction (XRD), Fourier transform infrared (FTIR), scanning electron microscope (SEM), and vibrating sample magnetometer (VSM) techniques. The  $Mn_{1/2}Fe_{1/2} \cdot (H_2PO_4)_2 \cdot 2H_2O$  and  $MnFeP_4O_{12}$  may be useful for fertilizers, (Mn- and Fe-micronutrients and P-macronutrients), ceramic pigments, magnetic materials, etc., in the future.

#### 2. EXPERIMENTAL SECTION

**2.1. Synthesis and Characterization.** The starting reagents are Mn (c; complexometric) (99.99%, Merck), Fe (c; complexometric) (99.99%, Fluka), and phosphoric acid (86.4% w/w  $\rm H_3PO_4$ , Merck). Following this procedure, 1.0988 g of Mn(c) and 1.1186 g of Fe(c) (a mole ratio corresponding to the nominal composition of Mn:Fe ratio of 1:1) were crushed into fine mixed powders using a mortar and pestle. Subsequently, 10 mL of acetone was rapidly added to the fine mixed powders, and then 10 mL of 50%  $\rm H_3PO_4$  (86.4% w/w  $\rm H_3PO_4$  dissolved in DI water) was added slowly to the resulting suspension with continuous stirring at ambient temperature until the cooled crystalline product was developed (30 min). The prepared solid was filtered by a suction pump, washed with acetone, and dried in air.

$$\begin{aligned} &Mn(s) + Fe(s) + 4H_{3}PO_{4} \\ &+ 2H_{2}O \xrightarrow[\text{room temperature}} 2Mn_{1/2}Fe_{1/2}(H_{2}PO_{4})_{2} \cdot 2H_{2}O(s) + 2H_{2} \end{aligned} \tag{1}$$

The water content was investigated by the TG curve in Figure 1, which reveals that its final decomposed product, MnFeP<sub>4</sub>O<sub>12</sub>, seemed to occur at temperatures above 673 K. The dried white gray precipitation then was calcined in a box furnace at 773 K for 3 h in air atmosphere. The manganese and iron contents of Mn<sub>1/2</sub>Fe<sub>1/2</sub>(H<sub>2</sub>PO<sub>4</sub>)<sub>2</sub>·2H<sub>2</sub>O and MnFeP<sub>4</sub>O<sub>12</sub> were determined by dissolving in 0.0126 M hydrochloric acid using atomic absorption spectrophotometer (AAS, Perkin-Elmer, Analyst100). The phosphorus content was determined by colorimetric analysis of the molybdophosphate complex. The structure and crystallite size of the synthesized sample and its decomposed product were studied by X-ray powder diffraction using an X-ray diffractometer (Phillips PW3040, The Netherland) with Cu K $\alpha$  radiation ( $\lambda$  = 0.15406 nm). The Scherrer method was used to evaluate the crystallite size.<sup>25</sup> The morphologies of the prepared samples were examined with a scanning electron microscope (SEM) using LEO SEM VP1450 after gold coating. The room temperature FTIR spectra were recorded in the range of 4000-370 cm<sup>-1</sup> with eight scans on a Perkin-Elmer Spectrum GX FT-IR/FT-Raman spectrometer with the resolution of 4 cm<sup>-1</sup> using KBr pellets (KBr, spectroscopy grade, Merck). The magnetic properties of the Mn<sub>1/2</sub>Fe<sub>1/2</sub>(H<sub>2</sub>PO<sub>4</sub>)<sub>2</sub>·2H<sub>2</sub>O and  $MnFeP_4O_{12}$  were examined at room temperature (293 K) using a vibrating sample magnetometer (VSM 7403, Lake Shore, U.S.).

**2.2.** Kinetic and Thermodynamic Studies. To evaluate the activation energies for the thermal decomposition of  $Mn_{1/2}Fe_{1/2}$ - $(H_2PO_4)_2 \cdot 2H_2O$ , a TG-DTA Pyris Diamond Perkin-Elmer Instrument was used. The experiments were performed in dynamic dry air, at heating rates of 5, 10, 15, and 20 K min<sup>-1</sup> over the temperature range from 303 to 673 K and the  $O_2$  flow rate of 100 mL min<sup>-1</sup>. The sample mass of about 6.0–10.0 mg

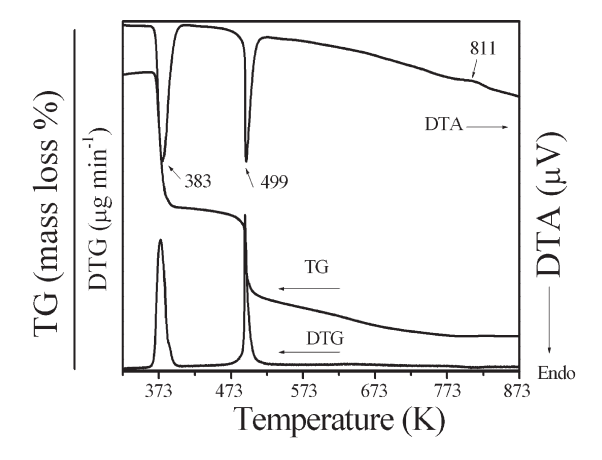


Figure 1. TG-DTG-DTA curves of  $Mn_{1/2}Fe_{1/2}(H_2PO_4)_2 \cdot 2H_2O$ .

was filled into an aluminum crucible without pressing. The thermogram of sample was recorded in an open aluminum crucible using  $\alpha\text{-Al}_2O_3$  as the reference material. Decomposition of crystal hydrates is a solid-state process of the type  $^{26-32}$  A(solid)  $\rightarrow$  B(solid) + C(gas). The kinetics of such reactions is described by various equations taking into account the special features of their mechanisms. The activation energies for the thermal transformation steps of  $Mn_{1/2}Fe_{1/2}(H_2PO_4)_2 \cdot 2H_2O$  were calculated from two peaks on the DTA curves using the Kissinger equation:  $^{33}$ 

$$\ln\left(\frac{\beta}{T_{\rm p}^{2}}\right) = -\frac{E_{\rm a}}{RT_{\rm p}} + \ln\left(\frac{AR}{E_{\rm a}}\right) \tag{2}$$

Here,  $\beta$  is the DTA heating rate (K min<sup>-1</sup>),  $E_{\rm a}$  is the activation energy for the phase transformation (kJ mol<sup>-1</sup>), R is the gas constant (8.314 J mol<sup>-1</sup> K<sup>-1</sup>), and  $T_p$  is the phase transformation temperature peak in the DTA curve (K). The fact that the  $T_p$ values for various heating rates can be precisely evaluated from nonisothermal data (DTA, DTG, or DSC curves) conferred to the Kissinger method to evaluate the kinetic parameters a high popularity. The plots of  $\ln(\beta/T^2)$  versus  $1/T_p$  should give the straight lines with the best correlation coefficients of the linear regression  $(R^2)$ , which have been proved to give the values of activation energy and pre-exponential factor by the slope and the intercept for the different thermal transformation stages of Mn<sub>1/2</sub>- $Fe_{1/2}(H_2PO_4)_2 \cdot 2H_2O$ . The advantage of Kissinger equation is that the values of  $E_a$  and A can be calculated on the basis of multiple thermogravimetric curves and do not require selection of particular kinetic model (type of  $g(\alpha)$  or  $\hat{f(\alpha)}$  functions).  $\hat{f(\alpha)}$ In addition, the  $E_a$  and A values obtained by this method are usually regarded as more reliable than those obtained by a single thermogravimetric curve.

The thermal decomposition mechanism could be determined from the shape factor (n) of ethe ndothermic peak represented by the following equation:<sup>34</sup>

$$n = \frac{2.5}{\Delta T} \cdot \frac{T_{\rm p}^2}{E_{\rm a}/R} \tag{3}$$

where n is the Avrami constant, and  $\Delta T$  is the full width at half-maximum of the endothermic peak;  $T_{\rm p}$  is the average temperature at different DTA curves; and  $E_{\rm a}$  is the activation energy of the Kissinger method.

From the activated complex theory (transition state) of Eyring,  $^{35-37}$  the following general equation may be written:

$$A = \left(\frac{e\chi k_{\rm B} T_{\rm ap}}{h}\right) \exp\left(\frac{\Delta S^*}{R}\right) \tag{4}$$

$$\Delta S^* = R \ln \left( \frac{Ah}{e\chi} k_{\rm B} T_{\rm ap} \right) \tag{5}$$

Because

$$\Delta H^* = E_{\rm a} - RT_{\rm ap} \tag{6}$$

$$\Delta G^* = \Delta H^* - T_{\rm ap} \Delta S^* \tag{7}$$

where A and  $E_a$  are the pre-exponential factor and the activation energy, respectively, obtained from the Kissinger method; e = 2.7183 is the Neper number;  $\chi$  is the transition factor, which is unity for monomolecular reactions;  $k_B$  is the Boltzmann constant; h is the Planck constant; and  $T_{\rm ap}$  is the average phase transformation temperature peak in DTA curves (K). The changes of the enthalpy  $\Delta H^*$  and Gibbs free energy  $\Delta G^*$  for the activated complex formation from the reagent can be calculated using the well-known thermodynamic equation. In this Article, we suggest the relation between kinetic ( $E_a$ , and A) and thermodynamic ( $\Delta H^*$ ,  $\Delta S^*$ ,  $\Delta G^*$ ) parameters of the thermal transformation of  $\mathrm{Mn}_{1/2}\mathrm{Fe}_{1/2}(\mathrm{H_2PO_4})_2\cdot 2\mathrm{H_2O}$  based on the Kissinger method and attract the interest of thermodynamic and kinetic scientists.

The specificity of the thermal decomposition was characterized by identification of the bonds to be selectively activated due to energy absorption at vibrational level. These bonds were assigned by comparing the calculated wavenumbers with the observed wavenumbers in the IR spectra. These breaking bonds are assimilated with a Morse oscillator  $^{28,37,38}$  coupled nonlinear with the harmonic oscillators of the thermic field. Following a theoretical treatment developed by Vlase et al., the relationship between the average phase transformation temperature peak in four DTA curves ( $T_{\rm ap}$ , K) and the wavenumber of the activated bond is given as follows:

$$\omega = \frac{k_b}{hc} T_{ap} = 0.695 T_{ap} \tag{8}$$

where c is the light velocity. Because the breaking bond has an unharmonic behavior, the specific activation is possible also due to more than one quanta, or by a higher harmonic:  $\omega_{\rm sp} = q \omega_{\rm calc}$ ,  $q \in N=1,2,3...$ , where  $\omega_{\rm sp}$  is the assigned spectroscopic number for the bond supposed to break, which relates to the evolved gas in the thermal decomposition step. In this Article, we suggested the maximum peak temperature  $T_{\rm ap}$  in the DTA curve for the calculated wavenumbes  $(\omega_{\rm sp})$  according to eq 8. Therefore, the use of  $T_{\rm p}$  (DTA) will be an alternative method for the calculated wave numbers for identification in each thermal transition step of interesting materials.

#### 3. RESULTS AND DISCUSSION

**3.1. Synthesis and Characterization.** According to the chemical analysis data, the P/(Mn + Fe) = 2.01 and  $H_2O/P = 1.82$  molar ratios in the synthesized phosphate differed very little from those calculated for binary metal dihydrogenphosphate

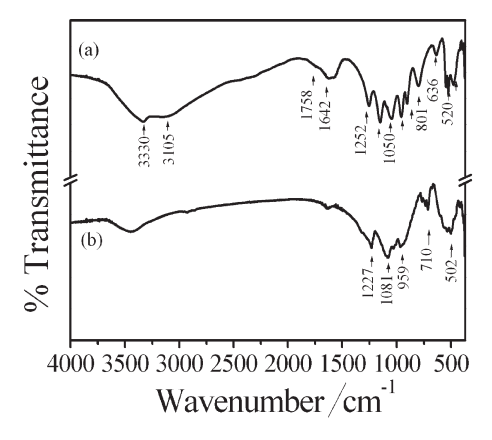


Figure 2. FTIR spectra of  $Mn_{1/2}Fe_{1/2}(H_2PO_4)_2 \cdot 2H_2O$  (a) and MnFeP<sub>4</sub>O<sub>12</sub> (b).

with the general formula  $Mn_{1/2}Fe_{1/2}(H_2PO_4)_2 \cdot 2H_2O$ . Similarly, the P/(Mn + Fe) = 1.98 molar ratio in the decomposed product practically corresponds to the MnFeP<sub>4</sub>O<sub>12</sub> stoichiometry, where Mn(II) and Fe(II) stand for divalent cations.

Figure 1 shows the TG-DTG-DTA curves of  $Mn_{1/2}Fe_{1/2}$  ( $H_2PO_4$ )<sub>2</sub>· $2H_2O$ . The TG curve of  $Mn_{1/2}Fe_{1/2}(H_2PO_4)_2$ · $2H_2O$  relating to the elimination of water molecules shows two well-defined mass loss stages in the range of 303-873 K. These two steps in the TG curve observed in the ranges of 373-423 and 473-673 K appear in the respective DTG and DTA as two endothermic peaks (383 and 499 K). The corresponding observed mass losses of 11.86 (1.89 mol of  $H_2O$ ) and 11.73 (1.86 mol of  $H_2O$ ) % by mass are assigned to the dehydration of coordination water molecules (eq 9) and an intramolecular dehydration of the protonated dihydogenphosphate groups (eq 10), respectively. The total mass loss of 23.58% (3.74 mol  $H_2O$ ) is in agreement with those reported for other binary dihydrogenphosphate dihydrate in the literature (1 < mole of water < 4). The thermal decomposition process of  $Mn_{1/2}Fe_{1/2}(H_2PO_4)_2 \cdot 2H_2O$  could be formally presented as:

$$\begin{array}{c} Mn_{1/2}Fe_{1/2}(H_{2}PO_{4})_{2} \cdot 2H_{2}O \xrightarrow{373-423 \text{ K}} Mn_{1/2}Fe_{1/2} \\ (H_{2}PO_{4})_{2} + 2H_{2}O \end{array} \tag{9}$$

$$Mn_{1/2}Fe_{1/2}(H_2PO_4)_2 \xrightarrow{473-673 \text{ K}} 1/2MnFeP_4O_{12} + 2H_2O$$
(10)

A stable intermediate compound, acid polyphosphate  $Mn_{1/2}Fe_{1/2} (H_2PO_4)_2$ , has been registered. This intermediate is similarly observed with other binary dihydrogen phosphates, as it is isostructural. <sup>1-9</sup> The plateau formed between 673 and 873 K on the TG curve indicated the formation of binary manganese iron cyclotetraphosphate,  $MnFeP_4O_{12}$ , as the final decomposed product. The thermal stability, mechanism, and phase transition temperature of the synthesized  $Mn_{1/2}Fe_{1/2}(H_2PO_4)_2 \cdot 2H_2O$  in water—acetone medium of this work are significantly different from those of  $Mn(H_2PO_4)_2 \cdot 2H_2O$ , <sup>40</sup>  $Fe(H_2PO_4)_2 \cdot 2H_2O$ , <sup>41</sup> and  $Mn_{0.5}Fe_{0.5}(H_2PO_4)_2 \cdot xH_2O$  synthesized without media agents. The obtained results are similar to those of the  $Mn(H_2PO_4)_2 \cdot 2H_2O^{22}$  synthesized by water—acetone medium reported in our previous works. On the basis of thermal results, we can conclude that the different thermal behaviors are caused by the

different interaction and position of Mn and Fe metals in the skeleton, the medium reagents, and reaction condition for precipitation.

The FT-IR spectra of  $Mn_{1/2}Fe_{1/2}(H_2PO_4)_2 \cdot 2H_2O$  (Figure 2a) and MnFeP<sub>4</sub>O<sub>12</sub> (Figure 2b) are very similar to those of  $M(H_2PO_4)_2 \cdot 2H_2O$  and  $M_2P_4O_{12}$  (M = Mn or Fe), respectively.  $^{1,2,18,22,40,41}$  The band position are shifted to the values between those of individual M(H<sub>2</sub>PO<sub>4</sub>)<sub>2</sub>·2H<sub>2</sub>O and M<sub>2</sub>P<sub>4</sub>O<sub>12</sub> (M = Mn or Fe), and sharp or weak bands are observed, indicating the inserting of different metal cations (Mn and Fe) in the skeleton. Consequently, vibrational bands are identified in relation to the crystal structure in terms of the fundamental vibrating units,  $H_2PO_4^-$  and  $H_2O$  for  $Mn_{1/2}Fe_{1/2}$ - $(H_2PO_4)_2 \cdot 2H_2O$  and  $[P_4O_{12}]^{4-}$  ion for  $MnFeP_4O_{12}$ , and are assigned according to the literature.  $^{1,2,18,42}$  It is known that the existence of short OH···O hydrogen bonds in a variety of strongly hydrogen-bonded solids is manifested by the appearance of the characteristic ABC structure of the  $\nu(OH)$  vibration. Usually, the ABC bands are very broad and consist of many ill-resolved components. The strongest band (A) is located in the 3100-2700 cm<sup>-1</sup> region, the B band appears at about 2600-2400 cm<sup>-1</sup>, and the C band is around 1700-1600 cm<sup>-1</sup>. The problem of the origin of the ABC trio is discussed in many studies on acidic salts, but an explanation of this behavior of strongly hydrogen-bonded systems is still to be found. One of the most popular interpretations of the ABC trio suggests a strong Fermi resonance between the  $\nu(OH)$  stretching fundamentals and the overtones [2 $\delta$ (OH) and 2 $\gamma$ (OH)] or combinations involving the  $\delta({\rm OH})$  and  $\gamma({\rm OH})$  vibrations.  $^{1,2,18,22}$  The second type of characteristic vibrations is associated with the phosphate groups. The stretching P-O and bending OPO vibrations of the phosphate groups appear in the ranges of 920–990 cm<sup>-1</sup> ( $\nu_1$ ), 990–1160 cm<sup>-1</sup> ( $\nu_3$ ), 460–375 cm<sup>-1</sup> ( $\nu_2$ ), and 460–650 cm<sup>-1</sup> ( $\nu_4$ ). In addition to the internal PO<sub>4</sub> vibrations, other vibrations involving OH motions are the characteristic of the protonated phosphate ions (H<sub>2</sub>PO<sub>4</sub><sup>-</sup>), both out-of-plane  $\delta(OH)$  and in-plane  $\gamma(OH)$  bending P-O-H vibrations, which appear at 1252 and 801 cm<sup>-1</sup>, respectively. The third spectra feature in the FTIR spectrum (Figure 2a) of  $Mn_{1/2}Fe_{1/2}(H_2PO_4)_2 \cdot 2H_2O$  is the water molecule vibrations. The  $\nu_{\rm OH}$  stretching modes of HOH appear at 3105 cm<sup>-1</sup> ( $\nu_{\rm 1}$  or band A) and 3330 cm<sup>-1</sup> ( $\nu_{\rm 3}$ ). The doublet bands (1642 and 1570 cm<sup>-1</sup>) contribute both to the band C and to the water bending band.<sup>2</sup> A weak band around 639 cm<sup>-1</sup> could be tentatively assigned to the rocking mode involving water librations.

The vibrational modes of  $P_4O_{12}^{4-}$  ion observed in the frequency range  $370-1400~\rm cm^{-1}$  (Figure 2b) are assigned according to the literature. The  $P_4O_{12}^{4-}$  anion contains the  $PO_2^{2-}$  radical and the P-O-P bridge, which are interpreted in the FTIR spectra from the viewpoint of the vibrations of these two groups. As the P-O bond strength in the P-O-P bridge is weaker than in the  $PO_2^{2-}$  radical, the stretching frequencies of the P-O-P bridge are expected to be lower than those in the  $PO_2^{2-}$  radical. The asymmetric and symmetric stretching frequencies of the  $PO_2^{2-}$  radical are generally observed in the areas of  $1350-1220~\rm and$   $1150-1100~\rm cm^{-1}$ , respectively. The P-O-P bridge has its asymmetric and symmetric stretching frequencies around  $1000-900~\rm and$   $900-700~\rm cm^{-1}$ , respectively. The bending modes are expected in the area of  $600-400~\rm cm^{-1}$  ( $PO_2^{2-}$  radical) and  $400-370~\rm cm^{-1}$  (P-O-P bridge). The metal-O stretching usually appears in the bending mode region as the bending modes of the P-O-P bridge and absorption

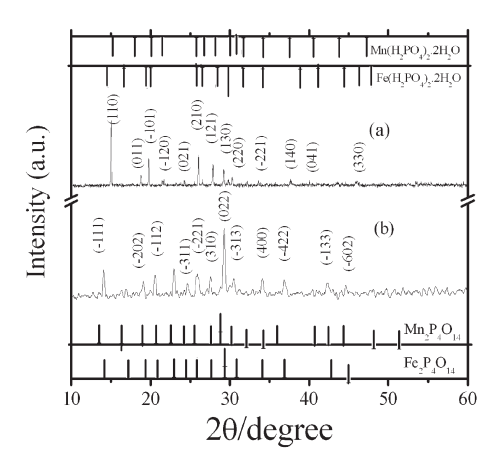


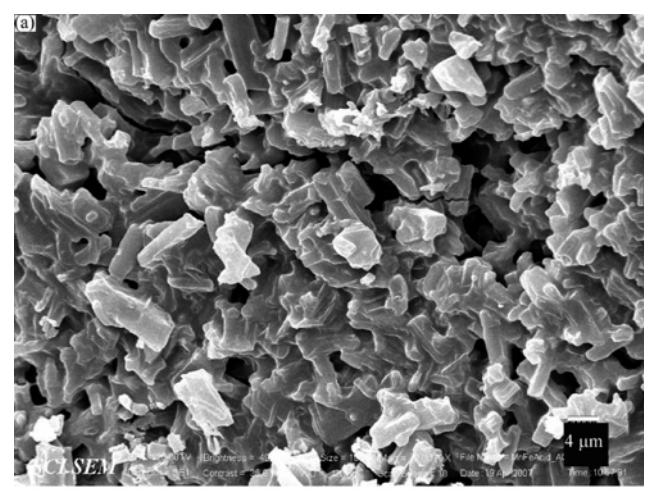
Figure 3. XRD patterns of  $Mn_{1/2}Fe_{1/2}(H_2PO_4)_2\cdot 2H_2O$  (a) and  $MnFeP_4O_{12}$  (b).

bands associated with these vibrations are usually very weak. The observation of a strong  $\nu_{\rm s} {\rm POP}$  band is known to be the most striking feature of the cyclotetraphosphate spectra, along with the presence of the  $\nu_{\rm as} {\rm OPO}^-$  band, which confirmed that the crystal structure is monoclinic (space group C2/c) with a cyclic structure of the  $\left[ {\rm P_4O_{12}} \right]^{4-}$  anion. <sup>42</sup>

Figure 3 shows the XRD patterns of Mn<sub>1/2</sub>Fe<sub>1/2</sub>(H<sub>2</sub>- $PO_4$ )<sub>2</sub>·2H<sub>2</sub>O and the decomposed product MnFeP<sub>4</sub>O<sub>12</sub>, which are similar to those obtained from the individual compounds  $(M(H_2PO_4)_2 \cdot 2H_2O)$  and  $M_2P_4O_{12}$  (M = Mn) and  $Fe)^{1,2,22,40,41}$ and the binary compounds  $(Mn_{0.5}Fe_{0.5}(H_2PO_4)_2 \cdot xH_2O)$  and  $MnFeP_4O_{12}$  in our previous work, <sup>18</sup> but the intensities are slightly different. The lower and higher intensities of XRD peaks indicate the differences of crystallization or amorphous phase as well as particle sizes of these materials. According to the hypothesis of isostructural, the systems of binary manganese iron solid solutions and individual metal dihydrogenphosphate (or manganese iron cyclotetraphosphate) show quite a similarity of the XRD peaks because the electronic charges of cations are equivalent and the radii of cations are close to each other. As compared to the published XRD data of the individual metal compounds (Mn( $H_2PO_4$ )<sub>2</sub>·2 $H_2O$  (PDF# 350010), Fe( $H_2$ - $PO_4$ )<sub>2</sub>·2H<sub>2</sub>O (PDF# 390699),  $Mn_2P_4O_{12}$  (PDF# 380314), and Fe<sub>2</sub>P<sub>4</sub>O<sub>12</sub> (PDF# 760223), both studied samples can be assigned to the  $Mn_{1/2}Fe_{1/2}(H_2PO_4)_2 \cdot 2H_2O$  and  $MnFeP_4O_{12}$ product, which are solid solutions and not a mixture of the individual ones. Consequently, all the reflections can be distinctly indexed as a pure monoclinic phase with space group  $P2_1/n$  (Z=2) for  $Mn_{1/2}Fe_{1/2}(H_2PO_4)_2 \cdot 2H_2O$  and C2/c (Z = 4) for the decomposed MnFeP<sub>4</sub>O<sub>12</sub>, which noted that these XRD patterns agreed well with those of standard data of  $M(H_2PO_4)_2 \cdot 2H_2O$ and  $M_2P_4O_{12}$  (M = Mn or Fe), respectively. The average crystallite sizes and lattice parameters of  $Mn_{1/2}Fe_{1/2}(H_2-$ PO<sub>4</sub>)<sub>2</sub>·2H<sub>2</sub>O and the decomposed product MnFeP<sub>4</sub>O<sub>12</sub> were calculated from XRD patterns and also tabulated in Table 1. The lattice parameters of Mn<sub>1/2</sub>Fe<sub>1/2</sub>(H<sub>2</sub>PO<sub>4</sub>)<sub>2</sub>·2H<sub>2</sub>O are larger than those of the standard data of  $Mn(H_2PO_4)_2 \cdot 2H_2O$  (PDF# 350010) and  $Fe(H_2PO_4)_2 \cdot 2H_2O$  (PDF# 390699). However, the lattice parameters of the decomposed MnFeP<sub>4</sub>O<sub>12</sub> are found to range between those of the standard data of  $Mn_2P_4O_{12}$  (PDF# 380314) and  $Fe_2P_4O_{12}$  (PDF# 760223). The average crystallite size of  $Mn_{1/2}Fe_{1/2}(H_2PO_4)_2 \cdot 2H_2O$  is larger than that of the calcined MnFeP<sub>4</sub>O<sub>12</sub>, which resulted from two decomposition

Table 1. Average Crystallite Sizes and Lattice Parameters of  $Mn(H_2PO_4)_2 \cdot 2H_2O$ ,  $Mn_{1/2}Fe_{1/2}(H_2PO_4)_2 \cdot 2H_2O$ ,  $Fe(H_2PO_4)_2 \cdot 2H_2O$ , and the Calcined Product MnFeP<sub>4</sub>O<sub>12</sub> Calculated from XRD Data

compound	a (Å)	b (Å)	c (Å)	$\beta$ (deg)	average crystallite size (nm)
PDF# 350010 (Mn(H <sub>2</sub> PO <sub>4</sub> ) <sub>2</sub> ·2H <sub>2</sub> O)	7.32	10.08	5.37	94.75	
this work $ (Mn_{1/2}Fe_{1/2}(H_2PO_4)_2 \cdot H_2O) $	7.90(0)	11.03(6)	6.10 (3)	95.04(6)	79 ± 11
PDF# 390699 (Fe(H <sub>2</sub> PO <sub>4</sub> ) <sub>2</sub> ·2H <sub>2</sub> O)	7.31	9.94	5.37	95.24	
PDF# 380314 (Mn <sub>2</sub> P <sub>4</sub> O <sub>12</sub> )	11.88	8.59	10.14	119.21	
this work $(MnFeP_4O_{12})$	12.06(8)	8.48(2)	10.12(4)	119.12(5)	$62 \pm 13$
PDF# 760223 (Fe <sub>2</sub> P <sub>4</sub> O <sub>12</sub> )	11.94	8.37	9.94	118.77	



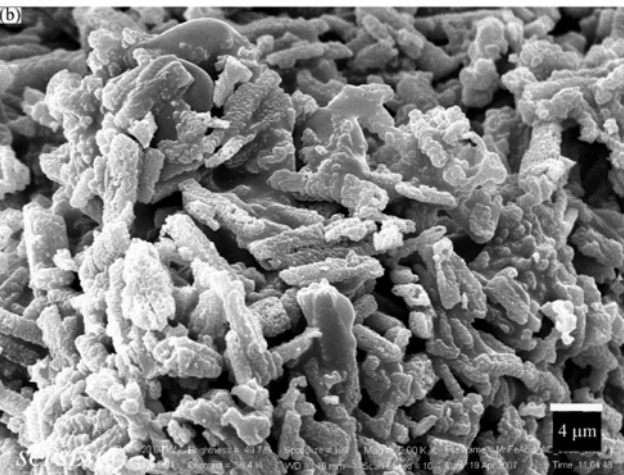


Figure 4. SEM micrographs of  $Mn_{1/2}Fe_{1/2}(H_2PO_4)_2 \cdot 2H_2O$  (a) and  $MnFeP_4O_{12}$  (b).

processes. The crystallite sizes of  $79\pm11$  nm for  $Mn_{1/2}Fe_{1/2}-(H_2PO_4)_2\cdot 2H_2O$  and  $62\pm13$  nm for  $MnFeP_4O_{12}$  in this work are smaller than those prepared from  $Mn(c)-Fe(c)-H_3PO_4$  without the medium system reported by Boonchom et al. (81  $\pm$  14 nm for  $Mn_{1/2}Fe_{1/2}(H_2PO_4)_2\cdot xH_2O$  and  $69\pm21$  nm for  $MnFeP_4O_{12}$ ). However, the crystallite sizes for both binary compounds in this work are larger than those from the single

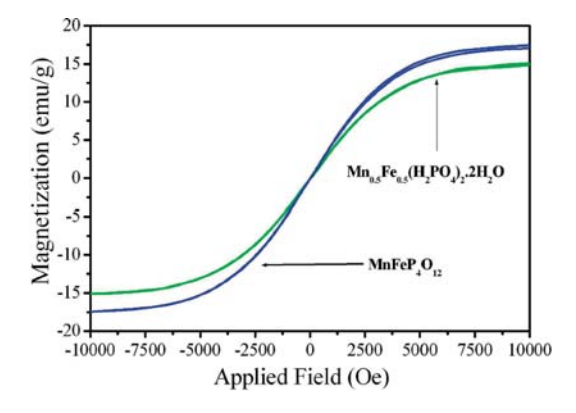


Figure 5. The specific magnetizations of  $Mn_{1/2}Fe_{1/2}(H_2PO_4)_2 \cdot 2H_2O$  and  $MnFeP_4O_{12}$  as a function of field, measured at 293 K.

metal compounds (52  $\pm$  14 nm for Mn(H<sub>2</sub>PO<sub>4</sub>)<sub>2</sub> · 2H<sub>2</sub>O, 28  $\pm$  4 nm for Fe(H<sub>2</sub>PO<sub>4</sub>)<sub>2</sub> · 2H<sub>2</sub>O, 29  $\pm$  9 nm for Mn<sub>2</sub>P<sub>4</sub>O<sub>12</sub>, and 27  $\pm$  6 nm for Fe<sub>2</sub>P<sub>4</sub>O<sub>12</sub>) in our previous studies. <sup>22,40,41</sup> These results confirmed that the differences in the crystallite sizes for the synthesized Mn<sub>1/2</sub>Fe<sub>1/2</sub>(H<sub>2</sub>PO<sub>4</sub>)<sub>2</sub> · 2H<sub>2</sub>O and MnFeP<sub>4</sub>O<sub>12</sub> depend on the medium, water, and metal compositions and the condition for precipitations.

The SEM micrographs of  $Mn_{1/2}Fe_{1/2}(H_2PO_4)_2 \cdot 2H_2O$  and  $MnFeP_4O_{12}$  are shown in Figure 4. The particle shape and size are changed throughout the whole decomposition product. The SEM micrograph of  $Mn_{1/2}Fe_{1/2}(H_2PO_4)_2 \cdot 2H_2O$  (Figure 4a) shows nonuniform particles, which appear as high agglomerates. The morphology of  $Mn_{1/2}Fe_{1/2}(H_2PO_4)_2 \cdot 2H_2O$  exhibits features different from those of  $Mn(H_2PO_4)_2 \cdot 2H_2O$ ,  $Fe(H_2PO_4)_2 \cdot 2H_2O$ , and  $Mn_{0.5}Fe_{0.5}(H_2PO_4)_2 \cdot xH_2O$  reported in our previous works.  $^{18,40,41}$  The morphology of  $MnFeP_4O_{12}$  shows a high agglomerate of nonuniform particles, which is not similar that for  $M_2P_4O_{12}$  (M=Mn or Fe) (Figure 4b) in the work previously reported.  $^{18,40,41}$  The high agglomerates of  $Mn_{1/2}Fe_{1/2}(H_2PO_4)_2 \cdot 2H_2O$  and  $MnFeP_4O_{12}$  powders are possibly caused by the process of dissolution and a rapid coprecipitation as well as the dehydration process.

Magnetization curves (M−H loop) of Mn<sub>1/2</sub>Fe<sub>1/2</sub>(H<sub>2</sub>-PO<sub>4</sub>)<sub>2</sub>·2H<sub>2</sub>O and the decomposed MnFeP<sub>4</sub>O<sub>12</sub> powders obtained from room temperature VSM measurements are shown in Figure 5. Both samples demonstrate typical superparamagnetic behavior with negligible coercivity and remanence, in accordance

Table 2. Values of Thermodynamics, Kinetics, and Spectroscopic Data for Two Decomposition Steps of  $Mn_{1/2}Fe_{1/2}(H_2PO_4)_2 \cdot 2H_2O$ 

step	$\Delta G^*/\mathrm{kJ}\;\mathrm{mol}^{-1}$	$\Delta H^*/\mathrm{kJ~mol}^{-1}$	$\Delta S^*/J \text{ mol}^{-1} \text{ K}^{-1}$	$A/s^{-1}$	$E_{\rm a}/{\rm kJ~mol}^{-1}$	$R^2$	$T_{\rm ap}/{ m K}$	$\omega_{ m cal}$	q	$q\omega_{\rm cal}/{ m cm}^{-1}$	band assignment
1	712.34	1119.78	105.46	$3.88\times10^{20}$	115.19	0.9995	386	268	2	537	$v_4  ({\rm PO_4}^{3-})$
									3	805	γ (OH)
									4	1074	$v_{\rm as}~({\rm PO}_2)$
									6	1611	$v_2$ (H <sub>2</sub> O)
									9	2416	B band $(H_2PO_4^-)$
									11	2953	A band $(H_2PO_4^-)$
									12	3222	$v_1 (H_2O)$
									13	2490	$\nu_3$ (H <sub>2</sub> O)
2	931.60	1883.50	188.69	$1.13 \times 10^{20}$	192.54	0.9971	504	350	2	701	$\nu$ (P-O <sub>h</sub> )
									3	1051	$\nu_{\rm s}~({ m PO}_2)$
									5	1753	C band $(H_2PO_4^-)$
									7	2454	B band $(H_2PO_4^{})$
									9	3155	A band $(H_2PO_4^{})$

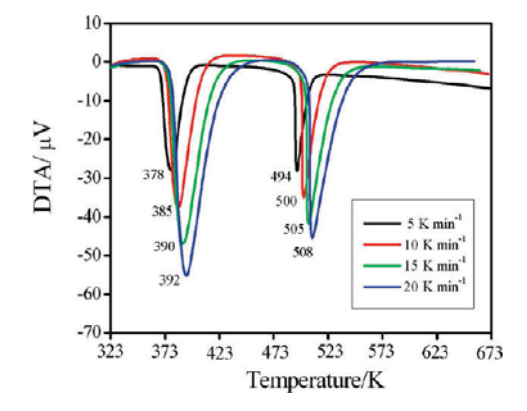


**Figure 6.** DTA curves of the synthesized  $Mn_{1/2}Fe_{1/2}(H_2PO_4)_2 \cdot 2H_2O$  at four different heating rates (5, 10, 15, and 20 K min<sup>-1</sup>).

with the theory that superparamagnetic behavior is often observed at room temperature.  $^{43-45}$  The specific magnetization curves are typical superparamagnetic behavior without any hysteresis in the field range of  $\pm 10\,000$  Oe. From the magnetization curves, specific saturated magnetization  $(M_s)$  values of the  $Mn_{1/2}Fe_{1/2}$  $(H_2PO_4)_2 \cdot 2H_2O$  and MnFeP<sub>4</sub>O<sub>12</sub> are 15.097 and 17.459 emu/g, respectively. The superparamagnetic solid solutions formed in  $Mn_{1/2}Fe_{1/2}(H_2PO_4)_2 \cdot 2H_2O$  and  $MnFeP_4O_{12}$  system in this work are different from ferromagnetic for Fe(H<sub>2</sub>PO<sub>4</sub>)<sub>2</sub>·2H<sub>2</sub>O (96.28 emu/g) and FeP<sub>4</sub>O<sub>12</sub> (85.01 emu/g),<sup>41</sup> and Mn<sub>1/2</sub>Fe<sub>1/2</sub>-found that the tendency of  $M_s$  to increase is consistent with the enhancement of crystallinity or particle sizes, and the saturation values of  $M_s$  for  $Mn_{1/2}Fe_{1/2}(H_2PO_4)_2 \cdot 2H_2O$  and  $MnFeP_4O_{12}$ are observed due to the obtained microstructure. These results indicate that the medium reagents for precipitation have the strong effect on the magnetic behaviors of Mn<sub>1/2</sub>Fe<sub>1/2</sub>-(H<sub>2</sub>PO<sub>4</sub>)<sub>2</sub>·2H<sub>2</sub>O and MnFeP<sub>4</sub>O<sub>12</sub>. Superparamagnetic properties of the Mn<sub>1/2</sub>Fe<sub>1/2</sub>(H<sub>2</sub>PO<sub>4</sub>)<sub>2</sub>·2H<sub>2</sub>O and MnFeP<sub>4</sub>O<sub>12</sub> samples reported for the first time are important for specific applications because the magnetic materials may be synthesized to have the multifunctions that can be applied in magnetic resonance imaging contrast agents, data lifetime in high density information storage, ferrofluid technology,

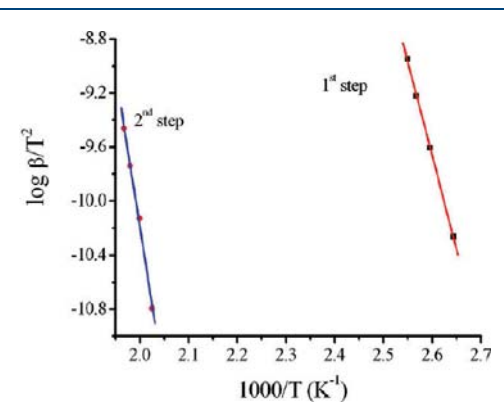


Figure 7. Kissinger plots indicating the activation energies involving two transformation steps from the synthesized  $Mn_{1/2}Fe_{1/2}(H_2PO_4)_2 \cdot 2H_2O$  to  $MnFeP_4O_{12}$ .

lithium batteries, magnetocaloric refrigeration catalytic, and/or adsorption processes. 45

3.2. Kinetic and Thermodynamic Results. The nonisothermal DTA method is desirable to analyze the reaction mechanism and calculate the activation energy of the solid state. 26-32 Several nonisothermal techniques have been proposed, which are quicker and less sensitive to previous and next transformations. The basic data of T were collected from the DTA curves of the decomposition of  $Mn_{1/2}Fe_{1/2}(H_2PO_4)_2 \cdot 2H_2O$  at various heating rates (5, 10, 15, and 20 K min<sup>-1</sup>) (Figure 6). Figure 7 shows the Kissinger plots of two transformation steps of the prepared  $Mn_{1/2}Fe_{1/2}(H_2PO_4)_2 \cdot 2H_2O$ . From the slopes of the curves (Figure 7), the activation energy values in two decomposition steps of the synthesized  $Mn_{1/2}Fe_{1/2}(H_2PO_4)_2 \cdot 2H_2O$  were determined as 115.19 and 192.54 kJ  $mol^{-1}$ , respectively. The activation energies of two decompositions of Mn<sub>1/2</sub>Fe<sub>1/2</sub>-(H<sub>2</sub>PO<sub>4</sub>)<sub>2</sub>·2H<sub>2</sub>O are different from those of Mn(H<sub>2</sub>PO<sub>4</sub>)<sub>2</sub>·  $2H_2O$  (105–104 kJ/mol for the first step and 199–200 kJ/ mol for the second step) and  $Fe(H_2PO_4)_2 \cdot 2H_2O(136-137 \text{ kJ/}$ mol for the first step). These activation energies are related to the vibrational frequencies and are the indication of the energy of the breaking bond of intermediate species. The reason may be relevant to the strengths of binding of water molecules in the crystal lattice. Hence, different dehydration temperatures and kinetic parameters are expected. The two mass loss steps

Table 3. Comparing Physical and Chemical Properties of the Studied Materials in the Present Work and in the Literature

ref no.	materials	different synthesis route
this work	$\rm Mn_{1/2}Fe_{1/2}(H_2PO_4)_2\!\cdot\!2H_2O$ and $\rm MnFeP_4O_{12}$	prepared by Mn(c)—Fe(c)—H <sub>3</sub> PO <sub>4</sub> system in water—acetone medium at ambient temperature for 30 min, and its final decomposed product was obtained at 773 K
17	$\rm Mn_{0.5}Co_{0.5}(H_2PO_4)_2{\boldsymbol\cdot}2H_2O$ and $\rm MnCoP_4O_{12}$	prepared by MnCO <sub>3</sub> -CoCO <sub>3</sub> -H <sub>3</sub> PO <sub>4</sub> system at ambient temperature for 15 min,
10	M E (UPO) AUO IMERO	and its final decomposed product was obtained at 773 K
18	$Mn_{0.5}Fe_{0.5}(H_2PO_4)_2 \cdot 2H_2O$ and $MnFeP_4O_{12}$	prepared by $\rm Mn(c)-Fe(c)-H_3PO_4$ system at ambient temperature for 30 min, and its final decomposed product was obtained at 773 K
19	$Co_{1/2}Fe_{1/2}(H_2PO_4)_2 \cdot 2H_2O$ and $CoFeP_4O_{12}$	prepared by $Fe(c)-CoCO_3-H_3PO_4$ system at ambient temperature for 15 min, and its final decomposed product was obtained at 773 K
20	$Mn_{0.5}Cu_{0.5}(H_2PO_4)_2\!\cdot\!1.5H_2O$ and $MnCuP_4O_{12}$	prepared by $Mn(c)$ — $CuO$ — $H_3PO_4$ system at ambient temperature for 15 min, and its final decomposed product was obtained at 673 K
21	$\rm Mn_{0.5}Ca_{0.5}(H_2PO_4)_2\!\cdot\!H_2O$ and $\rm MnCaP_4O_{12}$	prepared by Mn(c)—CaCO <sub>3</sub> —H <sub>3</sub> PO <sub>4</sub> system at ambient temperature for 30 min, and its final decomposed product was obtained at 673 K
22	$Mn(H_2PO_4)_2 \cdot 2H_2O$ and $Mn_2P_4O_{12}$	prepared by $Mn(c)$ – $H_3PO_4$ system in water—acetone medium at ambient temperature
		for 15 min, and its final decomposed product was obtained at 773 K
40	$Mn(H_2PO_4)_2\!\cdot\! 2H_2O$ and $Mn_2P_4O_{12}$	prepared by $\rm Mn(c) - \rm H_3PO_4$ and $\rm MnCO_3 - \rm H_3PO_4$ systems at ambient temperature
		for 15 min, and its final decomposed product was obtained at 673 $\mbox{\scriptsize K}$
41	$Fe(H_2PO_4)_2 \cdot 2H_2O$ and $Fe_2P_4O_{12}$	prepared by $Fe(c)$ — $H_3PO_4$ system at 313 K for 30 min, and its final decomposed production was obtained at 773 K
ref no.	materials	different thermal behavior
this work	$Mn_{1/2}Fe_{1/2}(H_2PO_4)_2 \cdot 2H_2O$ and $MnFeF$	$^{2}4O_{12}$ well-defined two thermal transformation steps in the range of 353–873 K
17	$\mathrm{Mn}_{0.5}\mathrm{Co}_{0.5}(\mathrm{H}_{2}\mathrm{PO}_{4})_{2}\!\cdot\!2\mathrm{H}_{2}\mathrm{O}$ and $\mathrm{MnCoF}$	
18	$Mn_{0.5}Fe_{0.5}(H_2PO_4)_2 \cdot 2H_2O$ and $MnFeP_4$	
19	$Co_{1/2}Fe_{1/2}(H_2PO_4)_2 \cdot 2H_2O$ and $CoFeP_4$	
20	$Mn_{0.5}Cu_{0.5}(H2PO_4)_2 \cdot 1.5H_2O$ and $MnC$	
21	$Mn_{0.5}Ca_{0.5}(H_2PO_4)_2 \cdot H_2O$ and $MnCaP_4$	
22	$Mn(H_2PO_4)_2 \cdot 2H_2O$ and $Mn_2P_4O_{12}$	well-defined two thermal transformation steps in the range of 353-1073
40	$Mn(H_2PO_4)_2 \cdot 2H_2O$ and $Mn_2P_4O_{12}$	more than three thermal transformation steps in the range of 353 $-773~\mathrm{K}$
41	$Fe(H_2PO_4)_2 \cdot 2H_2O$ and $Fe_2P_4O_{12}$	three thermal transformation steps in the range of $353-773~\mathrm{K}$
ref no.	materials	different morphologies
this work	$Mn_{1/2}Fe_{1/2}(H_2PO_4)_2 \cdot 2H_2O$ and $MnFeP_4O_{12}$	high agglomerates of nonuniform particles for both samples
17	$Mn_{0.5}Co_{0.5}(H_2PO_4)_2 \cdot 2H_2O$ and $MnCoP_4O_{12}$	rod-like shape and nonuniform particles
18	$Mn_{0.5}Fe_{0.5}(H_2PO_4)_2 \cdot 2H_2O$ and $MnFeP_4O_{12}$	rod-like tetrahedral shape and small spherical particles with high agglomerates
19	$Co_{1/2}Fe_{1/2}(H_2PO_4)_2 \cdot 2H_2O$ and $CoFeP_4O_{12}$	flower like shape for both samples
20	$Mn_{0.5}Cu_{0.5}(H_2PO_4)_2 \cdot 1.5H_2O$ and $MnCuP_4O_{12}$	many small and some large rod like and spherical shapes
21	Mn <sub>0.5</sub> Ca <sub>0.5</sub> (H <sub>2</sub> PO <sub>4</sub> ) <sub>2</sub> ·H <sub>2</sub> O and MnCaP <sub>4</sub> O <sub>12</sub>	roughness of many small and some large boundary surfaces and small and large spherical shape
22	Mn(H <sub>2</sub> PO <sub>4</sub> ) <sub>2</sub> ·2H <sub>2</sub> O and Mn <sub>2</sub> P <sub>4</sub> O <sub>12</sub>	small rod like shape and retexturing and coalescence in aggregates of irregularly shape
40	$Mn(H_2PO_4)_2 \cdot 2H_2O$ and $Mn_2P_4O_{12}$	large nonuniform polyhedral shape and retexturing and coalescence in aggregates of irregularly shape
41	$Fe(H_2PO_4)_2\!\cdot\! 2H_2O$ and $Fe_2P_4O_{12}$	coalescence in aggregates of irregularly shapes for both samples
ref no.	materials	different magnetic properties
this work	$Mn_{1/2}Fe_{1/2}(H_2PO_4)_2 \cdot 2H_2O$ and $MnFeP_4O_{12}$	superparamagnetic properties ( $M_s$ = 15.097 emu/g for Mn <sub>1/2</sub> Fe <sub>1/2</sub> (H <sub>2</sub> PO <sub>4</sub> ) <sub>2</sub> ·2H <sub>2</sub> O and $M_s$ = 17.459 emu/g for MnFeP <sub>4</sub> O <sub>12</sub>
17	$Mn_{0.5}Co_{0.5}(H_2PO_4)_2 \cdot 2H_2O$ and $MnCoP_4O_{12}$	not reported
18	$Mn_{0.5}Fe_{0.5}(H_2PO_4)_2 \cdot xH_2O$ and $MnFeP_4O_{12}$	ferromagnetic properties ( $M_s$ = 25.63 emu/g for Mn <sub>0.5</sub> Fe <sub>0.5</sub> (H <sub>2</sub> PO <sub>4</sub> ) <sub>2</sub> · $x$ H <sub>2</sub> O and $M_s$ = 13.14 emu/g for MnFeP <sub>4</sub> O <sub>12</sub> )
19	$\mathrm{Co}_{1/2}\mathrm{Fe}_{1/2}(\mathrm{H}_2\mathrm{PO}_4)_2\!\cdot\!2\mathrm{H}_2\mathrm{O} \text{ and } \mathrm{CoFeP}_4\mathrm{O}_{12}$	superparamagnetic properties ( $M_s$ = 0.045 emu/g for $Co_{1/2}Fe_{1/2}(H_2PO_4)_2 \cdot 2H_2O$ and $M_s$ = 12.502 emu/g for $CoFeP_4O_{12}$ )
20	$\rm Mn_{0.5}Cu_{0.5}(H_2PO_4)_2\!\cdot\!1.5H_2O$ and $\rm MnCuP_4O_{12}$	not reported
21	Mn <sub>0.5</sub> Ca <sub>0.5</sub> (H <sub>2</sub> PO <sub>4</sub> ) <sub>2</sub> ·H <sub>2</sub> O and MnCaP <sub>4</sub> O <sub>12</sub>	not reported
21	14110.5 Ca0.5(1121 O4)2 112O and 1411 Car 4O12	not reported

Table 3. Continued

	ittiliueu	
ref no.	materials	different magnetic properties
40	$Mn(H_2PO_4)_2 \cdot 2H_2O$ and $Mn_2P_4O_{12}$	not reported
41	$Fe(H_2PO_4)_2\!\cdot\!2H_2O$ and $Fe2P_4O_{12}$	ferromagnetic properties ( $M_s$ = 96.28 emu/g for Fe(H <sub>2</sub> PO <sub>4</sub> ) <sub>2</sub> · $x$ H <sub>2</sub> O and $M_s$ = 37.78 emu/g for Fe <sub>2</sub> P <sub>4</sub> O <sub>12</sub> )
ref no.	materials	different nonisothermal decomposition kinetic data $(E_a, A, n)$
this work	$\text{Mn}_{1/2}\text{Fe}_{1/2}(\text{H}_2\text{PO}_4)_2\!\cdot\!2\text{H}_2\text{O}$ and $\text{MnFeP}_4\text{O}_{12}$	$115.19~kJ~mol^{-1}, 3.88\times10^{15}~s^{-1}, 2.56~for~first~step~and~192.54~kJ~mol^{-1}, 1.13\times10^{20}~s^{-1}, 2.06~for~second~step$
17	$\rm Mn_{0.5}Co_{0.5}(H_2PO_4)_2\!\cdot\! 2H_2O$ and $\rm MnCoP_4O_{12}$	$E_{\rm a}$ values for four steps as 100.55, 88.90, 90.58, 308.58 kJ mol $^{-1}$ , respectively
18	$Mn_{0.5}Fe_{0.5}(H_2PO_4)_2\!\cdot\!2H_2O$ and $MnFeP_4O_{12}$	not reported
19	$\text{Co}_{1/2}\text{Fe}_{1/2}(\text{H}_2\text{PO}_4)_2\!\cdot\!2\text{H}_2\text{O}$ and $\text{CoFeP}_4\text{O}_{12}$	not reported
20	$Mn_{0.5}Cu_{0.5}(H_2PO_4)_2\!\cdot\!1.5H_2O$ and $MnCuP_4O_{12}$	$E_{\rm a}$ and $n$ values for two steps as 99.75, 202.84 kJ mol $^{-1}$ and 1.34, 1.93, respectively
21	$\mathrm{Mn}_{0.5}\mathrm{Ca}_{0.5}(\mathrm{H}_2\mathrm{PO}_4)_2\!\cdot\!\mathrm{H}_2\mathrm{O}$ and $\mathrm{Mn}\mathrm{CaP}_4\mathrm{O}_{12}$	$E_{\rm a}$ values for five steps as 147.85, 129.70, 89.41, 152.94, 236.97 kJ mol <sup>-1</sup> , respectively, A values for five steps as 1.41 $\times$ 10 <sup>20</sup> , 6.55 $\times$ 10 <sup>16</sup> , 4.48 $\times$ 10 <sup>9</sup> , 4.04 $\times$ 10 <sup>15</sup> , 1.01 $\times$ 10 <sup>20</sup> , respectively
22	$Mn(H_2PO_4)_2\!\cdot\! 2H_2O$ and $Mn_2P_4O_{12}$	$E_{\rm a}$ values for two steps as 86.45, 187.92 kJ ${ m mol}^{-1}$ , respectively
40	$Mn(H_2PO_4)_2 \cdot 2H_2O$ and $Mn_2P_4O_{12}$	not reported
41	$Fe(H_2PO_4)_2 \cdot 2H_2O$ and $Fe_2P_4O_{12}$	$E_{\rm a}$ value as 136.85 kJ mol $^{-1}$
ref no.	materials	different thermodynamic data ( $\Delta H^*$ , kJ mol $^{-1}$ ; $\Delta G^*$ , kJ mol $^{-1}$ ; and $\Delta S^*$ , J mol $^{-1}$ K $^{-1}$ )
this work	$Mn_{1/2}Fe_{1/2}(H_2PO_4)_2 \cdot 2H_2O$ and $MnFeP_4O_{12}$	1119.78, 712, 105.46 for first step and 1883.50, 931.60, 188.69 for second step
17	$\rm Mn_{0.5}Co_{0.5}(H_2PO_4)_2\!\cdot\!2H_2O$ and $\rm MnCoP_4O_{12}$	not reported
18	$Mn_{0.5}Fe_{0.5}(H_2PO_4)_2\!\cdot\!2H_2O$ and $MnFeP_4O_{12}$	not reported
19	$\text{Co}_{1/2}\text{Fe}_{1/2}(\text{H}_2\text{PO}_4)_2\!\cdot\!2\text{H}_2\text{O}$ and $\text{CoFeP}_4\text{O}_{12}$	not reported
20	$Mn_{0.5}Cu_{0.5}(H_2PO_4)_2\!\cdot\!1.5H_2O$ and $MnCuP_4O_{12}$	not reported
21	$\rm Mn_{0.5}Ca_{0.5}(H_2PO_4)_2 \cdot H_2O$ and $\rm MnCaP_4O_{12}$	144.65, 94.38, 130.34 for first step, 126.35, 99.64, 66.18 for second step, 85.50, 119.53-72.26 for
		third step, 148.71, 127.80, 41.10 for fourth step, and 231.85, 155.59, 123.73 for sixth
22	$Mn(H_2PO_4)_2 \cdot 2H_2O$ and $Mn2P_4O_{12}$	not reported
40	$Mn(H_2PO_4)_2 \cdot 2H_2O$ and $Mn_2P_4O_{12}$	not reported
41	$Fe(H_2PO_4)_2 \cdot 2H_2O$ and $Fe_2P_4O_{12}$	not reported

correspond to the loss of water of coordinated water in the first steps, subsequently to a continuous intermolecular polycondensation and the elimination of water of constituent in anion in the second step.  $^{26-28}$  The second step exhibits higher activation energy in comparison with the first step, and this is understandable because this step relates to true P-OH bond breaking, in connection with the polycondensation reaction.  $^{1,2,18,40,41}$  These activation energies are consistent with the former hypothesis that the intermediate nucleates and crystallizes as metastable phase with adequate growth kinetics before the stable phase MnFeP $_4$ O $_{12}$ . This result is consistent with TG-DTG-DTA data as shown in eqs 9 and 10.

The pre-exponential factor (A) can be estimated from the intercept of the plots of eq 2 (Table 2). All calculations were performed using a program compiled by ourselves. The pre-exponential factor (A) values in the Arrhenius equation for solid-phase reactions are expected to be in a wide range (6 or 7 orders of magnitude), even after the effect of surface area is taken into account. The low factors will often indicate a surface reaction, but if the reactions are not dependent on surface area, the low factor may indicate a "tight" complex. The high factors will usually indicate a "loose" complex. Even higher factors (after correction for surface area) can be obtained for complexes having free translation on the surface. Because in many cases the concentrations in solids are not controllable, it would have been convenient if the magnitude of the pre-exponential factor could provide the information for the reaction molecularity. With such bulk decomposition, any molecule is as likely to react with any

others, and no preference is shown toward corners, edges, surface, defects, or sites of previous decomposition. On the basis of these reasons, the thermal decomposition reaction of  $Mn_{1/2}\text{-}Fe_{1/2}(H_2PO_4)_2\cdot 2H_2O$  may be interpreted as "loose complexes" for the first and second steps, which correspond to the proposed mechanism in eqs 9 and 10.

The value of the Avrami exponent provides information regarding the morphology of the growing crystal.  $^{17,20-22,32,34}$  The value of n reflects the mechanism dominating crystallization. Here, smaller n values indicate that the crystallization is dominated by a surface crystallization or that the crystallization dimension is low. On the other hand, larger n values are expected only in case of increasing nucleation rates. For  $\mathrm{Mn_{1/2}Fe_{1/2}(H_2PO_4)_2 \cdot 2H_2O_7}$ , the n values are 2.56 for the first and 2.06 for the second decomposition steps, which are random nucleation and growth of nuclei for both decomposition steps.

As can be seen from Table 2, the entropy of activation ( $\Delta S^*$ ) values for all steps are positive values. It means that the corresponding activated complexes had lower degrees of arrangement than the initial state. Because the decomposition of  $\mathrm{Mn}_{1/2}$ -  $\mathrm{Fe}_{1/2}(\mathrm{H}_2\mathrm{PO}_4)_2 \cdot 2\mathrm{H}_2\mathrm{O}$  proceeds as two consecutive reactions, the formation of the second activated complex passed in situ. In terms of the activated complex theory (transition theory),  $^{35-37}$  a positive value of  $\Delta S^*$  indicates a malleable activated complex that leads to a large number of degrees of freedom of rotation and vibration. A result may be interpreted as a "fast" stage. On the other hand, a negative value of  $\Delta S^*$  indicates a highly ordered

activated complex, and the degrees of freedom of rotation as well as of vibration are less than they are in the nonactivated complex. These results may indicate a "slow" stage.  $^{26-30}$  With respect to these results, the first and second decomposed steps of  $\rm Mn_{1/2}$ -  $\rm Fe_{1/2}(H_2PO_4)_2 \cdot 2H_2O$  may be interpreted as "fast" stages. The positive values of the enthalpy  $\Delta H^*$  are in good agreement with two endothermic effects in the DTA results. The positive values of  $\Delta H^*$  and  $\Delta G^*$  for two stages show that they are connected with the introduction of heat and are nonspontaneous processes. The results of the kinetic and thermodynamic parameters of the second steps are higher than those of the first step, which correspond to that the second step needs a higher energy pathway and a lower rate reaction than the first step.

To corroborate the calculated data with the spectroscopic ones, we drew up the FT-IR spectra of the studied compound (Figure 2). Table 2 shows the comparison of the  $\omega_{\rm calc}$  values with the  $\omega_{\rm sp}$  values determined from this compound, together with the assignments of the corresponding vibrational modes in the literature. These wavenumbers are close to the vibrational modes of water of crystallization and dihydrogen phosphate group (H<sub>2</sub>PO<sub>4</sub> $^-$ ) reported in the literature. The results confirm that the loss of the water of crystallization and deprotonated dihydrogen phosphate group in the first step is followed by a continuous intermolecular polycondensation for the second step. The studied compound exhibited a very good agreement between the calculated wavenumbers from average  $T_{\rm p}$  (DTA) and the observed wavenumbers from IR spectra for the bonds that were suggested to be broken.

#### 4. CONCLUSION

The superparamagntic  $Mn_{1/2}Fe_{1/2}(H_2PO_4)_2 \cdot 2H_2O$  was prepared by a soft solution solid-state reaction from the Mn(c)—Fe-(c)-H<sub>3</sub>PO<sub>4</sub> system in water-acetone medium at ambient temperature with short time consumption (30 min).  $Mn_{1/2}$ -Fe<sub>1/2</sub>(H<sub>2</sub>PO<sub>4</sub>)<sub>2</sub>·2H<sub>2</sub>O decomposes in two steps, which correspond to the loss of water of crystallization in the first step, subsequently to a continuous intermolecular polycondensation and elimination of water of constituent in anion (the second step). Thermal kinetic study results indicate the activation energies, which relate to the vibrational frequencies of the breaking bond of thermal transformation of Mn<sub>1/2</sub>Fe<sub>1/2</sub>- $(H_1PO_4)_2 \cdot 2H_2O$ . The thermal behaviors, morphologies, particle sizes, superparamagnetic properties, kinetic and thermodynamic data of  $Mn_{1/2}Fe_{1/2}(H_2PO_4)_2 \cdot 2H_2O$ , and its thermal transformation product (MnFeP<sub>4</sub>O<sub>12</sub>) in this work are different from those of single metal and binary metal compounds in our previous reports (Table 3). The study results obtained are necessary for elaboration of technology to produce the dihydrogenphosphate and cyclotetraphosphate of transition metals, which may be useful for potential applications as catalytic, ceramic, and biomedical materials, etc.

#### AUTHOR INFORMATION

#### **Corresponding Author**

\*Tel.: +66-7750-6422 ext 4565. Fax: +66-7750-6411. E-mail: kbbanjon@gmail.com, kbbanjon@kmitl.ac.th.

#### ACKNOWLEDGMENT

This work is financially supported by the Thailand Research Fund (TRF) and the Commission on Higher Education (CHE): Research Grant for New Scholar and King Mongkut's Institute of

Technology Ladkrabang Research (KMITL Research), Ministry of Education, Thailand.

#### ■ REFERENCES

- (1) Koleva, V.; Mehandjiev, D. Characterization of  $M(H_2PO_4)_2 \cdot 2H_2O$  (M = Mn, Co, Ni) and their in situ thermal decomposition by magnetic measurements. *Mater. Res. Bull.* **2006**, *41*, 469.
- (2) Koleva, V.; Effenberger, H. Crystal chemistry of M[PO<sub>2</sub>-(OH)<sub>2</sub>]<sub>2</sub>·2H<sub>2</sub>O compounds (M = Mg, Mn, Fe, Co, Ni, Zn, Cd): Structural investigation of the Ni, Zn and Cd salts. *J. Solid State Chem.* **2007**, *180*, 966 and references therein.
- (3) Antraptseva, N. M.; Shchegrov, L. N.; Ponomareva, I. G. Thermolysis features of manganese(II) and zinc dihydrogenphosphate solid solution. *Russ. J. Inorg. Chem.* **2006**, *51*, 1493.
- (4) Trojan, M.; Brandová, D.; Paulik, F.; Arnold, M. Mechanism of the thermal dehydration of Co<sub>1/2</sub>Ca<sub>1/2</sub>(H<sub>2</sub>PO<sub>4</sub>)<sub>2</sub>·2H<sub>2</sub>O. *J. Therm. Anal. Calorim.* **1990**, *36*, 929.
- (5) Trojan, M.; Brandová, D. Mechanism of dehydration of Zn<sub>0.5</sub>Mg<sub>0.5</sub>(H<sub>2</sub>PO<sub>4</sub>)<sub>2</sub>·2H<sub>2</sub>O. *Thermochim. Acta* **1990**, *159*, 1.
- (6) Trojan, M.; Brandová, D. Study of thermal dehydration of  $Mn_{0.5}Mg_{0.5}(H_2PO_4)_2 \cdot 4H_2O$ . Thermochim. Acta 1990, 161, 11.
- (7) Brandová, D.; Trojan, M.; Arnold, M.; Paulik, F. Thermal study of decomposition of  $Cu_{1/2}Mg_{1/2}(H_2PO_4)_2 \cdot 0.5H_2O$ . *J. Therm. Anal. Calorim.* **1990**, *36*, 677.
- (8) Brandová, D.; Trojan, M.; Paulik, F.; Paulik, J.; Arnold, M. Study of the thermal dehydration of Mn<sub>1/2</sub>Ca<sub>1/2</sub>(H<sub>2</sub>PO<sub>4</sub>)<sub>2</sub>·2H<sub>2</sub>O. *J. Therm. Anal. Calorim.* **1990**, *36*, 881.
- (9) Viter, V. N.; Nagornyi, P. G. Synthesis of continuous substitutional solid solutions  $M_{1-x}Ni_x(H_2PO_4)_2 \cdot 2H_2O$  with M = Mg, Mn, Co, or Zn. Russ. J. Inorg. Chem. **2007**, 52, 14.
- (10) Trojan, M. Double tetrametaphosphates  $Mn_{2-x}Ca_xP_4O_{12}$  as special pigments. *Dyes Pigm.* **1990**, *12*, 35.
- (11) Trojan, M. Binary cyclotetraphosphates  $Zn_{2-x}Ca_xP_4O_{12}$  as new special pigments. *Dyes Pigm.* **1990**, *13*, 1.
- (12) Trojan, M.; Šulcová, P.; Mošner, P. The synthesis of binary zinc(II)-nickel(II)cyclo-tetraphosphates as new special pigments. *Dyes Pigm.* **2000**, *44*, 161.
- (13) Trojan, M.; Brandová, D. A study of the thermal preparation of  $c\text{-Cd}_{4/3}\text{Ca}_{2/3}\text{P}_4\text{O}_{12}$ . Thermochim. Acta **1990**, 160, 349.
- (14) Trojan, M.; Šulcová, P. Binary Cu(II)-Mn(II) cyclo-tetraphosphates. *Dyes Pigm.* **2000**, *47*, 291.
- (15) Trojan, M.; Šulcová, P. The binary Cd(II)-Zn(II) cyclo-tetra-phosphates. *Thermochim. Acta* **2000**, 343, 135.
- (16) Trojan, M.; Šulcová, P.; Skorová, L. Thermal analysis of Ba(II)-Sr(II) cyclo-tetraphosphates(V). *J. Therm. Anal. Calorim.* **2002**, *68*, 75.
- (17) Boonchom, B.; Youngme, S.; Danvirutai, C. A rapid co-precipitation and non- isothermal decomposition kinetics of new binary Mn<sub>0.5</sub>Co<sub>0.5</sub>(H<sub>2</sub>PO<sub>4</sub>)<sub>2</sub>·2H<sub>2</sub>O. *Solid State Sci.* **2008**, *10*, 129.
- (18) Boonchom, B.; Maensiri, S.; Youngme, S.; Danvirutai, C. A simple synthesis and room temperature magnetic properties of new binary  $Mn_{0.5}Fe_{0.5}(H_2PO_4)_2 \cdot 2H_2O$  obtained from a rapid co-precipitation at ambient temperature. *Solid State Sci.* **2009**, *11*, 485.
- (19) Boonchom, B.; Thongkam, M.; Kongtaweelert, S.; Vittayakorn, N. Flower-like microparticles and novel superparamagnetic properties of new binary  $Co_{1/2}Fe_{1/2}(H_2PO_4)_2 \cdot 2H_2O$  obtained by a rapid solid state route at ambient temperature. *Mater. Res. Bull.* **2009**, *44*, 2206.
- (20) Boonchom, B.; Danvirutai, C. Rapid coprecipitation and non-isotheraml decomposition kinetics of new binary Mn<sub>0.5</sub>Cu<sub>0.5</sub>(H<sub>2</sub>PO<sub>4</sub>)<sub>2</sub>·1.5H<sub>2</sub>O. *Ind. Eng. Chem. Res.* **2008**, 47, 2941.
- (21) Boonchom, B.; Danvirutai, C. Rapid synthesis, kinetics and thermodynamics of binary Mn<sub>0.5</sub>Ca<sub>0.5</sub>(H<sub>2</sub>PO<sub>4</sub>)<sub>2</sub>·H<sub>2</sub>O. *J. Therm. Anal. Calorim.* **2009**. 98. 717.
- (22) Boonchom, B.; Danvirutai, C.; Maensiri, S. Soft solution synthesis, non-isothermal decomposition kinetics and characterization of manganese dihydrogen phosphate dihydrate  $Mn(H_2PO_4)_2 \cdot 2H_2O$  and its thermal transformation products. *Mater. Chem. Phys.* **2008**, 109, 404.

- (23) Boonchom, B. Parallelogram-like microparticles of calcium dihydrogen phosphate monohydrate (Ca(H<sub>2</sub>PO<sub>4</sub>)<sub>2</sub>⋅H<sub>2</sub>O) obtained by a rapid precipitation route in aqueous and acetone media. *J. Alloys Compd.* **2009**, 482, 199.
- (24) Boonchom, B.; Baitahe, R.; Kongtaweelert, S.; Vittayakorn, N. Kinetics and thermodynamics of zinc phosphate hydrate synthesized by a simple route in aqueous and acetone media. *Ind. Eng. Chem. Res.* **2010**, 49, 3571.
- (25) Cullity, B. D. Elements of X-ray Diffraction, 2nd ed.; Addison-Wesley Publishing: Reading, MA, 1977.
- (26) Vlaev, L.; Nedelchev, N.; Gyurova, K.; Zagorcheva, M. A comparative study of non-isothermal kinetics of decomposition of calcium oxalate monohydrate. *J. Anal. Appl. Pyrolysis* **2008**, *81*, 253.
- (27) Vlase, T.; Vlase, G.; Birta, N.; Doca, N. Comparative results of kinetic data obtained with different methods for complex decomposition steps. *J. Therm. Anal. Calorim.* **2007**, *88*, 631.
- (28) Vlase, G.; Vlase, T.; Tudose, R.; Costisor, O.; Doca, N. Kinetic of decomposition of some complexes under non-isothermal conditions. *J. Therm. Anal. Calorim.* **2007**, *88*, 637.
- (29) Vlaev, L. T.; Georgieva, V. G.; Genieva, S. D. Products and kinetics of non-isothermal decomposition of vanadium(IV) oxide compounds. J. Therm. Anal. Calorim. 2007, 88, 805.
- (30) Vlaev, L. T.; Georgieva, V. G.; Gospodinov, G. G. Kinetics of isothermal decomposition of  $ZnSeO_3$  and  $CdSeO_3$ . *J. Therm. Anal. Calorim.* **2005**, *79*, 163.
- (31) Vlaev, L. T.; Tavlieva, M. P. Structural and thermal studies on the solid products in the system MnSeO<sub>3</sub>-SeO<sub>2</sub>-H<sub>2</sub>O. *J. Therm. Anal. Calorim.* **2007**, *90*, 385.
- (32) Chunxiu, G.; Yufang, S.; Donghua, C. Comparative method to evaluate reliable kinetic triplets of thermal decomposition reactions. *J. Therm. Anal. Calorim.* **2004**, *76*, 203.
- (33) Kissinger, H. E. Reaction kinetics in differential thermal analysis. J. Anal. Chem. 1957, 29, 1702.
- (34) Okada, K.; Kaneda, J.-I.; Kameshima, Y.; Yasumori, A.; Takei, T. Crystallization kinetics of mullite from polymeric Al<sub>2</sub>O<sub>3</sub>-SiO<sub>2</sub> xerogels. *Mater. Lett.* **2003**, *57*, 3155 and references therein.
- (35) Head, C.; Smith, A. C. K. Applied Physical Chemistry; McMilan Press: London, 1982; p 473.
- (36) Ŝesták, J. J. Thermodynamical Properties of Solids; Academia: Prague, 1984.
- (37) Young, D. Decomposition of Solids; Pergamon Press: Oxford, 1966.
- (38) Herzberg, G. Molekülspektren und Molekülstruktur. I. Zweiatomige Moleküle; Steinkopff: Dresden, 1939.
- (39) Colthup, N. B.; Daly, L. H.; Wiberley, S. E. Introduction to Infrared and Raman Spectroscopy; Academic Press: New York, 1964.
- (40) Danvirutai, C.; Boonchom, B.; Youngme, S. Nanocrystalline manganese dihydrogen phosphate dihydrate Mn(H<sub>2</sub>PO<sub>4</sub>)<sub>2</sub>·2H<sub>2</sub>O and its decomposition product (Mn<sub>2</sub>P<sub>4</sub>O<sub>12</sub>) obtained by simple precipitation route. *J. Alloys Compd.* **2008**, 457, 75.
- (41) Boonchom, B.; Danvirutai, C.; Youngme, S.; Maensiri, S. Simple synthesis, magnetic properties, and nonisothermal decomposition kinetics of Fe(H<sub>2</sub>PO<sub>4</sub>)<sub>2</sub>·2H<sub>2</sub>O. *Ind. Eng. Chem. Res.* **2008**, 47, 7642.
- (42) Ramakrishnan, V.; Aruldhas, G.; Bigotto, A. Vibrational spectra of Cu(II) and Co(II) tetrametaphosphates. *Infrared Phys.* **1985**, 25, 665.
- (43) Hui-li, M.; Xian-rong, Q.; Maitani, Y.; Nagai, T. Preparation and characterization of superparamagnetic iron oxide nanoparticles stabilized by alginate. *Int. J. Pharm.* 2007, 333, 177.
- (44) Gupta, A. K.; Gupta, M. Synthesis and surface engineering of iron oxide nanoparticles for biomedical applications. *Biomaterials* **2005**, 26, 3995.
- (45) Chen, Y. H.; Franzreb, M.; Lin, R. H.; Chen, L. L.; Chang, C. Y.; Yu, Y. H.; Chiang, P. C. Platinum-doped TiO<sub>2</sub>/magnetic poly(methyl methacrylate) microspheres as a novel photocatalyst. *Ind. Eng. Chem. Res.* **2009**, *48*, 7616–7623.



#### Contents lists available at ScienceDirect

#### Solid State Sciences

journal homepage: www.elsevier.com/locate/ssscie



## A simple synthesis and characterization of binary $Co_{0.5}Fe_{0.5}(H_2PO_4)_2 \cdot 2H_2O$ and its final decomposition product $CoFeP_4O_{12}$

Banjong Boonchom a,b,\*, Chanaiporn Danvirutai<sup>c</sup>, Naratip Vittayakorn b,d,e

- <sup>a</sup> King Mongkut's Institute of Technology Ladkrabang, Chumphon Campus, 17/1 M.6 Pha Thiew District, Chumphon 86160, Thailand
- <sup>b</sup> Advanced Materials Science Research Unit, Department of Chemistry, Faculty of Science, King Mongkut's Institute of Technology Ladkrabang, Bangkok 10520, Thailand
- <sup>c</sup>Department of Chemistry, Faculty of Science, Khon Kaen University, Khon Kaen 40002, Thailand
- <sup>d</sup> Department of Chemistry, Faculty of Science, King Mongkut's Institute of Technology Ladkrabang, Ladkrabang, Bangkok 10520, Thailand
- <sup>e</sup> College of KMITL Nanotechnology, King Mongkut's Institute of Technology Ladkrabang, Bangkok 10520, Thailand

#### ARTICLE INFO

# Article history: Received 25 July 2009 Received in revised form 5 July 2010 Accepted 21 October 2010 Available online 29 October 2010

Keywords: Co<sub>0.5</sub>Fe<sub>0.5</sub>(H<sub>2</sub>PO<sub>4</sub>)<sub>2</sub>·2H<sub>2</sub>O CoFe<sub>P4</sub>O<sub>12</sub> Superparamagnetic behavior Solid state method Non-uniform particles

#### ABSTRACT

This paper reports the synthesis of binary  $Co_{0.5}Fe_{0.5}(H_2PO_4)_2 \cdot 2H_2O$  by a simple, rapid and cost-effective method using  $CoCO_3-Fe(c)-H_3PO_4$  system in water—acetone media at ambient temperature. Thermal transformation of the synthesized powder was investigated by TG/DTG/DTA and DSC techniques, which indicate that its final decomposed product was a binary cobalt iron cyclotetraphosphate  $CoFeP_4O_{12}$ . The FTIR and XRD results of the synthesized  $Co_{0.5}Fe_{0.5}(H_2PO_4)_2 \cdot 2H_2O$  and the decomposed  $CoFeP_4O_{12}$  indicate the pure monoclinic phases with space group  $P2_1/n$  and C2/c, respectively. The morphologies of  $Co_{0.5}Fe_{0.5}(H_2PO_4)_2 \cdot 2H_2O$  and  $CoFeP_4O_{12}$  powders appear non-uniform particle shapes and high agglomerates, which are different from the cases of the single compounds  $M(H_2PO_4)_2 \cdot 2H_2O$  and  $M_2P_4O_{12}$  (where M = Co, Fe). The magnetic properties of the studied compounds are superparamagnetic behaviors, which are important for specific applications. The physical properties of the studied powders are comparable with those reported in our previous study, affected by medium and condition of preparation method.

© 2010 Elsevier Masson SAS. All rights reserved.

#### 1. Introduction

Binary metal phosphates with the general formula  $M'_x M''_{1-x} (H_2 P O_4)_2 \cdot n H_2 O$  (M'or M" = Mg, Ca, Ba, Mn, Co, Ni, Fe, Zn; x = 0-1; n = 1-4) have the incremented use in order to supply the demands of high modern technology [1-3]. This phosphate group is transformed to the corresponding binary metal(II) cyclotetraphosphate group  $M'_yM''_{2-y}P_4O_{12}$  (y=0-2) in the reactions of dehydration and deprotonation of dihydrogenphosphate groups at higher temperatures [4–6] Both  $M'_xM''_{1-x}(H_2PO_4)_2 \cdot nH_2O$  and  $M'_{\nu}M''_{2-\nu}P_4O_{12}$  compounds are isostructural with the single metal dihydrogenphosphate  $(M'(H_2PO_4)_2 \cdot nH_2O)$  and single metal(II) cyclo-tetraphosphate  $(M'_2P_4O_{12})$  groups, respectively [8–10]. Consequently, they have similar X-ray diffraction patterns and close unit cell parameters, which crystallize in monoclinic space group  $P2_1/n$  (Z=2) for the dihydrogenphosphate group and C2/c (Z=4) for cyclo-tetraphosphate group. Both binary metal phosphate groups can be used in a wide range of applications: catalysts and adsorbents,

E-mail address: kbbanjon@kmitl.ac.th (B. Boonchom).

ion-exchange materials, solid electrolytes for batteries, in linear and non-linear optical components, chelating agents, tooth powder and doughs, artificial teeth and bones, corrosion-resistant coating, sewage purifying agents, glass-ceramics, refratories, fire extinguishers, cements, soap powder, biomaterials and implantates, forages for animals, superionic conductors, piezo- and ferroelectrics, gas and moisture sensors, magnets, phosphors, detergents and highquality fertilizers [1,4,5,11,12] Therefore, the design, synthesis and characterization of the field of these phosphates have been very active during the twentieth century. However, the development of the chemistry of these phosphates was very slow, spreading along almost a century. So far, there were reports on the synthesis, the thermal analysis (TA) under quasi-isothermal and quasi-isobaric conditions of binary metal(II) dihydrogenphosphate hydrates  $M'_{x}M''_{1-x}(H_{2}PO_{4})_{2} \cdot nH_{2}O$  (M'or M" = Mg, Ca, Ba, Mn, Co, Ni, Fe, Zn; x = 0-1; n = 1-4) [1,4,5,8-12]. Recently, Viter and Nagornyi [13], Antraptseva et al. [4] and Koleva and Mehandjiev [12,14] reported the synthesis at low temperature (40-80 °C) with long time consumption (2–90 days) of  $M_{1-x}Ni_x(H_2PO_4)_2 \cdot 2H_2O$  (M = Mg, Mn, Co, Zn),  $Mn_{1-x}Zn_x(H_2PO_4)_2 \cdot 2H_2O$  and  $M(H_2PO_4)_2 \cdot 2H_2O$  (M = Co, Ni, Mn, Fe), respectively. Most recently, our research group reported the synthesis (10-20 min) of  $M(H_2PO_4)_2 \cdot 2H_2O$  $M_{1-x}A_x(H_2PO_4)_2 \cdot nH_2O$  (M and A = Ca, Mn, Fe, Cu, Co) at ambient

<sup>\*</sup> Corresponding author. King Mongkut's Institute of Technology Ladkrabang, Chumphon Campus, 17/1 M.6 Pha Thiew District, Chumphon 86160, Thailand. Tel.: +66 7750 6422x4565; fax: +66 7750 6410.

temperature [1,2,15,16]. However, it is obstacle to synthesize binary metal dihydrogenphosphates, binary metal cyclotetraphosphates and their solid solutions, which vary the composition of metal cations for obtaining homogeneity ranges and modified useful properties.

In this work, binary  $Co_{0.5}Fe_{0.5}(H_2PO_4)_2 \cdot 2H_2O$  was prepared by solid state method at ambient temperature with short time consumption (<10 min), which is a simple and cost-effective route. Thermal transformation of  $Co_{0.5}Fe_{0.5}(H_2PO_4)_2 \cdot 2H_2O$  was investigated by thermogravimetry/differential thermal gravimetry/differential thermal analysis (TG/DTG/DTA) and differential scanning calorimetry (DSC) techniques and its final decomposed product is  $CoFeP_4O_{12}$ . Furthermore, the synthesized  $Co_{0.5}Fe_{0.5}(H_2-PO_4)_2 \cdot 2H_2O$  and its decomposed product  $CoFeP_4O_{12}$  were characterized by X-ray powder diffraction (XRD), Fourier transform infrared (FTIR), scanning electron microscope (SEM) and vibrating sample magnetometer (VSM) techniques.

#### 2. Experimental

Phosphoric acid (H<sub>3</sub>PO<sub>4</sub>, Fluka, 86.4% w/w), cobalt carbonate (CoCO<sub>3</sub>, Merck, AR grade), iron metal (Fe, Merck, AR; c; complexometric) and acetone (CH<sub>3</sub>CH<sub>2</sub>OCH<sub>3</sub>CH<sub>2</sub>, Merck, AR grade) were used as precursors for phosphorous, Co(II), Fe(II) and media agent, respectively. Typically process, 2.00 mL of distilled water was added to 8.00 mL H<sub>3</sub>PO<sub>4</sub> and then H<sub>3</sub>PO<sub>4</sub> solution was added to 2.40 g of CoCO<sub>3</sub> and 1.12 g of Fe(c) (a mole ratio corresponding to the nominal composition of Fe:Co ratio of 1.0:1.0) in the presence of 15 mL acetone. This resulting suspension was continuously stirred at ambient temperature for 10 min and the prepared solid was aged for drying at room temperature. The presence of acetone reduced strong exothermic reaction and prevented the evolved H<sub>2</sub>(g) and CO<sub>2</sub>(g) in the precipitation process and developed the highly crystalline product. This method is a simple, rapid, cost-effective and environmental friendly route for synthesis of Co<sub>0.5</sub>Fe<sub>0.5</sub>(H<sub>2</sub>-PO<sub>4</sub>)<sub>2</sub>·2H<sub>2</sub>O. The prepared solid was recovered by filtration (suction pump), washed with acetone, and dried in air.

Thermogravimetric analysis (TGA) and differential thermal analysis (DTA) was carried out in a flow of air (100 mL min<sup>-1</sup>) with a heating rate of 10 °C min<sup>-1</sup> over the temperature range from 30 to 800 °C using a TG-DTG-DTA Pyris Diamond Perkin Elmer Instruments. Its final decomposed product seemed to occur at temperatures above 600 °C, so the prepared solid was calcined at 700 °C for 3 h. Differential scanning calorimetry was carried out for a sample (5–10 mg) in an aluminum crucible, over the temperature range of 303-823 K using differential scanning calorimetry (DSC), Perkin Elmer Pyris One. The heating rate employed was 10 K min<sup>-1</sup>. The cobalt and iron contents of the prepared solid and its final decomposed product were determined by dissolving in 0.0126 M hydrochloric acid using atomic absorption spectrophotometry (AAS, Perkin Elmer, Analyst 100). The phosphorus content was determined by colorimetric analysis of the molybdophosphate complex. The structure and crystallite size of the synthesized sample and its decomposed product were studied by X-ray powder diffraction using an X-ray diffractometer (Phillips PW3040, The Netherlands) with Cu K $\alpha$  radiation ( $\lambda = 0.15406$  nm). The Scherrer method was used to evaluate the crystallite size [17]. The photographs of scanning electron microscope (SEM) were obtained by LEO SEM VP1450 after gold coating. The room temperature FTIR spectra were recorded in the range of 4000–370 cm<sup>-1</sup> with 8 scans on a Perkin–Elmer Spectrum GX FT-IR/FT-Raman spectrometer with the resolution of 4 cm<sup>-1</sup> using KBr pellets (KBr, spectroscopy grade, Merck). The magnetic properties of the prepared solid and its decomposed product were examined at room temperature (20 °C) using a vibrating sample magnetometer (VSM 7403, Lake Shore, USA).

#### 3. Results and discussion

#### 3.1. Chemical analysis

According to chemical analysis data, the P/(Co+Fe)=2.13 and  $H_2O/P=1.92$  molar ratios in the synthesized phosphate differed very little from those calculated for binary metal dihydrogenphosphate with the general formula  $Co_{1/2}Fe_{1/2}(H_2PO_4)_2 \cdot 2H_2O$ . Similarly, the P/(Co+Fe)=2.01 molar ratio in the decomposed product practically corresponds to the  $CoFeP_4O_{12}$  stoichiometry, where Co(II) and Fe(II) stand for divalent cations.

#### 3.2. Thermal analysis

Fig. 1 shows the TG/DTG/DTA curves of  $Co_{0.5}Fe_{0.5}(H_2PO_4)_2 \cdot 2H_2O$ . The TG trace shows three mass loss stages in the range of 30–600 °C. In the first stage between 45 and 140 °C, the mass loss of 11.62% corresponds to the elimination of 1.87 mol water (H<sub>2</sub>O) of crystallization. The mass losses of 9.15% for the second stage (140-275 °C) and 5.85% for the third stage (275-600 °C) relate to the eliminations of 1.47 and 0.54 mol water of the deprotonated dihydrogenphosphate groups, respectively. Three endothermic effects in the DTA curve show over the temperature region at 119, 174 and 402 °C, which relate to three peaks in DTG curve at 114, 165, and 400 °C and closely correspond to the observed mass loss on the TG trace. Further, a small exothermic effect at 712 °C without appreciable mass loss is observed in the DTA curve, which can be ascribed to a transition phase form of CoFeP<sub>4</sub>O<sub>12</sub>. The thermal transformation of Co<sub>0.5</sub>Fe<sub>0.5</sub>(H<sub>2</sub>PO<sub>4</sub>)<sub>2</sub>·2H<sub>2</sub>O involves the dehydration of the coordination water molecule (2 mol H<sub>2</sub>O) and an intramolecular dehydration of the protonated dihydogenphosphate groups (2 mol H<sub>2</sub>O) as shown in Eqs. (1) and (3).

$$Co_{0.5}Fe_{0.5}(H_2PO_4)_2 \cdot 2H_2O \rightarrow Co_{0.5}Fe_{0.5}(H_2PO_4)_2 + \sim 2H_2O$$
 (1)

 $Co_{0.5}Fe_{0.5}(H_2PO_4)_2 \rightarrow Co_{0.5}(H_2P_2O_7)_{0.5} \cdot Fe_{0.5}(H_2P_2O_7)_{0.5} + \sim H_2O~(2)$ 

$$Co_{0.5}(H_2P_2O_7)_{0.5} \cdot Fe_{0.5}(H_2P_2O_7)_{0.5} \rightarrow 1/2CoFeP_4O_{12} + \sim H_2O$$
 (3)

An unstable intermediate compounds, such as acid polyphosphate  $Co_{0.5}Fe_{0.5}(H_2PO_4)_2$  and  $Co_{0.5}(H_2P_2O_7)_{0.5} \cdot Fe_{0.5}(H_2P_2O_7)_{0.5}$  and mixtures of intermediate of both have been registered and

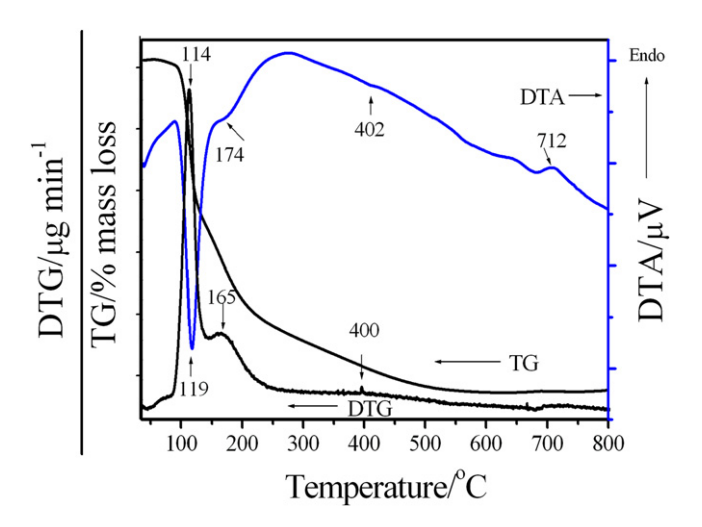


Fig. 1. TG/DTG/DTA curves of Co $_{0.5}$ Fe $_{0.5}(H_2PO_4)_2\cdot 2H_2O$  at the heating rate of 10  $^{\circ}$ C min $^{-1}$  in air atmosphere.

were similarly observed with the single hydrogen phosphates and other binary metal dihydrogenphosphates [2–8]. The binary cobalt iron cyclotetraphosphate, CoFeP<sub>4</sub>O<sub>12</sub> is found to be the final product of the thermal decomposition at  $T > 600\,^{\circ}$ C. The total mass loss is 26.62% (3.88 mol H<sub>2</sub>O), which is in agreement with those reported for other binary dihydrogenphosphate dihydrate in the literature (1 < mole of water < 4) [4,12–16]. The thermal stability, mechanism and phase transition temperature of the studied compound in this work are significantly different from those from the single metal compounds (Fe(H<sub>2</sub>PO<sub>4</sub>)<sub>2</sub>·2H<sub>2</sub>O [18] and Co(H<sub>2</sub>PO<sub>4</sub>)<sub>2</sub>·2H<sub>2</sub>O [19]). The different thermal behaviors were considered to be due to the different locations of the incorporation of Fe and Co metals in the skeleton and water constitution, which affect to the strengths of water molecule bonds in the studied compound.

The DSC curve of  $Co_{0.5}Fe_{0.5}(H_2PO_4)_2 \cdot 2H_2O$  (Fig. 2) shows four endothermic peaks at 121,167, 215 and 402 °C (onset peak at 98,162, 204 and 389 °C) which relate to the dehydration reactions for the first two peaks and the polycondensation reactions for the last two peaks, respectively. Three endothermic peaks at 121, 167 and 402 °C in the DSC curve are in good agreement with DTG and DTA curves as shown in Fig. 1. According to DSC experiment, the heat of dehydration reactions and the polycondensation reactions of this compound can be estimated and were found to be 154.80, 7.80, 20.98 and  $34.04 \, \mathrm{J} \, \mathrm{g}^{-1}$ , respectively.

#### 3.3. X-ray powder diffraction

Fig. 3 shows the XRD patterns of the  $Co_{0.5}Fe_{0.5}(H_2PO_4)_2 \cdot 2H_2O$  sample and its final decomposed product, which are very similar to those obtained from the single metal compounds of M  $(H_2PO_4)_2 \cdot 2H_2O$  and  $M_2P_4O_{12}$  (when M=Co and Fe), respectively. Compared with the published XRD data of the individual metal compounds  $(Co(H_2PO_4)_2 \cdot 2H_2O$  (PDF no 390698),  $Fe(H_2PO_4)_2 \cdot 2H_2O$  (PDF no 751444),  $Co_2P_4O_{12}$  (PDF no 842208) and  $Fe_2P_4O_{12}$  (PDF no 782285)), both studied samples can be assigned to the  $Co_{0.5}Fe_{0.5}(H_2PO_4)_2 \cdot 2H_2O$  and  $CoFeP_4O_{12}$  products. According to hypothesis of isostructural, the systems of binary cobalt iron solid solutions and individual metal dihydrogenphosphate (or cobalt iron cyclotetraphosphate) show quite similarity of the XRD peaks because the electronic charges of cations are equivalent and the radii of cations are close to each other. Consequently, we can draw a conclusion that the synthesized  $Co_{0.5}Fe_{0.5}(H_2PO_4)_2 \cdot 2H_2O$  and its

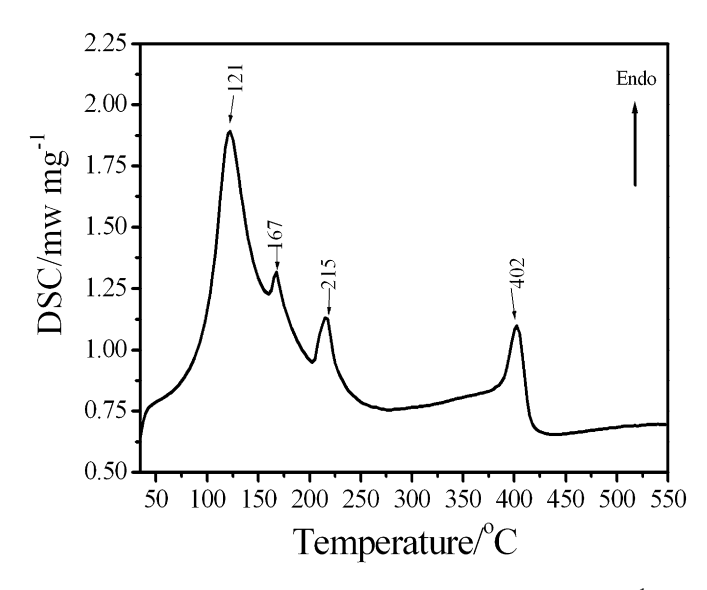


Fig. 2. DSC curve of  $Co_{0.5}Fe_{0.5}(H_2PO_4)_2\cdot 2H_2O$  at the heating rate of  $10~^\circ C$  min $^{-1}$  in  $N_2$  atmosphere.

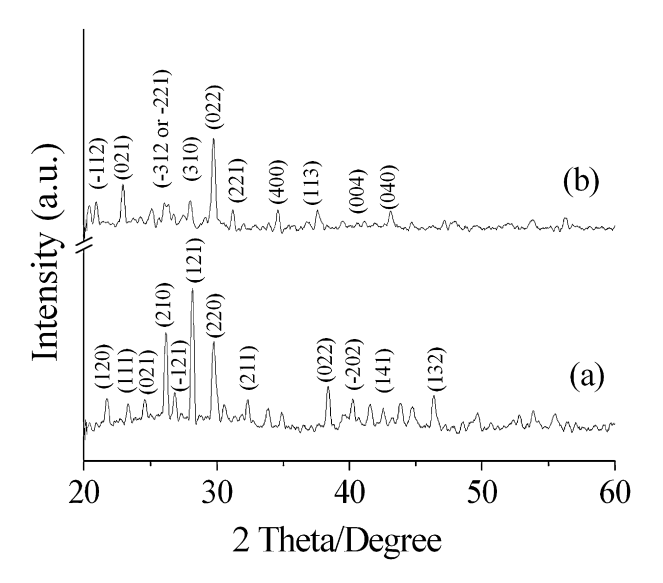


Fig. 3. XRD patterns of  $Co_{0.5}Fe_{0.5}(H_2PO_4)_2 \cdot 2H_2O$  (a) and its decomposed product  $CoFeP_4O_{12}$  (b).

final decomposed product are solid solutions and not a mixture of the individual ones. On the basis of XRD results, all the reflections can be distinctly indexed as pure monoclinic phases with space group  $P2_1/n$  (Z=2) for  $Co_{0.5}Fe_{0.5}(H_2PO_4)_2 \cdot 2H_2O$  and C2/c (Z=4) for  $CoFeP_4O_{12}$ . The average crystallite sizes and lattice parameters of both samples were calculated from the XRD patterns and were summarized in Table 1. The lattice parameters and crystallite sizes of  $Co_{0.5}Fe_{0.5}(H_2PO_4)_2 \cdot 2H_2O$  and  $CoFeP_4O_{12}$  are comparable to those of the single metal compounds reported in the standard data and our previous works [18,19]. As can seen from Table 1, the crystallite sizes for both binary compounds in this work are larger than those from the single metal compounds in our previous reports [18,19].

#### 3.4. FTIR spectroscopy

The FTIR spectra of Co<sub>0.5</sub>Fe<sub>0.5</sub>(H<sub>2</sub>PO<sub>4</sub>)<sub>2</sub>·2H<sub>2</sub>O and its final decomposed product CoFeP<sub>4</sub>O<sub>12</sub> are shown in Fig. 4. On the basis of isostructural, the FTIR spectra peaks of the binary metal and single metal of dihydrogenphosphate (or cyclotetraphosphate) are quite similar. Consequently, vibrational bands are identified in relation to the crystal structure in terms of the fundamental vibrating units namely  $H_2PO_4^-$  and  $H_2O$  for  $Co_{0.5}Fe_{0.5}(H_2PO_4)_2 \cdot 2H_2O$  and  $[P_4O_{12}]^{4-}$ ion for CoFeP<sub>4</sub>O<sub>12</sub>, which are assigned according to the literature [4,12–16]. The FTIR spectrum of  $Co_{0.5}Fe_{0.5}(H_2PO_4)_2 \cdot 2H_2O$  (Fig. 4a) is very similar to those observed by Koleva and Mehandjiev [12] and Boonchom et al. [18,19] The highest site symmetry of  $H_2PO_4^-$  ion is  $C_{2v}$ , in the crystallographic unit cell ( $P2_1/n$ , Z=2), but the four  $H_2PO_4^$ ions are located on the set of non-equivalent site symmetry of C<sub>1</sub>. A pair of H<sub>2</sub>PO<sub>4</sub> ions is related to each other by a center of symmetry. It is known that the existence of short OH···O hydrogen bonds in a variety of strongly hydrogen-bonded solids is manifested by the appearance of the characteristic ABC structure of the  $\nu(OH)$  vibrational. Usually, the ABC bands are very broad and consist of many ill-resolved components. The strongest band (A) is located in the  $3100-2700 \,\mathrm{cm}^{-1}$  region, the B band appears about 2600- $2400 \text{ cm}^{-1}$  and the C band around  $1700-1600 \text{ cm}^{-1}$ . The problem of the origin of the ABC trio is discussed in many studies on acidic salts, but an explanation of this behavior of strongly hydrogen-bonded systems is still to be found. One of the most popular interpretations of the ABC trio suggests a strong Fermi resonance between the  $\nu(OH)$ stretching fundamentals and the overtones [2 $\delta$ (OH) and 2 $\gamma$ (OH)] or combinations involving the  $\delta(OH)$  and  $\gamma(OH)$  vibrations. The IR

 Table 1

 Average crystallite sizes and lattice parameters of  $Co_{0.5}Fe_{0.5}(H_2PO_4)_2 \cdot 2H_2O$  and its decomposed product  $CoFeP_4O_{12}$  calculated from XRD data.

Compound	Method	a/Å	b/Å	c/Å	β/°	Average crystallite sizes/nm
Co(H <sub>2</sub> PO <sub>4</sub> ) <sub>2</sub> ·2H <sub>2</sub> O	PDF no 390698 Ref. [19]	7.27 7.21(3)	9.88 9.91(1)	5.33 5.29(5)	94.86 94.88(6)	26 ± 2
$Co_{0.5}Fe_{0.5}(H_2PO_4)_2 \cdot 2H_2O$	This work	7.29(0)	9.90(0)	5.35(0)	95.10(0)	$59\pm13$
$Fe(H_2PO_4)_2 \cdot 2H_2O$	PDF no 751444 Ref. [18]	7.30 7.25(1)	9.92 10.10(0)	5.34 5.32(0)	95.14 95.71(0)	$\begin{matrix} -\\ 28\pm 4\end{matrix}$
$Co_2P_4O_{12}$	PDF no 842208 Ref. [19]	11.8 11.83(8)	8.297 8.22(6)	9.923 9.94(0)	118.72 118.51(1)	$40\pm10$
CoFeP <sub>4</sub> O <sub>12</sub>	This work	11.62(1)	8.30(0)	9.65(2)	119.17(4)	$62\pm15$
Fe <sub>2</sub> P <sub>4</sub> O <sub>12</sub>	PDF no 782285 Ref. [18]	11.94 12.80(0)	8.37 8.80(4)	9.93 10.56(0)	118.74 118.67(4)	-000000000000000000000000000000000000

spectrum of Co<sub>0.5</sub>Fe<sub>0.5</sub>(H<sub>2</sub>PO<sub>4</sub>)<sub>2</sub>·2H<sub>2</sub>O in the region of the OH stretching modes is characterized by the appearance of a complex broad band between 3600 and 1600 cm<sup>-1</sup>. Two bands centered at 3145 and 2431 cm<sup>-1</sup> in the FTIR spectra are referred to as bands A and B, respectively. The third component (band C) is observed around  $1744-1640 \text{ cm}^{-1}$ . The intense band at about  $1260 \text{ cm}^{-1}$  is due to the in plane P-O-H bending  $(A_2)$ , while the out of plane bending  $(A_1)$  vibration is observed at about 815 cm<sup>-1</sup>. A strong band at about 1141 cm<sup>-1</sup> is assigned to  $PO_2$  asymmetric stretching ( $B_1$ ), while the other one at about 1043 cm<sup>-1</sup> corresponds to PO<sub>2</sub> symmetric stretching modes  $(A_1)$ . The FTIR frequency of the  $P(OH)_2$ asymmetric stretching  $(B_2)$  shows the strong band at about 945 cm<sup>-1</sup>. The weak band at about 906 cm<sup>-1</sup> is assigned to P(OH)<sub>2</sub> symmetric stretching modes  $(A_1)$ . The medium band at about  $560 \text{ cm}^{-1}$  is corresponding to PO<sub>2</sub> bending modes ( $B_1$ ). Two strong bands appeared at about 520 and 470 cm<sup>-1</sup> are attributed to PO<sub>2</sub> rocking modes as  $B_1$  and  $A_2$  vibrations, respectively. The bands of water vibrations are illustrated in Fig. 4a as doublet bands (1640 and  $1568 \, \mathrm{cm}^{-1}$ ) contribute both to the band C and to the water bending band. A weak band occurs in the FTIR spectra at approximately 638 cm<sup>-1</sup> is assigned to rocking mode involving water librations. The  $v_{OH}$  stretching modes of HOH in  $Co_{0.5}Fe_{0.5}(H_2PO_4)_2 \cdot 2H_2O$  appear at 3145 cm<sup>-1</sup> ( $\nu_1$  or A band) and 3322 cm<sup>-1</sup> ( $\nu_3$ ). The bands associated with the  $v_{OH}$  stretching frequencies in  $H_2PO_4^-$  ions are observed at about 2929 and 2431 cm<sup>-1</sup>.

The FTIR spectrum of  $CoFeP_4O_{12}$  is shown in Fig. 4b, which are very similar to those obtained from the individual  $M_2P_4O_{12}$  (M = Co

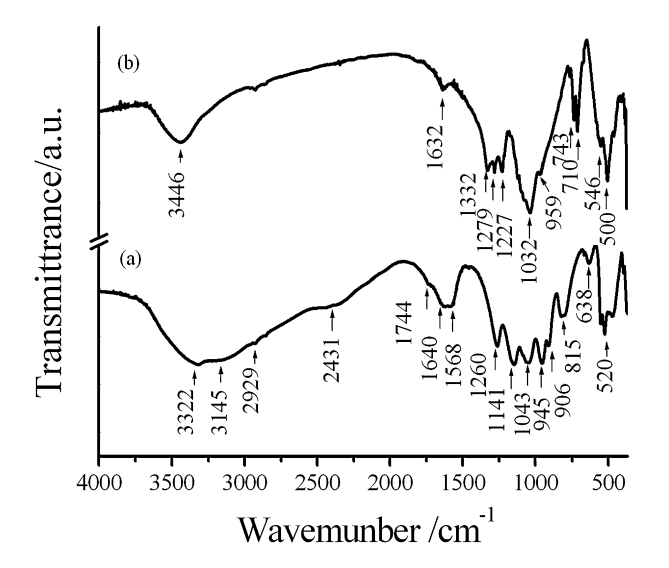


Fig. 4. FTIR spectra of  $Co_{0.5}Fe_{0.5}(H_2PO_4)_2 \cdot 2H_2O$  (a) and its decomposed product  $CoFeP_4O_{12}$  (b).

and Fe) [18,19]. The vibrational modes of  $P_4O_{42}^{1-}$  ion observed in the frequency range of 370–1400 cm<sup>-1</sup> are assigned according to the literature [20,21]. One of the most noteworthy features of the spectra is the presence of strong bands in the ranges of 1332–1227, 1150–1100, 1080–959, 780–700 and 600–400 cm<sup>-1</sup>. These bands can be assigned to  $\nu_{as}$ OPO<sup>-</sup>,  $\nu_{s}$ OPO<sup>-</sup>,  $\nu_{as}$ POP,  $\nu_{s}$ POP and metal–O vibrations, respectively. The observation of a strong  $\nu_{s}$ POP band is known to be the most striking feature of cyclotetraphosphate spectra, along with the presence of the  $\nu_{as}$ OPO<sup>-</sup> band. From X-ray diffraction data [20,21], it was shown that the crystal structure is monoclinic (space group C2/c) with a cyclic structure of the  $[P_4O_{12}]^{4-}$  anion. This has been confirmed by the FTIR measurements.

#### 3.5. Scanning electron microscopy

The SEM micrographs of  $Co_{0.5}Fe_{0.5}(H_2PO_4)_2 \cdot 2H_2O$  and  $CoFeP_4O_{12}$  are shown in Fig. 5. The particle shape and size are changed throughout the whole decomposition product. The SEM micrographs of  $Co_{0.5}Fe_{0.5}(H_2PO_4)_2 \cdot 2H_2O$  and  $CoFeP_4O_{12}$  show non-uniform particles and high agglomerates, which are different from those of the single metal compounds  $M(H_2PO_4)_2 \cdot 2H_2O$  and  $M_2P_4O_{12}$  (M=Co or Fe) [18,19]. Additionally, the particle sizes and surface morphologies of both compounds in this work are significantly different from those of these binary compounds  $(Co_{1/2}Fe_{1/2}(H_2PO_4)_2 \cdot 2H_2O)$  and  $CoFeP_{14}O_{12}$  reported by our previous work [22,23]. The different morphologies of the single metal compounds  $(M(H_2PO_4)_2 \cdot 2H_2O)$  and  $M_2P_4O_{12}$ , M=Co or Fe) and these binary compounds indicate the presence of Co ions in substitution position of Fe ions and the different conditions of preparation method, respectively.

#### 3.6. VSM magnetometer

Fig. 6 shows the specific magnetization curves of Co<sub>0.5</sub>Fe<sub>0.5</sub>(H<sub>2-</sub> PO<sub>4</sub>)<sub>2</sub>·2H<sub>2</sub>O and CoFeP<sub>4</sub>O<sub>12</sub> obtained from VSM measurements measured at 20 °C. Both samples demonstrate typical superparamagnetic behavior without any hysteresis in the field range of  $\pm 10,000$  Oe, which is in agreement with the theory of superparamagnetic behavior, is often observed at room temperature. Specific saturated magnetization ( $M_s$ ) values of 25.61 and 11.89 emu/ g are observed for the  $Co_{0.5}Fe_{0.5}(H_2PO_4)_2 \cdot 2H_2O$  and  $CoFeP_4O_{12}$ , respectively. The superparamagnetic behaviors of the studied compounds are different from the ferromagnetic properties of Fe (H<sub>2</sub>PO<sub>4</sub>)<sub>2</sub>·2H<sub>2</sub>O and Fe<sub>2</sub>P<sub>4</sub>O<sub>12</sub> and the diamagnetic properties of Co (H<sub>2</sub>PO<sub>4</sub>)<sub>2</sub>·2H<sub>2</sub>O and Co<sub>2</sub>P<sub>4</sub>O<sub>12</sub>. In addition, it is seen that magnetizations of the  $Co_{0.5}Fe_{0.5}(H_2PO_4)_2 \cdot 2H_2O$  and  $CoFeP_4O_{12}$  are lower than those of Fe(H<sub>2</sub>PO<sub>4</sub>)<sub>2</sub>·2H<sub>2</sub>O (96.28 emu/g) and Fe<sub>2</sub>P<sub>4</sub>O<sub>12</sub> (85.01 emu/ g) [18]. The  $M_s$  of  $Co_{0.5}Fe_{0.5}(H_2PO_4)_2 \cdot 2H_2O$  in this work is higher than that of  $Co_{1/2}Fe_{1/2}(H_2PO_4)_2 \cdot 2H_2O$  (0.045 emu/g) prepared from other method and reported by Boonchom et al. [23]. But the  $M_s$  of

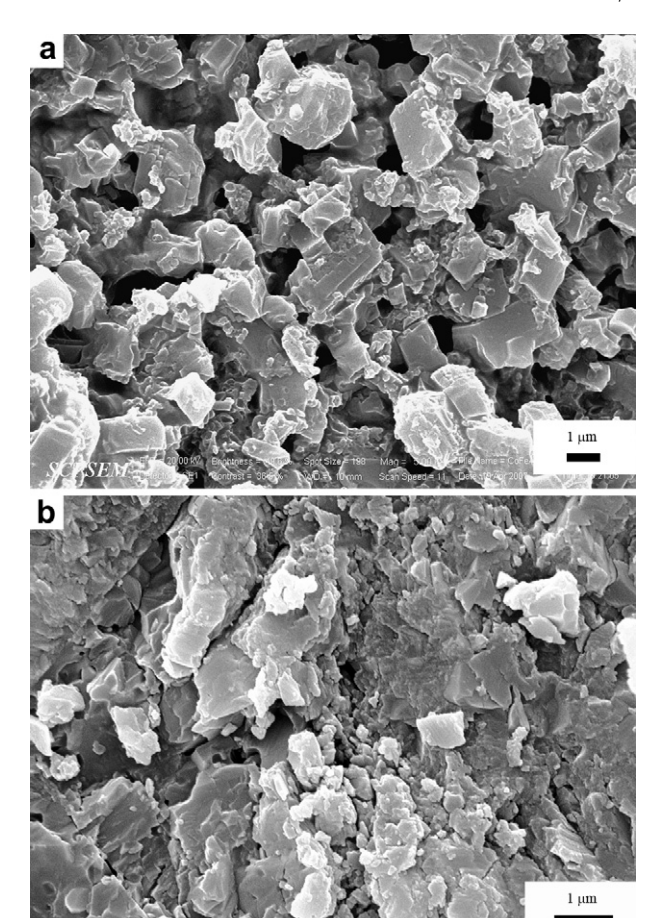


Fig. 5. SEM micrographs of Co<sub>0.5</sub>Fe<sub>0.5</sub>(H<sub>2</sub>PO<sub>4</sub>)<sub>2</sub>·2H<sub>2</sub>O (a) and its decomposed product CoFeP<sub>4</sub>O<sub>12</sub> (b).

CoFeP<sub>4</sub>O<sub>12</sub> in this work is smaller than that of the calcined Co<sub>1/2</sub>Fe<sub>1/2</sub>  $_2(H_2PO_4)_2 \cdot 2H_2O$  (12.502 emu/g) precursor at 700 °C and the obtained CoFeP<sub>4</sub>O<sub>12</sub> (14.243 emu/g) in our previous study [22,23]. These results confirmed that the differences in magnetic properties

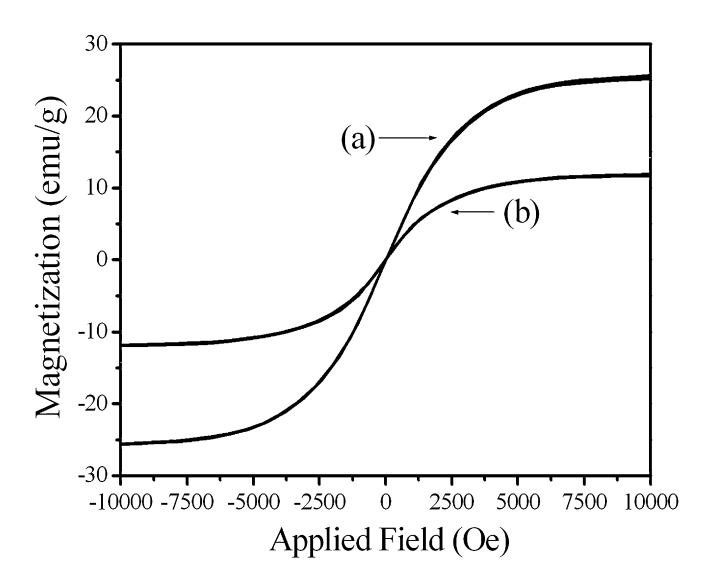


Fig. 6. The specific magnetizations of Co<sub>0.5</sub>Fe<sub>0.5</sub>(H<sub>2</sub>PO<sub>4</sub>)<sub>2</sub>·2H<sub>2</sub>O (a) and its decomposed product CoFeP<sub>4</sub>O<sub>12</sub> (b) as a function of field, measured at 293 K.

for the synthesized  $Co_{0.5}Fe_{0.5}(H_2PO_4)_2 \cdot 2H_2O$  and  $CoFeP_4O_{12}$  depend on the medium and condition for preparations.

#### 4. Conclusion

Co<sub>0.5</sub>Fe<sub>0.5</sub>(H<sub>2</sub>PO<sub>4</sub>)<sub>2</sub>·2H<sub>2</sub>O was successfully synthesized by a simple solid state method using CoCO3-Fe-H3PO4 system at ambient temperature with short time consuming (10 min). Thermal transformation of Co<sub>0.5</sub>Fe<sub>0.5</sub>(H<sub>2</sub>PO<sub>4</sub>)<sub>2</sub>·2H<sub>2</sub>O was investigated by TG/DTG/DTA and DSC techniques, which indicate the dehydration and the deprotonated dihydrogenphosphate reactions and its final decomposed product is CoFeP4O12. The structures, morphologies and magnetic properties of Co<sub>0.5</sub>Fe<sub>0.5</sub>(H<sub>2</sub>PO<sub>4</sub>)<sub>2</sub>·2H<sub>2</sub>O and its decomposed product CoFeP<sub>4</sub>O<sub>12</sub> were investigated. The XRD patterns and FTIR spectra suggest the formation of pure monoclinic phases of Co<sub>0.5</sub>Fe<sub>0.5</sub>(H<sub>2</sub>PO<sub>4</sub>)<sub>2</sub>·2H<sub>2</sub>O and CoFeP<sub>4</sub>O<sub>12</sub>. Both samples are superparamagnetic at room temperature, having no hysteresis loop in the range of -10,000 Oe < H < +10,000 Oe. This work presents the simple, cost-effective and short time consuming method for the alternative preparation of  $Co_{0.5}Fe_{0.5}(H_2PO_4)_2 \cdot 2H_2O$ and CoFeP<sub>4</sub>O<sub>12</sub> compounds, which may be used in many important applications such as catalytic, superionic conductors, piezo- and ferroelectrics, magnets, ceramic and electrochemical performance.

#### Acknowledgements

This work is financially supported by the Thailand Research Fund (TRF) and the Commission on Higher Education (CHE) and King Mongkut's Institute of Technology Ladkrabang Research (KMITL Research), Ministry of Education, Thailand.

#### Appendix. Supplementary data

Supplementary data associated with this article can be found in the online version, at doi:10.1016/j.solidstatesciences.2010.10. 012.

#### References

- [1] M. Trojan, P. Šulcová, Dyes Pigments 47 (2000) 291.
- [2] B. Boonchom, S. Maesiri, S. Youngme, C. Danvirutai, Solid State Sci. 11 (2009) 485.
- [3] B. Boonchom, C. Danvirutai, Ind. Eng. Chem. Res. 47 (2008) 2941 and references therein.
- [4] N.M. Antraptseva, L.N. Shchegrov, I.G. Ponomareva, Russ. J. Inorg. Chem. 51 (2006) 1493.
- M. Trojan, P. Šulcová, P. MoŠner, Dyes Pigments 44 (2000) 161.
- M. Trojan, D. Brandová, J. Therm. Anal. Calorim. 30 (1985) 159.
- M. Trojan, Dyes Pigments 12 (1990) 35. M. Trojan, Dyes Pigments 13 (1990) 1.
- [9] M. Trojan, Thermochim. Acta 159 (1990) 13.
- [10] M. Trojan, Thermochim. Acta 160 (1990) 361.
- M. Trojan, D. Brandová, Thermochim. Acta 160 (1990) 349.
- [12] V. Koleva, D. Mehandjiev, Mater. Res. Bull. 413 (2006) 469.
- [13] V.N. Viter, P.G. Nagornyi, Russ. J. Inorg. Chem. 52 (2007) 14
- [14] V. Koleva, H. Effenberger, J Solid Sate Chem. 180 (2007) 956.
   [15] B. Boonchom, S. Youngme, C. Danvirutai, Solid State Sci. 10 (2008) 129.
- [16] B. Boonchom, J. Danvirutai, J. Therm. Anal. Calorim. 97 (2009) 717.
- [17] B.D. Cullity, Elements of X-ray Diffraction, second ed. Addison-Wesley Publishing, 1977
- [18] B. Boonchom, C. Danvirutai, S. Youngme, S. Maesiri, Ind. Eng. Chem. Res. 47 (2008) 7642.
- B. Boonchom, C. Danvirutai, I. Chem. Eng. Data 54 (2009) 1225.
- W. Gunsser, D. Fruehauf, K. Rohwer, A. Zimmermann, A. Wiedenmann, J. Solid State Chem. 82 (1989) 43
- M. Bagieu-Beucher, M. Gondrand, M. Perroux, J. Solid State Chem. 19 (1976) 353.
- B. Boonchom, M. Thongkam, S. Kongtaweelert, N. Vittayakorn, J. Alloys Compd. 486 (2009) 689.
- [23] B. Boonchom, M. Thongkam, S. Kongtaweelert, N. Vittavakorn, Mater. Res. Bull. 44 (2009) 2206.

Provided for non-commercial research and education use. Not for reproduction, distribution or commercial use.



This article appeared in a journal published by Elsevier. The attached copy is furnished to the author for internal non-commercial research and education use, including for instruction at the authors institution and sharing with colleagues.

Other uses, including reproduction and distribution, or selling or licensing copies, or posting to personal, institutional or third party websites are prohibited.

In most cases authors are permitted to post their version of the article (e.g. in Word or Tex form) to their personal website or institutional repository. Authors requiring further information regarding Elsevier's archiving and manuscript policies are encouraged to visit:

http://www.elsevier.com/copyright

### Author's personal copy

Journal of Alloys and Compounds 509 (2011) 2304-2310



Contents lists available at ScienceDirect

### Journal of Alloys and Compounds

journal homepage: www.elsevier.com/locate/jallcom



## Effect of BiAlO<sub>3</sub> modification on the stability of antiferroelectric phase in PbZrO<sub>3</sub> ceramics prepared by conventional solid state reaction

Naratip Vittayakorn a,b,c,\*, Banjong Boonchom d

- <sup>a</sup> College of KMITL Nanotechnology, King Mongkut's Institute of Technology Ladkrabang, Bangkok 10520, Thailand
- <sup>b</sup> Department of Chemistry, Faculty of Science, King Mongkut's Technology Ladkrabang, Bangkok 10520, Thailand
- <sup>c</sup> Thailand Center of Excellence in Physics (ThEP), CHE, 328 Si Ayutthaya Rd., Bangkok 10400, Thailand
- d King Mongkut's Institute of Technology Ladkrabang, Chumphon Campus, 17/1 M.6 Pha Thiew District, Chumphon 86160, Thailand

#### ARTICLE INFO

# Article history: Received 7 September 2010 Received in revised form 28 October 2010 Accepted 28 October 2010 Available online 10 November 2010

Keywords: Energy storage materials Ferroelectrics X-ray diffraction Dielectric response

#### ABSTRACT

In this paper, we report on the polycrystalline  $(Pb_{(1-3x/2)}Bi_x)(Zr_{1-3x/4}Al_x)O_3$  (PZO-BAO) ceramics, with x = 0.0–0.3, prepared by conventional solid state reaction. The crystal structure and thermal and dielectric properties of the sintered ceramics were investigated as a function of composition by means of X-ray diffraction (XRD), differential scanning calorimetry (DSC) and dielectric spectroscopy. The results indicated that the presence of BiAlO<sub>3</sub>: BAO in the solid solution decreased the structural stability of the overall perovskite phase. Dielectric, thermal and P-E hysteresis results confirmed that no ferroelectric intermediate phase was seen in the PZO-BAO system. An antiferroelectric phase can be stable in a wide temperature range, indicating that BAO enhanced antiferroelectric phase stability in perovskite PZ manifests by "square" antiferroelectric behavior. Therefore, the  $(Pb_{(1-3x/2)}Bi_x)(Zr_{1-3x/4}Al_x)O_3$  solid solution offers a material system for high-energy-storage capacitors and electromechanical transducers.

© 2010 Elsevier B.V. All rights reserved.

#### 1. Introduction

Pure and compositionally modified lead zirconate (PbZrO<sub>3</sub>; PZO) ceramics are important materials used in energy storage applications for DC fields, due its antiferroelectric (AFE) nature. PZO has an orthorhombic structure, with the lattice parameters,  $a = 5.884 \,\text{Å}$ ,  $b = 11.768 \,\text{Å}$  and  $c = 8.22 \,\text{Å}$  [1]. The phase transition sequence has been found to follow the progressive heating of PZO orthorhombic AFE to rhombohedral ferroelectric (FE) (228 < T < 230 °C) to paraelectric (PE) cubic at  $T_c$  = 230 °C. The FE phase of between 228 and 230 °C is sometimes called the FE intermediate phase. The AFE-FE phase transition could occur spontaneously, due to several factors, for example, a change in stress configuration promoted by external mechanical driving fields, an increase in the amplitude of the applied AC electric field, hydrostatic pressure and/or temperature variations [2,3]. For electric field induced AFE to FE phases, transformation requires a very strong electric field in the AFE PZO, otherwise dielectric breakdown occurs instead. Therefore, most AFE ceramics are modified chemically by adding metal oxide at the A- and B-sites of the perovskite structure. The FE intermediate phase can be induced by adding Ba<sup>2+</sup>, Sr<sup>2+</sup>, and La<sup>3+</sup> at the Pb<sup>2+</sup>-site [2,4–7]. Moreover, our recent research found that the FE intermediate phase also can be induced by adding, for example, hybrid-doped Ni<sup>2+</sup>/Nb<sup>5+</sup>, Zn<sup>2+</sup>/Nb<sup>5+</sup>, Co<sup>2+</sup>/Nb<sup>5+</sup> and Mg<sup>2+</sup>/W<sup>6+</sup> at the Zr<sup>4+</sup>-site [8–14].

BiMO<sub>3</sub>;  $M = Fe^{3+}$ ,  $Mn^{3+}$  and  $Nd^{3+}$  has received a lot of attention recently as a multiferroic, and investigation of the solid solutions, BiMO<sub>3</sub>-PbTiO<sub>3</sub>, has shown that they improve ferroelectric properties of PbTiO<sub>3</sub>, reduce the amount of lead, and find new morphotropic phase boundary piezoelectrics [15-18]. However, very little has been known so far about experimental BiMO<sub>3</sub> with nonmagnetic ions (M=Al, Sc, Ga, and In). Furthermore, due to the relatively small size of  $Bi^{3+}$ ,  $Bi(M)O_3$  is not stable in perovskite form, and can be only synthesized under high pressure [19]. The smaller tolerance factor of Bi(M)O<sub>3</sub>, and easily polarized Bi<sup>3+</sup> ion, can enhance the transition temperature further, and with larger piezoelectric effect when solid solution with PbTiO<sub>3</sub> [15]. Crystallized BiAlO<sub>3</sub> is a noncentrosymmetric structure and isotypic with the well-known multiferroic, BiFeO<sub>3</sub>. Theoretical studies by Baettig et al. [20], on a unique ferroelectric phase bismuth aluminate (BiAlO<sub>3</sub>; BAO), predicted that BAO could be a promising novel candidate ferroelectric material, with a high curie temperature of  $\sim$ 530 °C. In 2005, Belik et al. [21] synthesized the compound of BAO by using a high-pressure, high-temperature technique at 6 GPa and 1000-1200 °C. BAO has rhombohedral (R3c) symmetry with lattice parameters given as a = b = 5.37546(5) Å and c = 13.3933(1) Å. Unfortunately, pure stable perovskite BAO ceramics have never been synthesized using a conventional sintering process, due to

<sup>\*</sup> Corresponding author at: Department of Chemistry, Faculty of Science, King Mongkut's Institute of Technology Ladkrabang, Bangkok 10520, Thailand. Fax: +66 2 326 4415.

E-mail address: naratipcmu@yahoo.com (N. Vittayakorn).

the small value of t and electronegativity difference between Aand B-site cations. Zuo et al. [22] investigated the phase transitional behavior and various electrical properties of  $(1 - x)K_{1/2}Na_{1/2}NbO_3$ ; KNN-xBAO ceramics. The results indicate that the addition of BAO significantly influences the sintering, microstructure, phase transition and electrical properties of KNN ceramics. The identification of phase transitional behavior confirms the formation of a MPB between orthorhombic and tetragonal ferroelectric phases in the composition range of  $0.005 \le x \le 0.01$ . Ranjan et al. [23] studied the crystal structure and solid solubility in the PbTiO<sub>3</sub>-BiAlO<sub>3</sub> system. Their study suggested that decrease in stability of the ferroelectric state, due to dilution of the Ti-sublattice by smaller sized Al<sup>3+</sup> ions, was compensated for by the increase in ferroelectric stability by Bi<sup>3+</sup> ions. Although the compositions of Bi(M)O<sub>3</sub>-PbTiO<sub>3</sub> have been investigated widely, few reports on Bi(M)O<sub>3</sub> with other lead perovskite end members are available. To the authors' knowledge, the literature has not reported BAO as incorporated into PZO for solid solutions. Moreover, the effects of substitution in both A- and Bsites on the antiferroelectric phase stability of PZO are still unclear. The  $Bi^{3+}$  ion and  $Al^{3+}$  ion are both smaller than the  $Pb^{2+}$  and  $Zr^{4+}$  ion, respectively. Therefore, in this paper, we report on the how antiferroelectric phase stability is changed by A- and B-site substitution and determine the solubility limit of BAO in PZO.

#### 2. Experimental procedures

#### 2.1. Synthesis

Ceramics of  $(Pb_{(1-3x/2)}Bi_x)(Zr_{1-3x/4}Al_x)O_3$ , with x=0.0–0.3, were synthesized using the conventional ceramic processing procedures [24]. Reagent grade oxide powders of  $Bi_2O_3$  ( $\ge 99.9$ % purity, Cerac), PbO ( $\ge 99.9$ % purity, Kento),  $ZrO_2$  ( $\ge 99.9$ % purity, Advance Material) and  $Al_2O_3$  ( $\ge 99.5$ % purity, Fluka) were weighed according to stoichiometric formula, and ball-milled with ethanol and yttrium-stabilized zirconia media for 18 h. The dried powders were calcined in crucibles at  $700-900\,^{\circ}C$  for 4 h, then ball-milled again for 6 h. The dried calcined powders were mixed with 5 wt% polyvinyl alcohol (PVA) and then pressed into pellets of 15 mm diameter and  $\sim 2$  mm thickness. After burning out PVA binder at  $550\,^{\circ}C$ , the pellets covered with extra powders were sintered in sealed crucibles at between  $1100\,^{\circ}C$  and  $1250\,^{\circ}C$  for 4 h.

#### 2.2. Characterizations

The densities of ceramics were obtained using the Archimedes method. The density of the sintered PZO-BAO pellets was measured by the Archimedes water immersion method. The relative density of all the sintered pellets was approximately 97-98% of the theoretical density. X-ray diffraction (XRD; Bruker-AXS D8) using  $\text{CuK}_{\alpha}$  radiation was utilized to determine the phases formed and optimum firing temperatures for formation of the desired phase for  $0.02 \le x \le 0.3$  compositions. For measuring the dielectric and ferroelectric characteristics, the specimens were polished to 1 mm thickness using sand paper after ultrasonic cleaning in an ethanol bath. Silver-paste (Heraeus C1000) was coated on both sides of the sintered samples by the screen printing method, and then subsequently fired at 650 °C for 30 min. For investigating the dielectric properties, capacitance was measured at 1 kHz using an automated measurement system. This system consisted of an LCR meter (HP-4284, Hewlett-Packard Inc.). The dielectric constant was then calculated from  $\varepsilon_r = Cd/\varepsilon_0 A$ , where C was the capacitance of the sample: d and A were the thickness and area of the electrode, respectively; and  $\varepsilon_0$  was the dielectric permittivity of  $vacuum\,(8.854\times 10^{-12}\,F/m).\,Polarizations, as\,a\,function\,of\,electric\,field\,(P-E\,loop)\,at$  $4\,Hz\,of\,the\,samples, were\,observed\,using\,a\,ferroelectrics\,test\,system\,(RT66B;\,Radiant\,A)$ Technologies, Inc.). The peak field was maintained at 40 kV/cm during measurement.

#### 3. Results and discussion

## 3.1. Crystal structure and physical properties of PZO–BAO solid solutions

The X-ray diffraction patterns of the sintered ceramics,  $(Pb_{(1-3x/2)}Bi_x)(Zr_{1-3x/4}Al_x)O_3$ ; x=0.02-0.3, at room temperature are shown in Fig. 1. The presence of diffraction peaks can be used to evaluate the structural order at long range or periodicity of the material [25]. The patterns indicate that the ceramics possess a phase of perovskite structure, and the crystalline symmetry is

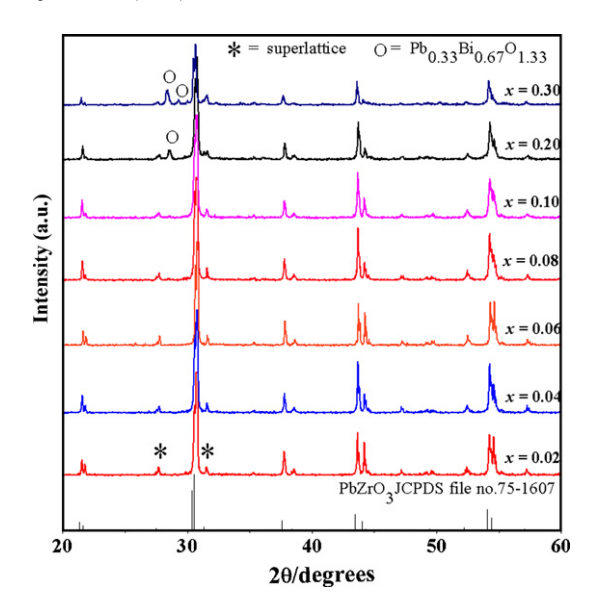


**Fig. 1.** XRD diffraction patterns of sintered  $(Pb_{(1-3x/2)}Bi_x)(Zr_{1-3x/4}Al_x)O_3$ ; x = 0.02 – 0.30 ceramics.

orthorhombic. Phase-pure perovskite structures, with orthorhombic symmetry, were obtained for  $x \le 0.1$ ; however  $x \ge 0.1$ , A cubic pyrochlore phase Pb<sub>0.33</sub>Bi<sub>0.87</sub>O<sub>1.33</sub> (Powder diffraction Files no. 85-0448), identified by "o", began to develop at  $x \ge 0.1$ , and increased in intensity with increasing BAO concentration. These results indicated that the presence of BAO in the solid solution decreases the structural stability of PZO perovskite phase, due to the instability of BAO perovskite under normal conditions and the tolerance factor. The solubility limit of  $(Pb_{(1-3x/2)}Bi_x)(Zr_{1-3x/4}Al_x)O_3$  ceramics is the composition, x = 0.1. The peak positions shifted to higher angles, indicating a slight decrease in the lattice parameter. This phenomenon can be explained qualitatively with respect to the unit cell volume caused by the Bi<sup>3+</sup> and Al<sup>3+</sup> incorporation. The ionic radii of Bi<sup>+3</sup> (Shannon radius = 1.17 Å for CN = 8) and Al<sup>+3</sup> (Shannon radius = 0.535 Å for CN = 6) are less than those of Pb<sup>+2</sup> (Shannon radius = 1.29 Å for CN = 8) and Zr<sup>+4</sup> (Shannon radius = 0.72 Å for CN = 6), respectively [26]. Therefore, Bi<sup>3+</sup> can enter the eight-fold coordinated A-site of the perovskite structure to substitute Pb<sup>2+</sup>, and Al<sup>3+</sup> can enter the six-fold coordinated B-site of the perovskite structure to substitute Zr4+, due to radius matching. The lattice parameters were calculated using the least square refinement from the UNITCELL-97 program [27]. Table 1 shows the lattice parameter and cell volume of  $(Pb_{(1-3x/2)}Bi_x)(Zr_{1-3x/4}Al_x)O_3$  ceramics. The substitution of the relatively smaller Bi<sup>3+</sup> and Al<sup>3+</sup> for the comparatively larger Pb<sup>2+</sup> and Zr<sup>4+</sup> led to a decrease in the unit cell volume. This seems to be the case for  $x \le 0.01$  only, as composition,  $x \ge 0.01$ , is close to the solubility limit, but this argument does not apply due to the inhomogeneous distribution factor.

Fig. 2 shows enlarged profiles of the  $1/4~(h\,k\,l)$  superlattice reflection (\*) and  $(2\,4\,0)/(0\,0\,4)$  for determining the crystal structure of as-sintered ceramics. By increasing BAO concentration, the remaining  $1/4~(h\,k\,l)$  superlattice reflection peaks indicated the remainder of antiparallel displacements of A-site ions in the perovskite structure. It is interesting to note that the substitution of BAO does not change the crystalline structure of PZO ceramics within the studied doping level. The influence of BAO addition on the phase structure of the PZO–BAO system is similar to that of the PT-BAO system [23,28]. The tolerance factor (t) for perovskite structure can be described by the general formula for ABO<sub>3</sub>;  $t=(R_A+R_O)/(\sqrt{2})(R_B+R_O)$ , where  $R_A$  is the radius of A(CN=8),  $R_B$  the radius of B(CN=6) and  $R_O$  the radius of oxygen(CN=8). When t is >1, the FE phase is stabilized, and when t is <1, the AFE phase is sta-

**Table 1** Summary of the lattice parameters of  $(Pb_{(1-3x/2)}Bi_x)(Zr_{1-3x/4}Al_x)O_3$ ; x = 0.02–0.1 ceramics.

Composition (x)	Lattice parameters	Lattice parameters			
	а	b	С		
0.00	$5.8835 \pm 0.0003$	$11.7672 \pm 0.0008$	$8.2177 \pm 0.0007$	568.93	
0.02	$5.8629 \pm 0.0207$	$11.7258 \pm 0.0414$	$8.2171 \pm 0.0273$	564.89	
0.04	$5.8609 \pm 0.0225$	$11.7221 \pm 0.0453$	$8.2116 \pm 0.0253$	564.15	
0.06	$5.8584 \pm 0.0237$	$11.7167 \pm 0.0473$	$8.2023 \pm 0.0195$	563.01	
0.08	$5.8545 \pm 0.0258$	$11.7113 \pm 0.0494$	$8.2022 \pm 0.0159$	562.37	
0.10	$5.8522 \pm 0.0275$	$11.7106 \pm 0.0527$	$8.2007 \pm 0.0124$	562.01	

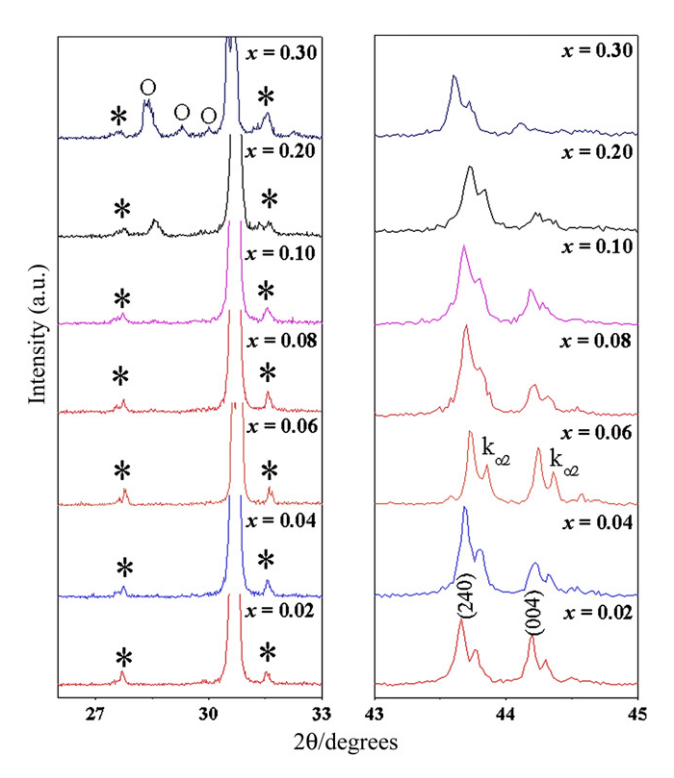


**Fig. 2.** X-ray diffraction profiles for the 1/4 (hkl) superlattice reflection (\*), pyrochlore phase ( $\bigcirc$ ) and (240)/(004) peaks of  $(Pb_{(1-3x/2)}Bi_x)(Zr_{1-3x/4}Al_x)O_3$ ; x = 0.02 - 0.30 ceramics.

bilized [29]. The average ionic radius of the A- and B-site ions in the  $(Pb_{(1-3x/2)}Bi_x)(Zr_{1-3x/4}Al_x)O_3$  can be calculated from the following equation:

$$r_{\text{A-site}} = \left(1 - \frac{3x}{2}\right) r_{\text{Pb}^{2+}} + x r_{\text{Bi}^{3+}}$$
 (1)

$$r_{\text{B-site}} = \left(1 - \frac{3x}{4}\right) r_{\text{Zr}^{4+}} + x r_{\text{Al}^{3+}} \tag{2}$$

where the ionic radii of Pb<sup>2+</sup>, Bi<sup>3+</sup>, Zr<sup>4+</sup> and Al<sup>3+</sup> are 1.29 Å, 1.17 Å, 0.72 Å and 0.535 Å, respectively [26]. The average ionic radius of the A- and B-site ions and tolerance factor in the  $(Pb_{(1-3x/2)}Bi_x)(Zr_{1-3x/4}Al_x)O_3$  ceramics are shown in Table 2. The calculated tolerance factor of the  $(Pb_{(1-3x/2)}Bi_x)(Zr_{1-3x/4}Al_x)O_3$ ; x=0.02-0.3 is between 0.8904 and 0.8202, indicating that AFE behavior is expected to be seen at room temperature. Dielectric and ferroelectric properties; later explained, support this assumption. Furthermore, as expected, the stability of perovskite structure decreases with increasing BAO concentration, due to the small tolerance factor value.

#### 3.2. Dielectric properties

Temperature dependence of relative permittivity  $(\varepsilon_r)$  and dielectric loss  $(\tan \sigma)$  for  $(Pb_{(1-3x/2)}Bi_x)(Zr_{1-3x/4}Al_x)O_3$ ; x = 0.02–0.3

**Table 2** Average ionic radius of A-site, B-site ions and tolerance factor in the  $(Pb_{(1-3x/2)}Bi_x)(Zr_{1-3x/4}Al_x)O_3$  ceramics.

Compositions (x)	$R_{A-site}$	$R_{\text{B-site}}$	Tolerance factor $(t)$	
0.02	1.2747	0.7199	0.8904	
0.04	1.2594	0.7198	0.8854	
0.06	1.2441	0.7197	0.8804	
0.08	1.2288	0.7196	0.8754	
0.10	1.2135	0.7195	0.8704	
0.20	1.1370	0.7190	0.8453	
0.30	1.0605	0.7185	0.8202	

ceramics were measured at 1, 10 and 100 kHz, as shown in Fig. 3. It is well known that pure PZO has two dielectric anomaly peaks reported at 228 and 230 °C, which corresponds to the phase transitions of orthorhombic antiferroelectric (AFE) phase to rhombohedral FE intermediate phase and rhombohedral FE intermediate phase to cubic paraelectric phase, respectively. Furthermore, the FE intermediate phase can be induced easily by adding  $Ba^{2+}$ ,  $Sr^{2+}$ , and  $Ca^{2+}$  at the  $Pb^{2+}$ -site [2,4–7] or  $Ni^{2+}/Nb^{5+}$ ,  $Zn^{2+}/Nb^{5+}$ ,  $Co^{2+}/Nb^{5+}$  and  $Mg^{2+}/W^{6+}$  at the  $Zr^{4+}$ -site [8–14]. As shown in Fig. 3, a single sharp dielectric permittivity peak arises in all ceramic samples. Interestingly, the dielectric results showed one sharp dielectric peak anomaly, indicating that the FE intermediate phase did not exist in  $(Pb_{(1-3x/2)}Bi_x)(Zr_{1-3x/4}Al_x)O_3$ ; x = 0.02-0.3 samples. Increasing BAO concentration resulted in a very small decrease in transition temperature. No frequency dependence of dielectric response or shift in transition temperature with frequency was observed under transition temperature, which indicated no evidence of relaxor-like Pb(Zr,Ni,Nb)O<sub>3</sub> [8,10] or (Pb,Ba)ZrO<sub>3</sub> [5,7]. Nevertheless, at high temperature, the dielectric data revealed an enhanced dielectric loss with increasing BAO concentration. At 1 kHz measurement, frequent higher losses were found to persist to a significantly lower temperature. These results demonstrated that the enhanced dielectric losses at higher temperatures are due to a space charge mechanism [30]. For the composition,  $x \ge 0.2$ , the maximum relative permittivity decreases steadily with increasing BAO content ( $\varepsilon_{\rm r}$  decreases from ~3700 in composition x = 0.1 - 700 in composition x = 0.3), and the lower value is attributed to the detrimental effect of the secondary pyrochlore phase.

#### 3.3. Thermal properties

The DSC technique was used as the second tool to confirm the phase transition of PZO–BAO ceramics. Fig. 4 shows the temperature dependences of the heat flow (DSC curves) obtained when heating the  $(Pb_{(1-3x/2)}Bi_x)(Zr_{1-3x/4}Al_x)O_3$ ; x=0.02-0.3 samples at the rate of  $10 \, \text{K/min}^{-1}$ . A single endothermic peak was observed for all compositions. The peaks shifted slightly to lower temperatures with increasing BAO concentrations. This transition temperature corresponds to the Curie temperature of the AFE to PE transformation. However, there is no significant difference in the temperature of AFE to PE phase transition in the composition,  $x \ge 0.08$ . This could be related to appearance of the pyrochlore phase. The DSC results

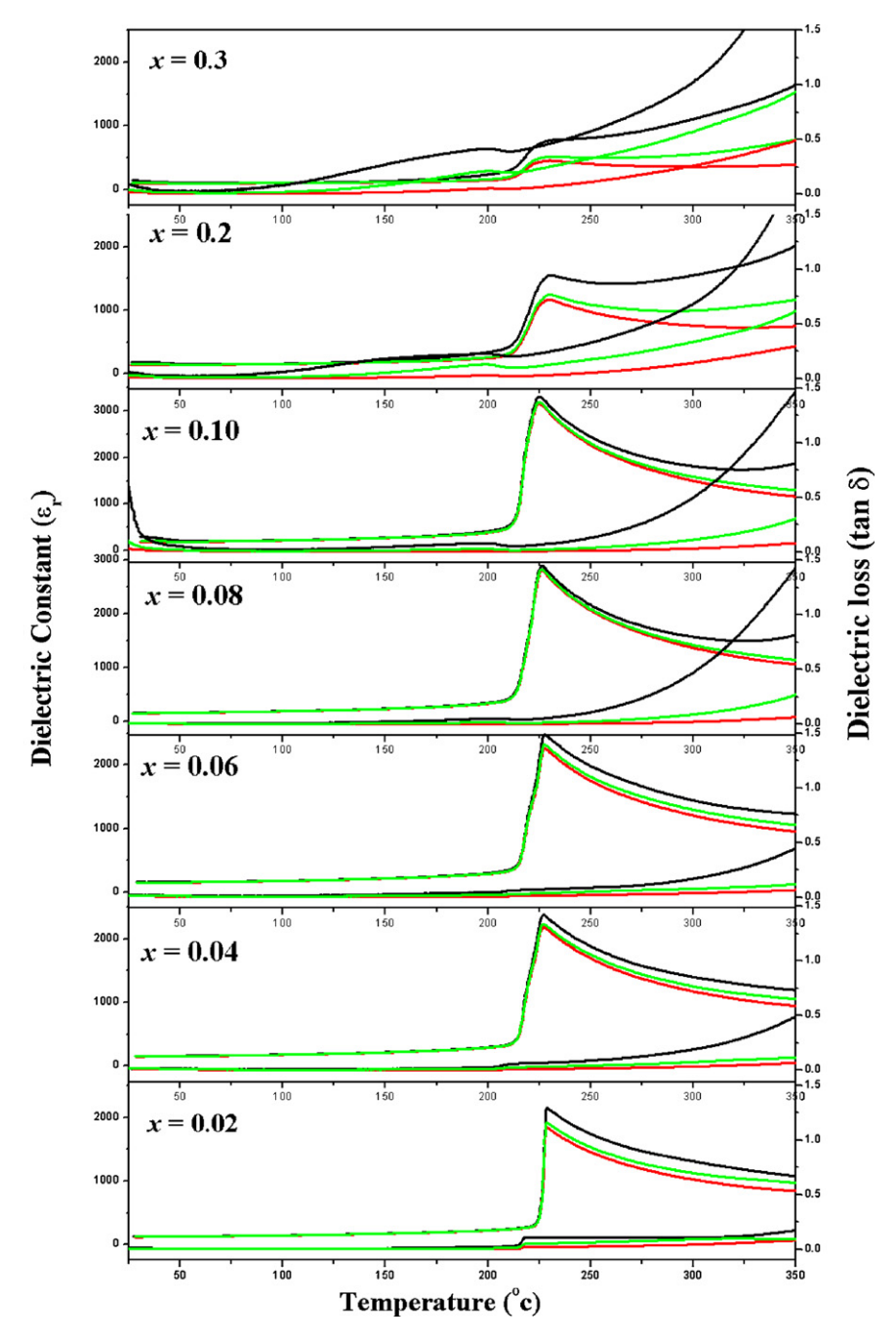


**Fig. 3.** Relative permittivity  $(\varepsilon_r)$  and dielectric loss  $(\tan \delta)$  as a temperature function of  $(Pb_{(1-3x/2)}Bi_x)(Zr_{1-3x/4}Al_x)O_3$ ; x = 0.02 - 0.3 ceramics.

observed are consistent with dielectric measurement results. It should be pointed out that the difference in AFE-PE transition temperature values in dielectric, ferroelectric and DSC measurement techniques is due to the difference in heating rate and well time of the measurement.

Thermodynamic parameter, enthalpy  $(\Delta H^*/J g^{-1})$ , heat capacity  $(C_p/J g^{-1} K^{-1})$ , entropy change  $(\Delta S^*/J g^{-1} K^{-1})$ , and Gibbs energy change  $(\Delta G^*/J g^{-1})$ , were calculated from the DSC results. The enthalpy change was calculated directly from the amount of heat change involved in each step per unit mass of the sample.  $\Delta H^*$ , thus determined, was implemented to calculate the specific heat capacity  $(C_p)$  using the following equation [31,32]

$$C_p = \frac{\Delta H}{\Delta T} \tag{3}$$

where  $\Delta T = T_2 - T_1$ ;  $T_1$  is the temperature at which the DSC peak begins to depart from the baseline; and  $T_2$  is the temperature at which the peak lands. Consequently, the changes of entropy ( $\Delta S^*$ ) and Gibbs energy ( $\Delta G^*$ ) were calculated using the following equations [31,32]

$$\Delta S^* = 2.303C_p \log \left(\frac{T_2}{T_1}\right) \tag{4}$$

$$\Delta H^* = \Delta G^* - T_p \Delta S^* \tag{5}$$

On the basis of the DSC data, the value of  $\Delta H^*$ ,  $\Delta S^*$ ,  $C_p$  and  $\Delta G^*$  for the phase transition can be calculated according to Eqs. (3)–(5), and is presented in Table 3. The peak value of heat capacity became weaker, and anomaly of heat capacity gradually broader, with increasing BAO concentration. These results indicated that the phase transition deviates gradually from the first

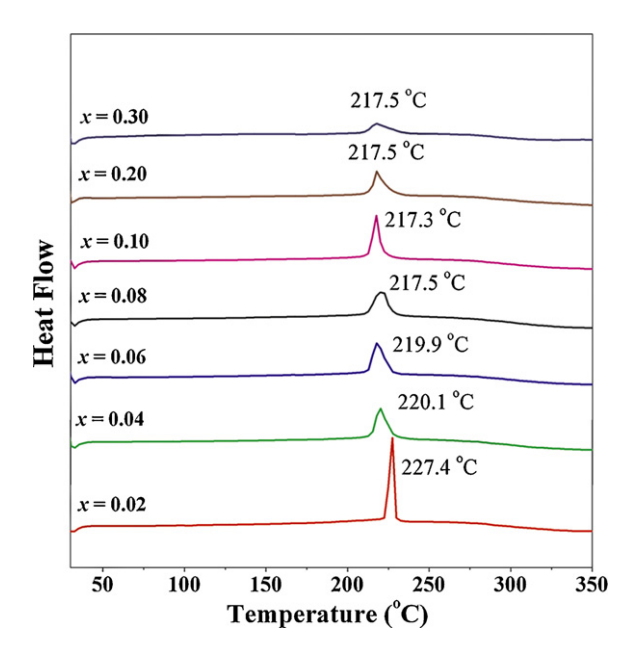


**Fig. 4.** Typical DSC curves for  $(Pb_{(1-3x/2)}Bi_x)(Zr_{1-3x/4}Al_x)O_3$ ; x = 0.02-0.3 ceramics.

order type. Furthermore, the enthalpy ( $\Delta H^*$ ) continues to decrease with increasing BAO content, indicating that BAO decreases the energy requirement for transition from AFE to FE. Stenger and Burggraaf [33] observed that the change in entropy ( $\Delta S^*$ ) correlates with the fluctuation probability in conjunction with a small spontaneous lattice deformation and polarization. With increasing BAO content, there is no significant change in  $\Delta S^*$ , indicating the stability of energy required to reorient the antiferroelectric sublattices in the PZO–BAO system [33]. On the other hand, the thermodynamic parameter,  $\Delta H^*$  and  $\Delta G^*$ , calculated according to Eqs. (3)–(5), gives the positive values, indicating that the AFE to PE phase transitions are connected to the introduction of heat, and phase transitions are non-spontaneous processes.

#### 3.4. Ferroelectric properties

In order to examine how the phase transition occurs with temperature, electrical polarization hysteresis loop measurements were performed under a peak field of  $40\,\text{kV/cm}$  at a series of temperatures for  $(\text{Pb}_{(1-3x/2)}\text{Bi}_x)(\text{Zr}_{1-3x/4}\text{Al}_x)\text{O}_3$  ceramics. A disk specimen, with a diameter of about 10 mm and thickness around  $600\,\mu\text{m}$  was used. The loop was recorded after the temperature was stabilized for at least 5 min. At  $30\,^{\circ}\text{C}$ , no ferroelectric hysteresis loop was observed for any compositions  $(0.0 \le x \le 0.3)$ . The linear polarization was observed, due perhaps to the extremely high coercive field, indicating that the composition,  $x \le 0.3$ , belongs to the AFE phase at room temperature. The Pb $_{0.94}\text{Bi}_{0.04}\text{Zr}_{0.97}\text{Al}_{0.04}\text{O}_3$  ceramic was selected for further investigation of the polarization behavior sequence during heating to  $220\,^{\circ}\text{C}$ . The polarization behavior of Pb $_{0.94}\text{Bi}_{0.04}\text{Zr}_{0.97}\text{Al}_{0.04}\text{O}_3$  ceramic as a function of temperature is

shown in Fig. 5. For the Pb<sub>0.94</sub>Bi<sub>0.04</sub>Zr<sub>0.97</sub>Al<sub>0.04</sub>O<sub>3</sub> composition, such linear behavior with minimum polarization remains at temperatures of up to 195 °C. When the temperature was raised to 200 °C, a double hysteresis loops started to develop, indicating the occurrence of electric field-induced antiferroelectric-to-ferroelectric phase transition. The transition from a minor loop at low field to a saturated double-shaped hysteresis loop at high field occurs at 205 °C by increasing the electric fields. This is expected because an antiferroelectric crystal generally has a zero net switchable dipole moment, due to the antiparallel alignment of elementary dipoles in its unit cell. When the external electric field is weak, the induced polarization is proportional to the electric field and demonstrates no macroscopic polarization hysteresis [34]. While the electric field exceeds a threshold value, called the critical field, the crystal becomes ferroelectric and the polarization displays hysteresis with respect to the field. A hysteresis loop also forms in the negative field, with the two loops being associated with antiparallel dipoles in adjacent unit-cell sublattices. As the temperature increases to 215 °C, the critical field is slowly reduced. This is caused by a higher temperature that provides higher thermal fluctuation to the polarization order parameter, which reduces the ferroelectric interaction among the dipoles.

In addition, when the temperature was increased to above 225 °C, a linear curve also was seen as an indication of the cubic paraelectric (PE) phase. Fig. 6 shows the polarization versus electric field hysteresis loops at 205 °C for the  $(Pb_{(1-3x/2)}Bi_x)(Zr_{1-3x/4}Al_x)O_3$ ; x = 0.02 - 0.08 ceramics. The double hysteresis behavior in polarization, with an applied electric field, clearly demonstrates the antiferroelectric nature of  $(Pb_{(1-3x/2)}Bi_x)(Zr_{1-3x/4}Al_x)O_3$ ; x = 0.02-0.08ceramics. The remanent polarization,  $P_r$ , slightly decreases between x = 0.02 and 0.08, from 23.26  $\mu$ C/cm<sup>2</sup> to 19.4  $\mu$ C/cm<sup>2</sup>. The AFE-FE switching field decreases for x = 0.02 and 0.08 from 29.23 kV/cm to13.81 kV/cm. In Berlincourt's [35] study of doped Pb(Zr,Sn,Ti)O<sub>3</sub> ceramics, two different types of AFE to FE transitions based on the character of the P-E hysteresis loop were described; the two types of double hysteresis loops have been termed "square" and "slanted". The "slanted" double hysteresis loop ceramics have far less hysteresis, small volume difference between AFE and FE phases, lower transition fields and a wider temperature range, over which the transition can be induced by electric fields. The "slanted" double hysteresis loop ceramics exhibit a small remanent polarization at zero fields, while the "square" loop ceramics do not. The P-E hysteresis loop measurements demonstrate that the ferroelectric properties of ceramics in the PZO-BAO system shift gradually from "square" to "slanted" antiferroelectric behavior, with increasing BAO concentrations. Interestingly, with increasing temperatures from room temperature to 250 °C, antiferroelectric to ferroelectric intermediate phase transition was not observed in any compositions, which indicated no ferroelectric intermediate phase in the PZO-BAO ceramics. Chu et al. [36] pointed out that the area enclosed by the decreasing field part of the polarizationelectric field trace represented a stored electrical energy density. The ferroelectric results show that the PZO-BAO ceramics have large polarization at a high electric field and a large area between the polarization axis and curve. There are indications that this

Values of thermodynamic parameters for phase transition of the  $(Pb_{(1-3x/2)}Bi_x)(Zr_{1-3x/4}Al_x)O_3$  ceramics calculated from DSC data.

$T_p/K$	$\Delta H^*/\mathrm{J}\mathrm{g}^{-1}$	$C_p/J g^{-1} K^{-1}$	$\Delta S^*/Jg^{-1}K^{-1}$	$\Delta G^*/\mathrm{J}\mathrm{g}^{-1}$
499	3.825	$7.665 \times 10^{-3}$	$6.145 \times 10^{-5}$	3.856
497	3.749	$7.543 \times 10^{-3}$	$6.163 \times 10^{-5}$	3.795
491	3.348	$6.819 \times 10^{-3}$	$6.438 \times 10^{-5}$	3.382
490	2.815	$5.745 \times 10^{-3}$	$6.336 \times 10^{-5}$	2.849
489	2.676	$5.461 \times 10^{-3}$	$6.193 \times 10^{-5}$	2.901
490	2.360	$4.816 \times 10^{-3}$	$6.851 \times 10^{-5}$	2.408
489	1.429	$2.922 \times 10^{-3}$	$5.985 \times 10^{-5}$	1.455
	499 497 491 490 489 490	499 3.825 497 3.749 491 3.348 490 2.815 489 2.676 490 2.360	$\begin{array}{cccccccccccccccccccccccccccccccccccc$	$\begin{array}{cccccccccccccccccccccccccccccccccccc$

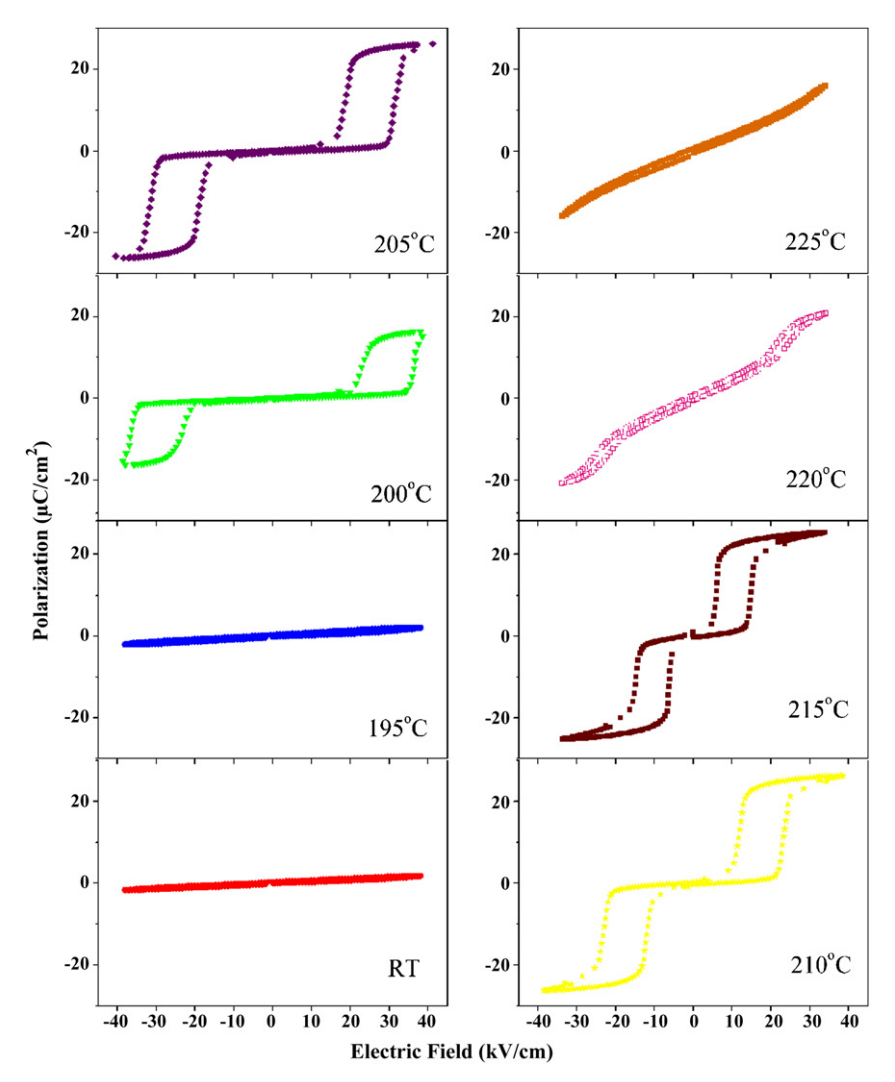


**Fig. 5.** Polarization hysteresis loops recorded from  $Pb_{0.94}Bi_{0.04}Zr_{0.97}Al_{0.04}O_3$  ceramic at 4 Hz during heating.

material can therefore store much more energy than either the ferroelectric or linear dielectric materials.

There is good agreement between results of the three different investigation techniques. The results indicated that BAO modification can stabilize an antiferroelectric state in perovskite PZO. It is well known that the ionic size and distribution of substituent on the A- and B-site have been shown to affect antiferroelectric phase stability. If A-site ions are replaced by larger ones or a B-site ion by a smaller one, ferroelectric phase stability is enhanced. However, if A-site ions are replaced by smaller ones, or a B-site ion by a larger one, then antiferroelectric phase stability is enhanced [37]. However, in the PZO-BAO system, the ionic radius of Bi<sup>3+</sup> (1.17 Å) and  $Al^{3+}$  (0.535 Å) are both smaller than  $Pb^{2+}$  (1.29 Å) and  $Zr^{4+}$  (0.72 Å), respectively. These results clearly demonstrate that the stability in antiferroelectric phase PZO, by substituting Pb<sup>2+</sup> (1.29 Å) with Bi<sup>3+</sup> (1.17 Å) in the A-site of the ABO<sub>3</sub> perovskite structure, are much more pronounced than substitution of Zr<sup>4+</sup> by Al<sup>3+</sup> in the B-site of the perovskite structure. This is because the decreasing average rate of radii in the A-site (0.765 Å/mol) is much higher than that in the B-site radii (0.005 Å/mol) as shown in Table 1. The decreasing average of radii in the A-site causes decreasing space in which the B-site cation is allowed to "rattle". This in turn decreases the polarizability, which facilitates a decrease in the Curie point. The results clearly demonstrated that the ionic radii of the substituent are an important factor in controlling the structure-property relations by compositional design.

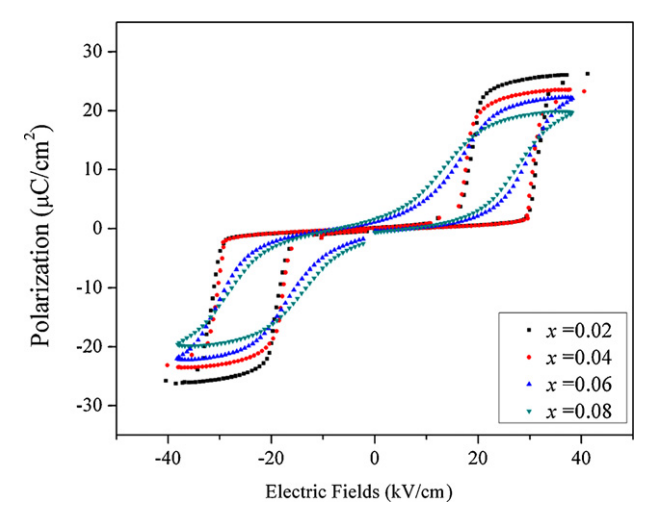


**Fig. 6.** Electric hysteresis loops of  $(Pb_{(1-3x/2)}Bi_x)(Zr_{1-3x/4}Al_x)O_3$ ; x = 0.02–0.08 ceramics at 205 °C.

#### 4. Conclusions

The investigation of  $(Pb_{(1-3x/2)}Bi_x)(Zr_{1-3x/4}Al_x)O_3$ ; x = 0.02-0.3 using X-ray diffraction, dielectric behavior, thermal properties and ferroelectric measurements have shown clearly that phase

N. Vittayakorn, B. Boonchom / Journal of Alloys and Compounds 509 (2011) 2304-2310

pure perovskite ceramics in the  $(Pb_{(1-3x/2)}Bi_x)(Zr_{1-3x/4}Al_x)O_3$  system can be prepared by the solid-state reaction method with up to 10 mol% of BiAlO<sub>3</sub>. Phase-pure perovskite structures with orthorhombic symmetry were obtained for  $x \le 0.1$ ; however  $x \ge 0.1$ , A cubic pyrochlore phase Pb<sub>0.33</sub>Bi<sub>0.87</sub>O<sub>1.33</sub> began to develop at  $x \ge 0.1$  and increased in intensity with increasing BAO concentration. The substitution of the relatively smaller Bi<sup>3+</sup> and Al<sup>3+</sup> for the comparatively larger  $Pb^{2+}$  and  $Zr^{4+}$  led to a decrease in the unit cell volume. Dielectric, thermal and P-E hysteresis results confirmed that there was no ferroelectric intermediate phase in the PZO-BAO system, and only antiferroelectric to paraelectric phase transition was obtained for a wide temperature range. The results confirmed that BAO is shown to be a stable antiferroelectric state in PZO in a wide temperature range. The stability in antiferroelectric phase PZO by substituting  $Pb^{2+}$  (1.29 Å) with  $Bi^{3+}$  (1.17 Å) in the A-site of the ABO<sub>3</sub> perovskite structure is much more pronounced than substitution of  $Zr^{4+}$  by  $Al^{3+}$  in the B-site of the perovskite structure. The  $(Pb_{(1-3x/2)}Bi_x)(Zr_{1-3x/4}Al_x)O_3$  solid solution offers a material system for possible applications in high-energy-storage capacitors and electromechanical transducers.

#### Acknowledgements

This research was supported by a grant from the Thailand Research Fund (TRF) National Research Council of Thailand (NRCT) and the National Nanotechnology Center (NANOTEC) NSTDA, Ministry of Science and Technology, Thailand, through its "Center of Excellence Network" program.

#### References

- [1] F. Jona, G. Shirane, F. Mazzi, R. Pepinsky, Phys. Rev. 105 (1957) 849-856.
- [2] D. Xunhu, Z. Xu, V. Dwight, J. Appl. Phys. 77 (1995) 5086-5094.
- [3] X. Dai, J.F. Li, D. Viehland, Phy. Rev. B 51 (1995) 2651-2655.
- [4] B.P. Pokharel, D. Pandey, J. Appl. Phys. 86 (1999) 3327–3332. [5] B.P. Pokharel, D. Pandey, Phys. Rev. B 65 (2002) 214108.
- [6] N. Vittayakorn, T. Bongkarn, G. Rujijanagul, Physica B 387 (2007) 415–420.
- [7] X. Hao, Z. Zhang, J. Zhou, S. An, J. Zhai, J. Alloys Compd. 501 (2010) 358-361.

- [8] S. Wirunchit, P. Laoratanakul, N. Vittayakorn, J. Phys. D: Appl. Phys. 41 (2008) 125406.
- [9] N. Vittayakorn, S. Wirunchit, Smart Mater. Struct. 16 (2007) 851-857.
- [10] S. Wirunchit, N. Vittayakorn, J. Appl. Phys. 104 (2008) 024103.
  [11] W. Banlue, N. Vittayakorn, Ferroelectrics 382 (2009) 122–126.
- [12] W. Banlue, N. Vittayakorn, Appl. Phys. A 93 (2008) 565-569.
- [13] N. Vittayakorn, W. Banlue, Ferroelectrics 382 (2009) 110-114.
- [14] P. Charoonsuk, S. Wirunchit, R. Muanghlua, S. Niemcharoen, B. Boonchom, N. Vittayakorn, J. Alloys Compd. 506 (1) (2010) 313-316.
- [15] R.E. Eitel, C.A. Randall, T.R. Shrout, P.W. Rehrig, W. Hackenberger, S.E. Park, Jpn. I. Appl. Phys. 40 (2001) 5999–6002.
- [16] C.J. Stringer, T.R. Shrout, C.A. Randall, I.M. Reaney, J. Appl. Phys. 99 (2006) 024106.
- [17] M.R. Suchomel, P.K. Davies, J. Appl. Phys. 96 (2004) 4405-4410.
- [18] M.R. Suchomel, P.K. Davies, Appl. Phys. Lett. 86 (2005) 262905.
- [19] M.R. Suchomel, A.M. Fogg, M. Allix, H. Niu, J.B. Claridge, M.J. Rosseinsky, Chem. Mater. 18 (2006) 4987-4989.
- [20] P. Baettig, C.F. Schelle, R. LeSar, U.V. Waghmare, N.A. Spaldin, Chem. Mater. 17 (2005) 1376–1380.
- [21] A.A. Belik, T. Wuernisha, T. Kamiyama, K. Mori, M. Maie, T. Nagai, Y. Matsui, E. Takayama-Muromachi, Chem. Mater. 18 (2005) 133-139.
- [22] R. Zuo, D. Lv, J. Fu, Y. Liu, L. Li, J. Alloys Compd. 476 (2009) 836–839.
- R. Ranjan, A.K. Kalyani, R. Garg, P.S.R. Krishna, Solid State Commun. 149 (2009) 2098-2101.
- [24] T. Badapanda, S.K. Rout, L.S. Cavalcante, J.C. Sczancoski, S. Panigrahi, T.P. Sinha, E. Longo, Mater. Chem. Phys. 121 (2010) 147-153.
- [25] L.S. Cavalcante, V.S. Marques, J.C. Sczancoski, M.T. Escote, M.R. Joya, J.A. Varela, M.R.M.C. Santos, P.S. Pizani, E. Longo, Chem. Eng. J. 143 (2008) 299-307.
- [26] R.D. Shannon, Acta Cryst. A 32 (1976) 751–767.
- [27] T.J.B. Holland, S.A.T. Redfern, Miner. Mag. 61 (1997) 65-77.
- [28] A.K. Kalyani, R. Garg, R. Ranjan, Appl. Phys. Lett. 94 (2009) 202903.
- [29] K.J. Rao, C.N.R. Rao, Phase Transitions in Solid: An Approach to the Study of the Chemistry and Physics of Solids, McGraw-Hill, New York, 1978.
- [30] M.E. Lines, A.M. Glass, Principles and Applications of Ferroelectrics and Related Materials, Clarendon press, Oxford, 1977
- [31] S.A. Halawy, N.E. Fouad, M.A. Mohamed, M.I. Zaki, J. Therm. Anal. Calorim. 82 (2005) 671–675.
- [32] R.H. Abu-Eittah, N.G. ZaKi, M.M.A. Mohamed, L.T. Kamel, J. Anal. Appl. Pyrol. 77 (2006) 1 - 11.
- [33] C. Stenger, A.J. Burggraaf, Phys. Stat. Sol. 61 (1980) 275–285.
- [34] F. Moura, A.Z. Simões, L.S. Cavalcante, M.A. Zaghete, J.A. Varela, E. Longo, J. Alloys Compd. 466 (1-2) (2008) L15-L18.
- [35] D. Berlincourt, IEEE Trans. Sonics Ultrason. Ind. Eng. Chem. SU-13 (1966) 116-124.
- [36] B. Chu, X. Zhou, K. Ren, B. Neese, M. Lin, Q. Wang, F. Bauer, Q.M. Zhang, Science 313 (2006) 334-336
- [37] Q. Tan, Z. Xu, D. Viehland, J. Mater. Res. 14 (1999) 4251.

Provided for non-commercial research and education use. Not for reproduction, distribution or commercial use.



This article appeared in a journal published by Elsevier. The attached copy is furnished to the author for internal non-commercial research and education use, including for instruction at the authors institution and sharing with colleagues.

Other uses, including reproduction and distribution, or selling or licensing copies, or posting to personal, institutional or third party websites are prohibited.

In most cases authors are permitted to post their version of the article (e.g. in Word or Tex form) to their personal website or institutional repository. Authors requiring further information regarding Elsevier's archiving and manuscript policies are encouraged to visit:

http://www.elsevier.com/copyright

### Author's personal copy

Journal of Alloys and Compounds 509 (2011) 2445-2449



Contents lists available at ScienceDirect

## Journal of Alloys and Compounds

journal homepage: www.elsevier.com/locate/jallcom



## Solution combustion synthesis and characterization of lead-free piezoelectric sodium niobate (NaNbO<sub>3</sub>) powders

Nopsiri Chaiyo <sup>a,b</sup>, Rangson Muanghlua <sup>c</sup>, Surasak Niemcharoen <sup>c</sup>, Banjong Boonchom <sup>d</sup>, Naratip Vittayakorn <sup>a,b,e,\*</sup>

- <sup>a</sup> Electroceramic Research Laboratory, College of KMITL Nanotechnology, King Mongkut's Institute of Technology Ladkrabang, Bangkok 10520, Thailand
- <sup>b</sup> ThEP Center, CHE, 328 Si Ayutthaya Rd., Bangkok 10400, Thailand
- c Department of Electronics, Faculty of Engineering, King Mongkut's Institute of Technology Ladkrabang, Bangkok 10520, Thailand
- d King Mongkut's Institute of Technology Ladkrabang, Chumphon Campus, 17/1 M. 6 Pha Thiew District, Chumphon 86160, Thailand
- e Department of Chemistry, Faculty of Science, King Mongkut's Institute of Technology Ladkrabang, Bangkok 10520, Thailand

#### ARTICLE INFO

#### Article history: Received 20 July 2010 Received in revised form 27 October 2010 Accepted 8 November 2010 Available online 13 November 2010

Keywords: Sodium niobate Modified solid state reaction

#### ABSTRACT

Nano-crystalline sodium niobate (NaNbO $_3$ ) powder was synthesized by the solution combustion synthesis of sodium nitrate (NaNO $_3$ ) and Nb $_2$ O $_5$  using glycine as the fuel. The chemical reaction, nucleation mechanisms and influence of the fuel-to-oxidizer ratio to phase formation were studied. The precursor and product powders were characterized, using thermo gravimetric analysis (TGA), differential thermal analysis (DTA), the X-ray diffraction technique (XRD), scanning electron microscope (SEM) and Fourier transform infrared (FTIR) spectroscopy. As-prepared powder possesses an orthorhombic crystal structure with an X-ray diffraction pattern that could be matched with the perovskite, NaNbO $_3$  JCPDS no. 82-0606. Perovskite NaNbO $_3$  phase, with a mean crystalline size (calculated by X-ray line broadening) ranging from 44.51  $\pm$  11.99 nm (ratio of 0.7) to 26.11  $\pm$  13.69 nm (ratio of 2.0) was obtained. The SEM image shows polyhedral-shaped powder with a mean particle size of 137  $\pm$  52 nm and 226  $\pm$  46 nm for as-prepared and calcined powder, respectively.

© 2010 Elsevier B.V. All rights reserved.

#### 1. Introduction

Sodium niobate (NaNbO<sub>3</sub>) is a perovskite with an inorganic complex oxide and the empirical formula, ABO<sub>3</sub>. It is among the candidates for lead-free substances that avoid toxicity of lead-based piezoelectric materials (e.g. PZT [1,2]), and is concerned about the environment. NaNbO<sub>3</sub> has been studied widely for its unusual structural transition series [3–7]. It has a ferroelectric rhombohedral phase below  $-100\,^{\circ}\text{C}$ , and is antiferroelectric with orthorhombic symmetry between  $-100\,^{\circ}\text{C}$  and  $640\,^{\circ}\text{C}$  [4]. Finally, it possesses cubic paraelectric above  $640\,^{\circ}\text{C}$  [5], and in addition, its antiferroelectric, perovskite-type nature can transform into a ferroelectric one by chemical doping, i.e. K<sup>+</sup> [6,7] and Li<sup>+</sup> [8].

Generally, alkali niobate powders are synthesized by conventional solid state reaction, where alkali metal carbonate or oxide compound of starting materials are heated at high temperature ( $800\,^{\circ}\text{C}$  or above) for a long duration [8,9]. High calcination temperature can cause volatilization of alkali metal, thus causing this

E-mail address: naratipcmu@yahoo.com (N. Vittayakorn).

classical method difficulty in achieving a homogeneous mixture of the component [8–10]. Powder agglomeration can occur during heating, which could affect properties such as low surface area and low sinterability [10]. Thus, this method does not always allow for the production of dense, homogeneous single phase ceramics. Therefore, development of alternative methods that can produce powder with high sinterability and controlled stoichiometric composition is necessary. In recent years, ultra fine ceramic powder, which is synthesized using mechanochemical synthesis [11], polymeric precursors [12], and hydrothermal and polymerized complex methods [13], has been described in the literature to enable production of desired compositions. While synthesizing powder rapidly, with the desired composition, high porosity and high sinterability remains a challenge, combustion synthesis (CS) has been found as a potential solution for this problem.

Combustion synthesis (CS) or self-propagating high temperature synthesis (SHS) is an effective, low-cost method for producing various industrially useful materials. It has been introduced as a quick, straightforward preparation process for producing homogeneous, very fine, crystalline and unagglomerated multicomponent oxide ceramic powders, without intermediate decomposition and/or calcination steps [14,15]. The combustion synthesis technique begins with a mixture of easily oxidized reactants (such as nitrates) and a suitable organic fuel (such as urea [16], tartalic acid

<sup>\*</sup> Corresponding author at: Department of Chemistry, Faculty of Science, King Mongkut's Institute of Technology Ladkrabang, Bangkok 10520, Thailand. Fax: +66 2 326 4415.

[17], alanine [18], glycine [19], etc.), which acts as a reducing agent. The mixture is then heated until it ignites, which is when the temperature of rapid exothermal chemical reaction commences, and a self-sustaining combustion reaction starts. This highly exothermic reaction produces a high temperature and duration long enough for the synthesis to occur, even in the absence of an external heating source [20]. Ultrafine nano-sized powder also can be prepared by releasing a large amount of gas from the system. This process results in a dry, fluffy, crystalline, unagglomerated and fine oxide powder. Metal nitrate was found to be the salt preferred, due to its water solubility, and homogeneous solution could be achieved easily by melting at a low temperature [16].

However, it was reported that an exothermic redox reaction (oxidation and reduction reaction taking place simultaneously) could be initiated only when the oxidizer and fuel are mixed intimately in a fixed proportion. The basis of the combustion synthesis process derives from the thermochemical concepts used in propellant chemistry [21,22]. The method consists of establishing a simple valency balance, irrespective of whether the elements are present in the oxidizer or fuel components of the mixture, and then calculating the stoichiometric composition of the starting mixture, which is equivalent to the release of maximum energy. The assumed valencies, which are presented as usual products of the combustion reaction, consist of CO<sub>2</sub>, H<sub>2</sub>O and N<sub>2</sub>. Therefore, carbon and hydrogen are considered as reducing elements with the corresponding valencies of +4 and +1, whereas oxygen is thought to be an oxidizing agent with a valency of -2, and nitrogen a valency of 0. To extrapolate the concept of combustion synthesis of ceramic oxide means considering metals as reducing agents with their valencies in the corresponding oxide or nitrate, i.e. +2 for magnesium (oxide), +3 for cerium (nitrate) and +4 for cerium (oxide). In the case of multiple valence elements, the final product is used for calculation.

The elemental stoichiometric coefficient,  $\varphi$ , which is the ratio between the total valencies of fuel (glycine; NH<sub>2</sub>CH<sub>2</sub>COOH) and that of the oxidizer (sodium nitrate), can be calculated following the method proposed by Jain et al. [21]:

$$\varphi = \frac{n(0_{(N)} + 2 \times 1_{(H)} + 4_{(C)} + 2 \times 1_{(H)} + 4_{(C)} - 2_{(O)} - 2_{(O)} + 1_{(H)})}{1_{(Na)} + 0_{(N)} + 3 \times -2_{(O)}}$$
(1)

where n is the mole of glycine. According to the propellant chemistry for stoichiometric redox reaction between fuel and an oxidizer, the  $\varphi$  ratio should be united (stoichiometric). A  $\varphi$  < 1 means oxidant-rich condition and  $\varphi$  > 1 means fuel-rich condition. To satisfy the principle in the present system, the sodium nitrate (oxidizing valency = 5 –) to glycine (reducing valency = 9+) molar ratio was found to be 1:0.56. The comprehensive reaction that formed NaNbO<sub>3</sub> can be written as:

$$36\text{NaNO}_3 + 18\text{Nb}_2\text{O}_5 + 20\text{NH}_2\text{CH}_2\text{COOH} \rightarrow 36\text{NaNbO}_3 + 50\text{H}_2\text{O} + 28\text{N}_2 + 40\text{CO}_2$$
 (2)

It should be noted that various fuel-to-oxidizer ratios should be carried out for investigating and comparing the effect of fuel-rich/fuel-lean mixtures on the synthesis of sodium niobate powder. In this study, sodium niobate powder was synthesized via the combustion synthesis technique for the first time. This process used sodium nitrate and niobium pentoxide as starting materials, and glycine was used as fuel. The different fuel-to-oxidizer molar ratios such as fuel-deficient (<0.56), equivalent stoichiometric (0.56) and fuel-rich (>0.56) condition were applied.

#### 2. Experimental procedure

For the combustion synthesis of perovskite sodium niobate powder, AR grade sodium nitrate (NaNO<sub>3</sub> 99.5%) and niobium pentoxide (Nb<sub>2</sub>O<sub>5</sub> 99.95%) were used as the oxidizer, and glycine (NH<sub>2</sub>CH<sub>2</sub>COOH 99.7%) as fuel. The appropriate amount

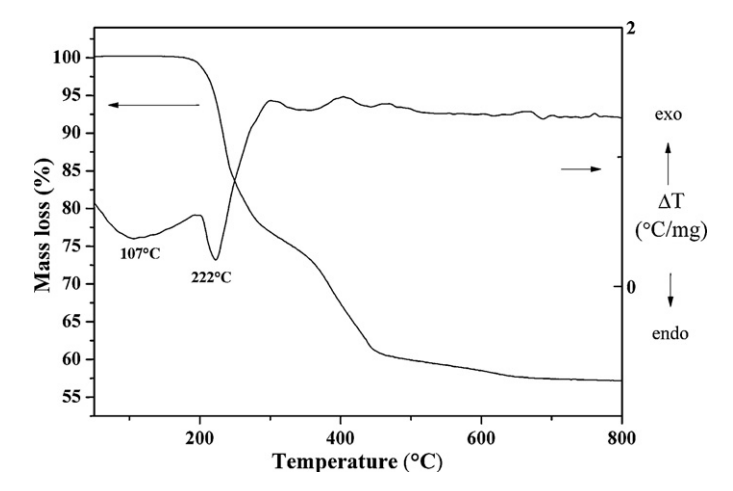


Fig. 1. TG-DTA curves of the precursor mixed in the stoichiometric proportion of NaNbO<sub>3</sub>.

of starting materials was weighed, mixed with de-ionized water in a glass beaker and stirred regularly for 30 min. The fuel (glycine) was then added and the mixture stirred for 30 min. After that, the solution precursor was boiled on a hotplate and then evaporated. Once the solution had thickened and begun to dry, the ignition took place when the temperature rapidly increased, which resulted in self-sustaining combustion with rapid evolution of a large volume of gas products, and formation of voluminous powder. For investigating thermal behavior of the precursor, the mixture of starting material was determined using thermo gravimetric analysis (TGA) and differential thermal analysis (DTA). The X-ray diffraction (XRD, Advance D8) technique was carried out on the combustion synthesized powder, using Ni-filtered  $\text{CuK}_{\alpha}$  radiation for phase identification and mean crystalline size estimation. The final powder product was characterized by using the Fourier transform infrared (FTIR) technique and scanning electron microscope (SEM, Hitachi S4700).

#### 3. Results and discussion

Fig. 1 shows the TG/DTA plots of the stoichiometric precursor for NaNbO<sub>3</sub> powder synthesis. From observations of the TGA curve, there appeared to be three-stages of weight loss from room temperature to 800 °C. The definition of initial temperature ( $T_{\rm in}$ ) is when the sample weight starts changing rapidly during the chemical reaction [23]. As the precursor was heated, a significant weight loss was observed as the temperature reached 170 °C, indicating that the  $T_{in}$  was around this heat. The weight loss did not stop until the temperature reached 480 °C. It was indicated clearly that this reaction belongs to a multi-stage reaction. The overall weight loss was found to be about 40%, which is close to the theoretical value of 36.87% that corresponds to the release of 50 mol H<sub>2</sub>O, 28 mol N<sub>2</sub> and 40 mol CO<sub>2</sub> related to Eq. (2). This outcome supported our conception that a hotplate can be used as a heating source because it is capable of initiating the combustion reaction at a temperature as low as that of the  $T_{in}$ .

The evolution XRD pattern of the combustion synthesized ceramic powder, with the fuel-to-oxidizer molar ratio, is illustrated in Fig. 2. The fuel-deficient (0.5) and equivalent stoichiometric ratio (0.56), were found (according to experimental observation) to have no ignition and combustion reaction in those compositions. Their XRD patterns correlated to detection results of the diffraction peaks of Nb<sub>2</sub>O<sub>5</sub> ( $\bullet$ ) (JCPDS file no. 30-0873) and NaNO<sub>3</sub> ( $\blacksquare$ ) (JCPDS file no. 85-0859) starting materials, with no evidence of perovskite NaNbO<sub>3</sub> phase found. Although the equivalent stoichiometric ratio (0.56) was calculated for maximum energy release, auto-ignition did not occur in this study. This could indicate that oxygen deficiency in the system and its environment might lead to combustion reaction and fail to follow the theory. The fuel-to-oxidizer molar ratio was increased by using the fuel-rich condition (>0.56), which was found to produce the perovskite NaNbO<sub>3</sub> ceramic powder, due to its diffraction peaks being detected for all different fuel contents

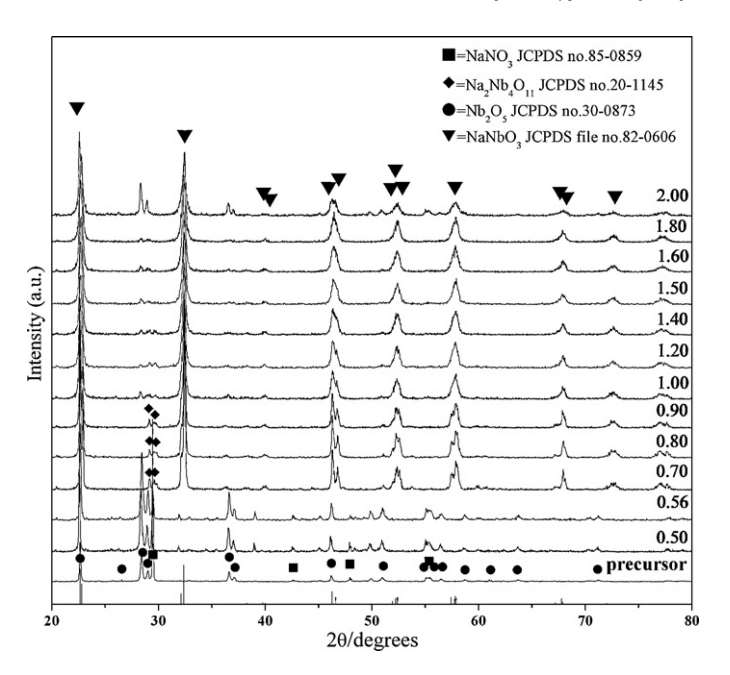


Fig. 2. X-ray diffraction patterns of NaNbO<sub>3</sub> powder obtained from various fuel-to-oxidant molar ratios.

(fuel-to-oxidizer molar ratio ranging from 0.7 to 2.0). This NaNbO<sub>3</sub> phase ( $\blacktriangledown$ ) was consistent with JCPDS file no. 82-0606, which corresponded to an orthorhombic structure with the space group, P2<sub>1</sub>ma (26). For a fuel-rich condition (fuel-to-oxidizer molar ratio of 0.7, 0.8 and 0.9), the NaNbO<sub>3</sub> phase ( $\blacktriangledown$ ) was detected with the accompanying pyrochlore phase of Na<sub>2</sub>Nb<sub>4</sub>O<sub>11</sub> ( $\spadesuit$ ), which matched JCPDS file no. 20-1145. No evidence of unreacted Nb<sub>2</sub>O<sub>5</sub> and/or NaNO<sub>3</sub> diffraction peak was found. As fuel content increased from the fuel-to-oxidizer molar ratio of 1.0–2.0, unreacted Nb<sub>2</sub>O<sub>5</sub> ( $\spadesuit$ ) (JCPDS file no. 30-0873) was found together with a majority of NaNbO<sub>3</sub> diffraction peaks. From the reflection peak, the average crystalline size (D) of NaNbO<sub>3</sub> powders was considered as a function of fuel content by using X-ray line broadening through Scherrer's equation [24]:

$$D = \frac{k\lambda}{\beta \cos \theta_B} \tag{3}$$

where D is the average crystalline size, k a constant taken as 0.89,  $\lambda$  the wavelength of X-ray radiation,  $\beta$  the full width at half maximum (FWHM) and  $\theta_B$  the diffraction angle. The consequent values are reported in Table 1. As the fuel content increased, the average crystalline size (D) was found to decreased from 44.51  $\pm$  11.99 nm (ratio of 0.7) to 26.11  $\pm$  13.69 nm (ratio of 2.0). This suggested that elevated fuel content could lead to the production of a smaller crystalline size (related to a small particle size) of powder. Nevertheless, as a consequence of additional cost and more carbon residual, an extremely high fuel-to-oxidizer molar ratio (fuel-rich ratio) did not always result in the desired production of powder [25].

Therefore, from findings on the fine nucleation condition of monophasic NaNbO<sub>3</sub> phase, the fuel-to-oxidizer molar ratio of 1.0 was selected to investigate the effect of calcination temperature. From this ratio, the volume fraction of the perovskite phase formation (%perovskite) of as-prepared powder was found to be as high as 93%. This relative value was considered by approximately calculating the ratio of the main X-ray peak intensities of NaNbO<sub>3</sub> and Nb<sub>2</sub>O<sub>5</sub> phases [26], according to the following equation; % perovskite =  $(I_{\text{perovskite}}/(I_{\text{perovskite}}+I_{\text{Nb}_2}O_5)) \times 100$ . Thus, the as-prepared powder was calcined at different temperatures for 4h with a heating/cooling rate of  $20\,^{\circ}\text{C/min}$ . The X-ray diffraction (XRD) patterns of sodium niobate (NaNbO<sub>3</sub>) powder, calcined for 4h at different temperatures, are illustrated in Fig. 3. As the XRD

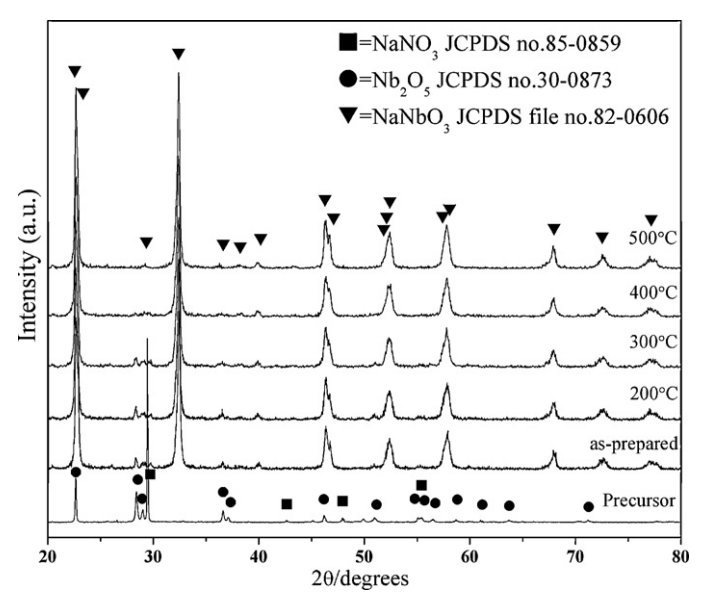


**Fig. 3.** X-ray diffraction patterns of NaNbO $_3$  powder (obtained from the fuel-to-oxidant molar ratio of 1.0) calcined at various temperatures for 4h with a heating/cooling rate of  $20 \, {}^{\circ}\text{C/min}$ .

pattern of as-prepared powder was composed of a slight Nb<sub>2</sub>O<sub>5</sub> ( $\bullet$ ) (JCPDS file no. 30-0873) phase, the intensity of that phase was found to decrease with increasing calcination temperature. The diffraction peak corresponded to the Nb<sub>2</sub>O<sub>5</sub>, which disappeared after calcination at 400 °C for 4 h, whereas monophasic perovskite NaNbO<sub>3</sub> phase was obtained. This result suggested that the perovskite NaNbO<sub>3</sub> powder could be synthesized by using the combustion synthesis process and calcinations at 400 °C for 4 h. This process was found to be a simple, rapid and cost-effective method when compared with the traditional solid-state reaction, which takes longer time and requires higher temperature [8,9]. In addition, the mean crystalline size (D), which is reported in Table 1, was not significantly varied between as-prepared powder (29.28  $\pm$  5.29 nm) and increasing calcination temperatures of up to 400 °C (27.84  $\pm$  7.12 nm). It can be suggested that calcina-

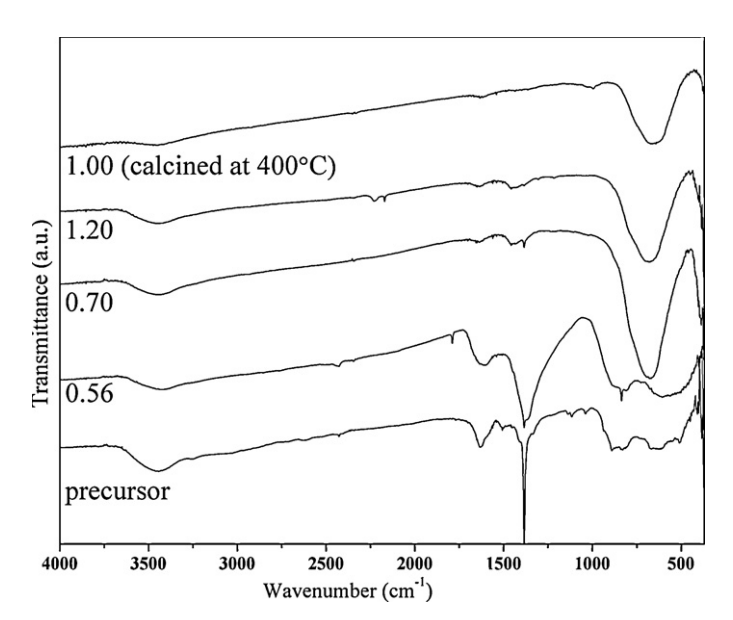


**Fig. 4.** FT-IR spectra of the precursor mixed in the stoichiometric proportion of NaNbO<sub>3</sub> powder obtained from various fuel-to-oxidant molar ratios and after the calcination step.

**Table 1**Mean crystalline size, *D*, of NaNbO<sub>2</sub> powder obtained from various fuel-to-oxidant molar ratios.

	Fuel-to-oxidant molar ratios								
	0.7	0.8	0.9	1.0	1.2	1.4	1.6	1.8	2.0
As-prepared	$44.51 \pm 11.99$	$42.59 \pm 11.54$	$37.31 \pm 8.54$	$29.09 \pm 5.29$	$27.45 \pm 5.86$	$26.29 \pm 5.97$	$24.40 \pm 4.92$	$23.79 \pm 5.52$	$26.12 \pm 13.69$
	Calcination temperature								
	200 °C	300 °C	400 °C	500 ∘	C 6	00 ° C	700 °C	800°C	900°C
Calcined powd	er 29.95 ±	4.51 31.51 ±	4.02 27.84±	7.12 30±8	32 ± 5.43 3	8.84±8.09	$60.72 \pm 8.09$	$70.87 \pm 9.22$	85.27 ± 15.65

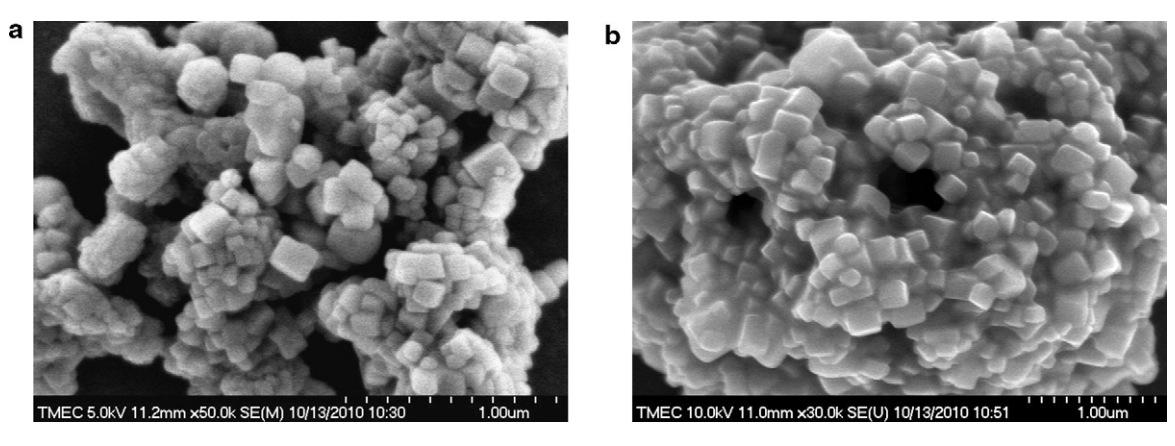


Fig. 5. SEM micrograph showing as-prepared NaNbO<sub>3</sub> powder synthesized using the fuel-to-oxidant molar ratio of 1.0 (a) and powder calcined at 400 °C for 4 h (b).

tions at this low temperature also produced a lower crystalline size when compared with the traditional solid state reaction method.

Fig. 4 shows the FT-IR spectroscopic studies of the crystalline NaNbO<sub>3</sub> obtained after combustion synthesis, its precursor without heat treatment and powder calcined at 400 °C for 4 h. For all powder, an IR band of around 3400 cm<sup>-1</sup> was assigned to O-H asymmetric stretching  $(v_3)$  [27], and on observation, it related to the moisture content of KBr. Regarding the precursor of NaNbO<sub>3</sub> powders without heat treatment, and as-prepared powder with a stoichiometric ratio (0.56), the IR spectrum indicated peaking of the characteristic band at  $\sim$ 1612,  $\sim$ 1385 and  $\sim$ 890 cm<sup>-1</sup>, which corresponded to the anti-symmetric carboxyl group stretching vibration, anti-symmetry NO<sub>3</sub><sup>-1</sup> stretching and bending vibration, respectively [28]. This result proved existence of the carboxyl and  $NO_3^{-1}$ group (belonging to the starting material) in those samples. With regard to fuel-rich ratios (0.7 and 1.2), the new broad absorption bands appeared after combustion at a low wave number of  $\sim$ 673 cm $^{-1}$ , suggesting that the Nb–O bond formation did occur. This Nb–O bond was believed to be the vibration ( $v_3$ ) mode in the corner-shared NbO<sub>6</sub> octahedron, according to reported IR spectra of niobate glass ceramics [28]. This result led to the assumption that the perovskite NaNbO3 phase was synthesized (which correlated to XRD analysis). However, the IR band of anti-symmetric COO<sup>-</sup> and that of anti-symmetry NO<sub>3</sub><sup>-1</sup> stretching vibration also were observed. This clearly indicated traces of existent carboxyl group and nitrate in as-prepared NaNbO3 powder, which cannot be detected when using the XRD technique. For powder calcined at 400 °C for 4 h, the spectra band of vibration  $(v_3)$  mode belonging to the Nb-O bond was found without observation of any starting material band. This can indicate that monophasic perovskite NaNbO<sub>3</sub> has been synthesized successfully after calcination at a temperature as low as 400 °C for 4 h. Fig. 5 shows an SEM micrograph of the as-prepared NaNbO<sub>3</sub> powder using the fuel-tooxidizer molar ratio of 1.0 (a) and powder calcined at 400 °C for 4 h (b). The powder was found to be polyhedral in shape, with uniform features. No evidence of a different or pyrochlore phase was found, which suggested the homogeneous character of the prepared powder. The average particle size, which can be estimated from micrographs, was found to be  $137\pm52\,\mathrm{nm}$  and  $226\pm46\,\mathrm{nm}$  for as-prepared and calcined powder, respectively. These particle size values are greater than the average crystalline size calculated from X-ray line broadening because a particle can be formed generally of many crystallites [29–31]. The particle growth for calcined powder seemed to be detected. It can be said that the firing process tends to produce agglomerated particles and grain growth, as reported by other works [32,33].

#### 4. Conclusions

Crystalline NaNbO $_3$  powder, with a volume fraction of the perovskite phase formation (% perovskite) as high as 93%, was synthesized directly via the solution combustion process using NaNO $_3$ , Nb $_2$ O $_5$  and glycine. Monophasic perovskite NaNbO $_3$  powder was obtained after calcination at 400 °C for 4 h. The fuel-to-oxidizer molar ratio was found to affect the combustion reaction and character of the powder obtained. The average crystalline size (D) was found to decrease from  $44.51\pm11.99\,\mathrm{nm}$  (ratio of 0.7) to  $26.11\pm13.69\,\mathrm{nm}$  (ratio of 2.0). This method is a simple, rapid, costand time-saving way of synthesizing stoichiometric, homogeneous and fine NaNbO $_3$  powder with a low calcination temperature. The powder obtained was found to be a uniform soft agglomerated particle.

#### Acknowledgements

This work was supported by the Thailand Research Fund (TRF), Thailand Graduate Institute of Science and Technology (TGIST), King Mongkut's Institute of Technology Ladkrabang Research (KMITL Research), and the National Nanotechnology Center (NANOTEC) NSTDA, Ministry of Science and Technology, Thailand through its "Center of Excellence Network" Program.

#### References

- [1] B. Jaffe, W.R. Cook Jr., H. Jaffe, Piezoelectric Ceramics, Academic Press, New York, 1971.
- [2] B. Jaffe, R.S. Roth, S. Marzullo, J. Appl. Phys. 25 (1954) 809-810.
- [3] N. Chaiyo, B. Boonchom, N. Vittayakorn, J. Mater. Sci. 45 (2010) 1443.
- [4] H.D. Megaw, Ferroelectrics 7 (1974) 87-89.
- [5] L.E. Cross, B. Nicholson, J. Phil. Magn. Ser. 46 (1955) 453-466.
- [6] G. Shirane, B. Newnham, R. Pepinsky, Phys. Rev. 96 (1954) 581-588.
- [7] Y. Shiratori, A. Magrez, C. Pithan, J. Eur. Ceram. Soc. 25 (2005) 2075–2079. [8] T. Nitta, J. Am. Ceram. Soc. 51 (1968) 626–629.
- [9] T. Rojac, O. Masson, R. Guinebretière, M. Kosec, B. Malič, J. Holc, J. Eur. Ceram. Soc. 17 (2007) 2265-2271.
- [10] C.C. Hwang, T.Y. Wu, J.S. Tsai, Mater. Sci. Eng. B 111 (2004) 49-56.
- [11] T. Rojac, M. Kosec, B. Malič, J. Holc, Mater. Res. Bull. 40 (2005) 341–345.
- [12] M.A.L. Nobre, E. Longo, E.R. Leite, J.A. Varela, Mater. Lett. 28 (1996) 215–220.
- [13] G. Li, T. Kako, D. Wang, Z. Zou, J. Ye, J. Phys. Chem. 69 (2008) 2487–2491.
   [14] K.C. Patil, S.T. Aruna, S. Ekambaram, Curr. Opin. Solid State Mater. Sci. 2 (1997)
- [15] K.C. Patil, S.T. Aruna, T. Mimani, Curr. Opin. Solid State Mater. Sci. 6 (2002) 507-512
- [16] D.A. Fumo, M.R. Morelli, A.M. Segadães, Mater. Res. Bull. 31 (1996) 1243-1255.
- [17] M.A. Raza, I.Z. Rahman, S. Beloshapkin, J. Alloys Compd. 485 (2009) 593-597.

- [18] M.W. Raja, S. Mahanty, P. Ghosh, R.N. Basu, H.S. Maiti, Mater. Res. Bull. 42 (2007) 1499-1506.

- [19] S.V. Chavan, P.U.M. Sastry, A.K. Tyagi, J. Alloys Compd. 456 (2008) 51–56.
  [20] N.P. Bansal, Z. Zhong, J. Power Sources 158 (2006) 148–153.
  [21] S.R. Jain, K.C. Adiga, V.R.P. Verneker, Combus. Flame 40 (1981) 71–79.
- [22] S.S. Manoharan, K.C. Patil, J. Am. Ceram. Soc. 75 (1992) 1012-1015.
- [23] L.A. Chick, L.R. Pederson, G.D. Maupin, J.L. Bates, L.E. Thomas, G.J. Exarthos, Mater. Lett 10 (1990) 6-12.
- [24] H.P. Klug, L.E. Alexander, X-ray Diffraction Procedure of Polycrystalline and
- Amorphous Materials, Jonh Wciley & Sons, New York, 1974. [25] A. Civera, M. Pavese, G. Saracco, V. Specchia, Catal. Today 83 (2003) 199–211.
- [26] G. Feng, H. Rongzi, L. Jiaji, L. Zhen, C. Lihong, T. Changsheng, J. Eur. Ceram. Soc. 29 (2009) 1687-1693.
- C. Weifan, L. Fengsheng, L. Leili, L. Yang, J. Rare Earths 24 (2006) 782–787.
- [28] S.H Xiao, W.F. Jiang, L.Y. Li, X.J. Li, Mater. Chem. Phys. 106 (2007) 82-87.
- [29] M.L. Lavčević, A. Turković, Scripta Mater. 46 (2002) 501–505.
- [30] W.-N. Wang, W. Widiyastuti, T. Ogi, I.W. Lenggoro, Chem. Mater. 19 (2007) 1723-1730.
- [31] N. Izu, W. Shin, I. Matsubara, N. Murayama, Sens. Actuators B 94 (2003) 222-227.
- [32] Y. Terashi, A. Purwanto, W.N. Wang, F. Iskandar, K. Okuyama, J. Eur. Ceram. Soc. 28 (2008) 2573.
- [33] R. Wongmaneerung, W. Chaisan, O. Khamman, R. Yimnirun, S. Ananta, Ceram. Int. 34 (2008) 813.

# Synthesis of potassium niobate (KNbO3) nano-powder by a modified solid-state reaction

Journal of Materials Science
Full Set - Includes

ISSN 0022-2461 Volume 46 Number 6

J Mater Sci (2010) 46:1585-1590 DOI 10.1007/ s10853-010-4967-5





Your article is protected by copyright and all rights are held exclusively by Springer Science+Business Media, LLC. This e-offprint is for personal use only and shall not be self-archived in electronic repositories. If you wish to self-archive your work, please use the accepted author's version for posting to your own website or your institution's repository. You may further deposit the accepted author's version on a funder's repository at a funder's request, provided it is not made publicly available until 12 months after publication.



# Synthesis of potassium niobate (KNbO<sub>3</sub>) nano-powder by a modified solid-state reaction

Nopsiri Chaiyo · Anucha Ruangphanit · Rangson Muanghlua · Surasak Niemcharoen · Banjong Boonchom · Naratip Vittayakorn

Received: 20 July 2010/Accepted: 29 September 2010/Published online: 15 October 2010 © Springer Science+Business Media, LLC 2010

**Abstract** Crystalline lead-free piezoelectric potassium niobate (KNbO<sub>3</sub>) powders have been synthesized through a modified solid-state reaction method. The thermal behavior of the K<sub>2</sub>C<sub>2</sub>O<sub>4</sub>·H<sub>2</sub>O and Nb<sub>2</sub>O<sub>5</sub> raw material mixture was investigated by thermogravimetric analysis (TGA) and differential thermal analysis (DTA). The X-ray diffraction technique (XRD) was used to investigate the phase formation and purity. The morphology of the powder obtained was characterized using a scanning electron microscope (SEM). The XRD pattern showed that the monophasic perovskite phase of KNbO<sub>3</sub> could be synthesized successfully at a

temperature as low as 550 °C for 240 min, with an average crystallite size of 36  $\pm$  8 nm. The SEM images suggested that the average particle size of the powder obtained was 278  $\pm$  75 nm.

#### N. Chaiyo · N. Vittayakorn Electroceramic Research Laboratory, College of KMITL Nanotechnology, King Mongkut's Institute of Technology

Nanotechnology, King Mongkut's Institute of Technolo Ladkrabang, Bangkok 10520, Thailand

N. Chaiyo · N. Vittayakorn

ThEP Center, CHE, 328 Si Ayutthaya Rd, Bangkok 10400, Thailand

#### A. Ruangphanit

Thai Micro Electronics Center (TMEC), National Electronics and Computer Technology Center, Chachoengsao, Chachoengsao, Thailand

#### R. Muanghlua · S. Niemcharoen

Faculty of Engineering, Department of Electronics, King Mongkut's Institute of Technology Ladkrabang, Bangkok 10520, Thailand

#### B. Boonchom

King Mongkut's Institute of Technology Ladkrabang, Chumphon Campus, 17/1 M. 6 Pha Thiew District, Chumphon 86160, Thailand

#### N. Vittayakorn (⊠)

Faculty of Science, Department of Chemistry, King Mongkut's Institute of Technology Ladkrabang, Bangkok 10520, Thailand e-mail: naratipcmu@yahoo.com

#### Introduction

Lead zirconate titanate (PZT) ceramics are used widely in piezoelectric applications, due to their superior piezoelectric properties near the morphotropic phase boundary (MPB) [1, 2]. However, more than 50% of the lead-based piezoelectric material contains poisonous lead, which is a major drawback [3]. It has been reported that the use of lead-based ceramics causes serious environmental problems and numerous physical symptoms [3]. Furthermore, EU legislation will enforce draft directives for waste from electrical and electronic equipment (WEEE), and restrictions on the use of certain hazardous substances in electrical and electronic equipment (RoHS) and end-of life vehicles (ELV) [4–6]. According to these issues, lead and other heavy metals should be phased out, and alternative lead-free piezoelectric materials are receiving considerable attention.

Among various alternative families, perovskite type (ABO<sub>3</sub>) ceramics have attracted much consideration. Among alkali metal niobates, potassium niobate (KNbO<sub>3</sub>) is a well-known perovskite oxide that possesses attractive physical and piezoelectric properties [6–9]. Furthermore, the electromechanical coupling factor of the thickness-extensional mode,  $k_{\rm t}$ , was reported to reach as high as 0.69 for the 49.5°-rotated X-cut on the Y-axis. This value of  $k_{\rm t}$  is the highest among current lead-free piezoelectrics [10]. However, the main hindrance regarding this alkali niobate-based material lies in the difficulty of preparing dense and stoichiometric controlled ceramics using the conventional



solid-state reaction and ordinary air sintering methods [11, 12]. These difficulties are caused by potassium volatility at high temperatures and excessive reactivity with moisture [13, 14]. Thus, different additive methods, hot pressing and spark plasma sintering have been used to improve ceramic densification [12, 15–19].

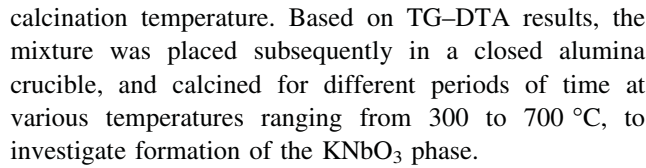
Several alternative ways for preparing alkali niobates have been investigated and developed: the hydrothermal [20] and hydrothermal-assisted sol-gel method [22], and glycothermal [23], nitrate-tartarate precursor technique [21], etc. However, most chemical synthesis routes require high purity reactants, which are more expensive and demand complicated procedures and specific apparatus. A modified solid-state reaction method has been used to synthesize the NaTaO<sub>3</sub> perovskite type material successfully, with reduced reaction temperature [24]. In this method, the carbonate compound was replaced by oxalate, and the addition of urea played an important role. Recently, this method also has been applied to synthesize lead-free sodium niobate (NaNbO<sub>3</sub>) powders (without fuel) [25]. By replacing sodium carbonate using oxalate as the raw material, a lower calcination temperature and fine powders with an average crystallite size of  $31.45 \pm 5.28$  nm were achieved.

In this study, a modified solid-state reaction method, with an expected lower reaction temperature, was used to synthesize KNbO<sub>3</sub> particles, using potassium oxalate as raw material without the addition of any fuel. Effects of the calcination conditions on the KNbO<sub>3</sub> phase development were investigated by the X-ray diffraction technique (XRD) and a scanning electron microscope (SEM).

#### **Experiment**

 $KNbO_3$  was synthesized by a modified solid-state reaction method. Reagent-grade potassium oxalate monohydrate ( $K_2C_2O_4\cdot H_2O$ , 99.9%) and niobium oxide ( $Nb_2O_5$ , 99.9%) were employed as the starting material. The raw materials were weighed in stoichiometric quantities following the equation below.

These starting materials were mixed by the ball-milling method using ethyl alcohol and partially stabilized zirconia balls for 18 h. Then, the mixture was dried on a hot plate with regular stirring for a suitable period. After drying, the precursor mixture was determined by thermo gravimetric analysis (TGA, Perkin Elmer) and differential thermal analysis (DTA, Perkin Elmer) for investigating the thermal behavior during heat treatment and finding the appropriate



Subsequently, calcined powders were inspected by room temperature X-ray diffraction (XRD, Advance D8), using Ni-filtered  $CuK_{\alpha}$  radiation to examine the effect of thermal treatment on the phase development and optimal calcination condition of crystalline KNbO<sub>3</sub> powder formation. The room temperature FTIR spectra were recorded in the range of 4,000–400 cm<sup>-1</sup> (Perkin-Elmer, Spectrum GX spectrometer), with eight scans and a resolution of 4 cm<sup>-1</sup> using KBr pellets. Powder morphologies and particle size were figured directly using a scanning electron microscope (SEM, Hitachi S4700).

#### Results and discussion

Figure 1 shows the TG–DTA curves of the stoichiometric precursor of KNbO<sub>3</sub>. The thermogravimetric (TG) curve of the KNbO<sub>3</sub> precursor shows three stages of weight loss from room temperature to 1,300 °C. Four endothermic peaks at 123, 398, 524 and 1,066 °C were observed in the differential thermal analysis (DTA) curve. Three weightloss steps were observed in the ranges of 50–121, 121–172, and 416–532 °C. The corresponding weight losses seen were 3.92, 1.07, and 16.00%. The overall weight loss was found to be about 21%, which is close to the theoretical value of 20.01%, and corresponds to the release of 1 mol H<sub>2</sub>O, 1 mol CO, and 1 mol CO<sub>2</sub> related to Eq. 1. In the temperature range from 50 to 121 °C (first stage), the initial weight loss of 3.92% showed decomposition of the oxalate molecule releasing water molecules (0.98 mol

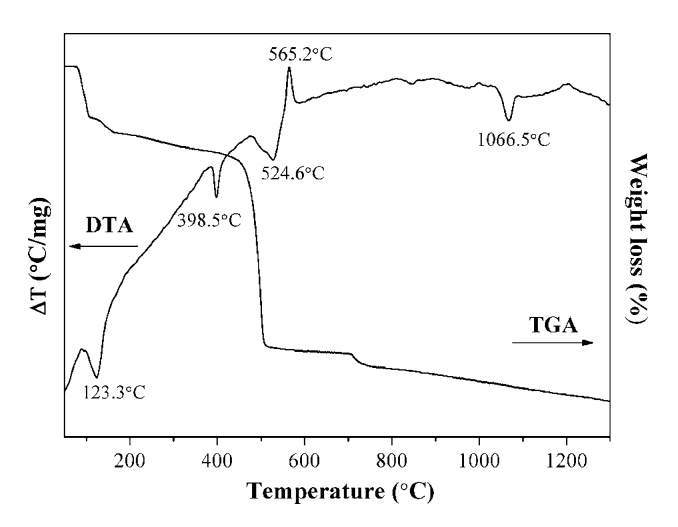


Fig. 1 TG–DTA curves of an uncalcined powder mixed in the stoichiometric proportion of  $\mbox{KNbO}_3$ 



J Mater Sci (2011) 46:1585–1590

 $H_2O$ ), which concurred with the theoretical value for releasing 1.00 mol  $H_2O$  (4.00%). This weight-loss corresponded to the endothermic peak, centered at 123 °C.

The second and third weight-loss steps illustrated the highest weight loss ( $\sim 17\%$ ), which indicated a large elimination of organic compound that could be related to the release of CO and CO<sub>2</sub> by combustion reactions according to Eqs. 2 and 3 (16% theoretically). In the temperature range from 121 to 532 °C, the DTA curve shows corresponding endothermic peaks (398 and 524 °C) that agree with the TG result.

$$K_2C_2O_4 \rightarrow K_2CO_3 + CO$$
 (2)

$$K_2CO_3 \rightarrow K_2O + CO_2$$
 (3)

However, an exothermic DTA peak was found centered at 565 °C. This implied that the third decomposition stage could lead to the formation of potassium niobate compound, which could be expected from the exothermic peak at 565 °C (as confirmed by XRD analysis in Fig. 2). As the temperature increased to 695 °C, weight loss was found to start again in the TGA curve, which could be correlated to the decomposition of the activated-K<sub>2</sub>CO<sub>3</sub> residue. It is well known that K2C2O4 decomposes to K<sub>2</sub>CO<sub>3</sub> at a higher temperature; however, this carbonate residue could decompose at a lower temperature when its degree of arrangement is lower than its initial state [26]. When heating further, an endothermic peak (without the observed weight-loss stage) could correspond to the phase transformation at 1,066 °C. Therefore, temperatures from the above TG-DTA analysis, which ranged from 300 to 700 °C, were selected for calcinations and investigation of the phase formation. The mixture of raw materials in the

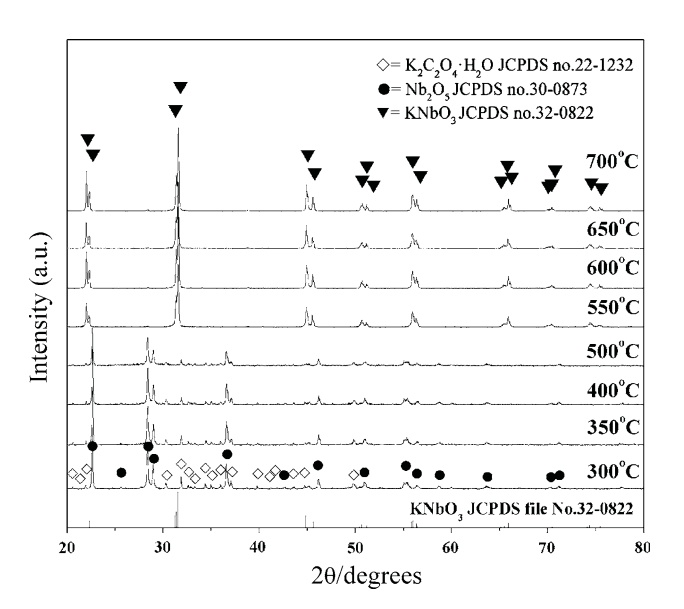


Fig. 2 X-ray diffraction patterns of KNbO<sub>3</sub> powder calcined at various temperatures for 4 h with a heating/cooling rate of 20 °C/min

required stoichiometric ratio was calcined in air using a heating/cooling rate of 20 °C/min at various temperatures and followed by the phase analysis using an X-ray diffractometer

The X-ray diffraction (XRD) patterns of potassium niobate (KNbO<sub>3</sub>) powders, calcined for 4 h at different temperatures, are illustrated in Fig. 2. The diffraction pattern of the powder calcined at 300 °C suggests a composition of potassium oxalate ( $\diamondsuit$ ) (JCPDS no.22-1232) and niobium oxide (●) (JCPDS no.30-0873) raw materials. No evidence of the KNbO3 perovskite phase was found. As calcination temperatures increased to 500 °C, diffraction peaks of un-reacted raw materials were also found, but with lower intensity. This could demonstrate that the completed reaction cannot occur at such a low temperature range. As the diffusion coefficient is a temperature dependent parameter, the rate of diffusion is affected greatly by higher temperatures [27], which also could improve higher atomic mobility [28]. Nonetheless, the powders calcined from 550 to 700 °C showed diffraction peaks that could correspond to the orthorhombic potassium niobate perovskite phase (KNbO<sub>3</sub>) JCPDS no.32-0822 (**▼**). Amplified peak intensities can be seen after calcinations at increased temperatures. However, this result indicates the formation of KNbO<sub>3</sub> perovskite phase powder, which passes through the calcination temperatures from 550 to 700 °C in 4 h. These temperatures were lower than those in the chemical synthesis of KNbO<sub>3</sub>, which used the polymerized complex method (PC method). This technique achieved the KNbO<sub>3</sub> compound after the calcination step at 900 °C [29], or once the citrate precursor route had obtained KNbO<sub>3</sub> nanopowder after heat treatment at 800 °C [30]. In addition, other chemical methods always require high purity reagent, which is more expensive, and involves complex procedures.

For a verdict on fine KNbO<sub>3</sub> nucleation condition, a temperature of 550 °C was chosen to find the effect of calcination dwell time. The mixture of raw material powder was calcined at 550 °C for 15-360 min. The XRD analysis of calcined powder, with a different dwell time (Fig. 3), revealed an amorphous phase for a calcination period of 15 min, and no distinct crystalline phase could be detected. The absence of reflection peaks that correspond to K<sub>2</sub>C<sub>2</sub>O<sub>4</sub>·H<sub>2</sub>O and Nb<sub>2</sub>O<sub>5</sub> indicated the amorphous nature of the powder obtained. The presence of reflection peaks for the XRD pattern of powder calcined at 550 °C for 20 min or longer could be ascribed to the crystalline phase of the sample. The different diffraction pattern of the powder, calcined for 20 min, suggests the nucleation condition of the KNbO<sub>3</sub> phase, which was confirmed by further soaking time. After the calcination step at 550 °C for 20 min or longer, the powder showed an XRD pattern that could be matched with the perovskite potassium niobate (KN) phase



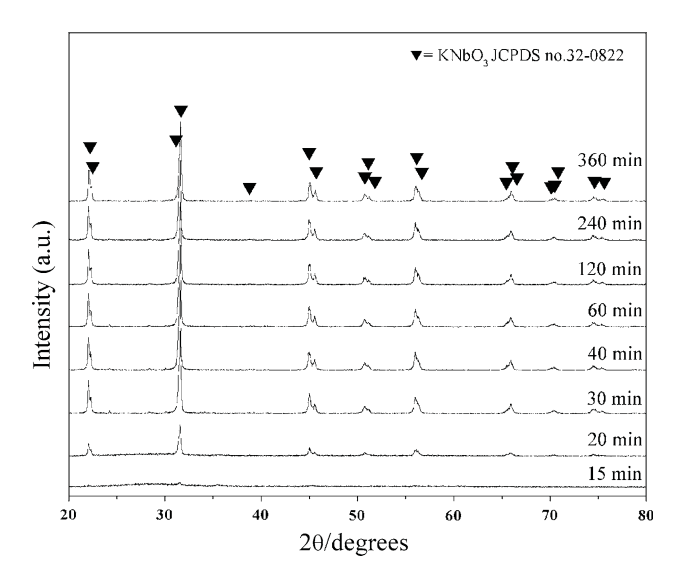


Fig. 3 X-ray diffraction patterns of  $KNbO_3$  powder calcined at the calcination temperature of 550 °C for various dwell times with a heating/cooling rate of 20 °C/min

JCPDS no.32-0822. These XRD analyses agreed with the TG-DTA analysis, in which crystallization of the KNbO<sub>3</sub> phase was found around the previously mentioned temperature range. During the course of calcinations, the rise in calcination temperature and dwell time resulted in increased diffraction peak intensities, which related to higher crystallinity of the powder. This was supported by the increase in lattice parameters and average crystallite size, as revealed below. Nevertheless, it has been confirmed that this modified solid state reaction method can synthesize pure KNbO<sub>3</sub> phase powder by using potassium oxalate monohydrate as starting material at the calcination temperature of 550 °C for 20 min. This calcination temperature is much lower than that used in a mixed oxide powder process, which lies in the range of 800 °C [9, 11, 13, 31, 32], or solution process (sol-gel and precipitation

methods) that requires calcination temperatures of over 600 °C [33, 34]. Since XRD analysis suggested an orthorhombic crystal structure for preparing KNbO<sub>3</sub> powder, lattice parameters of the sample could be deliberate by means of the UnitCell program package (ftp://rock.esc. cam.ac.uk/pub/minp/UnitCell/). The corresponding cell parameters, which are close to those reported from JCPDS file No.32-0822 ( $a=5.695~\rm nm,~b=5.721~\rm nm,~and~c=3.973~\rm nm$ ) are given in Table 1. The suggested orthorhombic crystal structure, obtained from matching with the JCPDS file, could be supported by this correlation of lattice parameters.

The average crystallite size of KNbO<sub>3</sub> powders was considered as a function of calcination temperature, and time for broadening the X-ray line of the reflection peak using Scherrer's equation [35]:  $D = k\lambda/\beta\cos\theta_{\rm B}$ , where D is the average crystallite size, k a constant taken as 0.89,  $\lambda$  the wavelength of X-ray radiation,  $\beta$  the full width at half maximum (FWHM), and  $\theta_B$  the diffraction angle. The corresponding values are reported in Table 2. The average crystallite size of powders, calcined from 550 to 700 °C for 4 h, was found to be about  $36 \pm 8$  to  $58 \pm 6$  nm. As the dwell time increased, it was found that the average crystallite size of calcined powders was increasing from  $33 \pm 9$  to  $36 \pm 8$  nm. The low D values suggest that the surface area of calcined powder was high enough to support high sinterability sufficiently [36]. The increase in crystallinity of the KNbO3 phase was affected by increasing dwell time and calcination temperature. This consequence may confirm that the dwell time and calcination temperature also play an important role in developing the pure phase creation.

Figure 4 shows the FT-IR spectroscopic studies of the crystalline potassium niobate (KNbO<sub>3</sub>) before and after the calcination step. The IR band for the uncalcined precursor was observed at 3,253 cm<sup>-1</sup>, due to O-H asymmetric

**Table 1** Lattice parameters of the KNbO<sub>3</sub> powder calcined at various calcination temperatures for 4 h

Table 2 Mean crystalline size,
D, of the KNbO <sub>3</sub> powder
calcined at different
temperatures for 4 h and for a
different dwell time at 550 °C

KNbO <sub>3</sub>	Calcinations temperature (°C)						
Lattice parameter	550	600	650	700			
a	$5.6929 \pm 0.0005$	$5.6876 \pm 0.0070$	$5.7019 \pm 0.0022$	$5.6952 \pm 0.0028$			
b	$5.6989\pm0.0080$	$5.6994 \pm 0.0048$	$5.7153 \pm 0.0108$	$5.6980\pm0.0060$			
<u>c</u>	$3.9802 \pm 0.0005$	$3.9768 \pm 0.0006$	$3.9912 \pm 0.0155$	$3.9777 \pm 0.0030$			

$KNbO_3$	Calcin	Calcination temperature (°C)							
	550		600	650		700			
D	36.40	± 8.25	$41.46 \pm 8.84$	53.59	± 6.56	$57.81 \pm 6.31$			
550 °C	Dwell time (min)								
	20	30	40	60	120	240			
D	$33.15 \pm 9.22$	$34.36 \pm 7.92$	$34.54 \pm 8.128$	$35.30 \pm 8.30$	$35.97 \pm 6.47$	$36.40 \pm 8.25$			



J Mater Sci (2011) 46:1585–1590

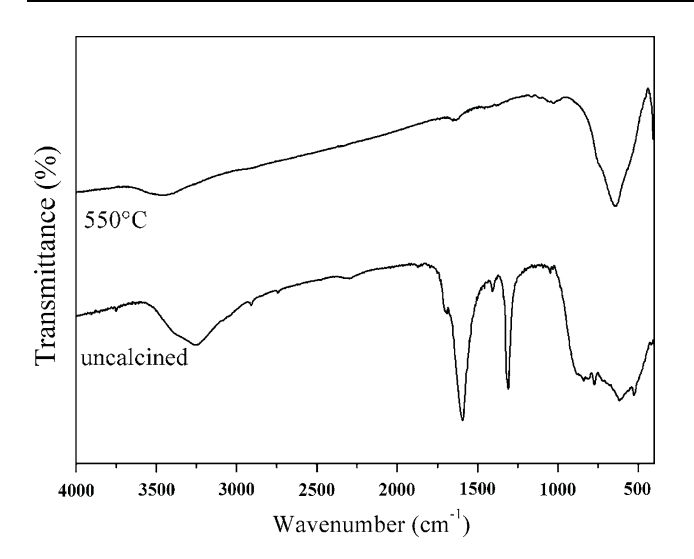


**Fig. 4** FT-IR spectra of an uncalcined powder mixed in the stoichiometric proportion of KNbO<sub>3</sub> and KNbO<sub>3</sub> particles calcined at 550 °C

stretching  $(v_3)$ , which related to the moisture content of the KBr pellet and scissor bending mode (v2) of HO-H at  $1,600 \text{ cm}^{-1} \text{ and } 1,310 \text{ cm}^{-1}$ . When KNbO<sub>3</sub> powders were calcined at 550 °C for 4 h, the absorption of bands at a low wave number range of 620 cm<sup>-1</sup> suggested occurrence of Nb-O bond formation, which was believed to be the vibration  $(v_3)$  mode in the corner-shared NbO<sub>6</sub> octahedron, according to the reported IR spectra of niobate glass ceramics [37]. This result shows that the perovskite KNbO<sub>3</sub> phase was synthesized, which correlated with other results. The TG result indicated that the mass loss in the TG curve at around 700 °C could be the result of the K<sub>2</sub>CO<sub>3</sub> residue decomposition, however, the FTIR band corresponding to the C-O stretching mode of carbonate at 1,450 cm<sup>-1</sup> [38] was not found in KNbO<sub>3</sub> powders calcined at 550 °C for 4 h. This observation could be described as the effect of dwell time.

Figure 5 shows SEM micrographs of KNbO<sub>3</sub> powder prepared using a modified solid state reaction method at 550 and 700 °C for 240 min. The KNbO<sub>3</sub> powder was found to be polyhedral in shape, with uniform features. The secondary phase could not be observed, which suggested the homogeneous character of the powder prepared. The mean particle sizes, which can be estimated from the micrographs, were found to be 278  $\pm$  75 and 341  $\pm$  80 for powder obtained at 550 and 700 °C, respectively. Particle growth was detected in powder calcined at a higher temperature. This value is greater than the average crystallite size, calculated from X-ray line broadening. It was believed that this contradictory value could indicate the agglomerate of the calcined powders. As reported by other studies [39, 40], the firing process tends to produce agglomerated particles and grain growth. No evidence of a different or pyrochlore phase was found. This outcome relates to the XRD result, in which the monophasic perovskite phase of KNbO3 can be established after calcinations at 550 °C for 240 min.

#### Conclusion

Crystalline KNbO<sub>3</sub> powder was prepared from a modified solid state reaction of  $K_2C_2O_4$ · $H_2O$  and  $Nb_2O_5$ . The final product was confirmed by XRD and SEM techniques. This is a simple cost- and time-saving method for synthesizing stoichiometric, homogeneous, and fine KNbO<sub>3</sub> powder, with a low calcination temperature of 550 °C for 240 min. This temperature is about 250 °C lower than others used, even in conventional methods. The powder obtained was found to be a uniform agglomerated particle that possesses an average crystallite size (defined by XRD) of between  $36 \pm 8$  and  $58 \pm 6$  nm, and a mean particle size (defined by SEM micrograph) of  $278 \pm 75$  nm.

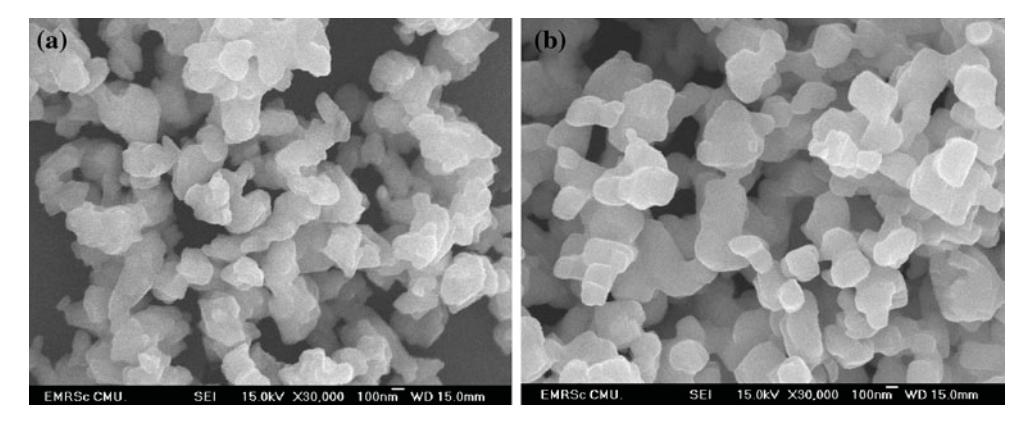


Fig. 5 SEM micrographs showing KNbO<sub>3</sub> powder synthesized at 550 °C (a) and 700 °C (b), for 4 h with a heating/cooling rate of 20 °C/min



1590 J Mater Sci (2011) 46:1585–1590

Acknowledgements This study was supported by the Thailand Research Fund (TRF), Thailand Graduate Institute of Science and Technology (TGIST), and the National Nanotechnology Center (NANOTEC) NSTDA, Ministry of Science and Technology, Thailand, through its "Center of Excellence Network" Program.

#### References

- Miclea C, Tanasoiu C, Miclea CF, Amarande L, Gheorghiu A, Spanulescu I, Plavitu C, Miclea CT, Cioangher MC, Trupina L, Iuga A (2007) J Eur Ceram Soc 27:4055
- Setter N (2002) Piezoelectric materials in devices. Ceramic lab, EPFL, Switzerland
- Lead and you: a guide to working safely with lead (2003) HSE (UK Health and Safety Executive). http://www.hse.gov.uk/ pubns/indg305.pdf. Accessed 25 Apr 2004
- Commission of the European Communities (2003) Directive 2002/ 96/EC of the European Parliament and of the Council of 27 January 2003 on waste electrical and electronic equipment (WEEE). Off J Eur Union, L37, 46:24
- Commission of the European Communities (2003) Directive 2002/ 95/EC of the European Parliament and of the Council of 27 January 2003 on the restriction of the use of certain hazardous substances in electrical and electronic equipment. Off J Eur Union, L37, 46:19
- Ichiki M, Zhang L, Tanaka M, Maeda R (2004) J Eur Ceram Soc 24:1693
- 7. Liu J-F, Li X-L, Li Y-D (2003) J Cryst Growth 247:419
- 8. Paula AJ, Parra R, Zaghete MA, Varela JA (2008) Mater Lett 62:2581
- 9. Yamanouchi K, Odagawa H, Kojima T, Matsumura T (1997) Electron Lett 33:193
- Nakamura K, Kawamura Y (1999) Proc IEEE Ultrason Symp 2: 1013
- Matsumoto K, Hiruma Y, Nagata H, Takenaka T (2008) Ceram Int 34:787
- 12. Makovec D, Pribošič I, Drofenik M (2008) Ceram Int 34:89
- 13. Lu CH, Lo SY, Lin HC (1998) Mater Lett 34:172
- Muthurajan H, Kumar HH, Samuel V, Gupta UN, Ravi V (2008) Ceram Int 34:671

- Kim MS, Lee DS, Park EC, Jeong SJ, Song JS (2007) J Eur Ceram Soc 27:4121
- Mgbemere HE, Herber R-P, Schneider GA (2009) J Eur Ceram Soc 29:1729
- 17. Wang R, Xie R, Sekiya T, Shimojo Y, Akimune Y, Hirosaki N, Itoh M (2002) Jpn J Appl Phys 41:7119
- 18. Ahn ZS, Schulze WA (1987) J Am Ceram Soc 70:18
- 19. Jaeger RE, Egerton L (1962) J Am Ceram Soc 45:209
- 20. Chang Y, Yang Z, Wei L, Liu B (2006) Mater Sci Eng A 437:301
- 21. Bhattacharyya K, Tyagi AK (2009) J Alloys Compd 470:580
- 22. Amini MM, Mirzaee M (2009) Ceram Int 35:2367
- 23. Lu C-H, Lo S-Y, Wang Y-L (2002) Mater Lett 55:121
- 24. Xu J, Xue D, Yan C (2005) Mater Lett 59:2920
- Chaiyo N, Boonchom B, Vittayakorn N (2010) J Mater Sci 45:1443. doi:10.1007/s10853-009-4098-z
- Vlaev L, Nedelchev N, Gyurova K, Zagorcheva M (2008) J Anal Appl Pyrolysis 81:253
- Hsiao Y-J, Chang Y-H, Chang Y-S, Fang T-H, Chai Y-L, Chem G-J, Huang T-W (2007) Mater Sci Eng B 136:129
- 28. Callister WD (2007) Materials science and engineering: an introduction. Wiley, New York
- Pribošič I, Makovec D, Drofenik M (2005) J Eur Ceram Soc 25:2713
- 30. Kakimoto K, Ito T, Ohsato H (2008) Jpn J Appl Phys 47:7669
- Malic B, Bernard J, Bencan A, Kosec M (2008) J Eur Ceram Soc 28:1191
- Chang Y, Yang Z-P, Ma D, Liu Z, Wang Z (2008) J Appl Phys 104:024109
- 33. Amini MM, Sacks MD (1991) J Am Ceram Soc 74:53
- 34. Kim KJ, Matijevic E (1992) J Mater Res 7:912
- 35. Klug HP, Alexander LE (1974) X-ray diffraction procedure of polycrystalline and amorphous materials. Wiley, New York
- Lanfredi S, Dessemond L, Rodrigue ACM (2000) J Eur Ceram Soc 20:983
- de Andrade JS, Pinheiro AG, Vasconcelos IF et al (1999) J Phys Condens Matter 11:4451
- Böke HA, Akkurt S, Özdemir S, Göktürk EH, Saltik ENC (2004) Mater Lett 58:723
- Terashi Y, Purwanto A, Wang WN, Iskandar F, Okuyama K (2008) J Eur Ceram Soc 28:2573
- Wongmaneerung R, Chaisan W, Khamman O, Yimnirun R, Ananta S (2008) Ceram Int 34:813





Contents lists available at ScienceDirect

## **Current Applied Physics**

journal homepage: www.elsevier.com/locate/cap



# Phase transition behaviour and electrical properties of lead-free $(K_{0.5}Na_{0.5})$ $NbO_3$ -LiNbO<sub>3</sub>-LiSbO<sub>3</sub> piezoelectric ceramics

Rangson Muanghlua <sup>a</sup>, Surasak Niemcharoen <sup>a</sup>, Manoon Sutapun <sup>b,e</sup>, Banjong Boonchom <sup>c</sup>, Naratip Vittayakorn <sup>b,d,e,\*</sup>

- <sup>a</sup> Department of Electronics, Faculty of Engineering, King Mongkut's Institute of Technology Ladkrabang, Bangkok 10520, Thailand
- b Electroceramic Research Laboratory, College of KMITL Nanotechnology, King Mongkut's Institute of Technology Ladkrabang, Bangkok 10520, Thailand
- <sup>c</sup> King Mongkut's Institute of Technology Ladkrabang, Chumphon Campus, 17/1M. 6 Pha Thiew District, Chumphon 86160, Thailand
- <sup>d</sup> Department of Chemistry, Faculty of Science, King Mongkut's Institute of Technology Ladkrabang, Bangkok 10520, Thailand
- e ThEP Center, CHE, 328 Si Ayutthaya Rd., Bangkok 10400, Thailand

#### ARTICLE INFO

Article history:
Received 28 September 2009
Received in revised form
21 July 2010
Accepted 18 August 2010
Available online 9 September 2010

Keywords: Lead-free piezoelectric Dielectric properties Perovskite structure (K<sub>0.5</sub>Na<sub>0.5</sub>)NbO<sub>3</sub> LiNbO<sub>3</sub>

#### ABSTRACT

The ternary system of  $0.945(K_{0.5}Na_{0.5}NbO_3)-(0.055-x)LiNbO_3-xLiSbO_3$  [0.945KNN-(0.055-x)LN-xLS]; x=0.0-0.055 lead-free piezoelectric ceramics was fabricated by the conventional mixed oxide method with normal sintering. The crystal structure was studied by means of X-ray diffraction (XRD). The results of XRD patterns show that complete solid solutions of the mixed phase between the orthorhombic and tetragonal perovskite phase were observed. The DSC and dielectric data show that the amount of LiSbO\_3 in  $K_{0.5}Na_{0.5}NbO_3-LiNbO_3$  solid solution slightly decreases the paraelectric cubic-ferroelectric tetragonal phase transition ( $T_C$ ) to a low temperature. Furthermore, good dielectric and piezoelectric properties were observed at composition, x=0.03. The polymorphic phase transition between the orthorhombic and tetragonal phases plays a very important role in enhancement of the piezoelectric properties of KNN-LN-LS ceramics.

© 2010 Elsevier B.V. All rights reserved.

#### 1. Introduction

Lead-based piezoelectric materials such as Pb(Zr,Ti)O<sub>3</sub> (PZT) ceramics are the most widely used, due to their superior piezoelectric performances [1]. However, the toxicity of lead oxide, which contains more than 60 wt%, can cause damage to the kidney, brain and nervous system [2]. In recent years, many countries have required that all electronic equipment be lead-free for human health and environmental protection. Therefore, urgent development of lead-free piezoelectric ceramics, with outstanding properties for replacing lead-based ceramics, is necessary, and recent attention on this topic has been paid to (K,Na)NbO<sub>3</sub> and (KNN)-based ceramics, due to their good piezoelectric properties and high Curie temperature [3]. It is well known that not only the morphotropic phase boundary (MPB) between orthorhombic and tetragonal phase, but also the polymorphic orthorhombic and tetragonal phase transition

E-mail address: naratipcmu@yahoo.com (N. Vittayakorn).

temperature play an important role in the electrical properties of KNN-based ceramics [4,5]. It was reported that the polymorphic orthorhombic-tetragonal phase transition temperature (PPT) strongly affects the electrical properties of KNN-based ceramics, and a PPT near room temperature would be helpful in obtaining enhanced electrical properties. Recently, Guo et al observed excellent electrical properties in the  $(1-x)(K_{0.5}Na_{0.5})NbO_3-xLiNbO_3$ system [6]. The coexistence of orthorhombic-tetragonal phase was found at 0.05 < x < 0.07. Excellent piezoelectric and electromechanical responses;  $d_{33} = 235$  pC/N,  $k_p = 44\%$ , and  $k_t = 48\%$ , were obtained as samples, with the composition, x = 0.052. Recent studies have also found that the binary system of  $(1 - x)K_{0.5}Na_{0.5}NbO_3 - x$ LiSbO<sub>3</sub>; [(1-x)KNN-xLS] at the composition,  $x \sim 0.052$ , exhibited good piezoelectric properties at room temperature, with electromechanical coupling factors of  $k_{33} \sim 62\%$  and  $k_{31} \sim 30\%$ , and piezoelectric coefficients of  $d_{33} \sim 265 \text{ pC/N}$  and  $d_{31} \sim -116 \text{ pC/N}$ [7]. The piezoelectric, electromechanical, and elastic properties were determined as a function of temperature, showing anomalous behaviour at around room temperature, which related to the orthorhombic to tetragonal polymorphic phase transition (PPT) [7]. Since both the 0.945KNN-0.055LN [6] and 0.948KNN-0.052LS [7]

 $<sup>^{*}</sup>$  Corresponding author. Department of Chemistry, Faculty of Science, King Mongkut's Institute of Technology Ladkrabang, Bangkok 10520, Thailand. Fax:  $\pm$ 66 2 3264415.

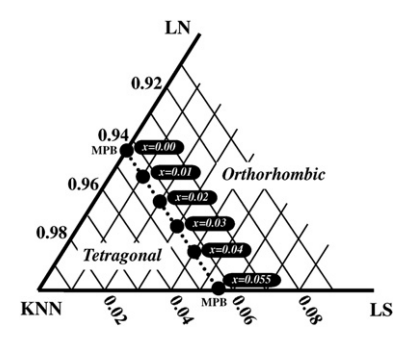


**Fig. 1.** Composition studied in the  $0.945K_{0.5}Na_{0.5}NbO_3$ — $(0.055-x)LiNbO_3$ — $xLiSbO_3$  ternary solid solution.

compositions have excellent electrical properties; the combination of these two systems to form a KNN–LN–LS ternary solid solution is very interesting. In this study, the ternary solid solution of  $0.945 \mathrm{KNN} - (0.055 - x) \ \mathrm{LN} - x \mathrm{LS}$ , where x = 0 - 0.055, was synthesized. To obtain a homogeneous perovskite solid solution and better electrical properties, the samples were prepared by a conventional solid state reaction process. Fig. 1 schematically shows the composition range that was studied in this work. In this study, the influence of LiNbO3 (LN) and LiSbO3 (LS) addition on phase transitions, and electrical properties of KNN ceramics are also reported.

#### 2. Experiment

The sample, 0.945KNN-(0.055-x)LN-xLS, where x = 0.00, 0.01, 0.02, 0.03, 0.04 and 0.055, was prepared using the conventional solid state reaction process with normal sintering. Reagentgrade oxide and carbonate powders of K<sub>2</sub>CO<sub>3</sub> (99.0%), Na<sub>2</sub>CO<sub>3</sub> (99.5%), Li<sub>2</sub>CO<sub>3</sub> (99.9%), Nb<sub>2</sub>O<sub>5</sub> (99.5%) and Sb<sub>2</sub>O<sub>3</sub> (99.9%) were used as starting raw materials. The powders were weighed according to the stoichiometric formula and ball milled in absolute ethanol for 24 h. The dried slurries were calcined at 850 °C for 4 h, then ball milled again for 24 h. The granulated powders were pressed into disks of 15 mm diameter and 1 mm thickness and then pressed using a cold isostatic pressing (CIP) technique under 300 MPa. These disks were sintered in air at 1030-1070 °C for 2 h. The density of the fired samples was determined by Archimedes method and found to be greater than 95% theoretical. Silver paste (Heraeus C1000) was fired on both sides of the samples at 550 °C for 10 min, as electrodes for dielectric measurements. The crystal structures were determined by X-ray diffraction (XRD) analysis

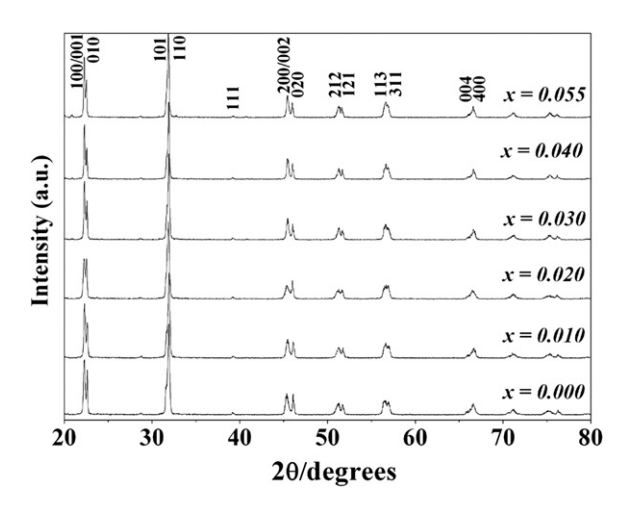
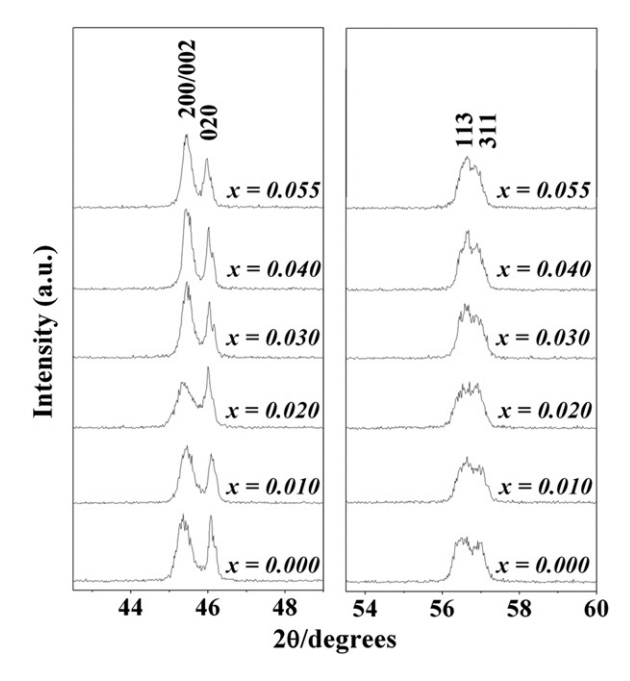


Fig. 2. XRD patterns of  $0.945 K_{0.5} Na_{0.5} NbO_3 - (0.055-x) LiNbO_3 - x LiSbO_3$  ceramics at room temperature.



**Fig. 3.** XRD patterns of the (200) and (113) peaks of  $0.945K_{0.5}Na_{0.5}NbO_3-(0.055-x)$  LiNbO<sub>3</sub>-xLiSbO<sub>3</sub> ceramics.

obtained by using  $\text{Cu}\text{K}\alpha$  radiation (Bruker-D8 Advance). The temperature dependence of the samples' dielectric constant was examined using a programmable furnace with an LCR analyzer (HP-4284, Hewlett–Packard Inc.). A differential scanning calorimeter (DSC) was used to follow the phase transitions of sintered ceramics. The ceramics were poled for piezoelectric measurement in a silicone oil bath at room temperature for 30 min and field strength of 3–4 kV/mm. The piezoelectric coefficient,  $d_{33}$ , of the samples, which were left for 24 h after poling, was measured using a  $d_{33}$  meter (Model 8000, Penne baker). The planar electromechanical coupling factor,  $k_{\rm p}$ , was calculated from the resonance and antiresonance frequencies, based on IEEE standards.

#### 3. Results and discussion

Fig. 2 displays the XRD pattern of 0.945KNN-(0.055 - x)LN-xLS ceramics sintered at 1050 °C. A series of continuous solid solutions between KNNLN and KNNLS was clearly formed. The phase structure in all samples was a pure perovskite phase and no secondary

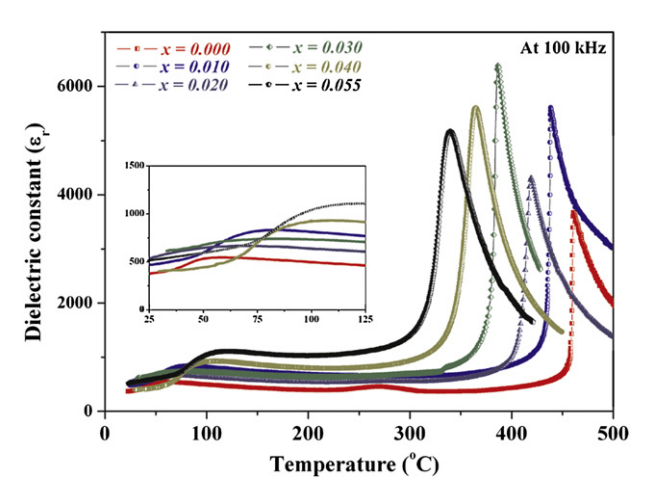


**Fig. 4.** Temperature dependence of the dielectric constant  $(ε_r)$  at 100 kHz of 0.945K<sub>0.5</sub>Na<sub>0.5</sub>NbO<sub>3</sub>—(0.055 – x)LiNbO<sub>3</sub>—xLiSbO<sub>3</sub> ceramics as a function of x.

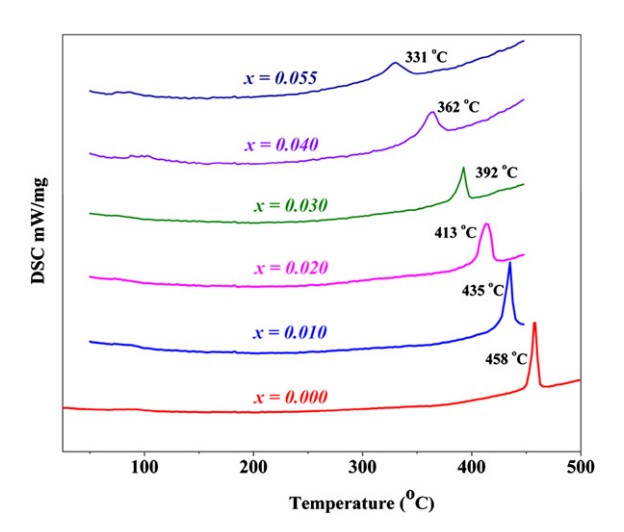


**Fig. 5.** DSC heating curves of 0.945K<sub>0.5</sub>Na<sub>0.5</sub>NbO<sub>3</sub>—(0.055 – *x*)LiNbO<sub>3</sub>—*x*LiSbO<sub>3</sub> ceramics as a function of *x*.

impurity could be certified. The result indicated that the dopants were completely diffused into the (K<sub>0.5</sub>Na<sub>0.5</sub>)NbO<sub>3</sub> lattices, with Li<sup>+</sup> entering the  $(Na_{0.5}K_{0.5})^+$  sites and  $Sb^{5+}$  occupying the  $Nb^{5+}$  sites, to form a new solid solution in all compositions. Fig. 3 shows the XRD patterns of 0.945KNN–(0.055 – x)LN–xLS ceramics in the  $2\theta$  range of 43-48° and 54-60°. The compositions in this study were selected across the orthorhombic-tetragonal coexistence region between the KNN-LS and KNN-LN system. As expected, coexistence of the orthorhombic-tetragonal phase was observed in all compositions. Interestingly, with an increasing x value, the diffraction peaks located at a higher angle, and (113) and (311) peaks near  $2\theta = 57^{\circ}$ , tended to merge into a single peak, which indicated that the crystalline structure varied from the orthorhombic—tetragonal phase to the orthorhombic-rich phase. Similar behaviour was observed in the  $xPb(Zn_{1/3}Nb_{2/3}O_3)-(0.2-x)Pb(Ni_{1/3}O_3)$  $_3Nb_{2/3})O_3-0.8Pb(Zr_{1/2}Ti_{1/2})O_3$  ternary system [8].

The temperature dependence of the dielectric constant,  $(\varepsilon_r)$  of 0.945KNN-(0.055 - x)LN-xLS ceramics, at the frequency of 100 kHz is shown in Fig. 4, together with the temperature dependence of  $\varepsilon_r$  for all ceramic samples; showing two phase transitions that correspond to those of ferroelectric tetragonal to paraelectric cubic  $(T_C)$  and polymorphic ferroelectric orthorhombic to tetragonal ferroelectric  $(T_{\rm O-T})$  for high and low transition temperatures, respectively. The  $T_{\rm c}$ decreases with increased composition x, however;  $T_{O-T}$  tends to decrease with increasing composition x up to 0.03 and continues to increase with a further increase of x. The  $T_{0-T}$  was approximately 52, 53, 49, 48, 85 and 95 °C for compositions x = 0.00, 0.01, 0.02, 0.03,0.04 and 0.055, respectively. Interestingly, the  $T_{O-T}$  phase transition temperature for the composition, x = 0.03, is close to room temperature and this composition is expected to attribute to high piezoelectric responses. The phase transition temperature; clearly confirmed by DSC measurement, is presented in Fig. 5. At the composition, x = 0.00, a sharp peak was observed near the

**Table 1** The values of  $\varepsilon_{\rm max}$ ,  $T_{\rm max}$ ,  $T_{\rm t}$ ,  $\Delta H$ ,  $\Delta S$  and  $\Delta S/T_{\rm t}$  of KNN–LN–LS ceramics.

Compositions	$\varepsilon_{ ext{max}}$	$T_{o-T}$	$T_{\text{max}}$	$T_{\rm t}$	ΔΗ	$\Delta S \times 10^3$	$(\Delta S/T_{\rm t}) \times 10^6$
		(°C)	(°C)	(°C)	$\overline{(Jg^{-1})}$	$\overline{(\mathrm{J}\mathrm{g}^{-1}\mathrm{K}^{-1})}$	$(J g^{-1} K^{-2})$
x = 0.000	4800	52	460	458	4.174	9.114	19.900
x = 0.010	5750	53	439	435	3.471	7.979	18.343
x = 0.020	4400	49	419	413	2.858	6.920	16.755
x = 0.030	6700	48	388	392	1.800	4.592	11.714
x = 0.040	5700	85	363	362	0.987	2.727	7.533
x = 0.055	5250	95	340	331	0.014	0.042	0.127

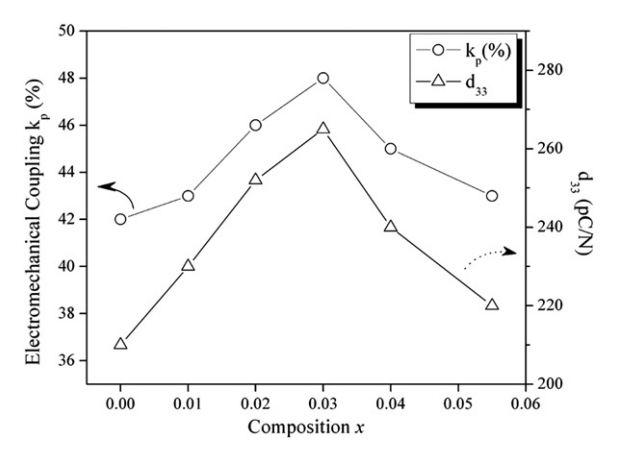


**Fig. 6.** Planar electromechanical coefficient and piezoelectric constant of 0.945K<sub>0.5</sub>Na<sub>0.5</sub>NbO<sub>3</sub>-(0.055 – *x*)LiNbO<sub>3</sub>-*x*LiSbO<sub>3</sub> ceramics as a function of *x*.

ferroelectric tetragonal to paraelectric cubic phase transition temperature, and the transition is of the first order, due to its association with a significant value of  $\Delta H$ . The transition temperature defined by maximum heat capacity, which closely followed the ferroelectric to paraelectric transition temperature revealed by the dielectric measurement, is shown in Fig. 4. The peak value of heat capacity became weaker, and heat capacity anomaly gradually broader, with increasing LS concentration. These results indicated that the phase transition deviates gradually from the first order type. Stenger and Burggraaf et al. [9] observed that the change in entropy  $(\Delta S)$  and  $\Delta S/T_t$  correlates with the fluctuation probability in conjunction with a small spontaneous lattice deformation and polarization. They explained that large values of the ratio,  $\Delta S/T_{\rm t}$  give sharp transition and lower values, which lead to diffuse behaviour. Table 1 shows that the  $\Delta S$  and  $\Delta S/T_t$  values are small for the LS doped sample, when compared to the KNN-LN sample. This indicates the existence of diffuseness in the phase transition behaviour, which increases with increasing LS content, and coincides well with the dielectric results in the composition range investigated. This behaviour can originate from the more complex occupation of the A and B sites in an ABO<sub>3</sub> perovskite structure and heterogeneous compositions, which also give rise to random fields that tend to make the phase transition "diffuse" instead of sharp, as in a normal ferroelectric. Fig. 6 shows the piezoelectric constant,  $d_{33}$ , and planar electromechanical coupling factor,  $k_{\rm p}$ , of polarized 0.945KNN-(0.055 - x) LN—xLS ceramics as a function of LiSbO<sub>3</sub> concentration. It can be seen that the property exhibits a compositional dependence when  $d_{33}$  and  $k_{\rm p}$  of the composition, x = 0.00, show values of 210 pC/N and 0.42, respectively, with increasing x,  $d_{33}$  and  $k_p$  to the maximum values of 265 pC/N and 0.48 at x = 0.03. As expected, the composition, x = 0.3, shows the maximum  $d_{33}$  and  $k_p$  value in the KNN-LN-LS system. Therefore, it can be concluded that the polymorphic phase transition between the orthorhombic and tetragonal phases plays a very important role in enhancement of the piezoelectric properties of KNN-LN-LS ceramics. Similar behaviour was observed in the KNN-LN [6] KNN-LT [10] and KNN-LT-BNT-BT [11] system. The KNN-LN-LS samples showed good piezoelectric properties when compared with the KNN-LN [6] and KNN-LS system [7].

#### 4. Conclusion

In this study,  $0.945K_{0.5}Na_{0.5}NbO_3-(0.055-x)LiNbO_3-xLiSbO_3$  ceramics were prepared by the conventional solid state reaction process with normal sintering. All ceramics with a perovskite structure are mixed phase of orthorhombic and tetragonal phase. The phase transition temperature of tetragonal–cubic ( $T_C$ ) was

decreased with increasing x. Furthermore, good dielectric and piezoelectric properties were observed at composition, x = 0.03. The polymorphic phase transition between the orthorhombic and tetragonal phases plays a very important role in enhancement of the piezoelectric properties of KNN-LN-LS ceramics.

#### Acknowledgements

This work was supported by the Thailand Research Fund (TRF), and the National Nanotechnology Center (NANOTEC) NSTDA, Ministry of Science and Technology, Thailand, through its "Center of Excellence Network" program.

#### References

- [1] B. Jaffe, W.R. Cook, H. Jaffe, Piezoelectric Ceramics. Academic, USA, 1971.
- [2] Y. Saito, H. Takao, T. Tani, T. Nonoyama, K. Takatori, T. Homma, T. Nagaya, M. Nagamura, Nature 432 (2004) 84.
- [3] T.R. Shrout, S.J. Zhang, J. Electroceram. 19 (2007) 113.

- [4] G.H. Haertling, J. Am. Ceram. Soc. 50 (1967) 329.
  [5] K. Kakimoto, I. Masuda, H. Ohsato, J. Eur. Ceram. Soc. 25 (2005) 2719.
  [6] Y. Guo, K. Kakimoto, H. Ohsato, Appl. Phys. Lett. 85 (2004) 4121.
- [7] S. Zhang, R. Xia, T.R. Shrout, J. Appl. Phys. 100 (2006) 104108.
  [8] S. Nabunmee, G. Rujijanagul, N. Vittayakorn, D.P. Cann, J. Appl. Phys. 102 (2007) 094108.
- [9] C. Stenger, A.J. Burggraaf, Phys. Stat. Sol. 61 (1980) 275.
  [10] Y. Dai, X. Zhan, G. Zhou, Appl. Phys. Lett. 90 (2007) 26290.
  [11] Y. Dai, X. Zhang, J. Eur. Ceram. Soc. 28 (2008) 3193.